Karlsruhe Institute of Technology

Influence of the magnetic field on the transmission characteristics and the neutrino mass systematic of the KATRIN experiment

Zur Erlangung des akademischen Grades eines
Doktors der Naturwissenschaften
von der Fakultät für Physik
des Karlsruher Instituts für Technologie
genehmigte
Dissertation

von

Dipl.-Phys. Moritz Gérard Erhard

aus Stuttgart

Referent:	Prof. Dr. Guido Drexlin Institut für Experimentelle Kernphysik, KIT
Korreferent:	Prof. Dr. Wim de Boer Institut für Experimentelle Kernphysik, KIT

Tag der mündlichen Prüfung: 1.7.2016

Declaration of authorship

I hereby declare that this thesis is my own work and effort and that it has not been submitted anywhere for any award. Where other sources of information have been used, they have been acknowledged.

Hiermit versichere ich, die vorliegende Arbeit selbstständig verfasst und keine anderen als die angegebenen Quellen und Hilfsmittel benutzt sowie die Zitate deutlich kenntlich gemacht zu haben.

Karlsruhe, 15.06.2016 Moritz Erhard

Abstract

The thesis at hand has successfully investigated and characterized the extended magnet system of the KATRIN experiment and implemented a detailed simulation model to take into account all field contributions. A concise modeling and understanding of the magnetic field close to the analyzing plane is crucial for a precise measurement and analysis of the neutrino mass with a sensitivity of 200 meV (90 % C.L.). A key aspect of the work performed here is that the contributions of individual magnets to the field in the analyzing plane in the spectrometer have been identified for various configurations. Based on these measurements, the previously undetermined remaining magnetic background field could be quantified. The advanced magnetic field model of this thesis allows to significantly reduce previously unexplained field deviations, verified by an in-depth analysis of extensive transmission function measurements with an electron gun, offering a sharp energy distribution and small angular spread. Of key importance thereby was a precise reconstruction of the emitted electrons of the electron gun in Monte Carlo simulations and the implementation of a realistic electron spectrum of the electron gun in the analysis framework. When all magnetic field contributions are taken into account, the transmission properties of the spectrometer can be determined with an accuracy level which is improved by a factor 3 in comparison to previous analyses. Correspondingly, the magnetic field there is determined to an unprecedented accuracy with a deviation between measurement and simulation of $(3 \pm 11)\,\mu\mathrm{T}$ when a field of $363\,\mu\mathrm{T}$ is applied. Finally, the influence of identified magnetic field deviations on the neutrino mass sensitivity of the KATRIN experiment is studied by means of extensive ensemble tests. From this, an upper limit on the magnetic field of $585\,\mu\mathrm{T}$ in the KATRIN spectrometer is deduced to restrict the additional contribution to the systematic uncertainty budget to a level of 1 % for an optimal measurement of the neutrino mass.

Introduction and Objectives

Neutrino physics is arguably one of the most interesting fields of research in modern physics. Being the only fundamental electrically neutral fermions, neutrinos participate solely in the weak interaction. Oddly enough, they are also by far the most abundant known fermionic matter particles in the universe. Neutrinos thus form an important link between particle physics and cosmology offering many opportunities to probe physics beyond the Standard Model.

A key approach to study new physics is the investigation of neutrino masses and mixing. In various neutrino oscillation experiments a non-vanishing neutrino mass has been established. However, owing to their very nature, oscillation experiments can observe only the mass differences between the neutrino flavors. Attempts to identify the absolute scale of the neutrino mass could only establish upper limits so far, suggesting neutrino masses in the sub-eV regime. Non zero neutrino masses are a clear indication of physics beyond the Standard Model that could lead to the detection of a violation of the lepton number and further CP violation, the Majorana-nature of neutrinos and, correspondingly a new energy scale.

A key project to directly measure the effective electron neutrino mass $m_{\bar{\nu}_e}$ is the Karlsruhe TRitium Neutrino (KATRIN) experiment, the most advanced tritium β-decay based experiment. With all sub components now being on-site at the Karlsruhe Institute of Technology (KIT) in Germany, the KATRIN experiment has entered the final phase of its commissioning. It is designed to improve the current sensitivity by one order of magnitude to an unprecedented value of $m_{\bar{\nu}_e}$ of 200 meV at 90 % C.L. after 3 effective years of data taking. To reach this ambitious goal, KATRIN will combine a high-luminosity windowless gaseous source of molecular tritium with a large volume high-resolution integrating spectrometer based on the MAC-E filter principle.

The 10^{10} β-decay electrons emitted from the source will be guided by a system of 23 superconducting solenoids and 16 normal conducting magnets along a 70 m-long beam line to the detector system. A crucial role therein is the probability of an electron to be transmitted through the spectrometer, which depends on its energy as well as on the angle relative to the magnetic field. This complex functionality is referred to as transmission function. Due to the isotropic electron emission in the source and the integrating properties of the MAC-E filter technique, a precise knowledge of the transmission function is indispensable.

As a narrow-width transmission function is advantageous, the MAC-E filter principle calls for a large reduction of the guiding magnetic field of several T down to 100 µT. Throughout the entire setup the field must be controlled and monitored precisely, which is especially challenging in the low-field region in the central analyzing plane of the main spectrometer.

Objectives

This doctoral thesis focuses on a precision magnetic field model for the low field region of the spectrometer by closely examining the following topics:

- Take into account the fields of all magnet systems in the KATRIN beam-line to obtain a complete picture of the effective magnetic field in the low field regions. This task requires to determine the alignment of the individual magnets and to identify deviations from design specifications. With this information included in the software framework of KATRIN a detailed magnetic field model is generated.
- Commissioning of the precision magnetic field monitoring system in the low fields region of the main spectrometer to enable a verification of the magnetic field model. The monitoring system is not only the primary tool to study the field layout and stray fields in the commissioning phases, but also to allow long-term monitoring of the magnetic field during neutrino mass measurements.
- Precision investigation of the transmission characteristics of the main spectrometer. Measurements with a quasi mono-energetic and angular selective electron gun provide the means to study the transmission function with the required accuracy. In particular, this allows to map the retarding potential and magnetic field in the main spectrometer. In addition, these measurements represent an independent verification of the monitoring system results.
- Quantify the impact of magnetic field properties on the neutrino mass systematic and sensitivity. Up to now, the magnetic field and related uncertainties were not included in the KATRIN systematic uncertainty budget. Accordingly, all properties of the magnetic field that influence the neutrino mass sensitivity must be identified and their respective impact evaluated.

Outline

A brief introduction to neutrino physics will be given in the first chapter. The first part focuses on the phenomenology of neutrino flavor oscillations and models for neutrino mass generation. Secondly, former, present and upcoming experiments to identify the neutrino mass are reviewed.

The second chapter is dedicated to the KATRIN experiment, with the working principle of the MAC-E filter technique together with the transmission function being detailed. Finally, the main components of the experimental beam-line are introduced.

The setup in use during the 2014/15 commissioning measurements with the spectrometer are presented in the third chapter. This includes a detailed overview of all hardware and software systems as well as the analysis framework.

The large air coil system is the dominant source to shape the low field region of the main spectrometer. The ensemble of specific field configurations are characterized thoroughly in the fourth chapter.

The fifth chapter details the in-depth analysis of the magnetic field with the field monitoring system. This includes all super conducting and normal conducting coils as well as the remaining magnetic field. In addition, a straight forward technique to minimize the background magnetic field is introduced.

Measurements of the electromagnetic properties of the main spectrometer are described in the sixth chapter, where the measurement strategy and analysis methods are presented. The focus here is on a precise characterization of the electron gun properties to deduce the spectrometer properties with unprecedented accuracy.

In the seventh chapter the identified magnetic field perturbations are incorporated into Monte-Carlo based ensemble tests with respect to their impact on neutrino mass systematics. A total of four distinct effects are tested in five field configurations. The results are derived in a generalized formulation of the neutrino mass shift as a function of the absolute field.

In the final chapter the results of this thesis are summarized and its implications on upcoming measurements are presented.

Contents

CHAPTER 1

Neutrino physics

> Neutrino physics is largely an art of learning a great deal by observing nothing.
> *Harari, Haim* (ref. [Sch88])

Neutrino physics is one of the most exciting fields of science due to major breakthroughs that have been accomplished in the last decades. With the recent Nobel Prize in 2015, awarded to T. Kajita and A. B. McDonald for the experimental observation of neutrino oscillations, another boost has been given to the neutrino research and emphasizes the important role of neutrinos to extend the frontiers of physics. Many neutrino properties remain unknown today due to their weak interaction. One of these is its mass, a characteristic implication of neutrino oscillation.

In section 1.1 the implementation of neutrinos in the standard model of physics is outlined, from their postulation and discovery up to our modern view. As neutrino oscillation is the gateway to physics beyond the standard model (SM), its theoretical principle and the experimental methods to discover key parameters of oscillation are introduced in section 1.2. Finally, various approaches to identify the neutrino mass scale are presented in section 1.3, including previous, recent and future experiments. The KATRIN experiment is a flagship of the direct search for the neutrino mass where this thesis is embedded in.

This chapter invokes several text books which can be consulted for deeper and broader information about neutrino physics (ref. [Zub12], [Per04], [Alt03], [Sch97]).

1.1 Neutrinos in the Standard Model

In the beginning of the 20th century radioactive decay processes were discovered (ref. [Bec01]). Three different modii were identified, called α-, β- and γ-decay (ref. [DSc03]). In case of the β-decay a continuous spectrum was observed (ref. [Cha14], [Sco35]) which could only be explained when the process is interpreted as an three-body decay

$$\mathrm{n} \rightarrow \mathrm{p} + \mathrm{e}^- + \bar{\nu}_\mathrm{e} \tag{1.1}$$

with the neutrino as an additional particle (ref. [Pau30]). Shortly after, an adequate theoretical description of the β-decay was published (ref. [Fer34]). Fermi's theory is not only a milestone in particle physics, but a still valid and vital part of the theoretical foundation of the KATRIN experiment.

The tiny cross-section with matter of about $10^{-44}\,\mathrm{cm}^2$ of low-energy neutrinos prevented the experimental discovery for the next 20 years (ref. [Bet34]). When the Poltergeist experiment was exposed to the intense neutrino flux of a nuclear reactor the electron anti-neutrino could finally be detected (ref. [Cow56], [Rei60]). Subsequently two further neutrino flavors were discovered in accelerator experiments. At Brookhaven National Laboratory the muon-neutrino ν_μ was observed with the AGS accelerator via pion decay (ref. [Dan62]) and the tau-neutrino in a similar way by the DONUT collaboration (ref. [Kod01]).

The three generations of the neutrino are embedded in the SM of physics. The SM splits the group of elementary particles in quarks and leptons together with their interactions via intermediating gauge bosons of the fundamental weak, strong and electromagnetic force. As a fully closed, renormalizable quantum description of the gravitational force remains to be found, gravitation is neglected in the further discussion. The masses of particles can be explained within the SM by spontaneous symmetry breaking. This mechanism also predicts the last particle of the SM, the Higgs boson, that was just recently discovered (ref. [Aad12], [Cha12]). In the SM all quarks and leptons are fermions, each group split in three generations. Labeled by weak interacting eigenstates, the neutrinos are grouped in doublets with their leptonic counterparts. However, only left-handed neutrinos and right-handed antineutrinos are observed in weak interactions. As the charged current weak interaction is described by a pure V-A coupling, parity is maximally violated. Due to the underlying SU(2) gauge-symmetry neutrinos remain massless in the original SM.

1.2 Neutrino oscillation

In contradiction to the SM assumption of massless neutrino, the theory of neutrino oscillation requires at least two neutrinos of non-vanishing masses. The discovery of the neutrino oscillation is therefore a first step towards physics beyond the SM.

Experimental hints of the neutrino oscillation originate from the solar neutrino problem (section 1.2.1). The core concept of neutrino oscillation is to disentangle the flavor and mass-eigenstates which are discussed in section 1.2.2. By this mechanism further eigenstates are introduced. These are associated with so-called sterile neutrinos that interact purely via the gravitational force. Beside sterile neutrinos, other processes to generate a neutrino mass are possible. A brief introduction to the nature and origin of the neutrino mass is given in section 1.2.3.

1.2.1 Solar neutrino problem

In the core of the sun, nuclear fusion processes release an enormous amount of energy and neutrinos. Protons are fused to form helium in the netto reaction of

$$4\mathrm{p} \rightarrow {}^4\mathrm{He} + \mathrm{e}^+ + 2\nu_\mathrm{e} + 26.73\,\mathrm{MeV}, \tag{1.2}$$

where two electron neutrinos are generated. More precisely, the fusion reaction is split in different sub-processes such as the pp-cycle and the CNO-cycle. The standard solar model (SSM) describes the reactions in the sun (ref. [Bah64a], [Bah64b]), in all of which electron neutrinos are the only generated neutrino flavor (fig. 1.1).

The first experiment to measure the neutrino flux from the sun started in 1970. Located in the Homestake mine 1.478 km under ground, where 615 t of liquid Tetrachloroethene CCl_4

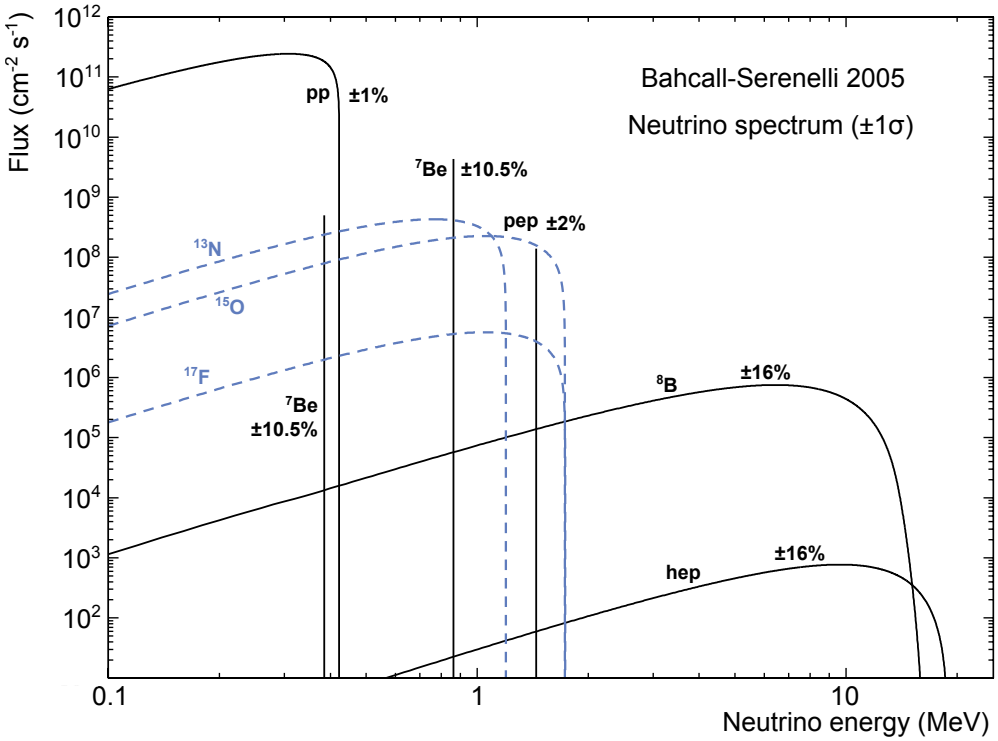

Figure 1.1: Flux of solar neutrinos for various fusion processes in the sun. Depicted ratios are based on the predictions of the solar standard model. The ^{8}B neutrinos are the easiest ones to detect, despite the reduced flux. Figure adapted from ref. [Bah05].

served as a target to observe the inverse β decay

$$\nu_{\mathrm{e}} + {}^{37}\mathrm{Cl} \rightarrow {}^{37}\mathrm{Ar} + \mathrm{e}^{-}. \tag{1.3}$$

The extracted and purified Argon is detected via electron capture and thereby the solar neutrino flux is assessed (ref. [Dav64]). In 20 years of operation, the experiment established a neutrino deficit of 2/3 compared to the SSM prediction, referred to as the solar neutrino problem (ref. [Jr79], [Bah95]). This significant deviation from theory was confirmed by other radio-chemical experiments, such as GALLEX (ref. [Ham99]), SAGE (ref. [Abd02]), and GNO (ref. [Alt05]). In the Kamiokande experiment, a Cherenkov detector is deployed to observe neutrino electron scattering in a water tank, where the deficit was confirmed as well (ref. [Fuk96], [Mak62]).

Several explanations for a description of the solar neutrino problem were proposed, one of which was the concept of neutrino oscillations. Already introduced in the 1960', it allows a flavor change ($\nu_{\mathrm{e}} \rightarrow \nu_{\mu,\tau}$) along the path from the source to the detector (ref. [Pon68]). Consequently, the absolute neutrino flux calculation based on the SSM are correct but the composition of neutrino flavors observed on earth is changed. As all of the mentioned experiments were sensitive to the electron neutrino flux only, the neutrino oscillation could not be evaluated at this stage and the solar problem remained unresolved.

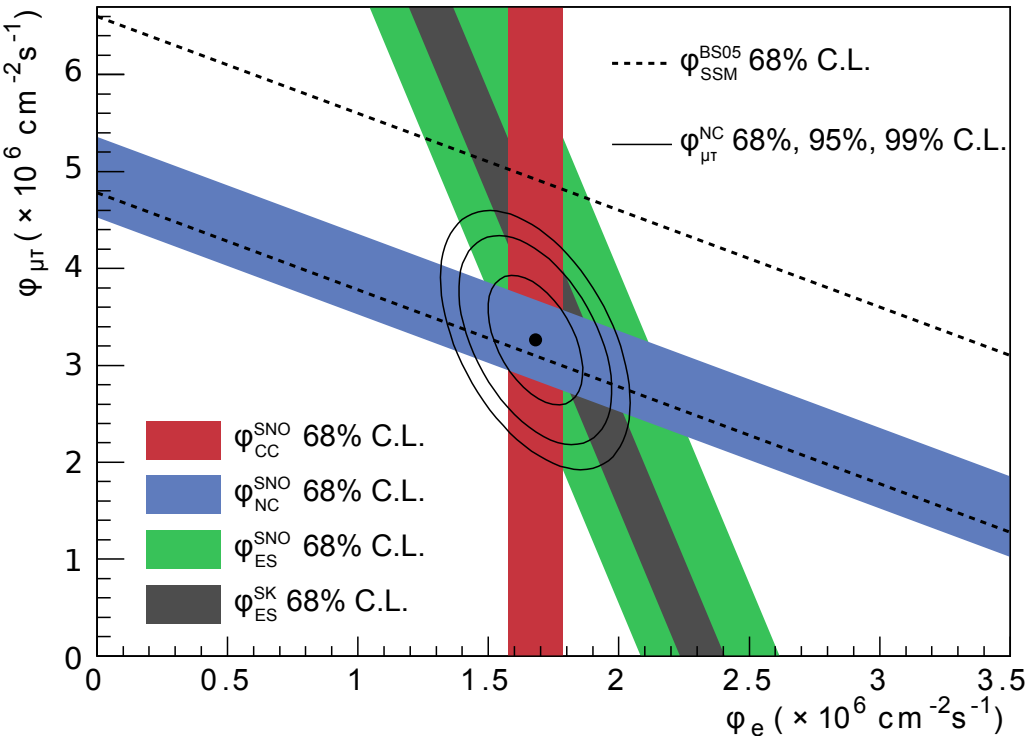

Figure 1.2: Flux of ^{8}B solar neutrinos deduced from the SNO salt phase. Measured flux $\phi_{\mu,\tau}$ as a function of the electron-neutrino flux ϕ_e, separated in the individual channels in eq. (1.4). In addition, the observed ES-reactions results of the Super-Kamiokande (SK) detector are shown in black (ref. [Fuk02]) and the 68 % C.L. band of the SSM prediction as dashed lines (ref. [Bah05]). The intersection of the channels is indicated by a dot with confidence levels of 68 %, 95 % and 99 %. Figure adapted from [Oli14].

A verification was finally possible with the Sudbury neutrino observatory (SNO) experiment (ref. [Bog00]). Equipped with 10 000 photomultiplier tubes surrounding a 1000 t heavy water tank as a Cherenkov detector, not only the charged current (CC), but the neutral current (NC) and elastic scattering (ES) could be measured as well,

$$\begin{aligned} \nu_e + d &\rightarrow p + p + e^- \quad \text{(CC)}, \\ \nu_x + d &\rightarrow \nu_x + p + n \quad \text{(NC)}, \\ \nu_x + e^- &\rightarrow \nu_x + e^- \quad \text{(ES)}. \end{aligned} \tag{1.4}$$

Thereby a verification of the full neutrino flux regardless of the flavor was possible via NC together with ES. At the same time the CC channel was used to detect the electron neutrino flux explicitly (ref. [Hel02]). The result showed not only a non-vanishing ν_μ and ν_τ flux, but an agreement of the total flux with the SSM (ref. [Aha05], fig. 1.2). A vast number of experiments utilize the neutrino oscillation nowadays to invest various neutrino sources of different flavor composition and in a huge energy range.

1.2.2 Theory of neutrino oscillation

To describe the neutrino oscillation an analogy with the Cabibbo-Kobayashi-Maskawa-Matrix (CKM-Matrix) is found (ref. [Cab63], [KOB73]). A unitary $n \times n$ matrix associates the flavor-eigenstates $|\nu_\alpha\rangle$ of the weak interaction with mass-eigenstates $|\nu_k\rangle$ to enable the transition between flavors by

$$|\nu_\alpha\rangle = \sum_k \mathrm{U}_{\alpha k} |\nu_k\rangle \quad \text{and} \quad |\bar{\nu}_\alpha\rangle = \sum_k \mathrm{U}^*_{\alpha k} |\bar{\nu}_k\rangle \,, \tag{1.5}$$

where α are the flavor eigenstates e, μ, τ, and $k = 1, 2, 3$ denotes the mass eigenstates. The so-called Pontecorvo–Maki–Nakagawa–Sakata (PMNS) mixing matrix can be parameterized by $n(n-1)/2$ mixing angles θ_{ij}, CP-violating $(n-2)(n-1)/2$ Dirac phases δ_d and $(n-1)$ Majorana phases δ_{Mi} (ref. [Oli14]).

A solution of the Dirac equation for the stationary mass-eigenstates $|\nu_k\rangle$ is found together with the time-evoultion for a given momentum $\vec{p}_k$ and spatial coordinates $\vec{x}$ in

$$|\nu_k\,(\vec{x}, t)\rangle = e^{-i/\hbar(E_k t - \vec{p}_k \vec{x}_k)} |\nu_k\rangle \,. \tag{1.6}$$

The energy E_k depends on the mass m_k, consequently a propagation in different phases is possible when $m_k \neq m_l$. As the neutrino flavor is a super position of mass-eigenstates the propagation enables a flavor transformation, where a short calculation yields to the oscillation probability

$$P_{\nu_\alpha \to \nu_\beta}\,(L,E) = \sum_k \left|\mathrm{U}_{\alpha k} \mathrm{U}^*_{\beta k}\right|^2 + 2\mathrm{Re} \sum_{k<l} \mathrm{U}_{\alpha k} \mathrm{U}^*_{\alpha l} \mathrm{U}^*_{\beta k} \mathrm{U}_{\beta l} \exp\left(-i(L/E)(\Delta m^2_{kl}/2)\right) \tag{1.7}$$

for an oscillation from a flavor α to flavor β. The key parameters introduced here are the squared mass differences $\Delta m^2 = m_k^2 - m_l^2$ of the eigenstates and the baseline-length $L = |\vec{x}|$. In the simplified case of an α to β transition, only two mass eigenstates ν_1 and ν_2 and a single angle θ_{12} are required for neutrino oscillation. This generic approach in textbooks applies without loss in generality (ref. [Zub12], [Ams07]). Neutrino oscillation occur for a non-diagonal PMNS and at least one non-vansihing neutrino mass

$$\begin{pmatrix} \nu_\alpha \\ \nu_\beta \end{pmatrix} = \begin{pmatrix} \cos(\theta) & \sin(\theta) \\ -\sin(\theta) & \cos(\theta) \end{pmatrix} \cdot \begin{pmatrix} \nu_1 \\ \nu_2 \end{pmatrix}, \tag{1.8}$$

which results in a transition probability of

$$P_{\nu_\alpha \to \nu_\beta}\,(L,E) = \sin^2(2\theta) \sin^2\left(\frac{L}{E} \frac{\Delta m^2_{12}}{4\hbar}\right). \tag{1.9}$$

Evidently, the angle θ determines the amplitude of the oscillation and the mass difference the characteristic oscillation length

$$L_0 = \frac{4\pi\hbar}{c^3} \frac{E}{\Delta m^2}. \tag{1.10}$$

The baseline length (eq. (1.10)) is an important design parameter to be considered in the

setup of an neutrino oscillation experiment. Based on the angles and mass difference that an experiment investigates, it searches in the appearance or disappearance channel and selects the appropriate neutrino source. Either way, a detailed knowledge about the total flux and energy of the emitted neutrinos are essential for an accurate measurement. Examples of the neutrino oscillation experiments are given in the following paragraphs, sorted by their neutrino sources. Latest results of the neutrino oscillation parameters are summarized in table 1.1.

Solar neutrinos

As only electron neutrinos are emitted from the sun, the focus is on the disappearance of ν_e into ν_μ or ν_τ. With the long baseline L_0 of 15×10^7 km, solar neutrinos are excellent candidates to measure a tiny mass difference Δm^2_{12} and mixing angle θ_{12}, like the previously mentioned SNO experiment (ref. [Aha13]) However, due to energies up to 15 MeV, the matter enhanced oscillation due to the Mikheyev-Smirnov-Wolfenstein (MSW) effect above the critical energy E^ν_{crit} of 1.9 MeV (ref. [Hax13]) needs to be considered in the analyses. Especially when the experiment is focused on the high energy end of the solar-ν spectrum as the Super-Kamiokande Cherenkov detector (ref. [Fuk02]). On the low energy end, the Borexino experiment measured the pep- and pp-channel with an ultra pure 278 t organic scintillator (ref. [Bel14b]). The combined analysis confirmed the MSW effect (ref. [Bel14a]).

Atmospheric neutrinos

Cosmic rays of protons and α particles with energies on the GeV-scale generate a cascade of secondary particles in the upper atmosphere. The decay of the generated pions has a distinct signature with a neutrino ratio $\nu_\mu/\nu_e = 2$ and energies E_ν of 2 GeV. Depending on the primary direction, the baseline from source to detector various over several orders of magnitudes, introducing an up-down asymmetry. A ν_μ deficit in the up-down asymmetry of the atmospheric neutrino flux was confirmed by Super-Kamiokande, the IMB experiment and Sourcan-2 while the ν_e was within expectations (ref. [Fuk98], [Bec92], [All97]). The deficit was identified with an appearance of an additional ν_τ flux. Together with other recent publications from Super-Kamiokande and the IceCube experiment (ref. [Abe13], [Aar15]) Δm^2_{32} and mixing angle θ_{23} are now well established parameters of the neutrino mixing.

Accelerator neutrinos

Neutrino beams can be produced by particle accelerators when high-energy protons irradiate a fixed target, such as aluminum (ref. [Zub12]). The initially generated pions decay in a tunnel to produce a beam of focused ν_μ-neutrinos. The advantage is the adjustable neutrino energy, typically in the GeV-range for an optimization of the sensitivity for a given baseline length.

The KEK to Kamioka (K2K) experiment and its successor Tokai to Kamioka (T2K) have a 295 km long baseline from the J-PARC facility to the Super-Kamiokande detector. A mass splinting Δm^2_{32} was expected to be observed An observation of the expected Δm^2_{32} mass splinting based on atmospheric experiments eq. (1.10), neutrino energies of about 300 MeV yield an optimal significance. In this setup, together with the Main Injector Neutrino Oscillation Search (MINOS) and the Oscillation Project with Emulsion Tracking Apparatus (OPERA) experiment, the results of the atmospheric experiments could reproduce θ_{23} in the $\nu_\mu \to \nu_\tau$ appearance channel (ref. [Ahn06], [Abe15], [Ada13], [Aga15]).

Table 1.1: Summary of neutrino oscillation parameters. The individual parameters are the result of the combined analyses in [Oli14]. Masses refer to the normal mass hierarchic $m_1 < m_2 < m_3$ whereas brackets indicate the inverted scenario $m_3 < m_1 < m_2$. The squared mass difference is defined as $\Delta m^2 = m_3^2 - (m_2^2 + m_1^2)/2$.

parameter	best fit ($\pm 1\sigma$)
Δm^2_{21}	$(7.53 \pm 0.18) \times 10^{-5}\,\mathrm{eV}^2$
Δm^2_{32}	$(2.44 \pm 0.06) \times 10^{-3}\,\mathrm{eV}^2$ ($(2.49 \pm 0.06) \times 10^{-3}\,\mathrm{eV}^2$)
$\lvert\Delta m^2\rvert$	$(2.43 \pm 0.06) \times 10^{-3}\,\mathrm{eV}^2$ ($(2.38 \pm 0.06) \times 10^{-3}\,\mathrm{eV}^2$)
$\sin^2(\theta_{12})$	0.304 ± 0.014
$\sin^2(\theta_{23})$	$0.514^{+0.055}_{-0.056}$ (0.511 ± 0.055)
$\sin^2(\theta_{13})$	$(8.5 \pm 0.5) \times 10^{-2}$
δ_d/π (2σ range)	$1.39^{+0.37}_{-0.27}$ ($1.31^{+0.29}_{-0.33}$)

Moreover, the well known conditions of neutrino beams generated by accelerators combined with an analysis that accounts for a three-flavor oscillation, other neutrino mixing parameters such as the Dirac phase δ_d can be studied (ref. [Abe15]). With a long baseline detector like NuMI Off-Axis ν Appearance (NOνA) experiment, it might be possible to identify the mass hierarchy (ref. [Ada16b], [Ada16a]).

Reactor neutrinos

Nuclear fission reactors are the strongest permanent neutrino sources available on earth. An electric-power reactor of 1 GW yields a total electron anti-neutrino flux of $\phi(\bar{\nu}_e) = 2 \times 10^{20}\,\mathrm{s}^{-1}$ (ref. [Zub12]).

The neutrino energies generated in neutron-rich fission products of uranium or plutonium fission are of a few MeV, making a baseline length of 1 km to 2 km advantageous to study Δm^2_{31} and θ_{13}. When combined with a second detector direct next to the reactor, systematic uncertainties related with the reactor activity are reduced significantly (ref. [Dwy15]). Recent experiment like Daya Bay (China), Reactor Experiment for Neutrino Oscillations (RENO) (South Korea) and Double Chooz (France) utilized the $\bar{\nu}_e$ disappearance to provide clear evidence for the scale of Δm^2_{31} and θ_{13} (ref. [An12], [Ahn12], [Abe12]).

1.2.3 Neutrino mass generation

Neutrino oscillation experiments could identify many properties of the neutrino mixing already, but important parameters are still missing (ref. [Qia15]). The sign of Δm^2_{32} and the absolute mass scale are not determined yet, where the latter can not even be attacked by oscillation experiments. Therefore, different scenarios for the mass hierarchy are allowed, denoted as the so-called normal ($m_1 < m_2 \ll m_3$), the inverted ($m_3 < m_1 \ll m_2$), and the quasi degenerated ($m_1 \cong m_2 \cong m_3 \approx 10^{-3}\,\mathrm{eV}^2$) mass hierarchy. Current experimental results show a tendency towards the first two options (fig. 1.3). The determination of the neutrino mass hierarchy will give hints to indicate the nature of neutrinos and the associated mass generation mechanism (ref. [BIL12]).

Two fundamentally different approaches to introduce a neutrino mass are possible:

- Allow a singlet of a right-handed (left-handed) neutrino (anti-neutrinos) to generate

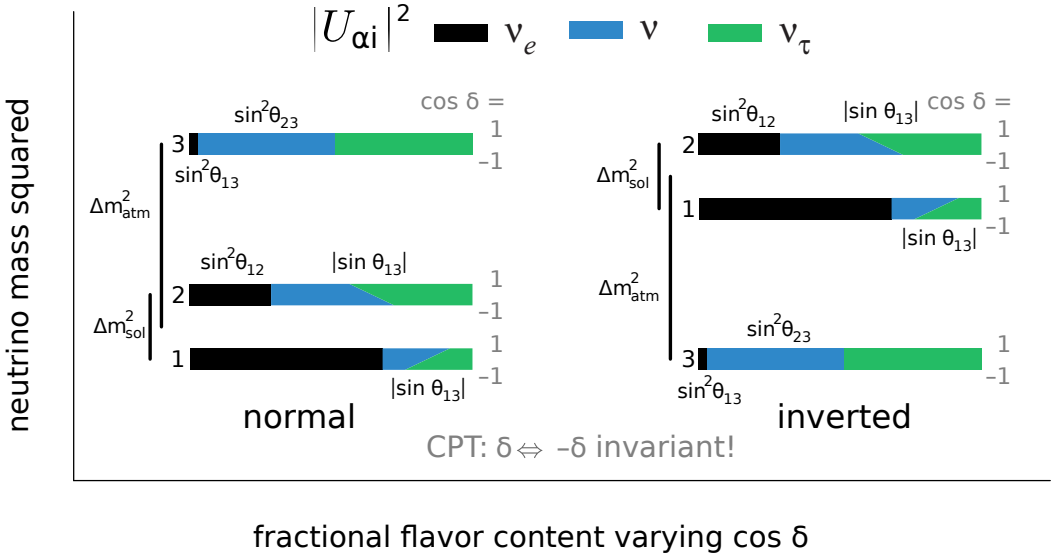

Figure 1.3: Flavor fraction of the three neutrino mass eigenstates. The mass scenarios include the influence of the mass hierarchy as well as the CP violating phase δ. Figure inspired by [Par08].

a neutrino-mass term by a Yukawa coupling with the Higgs-field. These are sterile neutrinos, interacting purely via the gravitational force (ref. [Him15]).

- Describe the neutrino not by a Dirac-spinor, but a Majorana-spinor ($\nu_\alpha = \bar{\nu_\alpha}$) instead (ref. [Maj37]). The neutrino masses and the huge difference in comparison to the masses of charged leptons can then be explained by the See-Saw-mechanism.

The mass terms in a Lagrangian $\mathcal{L}$ of a four-component Dirac spinor field ψ must be Lorentz-invariant and Hermitian (ref. [Sch97]). The general case of a mass term (Dirac-Majorana mass term) of a free neutrino with the fields ψ_L, ψ_R^c, ψ_R, and ψ_L^c in the chiral representation (Weyl-spinors) of the ferminonic field is

$$2\mathcal{L} = (\bar{\psi_L}, \psi_L^c) \cdot \underbrace{\begin{pmatrix} m_L & m_D \\ m_D & m_R \end{pmatrix}}_{M} \cdot \begin{pmatrix} \psi_R^c \\ \psi_R \end{pmatrix} + \text{h.c.}\,, \tag{1.11}$$

where the index c donates the charge conjugation and h.c. the hermitian conjugate. This is a combination of the Dirac mass term

$$\mathcal{L} = m_D \left(\bar{\psi_L}\psi_R + \bar{\psi_R}\psi_L\right), \tag{1.12}$$

and the Majorana mass terms

$$\mathcal{L}_M^L = \frac{1}{2} m_L \bar{\psi_L}\psi_R^c + \text{h.c.} \qquad \mathcal{L}_M^R = \frac{1}{2} m_R \bar{\psi_L^c}\psi_R + \text{h.c.} \tag{1.13}$$

The matrix M can be diagonalized and from $\mathrm{Det}(M - m)$ the mass eigenvalues yield

$$\tilde{m}_{1,2} = \frac{1}{2}\left[(m_\mathrm{L} + m_\mathrm{R}) \pm \sqrt{(m_\mathrm{L} - m_\mathrm{R})^2 + 4m_\mathrm{D}^2}\right] \quad , \tag{1.14}$$

where $\tilde{m}_{1,2}$ is identified with $\varepsilon_{1,2} \cdot m_{1,2}$ together with the CP eigenvalues of the Majorana neutrino, selected to result in positive eigenvalues $\tilde{m}_{1,2}$. An important example of the latter case is the See-Saw mechanism (ref. [Yan80]) with $m_R \gg m_\mathrm{D}$, $m_L = 0$ and $m_\mathrm{D}/m_R \ll 1$ to result in eigenvalues of the mass matix of

$$m_1 = \frac{m_\mathrm{D}^2}{m_R}, \qquad m_2 = m_R\left(1 + \frac{m_\mathrm{D}^2}{m_R^2}\right) \approx m_R \quad \text{with} \quad \varepsilon_{1,2} = \mp 1. \tag{1.15}$$

The associated Majorana fields are $\phi_1 \approx \psi_L \psi_R^c$ and $\phi_2 \approx \psi_L^c \psi_R$, which correspond to a light weak-interacting neutrino and a heavy sterile neutrino. In models of the Grand Unified Theory (GUT) the Dirac mass is of the order of a charged ferminon (MeV to GeV) and the Majorana mass around the GUT scale 10^{14} GeV to 10^{16} GeV (ref. [Boe94]).

1.3 Determination of the neutrino mass

Neutrino oscillation experiments validated a variety of neutrino properties with great precision. By their very nature, they can merely detect differences of the squared masses, but the absolute scale remains concealed. Other experimental means are required, comprising indirect approaches that are based on cosmological assumptions and direct measurements like the KATRIN experiment, relying on kinematics of the nuclear β-decay only. In the following, the most noticeable approaches are discussed.

1.3.1 Cosmology

Within the standard ΛCDM cosmological model, the evolution of the universe from the initial Big Bang to the current state, dominated by dark energy (ΛC) and cold dark matter (CDM), is described. The predicted cosmic microwave background is nowadays well established with a temperature of $(2.7255 \pm 0.0006)\,\mathrm{K}$ (ref. [Fix09], [Pla16]). Thereby many cosmological parameters could be constrained and with the focus on polarization, CMB measurements are now searching for new physics.

Another prediction by ΛCDM is the cosmic neutrino background (CνB) of relic neutrinos. Despite the large neutrino density of $110\,\mathrm{cm}^{-3}$ per flavor at a temperature of 1.95 K, they could not be verified yet due to their extremely low cross section with matter (ref. [Zub12]). A significant contribution to the total radiation energy Ω_tot is predicted, however only the sum of all neutrino masses

$$\sum_k m_k = 93\Omega_\nu h^2\,\mathrm{eV} \tag{1.16}$$

are of relevance, where h is the dimensionless Hubble parameter.

In the latest publication of the Planck collaboration an upper limit is given

$$\sum m_\nu < 0.23\,\mathrm{eV} \quad (95\,\%) \tag{1.17}$$

for the masses of the active neutrinos (ref. [Pla14]). This value can only be obtained when rather strict restrains and theoretical assumptions are made. The analysis incorporates information obtained from baryon acoustic oscillations (BAO) measurements (ref. [Beu11]), a fixed number N_{eff} of neutrino generations, a joint light-curve analysis from SNLS and SDSS supernovae surveys, together with an input from low redshift supernovae (ref. [Bet14]).

1.3.2 Neutrinoless double beta-decay

The Bethe-Weizsäcker equation describes the binding energy of nucleons in nuclei (ref. [Wei35]). Nucleons of even mass number A feature a degenerated mass parabola where the even-even (odd-odd) configuration of N and Z yields on average higher (lower) binding energies. This may result in a configuration where a single β-decay is energetically forbidden and only the double β-decay of two neutrons simultaneously into two protons ($2\nu\beta^-\beta^-$-decay) can be observed. The $2\nu\beta^-\beta^-$-decay is a suppressed processes of the weak interaction, consequently the half-lives are long and in the order of 10^{20} years (ref. [Goe35], [Kir69]).

When the neutrino is considered to be of Majorana nature and therefore its own anti-particle (ref. [Maj37]), a neutrinoless double β-decay ($0\nu\beta\beta$)

$$2\text{n} \rightarrow 2\text{p} + 2\text{e}^- \tag{1.18}$$

is possible. At the vertex of the charged leptons a Majorana neutrino ν_{m} is exchanged and the leptonic energy corresponds to the full Q value. The originally continuous spectrum of the double β-decay becomes a discrete value when nuclear recoil is neglected (fig. 1.4). This process not only violates the lepton number conservation ($L_{\text{initial}} \neq L_{\text{final}}$), but requires massive neutrinos to allow a sign change of the helicity.

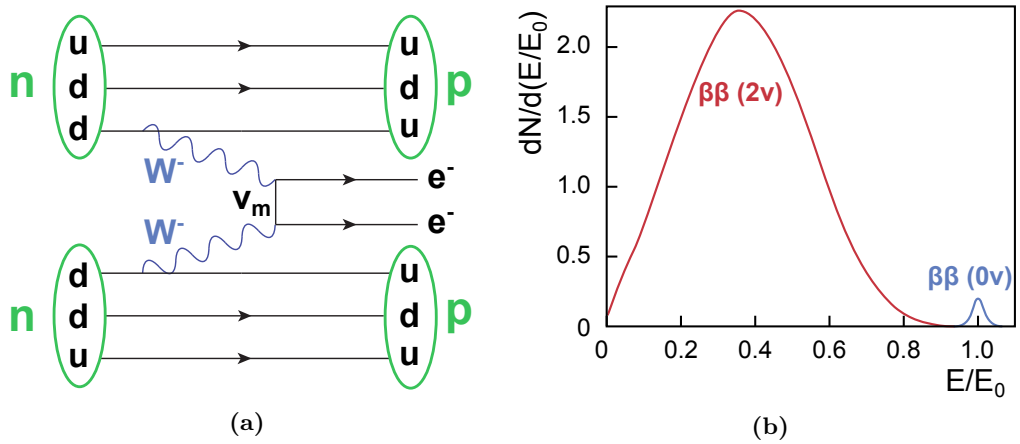

(a) (b)

Figure 1.4: The double β-decay. The Feynman diagram of the $0\nu\beta\beta$ is shown in 1.4(a). A virtual Majorana-like neutrino ν_{m} is exchanged to transform two neutrons in two protons and electrons. Figure adapted from [Sch14b]. The energy spectrum of a double β-decay in 1.4(b) is scaled to 1 (0.2) in case of the $2\nu\beta\beta$-decay ($0\nu\beta\beta$-spectrum). The energy resolution at the endpoint is taken as 5%. Figure adapted from [Sch13].

The effective Majorana neutrino mass is the coherent sum of the mass eigenstates

$$\langle m_{\beta\beta}\rangle^2 = \left|\sum_{k=1}^{3} U_{ek}^2 m_k\right|^2 = \left|\sum_{k=1}^{3} |U_{ek}|^2 e^{\alpha_{k1}} m_k\right|^2 \quad , \tag{1.19}$$

where cancellations CP-violating Majorana phases δ_{Mi_i} can lead to a reduction of the effective mass $\langle m_{\beta\beta}\rangle^2 < m_i$ (ref. [Ell02]).

For an experimental verification of ν_{m}, the half-life of a $0\nu\beta\beta$ is measured

$$\left(t_{1/2}^{0\nu}\right)^{-1} = G^{0\nu}(E_0, Z) \cdot \left| M_{\mathrm{GT}}^{0\nu} - \frac{g_{\mathrm{V}}^2}{g_{\mathrm{A}}^2} M_{\mathrm{F}}^{0\nu} \right|^2 \cdot \langle m_{\beta\beta}\rangle^2 \quad , \tag{1.20}$$

which also depends on the phase space integral $G^{0\nu}(E_0, Z)$ and the matrix element of the V−A weak current transition. The latter two parameters require extensive calculations for a precise estimation of the neutrino mass, the major contribution to the systematic uncertainty.

The Germanium Detector Array (GERDA) experiment searches in the decay of ^{76}Ge for a double electron event with a Q value of 2039 keV. In phase-I of GERDA (ref. [Ago13]), a lower limit on the $0\nu\beta\beta$ half-life was derived of

$$^{76}\mathrm{Ge} \;\rightarrow\; ^{76}\mathrm{Se} + 2\mathrm{e}^- \,, \tag{1.21}$$

corresponding to an upper limit of ν_{m} of

$$\langle m_{\beta\beta}\rangle < (0.2 - 0.4)\mathrm{eV/c}^2. \tag{1.22}$$

The $0\nu\beta\beta$-decay is the research topic of GERDA (ref. [Maj15]), Cadmium Zinc Telluride 0-Neutrino Double-Beta Research Apparatus (COBRA) (ref. [Won15]), Enriched Xenon Observatory (EXO-200) (ref. [Aug12]), Majorana (ref. [N A14]) and others; so far only upper limits could be claimed.

1.3.3 Single beta-decay

The most straightforward approach to determine the neutrino masses is to study the three body process (eq. (1.1)) of the single β^- decay. The kinematics of this process are so thoroughly tested, that this method is regarded to be model independent. Due to the very large mass difference between the decay products and the remaining nucleus, its recoil energy can be neglected in first order. Consequently the decay energy is only distributed among the electron and the neutrino, where the neutrino energy is given by

$$E_\nu = \sqrt{m_\nu^2 c^4 + p_\nu^2 c^2}, \tag{1.23}$$

with its rest mass m_ν. A non-vanishing neutrino-mass therefore shows up as a missing energy in the energy spectrum of the electron, although its momentum is close to zero. As a result, plainest evidence for a variation in the shape of the energy spectrum can be found close to the end point (fig. 1.5).

From Fermi's Golden Rule (ref. [Fer34]) the transition rate $\Gamma_{i\rightarrow f}$ of the decay from the

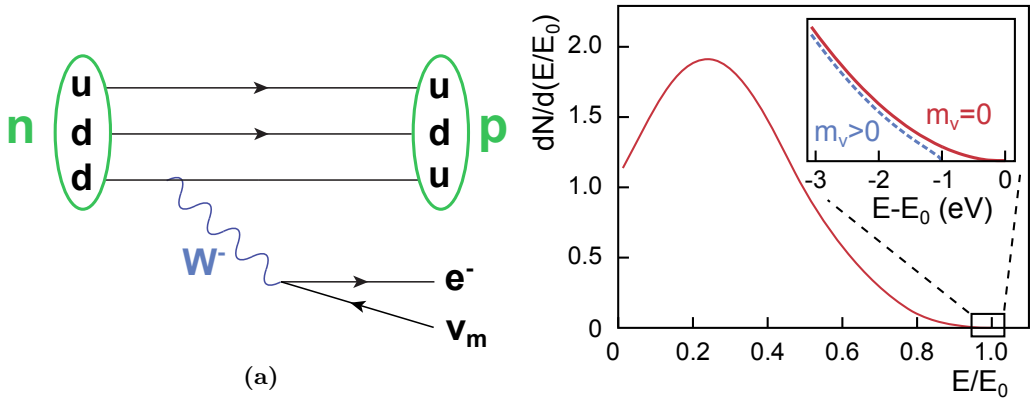

(a) (b)

Figure 1.5: The single β-decay. The Feynman diagram of the β-decay is shown in 1.5(a). A neutron transforms into a proton by emitting an electron e^- and an electron anti-neutrino $\bar{\nu}_e$. Figure adapted from [Sch14b]. The energy spectrum of the single β-decay is shown schematically in 1.5(b). The x-axis is scaled to the endpoint energy E_0, while the y-axis represents the probability density. The inlet is focused on the important endpoint region. The shape of the spectrum is shown for a vanishing neutrino mass (a neutrino mass of 1 eV) by a red solid line (blue dashed line). Figure adapted from [Sch13].

initial state $|i\rangle$ to the final state is calculated to be

$$\Gamma_{i\to f} = \frac{\mathrm{d}N^2}{\mathrm{d}E\mathrm{d}t} = \frac{2\pi}{\hbar} |\mathcal{M}_{fi}|^2 \, \rho(E_f) \,, \tag{1.24}$$

where $\mathcal{M}_{fi}$ represents the transition matrix element between the two states and $\rho(E_f)$ corresponds to the density of final states of energy E_f. Applying a relativistic relation of the energy-momentum for the confined case of a super-allowed nuclear transitions, the integrated rate over all possible discrete and continuous final states can be obtained

$$\frac{\mathrm{d}N^2}{\mathrm{d}E\mathrm{d}t} = C \cdot F(Z', E) \cdot p \cdot (E + m_e c^2)(E_0 - E) \cdot \sqrt{(E_0 - E)^2 - m_{\bar{\nu}_e}^2 c^4} \cdot \Theta(E_0 - E - m_{\bar{\nu}_e} c^2) \,, \tag{1.25}$$

where $F(Z', E)$ accounts for the Coulomb interaction between the emitted electron, the daughter nucleus of charge Z', E_0 is the maximal endpoint energy and the Heaviside function Θ is introduced to fulfill energy conservation. All fundamental constants and the nuclear matrix element are confined in

$$C = \frac{G_F^2 \cdot \cos^2(\theta_C)}{2\pi^3 c^5 \hbar^7} \cdot |\mathcal{M}|^2 \,, \tag{1.26}$$

where G_F is the Fermi coupling constant, θ_C is the Cabbibo mixing angle, and $\mathcal{M}$ corresponds to the energy-independent nuclear matrix element (ref. [Ott10], [Dre13], [Alt03]).

The experimental observable is the incoherent sum of the squared neutrino masses of the

three neutrino mass eigenstates

$$m^2_{\overline{\nu}_e} = \sum_i \left|U^2_{ei}\right| m^2_{\nu_i}. \tag{1.27}$$

The resulting fine structure can only be resolved with a sufficiently small energy resolution ΔE, however the appropriate technology to do so is not available yet.

Several elements and techniques are conceivable to study the single β decay, some are presented in the following.

Rhenium and Holmium experiments

A low Q-value is in favor as the signal rate of β-electrons in the endpoint region[1] scales with E_0^{-3}. The two elements with the lowest Q-β-values are ^{115}In and ^{187}Re. Technical difficulties inhibit to utilize ^{115}In in an experiment (ref. [Rem16], [Wie09]). The β-decay of the other candidate

$$^{187}\mathrm{Re} \;\rightarrow\; ^{187}\mathrm{Os}^{+} + \mathrm{e}^{-} + \overline{\nu}_e \tag{1.28}$$

is feasible in an experiment (ref. [Sis04]). Considering the long half-life of ^{187}Re of $(4.32 \pm 0.02) \times 10^{10}$ years, the amount of material is a decisive criterion to achieve a reasonable active source (ref. [Dvo11]).

Due to the low endpoint energy, the β electrons can not be extracted from a solid ^{187}Re source and the information about the electron energy remains within the source. Therefore, the source is used as detector simultaneously in a so-called calorimetric measurement. The required technique is implement in cryogenic micro-calorimeters, where the deposited energy is detected as a thermal signal. To discriminate individual decays the ^{187}Re material is split in many small units of detector arrays to reduce systematic uncertainties (ref. [Sis04], [And07]).

The upper limit on $m_{\overline{\nu}_e}$ determined by a ^{187}Re experiment is

$$m_{\overline{\nu}_e} < 15\,\mathrm{eV} \quad (90\%\ \mathrm{C.L.})\,, \tag{1.29}$$

which is the lowest limit from direct, but non-tritium based, neutrino mass measurements (ref. [Sis04]).

However, a further improvement of the sensitivity of ^{187}Re detectors is impaired by complicated thermalization of energy in superconducting materials (ref. [Cos93]). The focus of the microcalorimeters community is therefore shifted nowadays towards ^{163}Ho with a Q-value of $(2833 \pm 30)\,\mathrm{eV}$ via electron capture (ref. [Eli15]). Experiments like Electron Capture ^{163}Ho (ECHo) experiment aim for an energy resolution in the sub-eV regime and a rise time as low as 1 µs to investigate the electron neutrino mass (ref. [Gas14]).

1 This is in counteraction to the overall increased rate of a β-decay proportional to E_0^5.

Tritium experiments

The vast majority of successful β-decay based neutrino-mass experiments have been performed with tritium. Such measurements rely solely on kinematics of the super-allowed transition

$$^3\mathrm{H} \rightarrow {}^3\mathrm{He}^+ + \mathrm{e}^- + \bar{\nu}_\mathrm{e}\,, \tag{1.30}$$

where the spectral shape is basically described by eq. (1.25). In addition, tritium features the advantages of a low endpoint energy of 18.6 keV and a short half life of (12.32 ± 0.02) years (ref. [Rob88], [Bea80], [Kru83], [Luc00]).

A promising approach is the "Project 8" which uses the cyclotron radiation of electrons in an external magnetic field given by

$$\omega = \frac{\omega_0}{\gamma} = \frac{qB}{m_\mathrm{e}\mathrm{c}^2 + E}\,, \tag{1.31}$$

where ω_0 is the unshifted cyclotron frequency, and γ is the Lorentz factor of the electron with mass m_e, the kinetic energy E and charge q. Antennas detect the radiation ω of about 27 GHz close to the endpoint to reconstruct the spectrum (ref. [Mon09]). First tests with ^{83m}Kr have been finished successfully (ref. [Obl13]).

The best experimental results were obtained by means of the MAC-E filter technique (section 2.1) in Mainz and Troitsk (ref. [Ott94], [Lob85]). The combined analysis of the Mainz phase II with a quench-condensed tritium source and the windowless source of molecular tritium in Troitsk yield

$$m_{\bar{\nu}_\mathrm{e}} < 2.0\,\mathrm{eV} \quad (95\,\%\,\mathrm{C.L.}) \tag{1.32}$$

as released by the Particle Data Group (ref. [Oli14]). This is currently the model-independent upper limit on the effective mass of the electron anti-neutrino. The KATRIN experiment represents the next-generation tritium based experiment, targeted to advance the neutrino mass search into the sub-eV regime.

CHAPTER 2

KATRIN Experiment

The Karlsruhe tritium neutrino (KATRIN) experiment is targeted to determine the effective mass of the electron anti-neutrino in a model-independent measurement of tritium β-decay. It is designed to improve the current neutrino mass sensitivity by one order of magnitude to 200 meV/c^2 at 90 % C.L. (350 meV/c^2 at 5σ) after five calender years of operation (ref. [KAT05]). This is achieved by a measurement of the electron-energy spectrum close to the kinematic endpoint of $E_0 \approx 18.6$ keV with an electrostatic high-pass filter. Since only $\approx 10^{-13}$ of all β-decays of the tritium spectrum occur in the last 1 eV-region, a high-luminosity electron source is required. This is achieved by a combination of a high-luminosity source with a high angular acceptance, and an excellent energy resolution based on the magnetic adiabatic collimation with electrostatic filtering (MAC-E filter) principle. This principle was first introduced in 1970' (ref. [Hsu76]) and 1980' (ref. [Bea80], ref. [Kru83]) and quickly after elaborated and adapted for neutrino-mass measurements in Troitsk (ref. [Lob85]) and Mainz (ref. [Pic92]).

The first section section 2.1 is dedicated to the introduction of this measurement technique. In particular the so-called transmission function is presented, as it defines the energy resolution of the spectrometer (section 2.1.1), a major aspect of this thesis. The sophisticated interplay between the electrostatic- and the magnetic-field setup defines the properties of a MAC-E filter spectrometer (section 2.1.2).

Since summer 2015, all-sub components of the KATRIN beam line are on-site at KIT and are being commissioned at the moment. The final setup is of a length of about 70 m and fulfills high technical demands that are described in section section 2.2. Here the major sub-systems are discussed, such as the high-luminosity source (section 2.2.1), the transport section that guides signal electrons and reduces the gas flow (section 2.2.2), the spectrometers for a high-precision energy analysis (section 2.2.3), and finally the detector to count transmitted particles (section 2.2.4). A special roll has the monitor spectrometer, which is not part of the main KATRIN beam-line, but is dedicated to measure the stability of the retarding potential (section 2.2.5).

Finally, an introduction to the calculations of the sensitivity level for a neutrino-mass discovery of the KATRIN experiment and considerations of the overall uncertainty budget are given in section 2.3.

2.1 Measurement principle of a MAC-E filter

An energy analysis based solely on an electrostatic field in a strong magnetic-field would be inaccurate, as it discriminates against the kinetic energy parallel to the magnetic field and not the total kinetic energy. To avoid this difficulty, the electron source is placed in a high magnetic field and a minimization of the magnetic field at the position of the retarding potential (fig. 2.1). At the source and detector side of the spectrometer strong superconducting magnets are placed. The maximal magnetic field B_{max} is in the center of a magnet and drops significantly towards the center of the spectrometer. The minimal magnetic field region B_{min} defines the so-called analyzing plane in the center of the spectrometer. The MAC-E filter principle is discussed in detail below based on ref. [KAT05], [Gro15], [Zac14].

Formulas in this section are given in a non-relativistic approximation, which is reasonable as tritium β-decay electrons have a maximal kinetic energy of $E_{\mathrm{kin}} \approx 18.6\,\mathrm{keV}$. Consequently the Lorentz-factor of an electron is

$$\gamma_{\mathrm{max}} = \frac{1}{\sqrt{1 - \frac{v^2}{c^2}}} = 1.04 \approx 1. \tag{2.1}$$

Electrons that originate from a β-decay in the source region are isotropically emitted. Due to the Lorentz force, the electrons will perform a cyclotron motion along a magnetic field line, defined by their polar angle Θ relative to the magnetic field (fig. 2.2). The kinetic energy of an electron is then defined as

$$E_{\mathrm{kin}} = E_{\parallel} + E_{\perp} = E_{\mathrm{kin}} \cos^2(\Theta) + E_{\mathrm{kin}} \sin^2(\Theta) \tag{2.2}$$

In principle, half of the electrons emitted from the source can reach the detector with a large acceptance angle of 2π.

In the spectrometer the energy of an electron is analyzed by an electrostatic retarding potential of an electric field parallel to the magnetic field. The electric potential has a minimum of $U_0 \approx -18.6\,\mathrm{kV}$ and is symmetrically shaped relative to the spectrometer center. Thus, based on the initial kinetic-energy, electrons either pass the potential barrier to the detector or are reflected back to the source where they are absorbed at the rear wall. However, only the longitudinal energy $E_{\parallel}$ of an electron is sensitive to the applied retarding potential and most electrons have a significant fraction of transversal energy $E_{\perp}$. Therefore, it is required to transform the transversal energy into longitudinal energy.

The transversal kinetic energy defines the cyclotron motion of a electron, represented by a magnetic moment

$$\mu = |\vec{\mu}| = \frac{-e}{2m_{\mathrm{e}}}|\vec{l}| = \frac{E_{\perp}}{B}, \tag{2.3}$$

where $\vec{l}$ is the orbital angular momentum and B the magnetic-field strength. In case of an adiabatic motion of the electrons, the orbital magnetic moment

$$\mu = \frac{E_{\perp,i}}{B_i} = \frac{E_{\perp,f}}{B_f} = \mathrm{const} \tag{2.4}$$

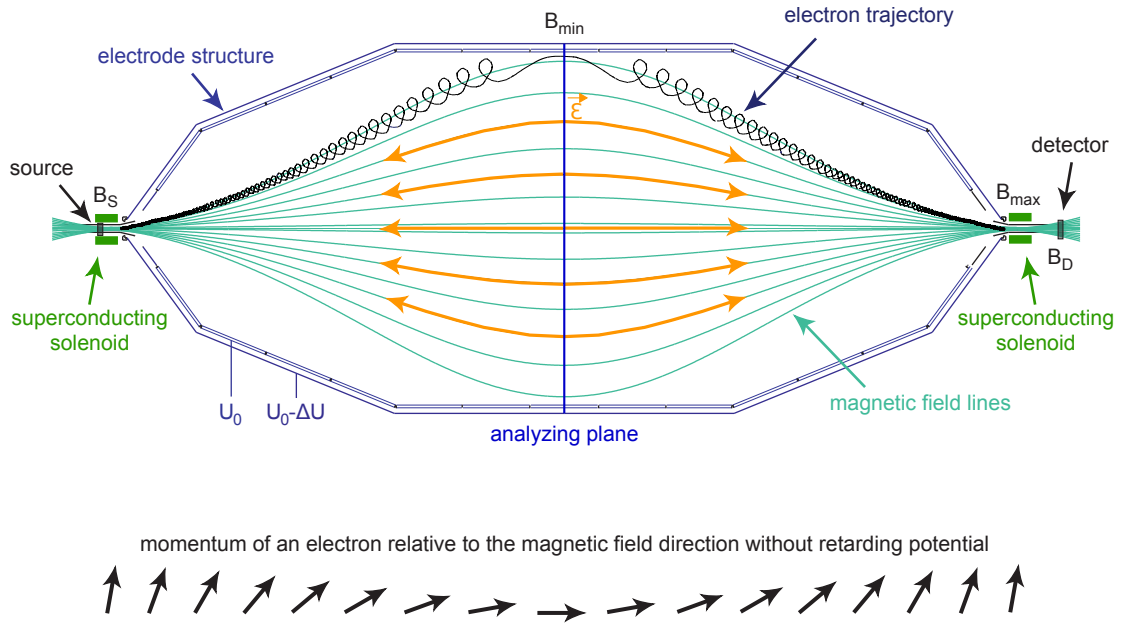

Figure 2.1: MAC-E filter princple, including an electron source and detector. An electrostatic retarding potential U is generated by the electrode system (blue). Superconducting magnets at the entrance and exit of the spectrometer generate a magnetic field (green). An electron trajectory is along a magnetic field-line (turquois) from the source to the detector and can feature a cyclotron motion (black), where the magnetic field strengths are $B_S < B_{\mathrm{max}}$ and $B_S < B_{\mathrm{det}}$. On the bottom, the adiabatic transformation of the momentum of an electron is illustrated, the influence of the electric retardation potential is neglected. Figure inspired by ref. [Sch14b].

becomes invariant for a initial and final state. Consequently, the kinetic energy is conserved. If the variation of the magnetic-field strength is sufficiently low $\Delta B/B \ll 1$ within one cyclotron period, adiabatic motion of an electron can be assumed. A continuous small reduction of the magnetic-field strength can then reduce the ratio $E_\perp/E_\parallel$ by transforming transversal energy $E_\perp$ to $E_\parallel$. This process is called magnetic adiabatic collimation. If the electron moment and the magnetic field are known for a initial position i, the ratio $E_\perp/E_\parallel$ can be calculated for any final position f. Together with the electron polar angle eq. (2.2) can be rewritten as

$$\sin^2(\Theta_f) = \sin^2(\Theta_i)\frac{B_f}{B_i}. \tag{2.5}$$

Equation (2.5) explains the transformation of the polar angle in fig. 2.1. The total length of the KATRIN main spectrometer of 23.3 m is appropriate for a sufficient the magnetic adiabatic collimation.

Simultaneous to the magnetic adiabatic collimation, the retarding potential is increased. These two processes must be fine-tuned to each other to prevent the so-called early retardation (ref. [Val09]). Early retardation is observed in a strong magnetic field and a high electrostatic potential. In this case, the electron energy is not yet sufficiently transformed to $E_\parallel$ and

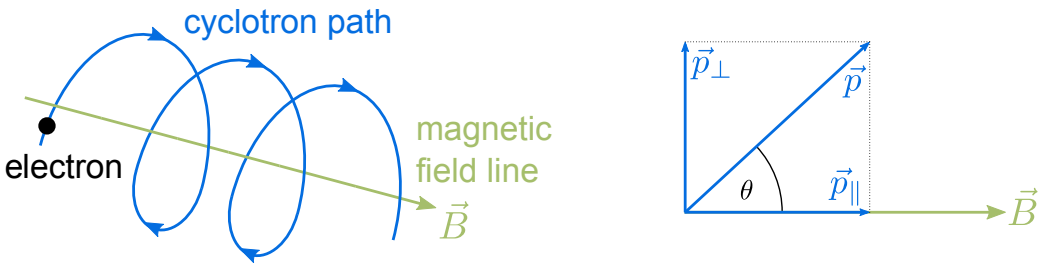

Figure 2.2: Sketch of the cyclotron motion of an electron of in a homogeneous magnetic field (left). The polar angle Θ is defined as the angle between the electron momentum and the magnetic field (right). Figure inspired by ref. [Gro15].

electrons are reflected by the retarding potential, although the total kinetic energy would allow them to pass the analyzing plane. This effect is avoided by a slow increase of the electrostatic potential with $\Delta E/E \ll 1$. At the KATRIN experiment this is realized by a reduced potential of the so-called steep cones at the entrance and exit region of the main spectrometer (section 3.1.2).

Based on eq. (2.5), two important magnetic field ratios can be identified:

- The magnetic-field ratio $B_\mathrm{s}/B_\mathrm{max}$ at the starting position and its maximal strength along the electron path. Thereby, the maximal acceptance angle Θ_max and luminosity of the source is controlled.
- The ratio $B_\mathrm{min}/B_\mathrm{max}$ of the maximal and minimal magnetic-field defines the maximal adiabatic-collimation. The energy resolution of a MAC-E filter spectrometer emerges from this relation.

Therefore, only three magnetic field values are required to describe the fundamental properties of a MAC-E filter, which are discussed in detail below.

The maximal acceptance angle is a consequence of the magnetic-mirror effect, where electrons are reflected magnetically, independent of their kinetic energy. If an electron propagates into a region of a higher magnetic field, its polar angle θ is increased, and thereby its longitudinal kinetic-energy is converted to the transversal component ($E_\parallel \rightarrow E_\perp$). A polar angle $\Theta = 90°$ corresponds to a vanishing longitudinal energy $E_\parallel = 0\,\mathrm{eV}$ and an electron is reflected. In an experimental setup, where the magnetic field at the source section is smaller than the maximal magnetic-field ($B_\mathrm{s} < B_\mathrm{max}$), the maximum accepted angle is given by eq. (2.5)

$$\Theta_\mathrm{max} = \arcsin\sqrt{\frac{B_\mathrm{s}}{B_\mathrm{max}}} = 50.77°. \tag{2.6}$$

In eq. (2.6), the design values of KATRIN for the fields at the source $B_\mathrm{s} = 3.6\,\mathrm{T}$ and at the pinch magnet $B_\mathrm{max} = 6\,\mathrm{T}$ are applied. Hence, 2/3 of all forward emitted electrons are

magnetically reflected. The benefit of a limiting maximal acceptance angle $\Theta_{\max}$ is to exclude electrons with a large path length trough the beam line due to an increased cyclotron motion. Such electrons are more likely to loose energy via scattering processes and have an increased energy loss via synchrotron radiation. Thereby, the systematic uncertainty of the electron energy is significantly increased.

The ratio $B_{\min}/B_{\max}$ defines the fraction of the kinetic energy that can not be transformed to the longitudinal component. As the magnetic field in the center of the MAC-E filter does not reach $B_{\min} = 0\,\mathrm{T}$, a finite component of transversal energy can be observed for electrons in the analyzing plane. Consequently, the transmission of an electron trough the spectrometer does not purely dependent on the applied retarding potential U_0, but on the ratio $B_{\min}/B_{\max}$ and the polar angle Θ as well. E.g. an electron of an kinetic energy $E_{\mathrm{kin}} = 18.6\,\mathrm{kV}$ can only reach the detector with a polar angle $\Theta = 0°$, otherwise additional surplus energy is required.

The maximal possible amount of transversal energy an electron can have in the analyzing plane defines the energy resolution. The width is defined by the maximal kinetic-energy E_0 and can be derived from eq. (2.4) with

$$\Delta E = E \cdot \frac{B_{\min}}{B_{\max}}. \tag{2.7}$$

The maximal magnetic-field $B_{\max} = 6\,\mathrm{T}$ of KATRIN is generated by a superconducting solenoid on the detector side of the spectrometer and drops towards the spectrometer center by a factor 2×10^4 to $B_{\min} = 30\,\mu\mathrm{T}$. Hence, the energy resolution of KATRIN is $\Delta E = 0.93\,\mathrm{eV}$. The energy resolution is a key parameter of the so-called transmission function.

2.1.1 Transmission function

The transmission function describes the transmission probability of electrons through a MAC-E filter setup as a function of their surplus energy. The shape of the transmission function is influenced by the electromagnetic setup as well as the initial angular distribution of the electrons. An isotropic electron emission is assumed for the tritium β-decay. In this section the transmission function of an ideal MAC-E filter and the additional characteristics of a realistic MAC-E filter are discussed. The spatial extent of the spectrometer is neglected in the ideal setup, and thereby refers to a punctual electron source and a single field-line.

Transmission function of an ideal MAC-E filter

The electron count-rate as a function of the retarding potential, as observed by the detector, is proportional to

$$R(qU_0) \propto \int_{qU_0}^{E_0} \frac{\mathrm{d}N}{\mathrm{d}E}(E_0, m_\nu^2) \cdot T(E, qU_0)\mathrm{d}E, \tag{2.8}$$

where $\frac{\mathrm{d}N}{\mathrm{d}E}(E_0, m_\nu^2)$ is the differential tritium β-decay spectrum and $T(E, qU_0)$ the transmission function. The fact, that all electrons with a sufficiently large surplus energy are transmitted trough the MAC-E filter, is reflected by the integral. As the differential β-spectrum contains the information of the neutrino mass, an accurate knowledge of the transmission function is indispensable to deconvolute the integral spectrum. Example plots of the tritium β-decay

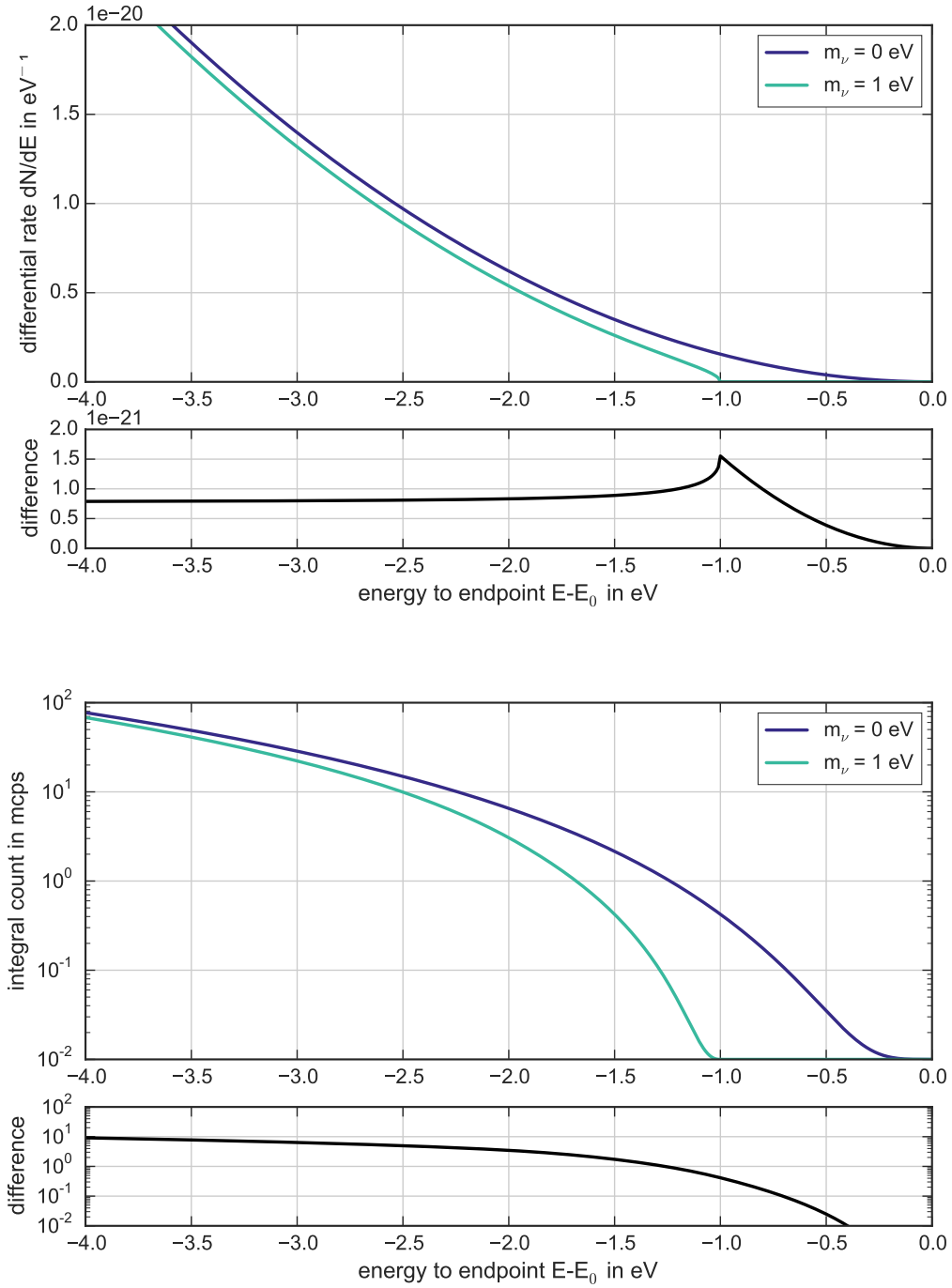

Figure 2.3: Tritium β-decay spectra in its differential (upper plot) and integrated form (lower plot). A spectrum with a vanishing neutrino mass is shown in blue and a spectrum with a neutrino mass of $m_\nu = 1\,\text{eV}$ in green. A constant background of 10 mcps is added to the integral spectra. For both plots, the difference of the two spectra is shown; in case of the differential spectrum a kink is clearly visible. To be as sensitive to a neutrino mass with the integral spectrum, a precise knowledge of the transmission function is mandatory for a deconvolution of the spectra. The spectra are calculated with the KATRIN software Kasper (section 3.2.3), energy losses and energy variations are neglected.

spectrum with $m_{\nu_e} = 0\,\mathrm{eV}$ and $m_{\nu_e} = 1\,\mathrm{eV}$ in differential and integral form are given in fig. 2.3. In these graphs, energy losses in the source and transport section are neglected.

In a first approach, the transmission function can be described fully analytically. The transmission function depends in this ideal setup only on the magnetic field in the source B_s, the maximal magnetic field B_max, the analyzing plane magnetic field B_a, the electrostatic potential U_0 and the initial kinetic energy of the electrons E_0. The fraction of transmitted electrons derives from eq. (2.2), based on the fact that only the longitudinal kinetic energy

$$E_\parallel = E_\mathrm{s}\left(1 - \sin^2(\Theta)\frac{B_\mathrm{a}}{B_\mathrm{s}}\right) - qU_0 \tag{2.9}$$

is analyzed. As the initial polar angle Θ of the electrons determines the longitudinal energy-component of the electron in the analyzing plane, the transmission function is split in three distinct sections, defined by the retarding potential U_0 and the energy resolution eq. (2.7). The exact shape of the transmission function depends on the angular distribution of the electrons in the source. Exploiting the relation $\cos\left(\arcsin\left(\sqrt{x}\right)\right) = \sqrt{1-x}$, the transmission function for an isotropic angular distribution is described by

$$T(E,qU_0) = \begin{cases} 0 & E - qU_0 < 0 \\ 1 - \sqrt{1 - \frac{E-qU_0}{E}\frac{B_\mathrm{s}}{B_\mathrm{a}}} & 0 \leq E - qU_0 \leq \Delta E \\ 1 - \sqrt{1 - \frac{B_\mathrm{s}}{B_\mathrm{max}}} & E - qU_0 > \Delta E. \end{cases} \tag{2.10}$$

The full transmission rate is reduced due to the maximal acceptance angle Θ_max eq. (2.6) that narrowed the solid angle

$$\frac{\Delta\Omega}{2\pi} = 1 - \cos(\Theta)\,. \tag{2.11}$$

A transmission probability is derived from the normalized transmission function by the factor $T_\mathrm{max} = 1 - \sqrt{1 - \frac{B_\mathrm{s}}{B_\mathrm{max}}}$. The resulting transmission function is visualized in fig. 2.4.

Transmission function of a realistic MAC-E filter

Constant input values of the electromagnetic parameters in the transmission-function calculation can not be assumed when the spatial extent of the experimental apparatus is incorporated. Instead the magnetic flux

$$\Phi = \int_A \vec{B}\cdot\mathrm{d}\vec{A} = \int_0^{r_\mathrm{max}} B(r) r \mathrm{d}r = \mathrm{const} \approx B\cdot A. \tag{2.12}$$

is the conserved quantity throughout the entire KATRIN beam line. The KATRIN experiment is designed for a magnetic flux of $\Phi = 191\,\mathrm{Tcm}^2$. Based on eq. (2.12), a geometric flux-tube area at the source of $A_\mathrm{source} \approx 32\,\mathrm{cm}^2$ leads to a large radial expansion of $r_\mathrm{max} = 4.5\,\mathrm{m}$ in the low field region of the spectrometer.

As electrons are confined within the magnetic flux-tube Φ, eq. (2.12) serves as a boundary condition to modulate the electromagnetic parameters of the transmission function (eq. (2.10)) on different radii. Most striking consequences are reflected by the following effects:

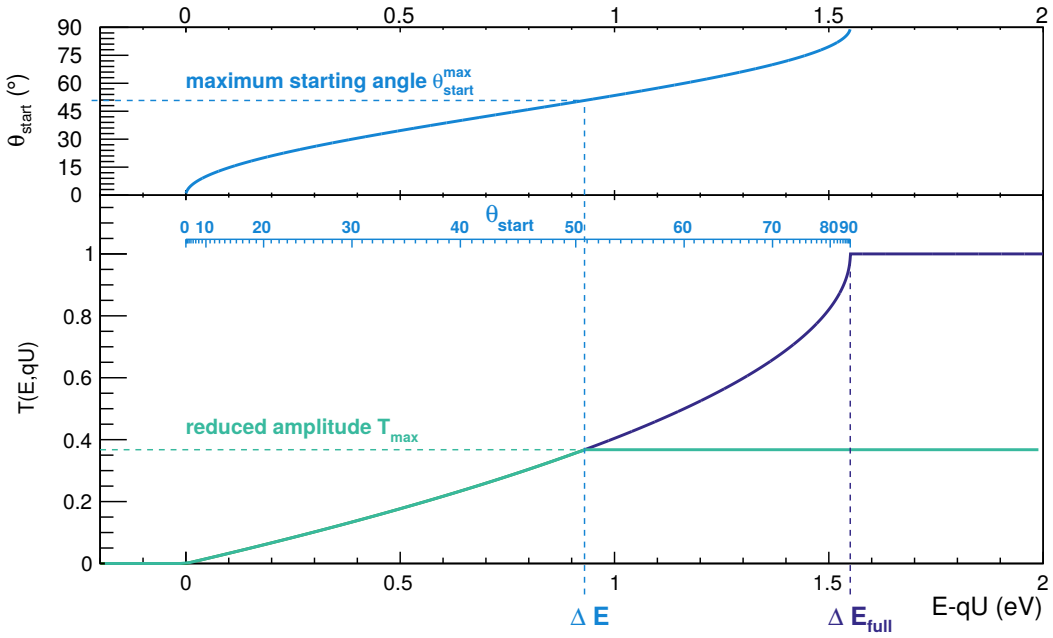

Figure 2.4: Transmission function of an isotropic source. The lower plot shows the transmission function with the KATRIN design values $U_0 = 18.6\,\mathrm{kV}$, $B_\mathrm{s} = 3.6\,\mathrm{T}$, $B_\mathrm{a} = 3\,\mu\mathrm{T}$ and $B_\mathrm{max} = 6\,\mathrm{T}$. The upper plot shows the polar angle Θ as a function of a given transmission energy. An additional axis illustrates the minimal required transmission energy. The observed electron rate is reduced, due to the maximal acceptance angle Θ_max in eq. (2.6). The dark blue curve corresponds to $\Theta_\mathrm{max} = 2\pi$ and the green curve to $\Theta_\mathrm{max} = 50.77°$. Figure adapted from ref. [Zac14].

- The electrostatic potential and magnetic field in the analyzing plane feature a radial inhomogeneity. The retarding potential is generated by an electrode system in the spectrometer. However, beam tube components at the entrance and exit of the spectrometer are on ground potential and modify the effective potential in the analyzing plane (section 3.1.2). Towards smaller radii the retarding potential becomes more positive, where the most positive value is found in the spectrometer center. Similar considerations lead to a radial dependency of the magnetic field in the analyzing plane (section 4.1.1). The resulting shape of the retarding potential and magnetic field in the analyzing plane is shown in fig. 2.5 for the most common settings used throughout this theses. Depending on the electromagnetic field setting, the transmission function is significantly widened, up to 50 %. As a countermeasure, a radially pixelated detector is deployed at the KATRIN experiment (section 2.2.4). When the transmission function is calculated for every pixel individually, the radial potential- and radial magnetic-field inhomogeneity per pixel is reduced significantly.
- Position of the analyzing plane. In the previous section, the analyzing plane was introduced as a plane orthogonal to the electron beam in the spectrometer center,

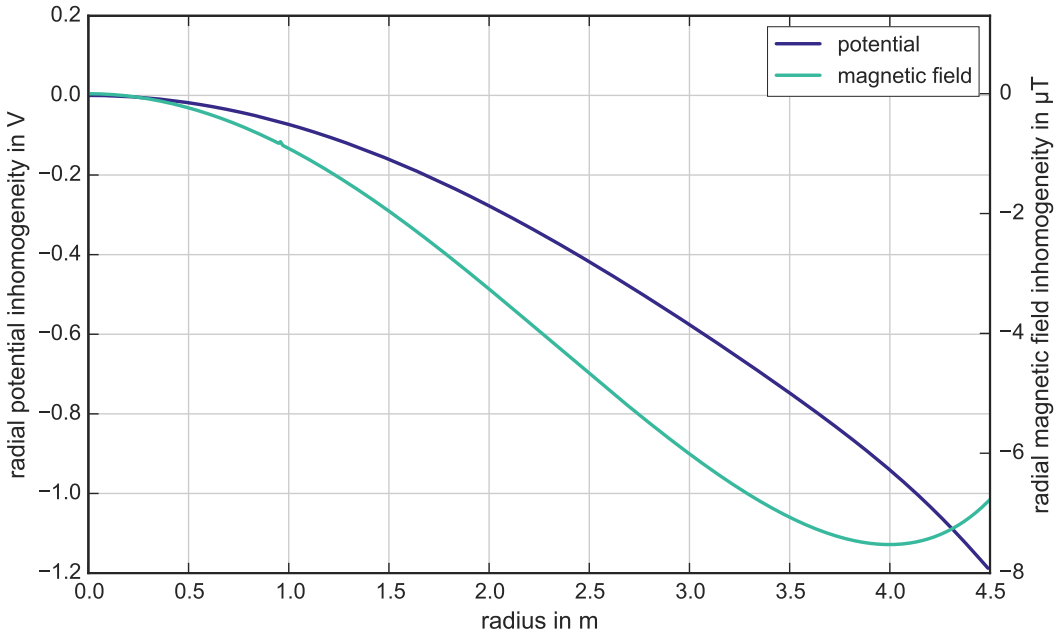

Figure 2.5: Radial inhomogeneity of the electrostatic potential and the magnetic-field in the analyzing plane at $z = 0\,\mathrm{m}$. The plot shows the difference to the potential and the magnetic-field values in the spectrometer center. The shape of these two quantities is defined by the three dimensional potential and magnetic field distribution in the main spectrometer. Here, the most common settings used throughout this thesis are applied (see chapter 3 and chapter 4).

but this is only an approximation. Instead, eq. (2.9) defines the location where the longitudinal energy is minimal. Thus, the analysis position depends on the inital polar angle of the electron and, due to the radial electromagnetic field inhomogeneity, also on the actual electron trajectory. Consequently, the positions of the analyzing points may vary by several cm and in extreme cases up to 0.5 m to 1 m in axial direction. A thoroughly optimization of the electromagnetic-field setting can minimize this effect in the sub-cm regime (section 4.1.2).

- Axial inhomogeneity of the initial magnetic-field at the location the β-decay of the analyzed electrons. Minor field variations of a few percent occur within the active volume of the source section due to small gaps between the solenoids. As a result, the maximal polar angle θ_{max} features variations also. Consequently, an integration of the transmission function along the source section, weighted by the tritium density, is necessary.
- The acceleration of charged particles in electromagnetic fields leads to an energy loss due to synchrotron radiation. Although the maximal radiative energy losses are less than 100 meV, the shape of the transmission function gets modified significantly in the endpoint region (ref. [Gro15]).

Consequences for an optimal operation of KATRIN are explained in the next section.

2.1.2 Requirements for the electromagnetic design of the main spectrometer

The magnetic field is essential for the KATRIN experiment to optimize the background and transmission properties of the MAC-E-filter (ref. [Noe06], [Glü09]). In the KATRIN setup, the main contribution to the magnetic field is provided by superconducting solenoids with field strenghts in a regime >1 T. In the source and transport section, the magnetic field must ensure that electrons are transmitted to the spectrometers without any interference with vacuum components (ref. [KAT05], [Gro15], [Bab14], [Stu12], [Com15]). For the main spectrometer, where the field strength decreases by about a factor of 5×10^{-5}, meeting these requirements is more challenging. Due to the low field strength, external influences are more pronounced and the magnet flux tube susceptible to deformations.

Several requirements for the electromagnetic design of the main spectrometer were identified (ref. [Glü13], [Wan13a], [Hug08]), concerning the:

1. magnetic guidance. All β-electrons within the 191 Tcm^2 flux tube are transported to the FPD detector for an optimal signal-to-noise ratio. Otherwise signal electrons would be lost when the magnetic flux-tube collides with any spectrometer structure, and furthermore, secondary electrons would be guided onto the FPD detector.
2. transmission conditions. For an analytic calculation of the transmission function of a certain magnetic field line, the analyzing point eq. (2.9) must be independent of the electron polar angle. The analyzing point is located where an electrons with an energy below the retarding potential are reflected. Therefore, the magnetic field and electrostatic potential are relevant only at one point. Further simplification of the transmission-function calculation is achieved when all analyzing points of the individual field-lines reside within a common plane. This is the so-called analyzing plane, perpendicular to the spectrometer axis. Both conditions can only be fulfilled for a symmetric magnetic-field along the spectrometer axis.

   In section 2.1 the derivation of the analyzing point calculation is given and in section 6.5.1 a discussion of the realistic shape of the analyzing plane can be found.
3. radial homogeneity. If the transmission conditions are fulfilled, also the radial homogeneity is optimized and thereby a major uncertainty parameter of the transmission function minimized. However, radial inhomogeneities of the electrostatic potential and the magnetic field across the analyzing plane are inevitable due to the finite size of the main spectrometer. Generally those inhomogeneities increase towards outer radii, a characteristic which is reflected in the FPD pixel layout.
4. magnetic shielding. Charged particles move along magnetic field lines on a cyclotron motion, and hence, the field has an intrinsic shielding effect against any charged particle created outside the sensitive flux tube. A stronger magnetic field can increase this effect by enlarged distance to surfaces as shown in experiments at the Mainz neutrino mass experiment (ref. [Mül02]), the prespectrometer (ref. [Lam09], [Gro10], [Frä10]) and the main spectrometer (ref. [Sch14b]). Also, the relative influence of azimuth field disturbances is reduced (ref. [Lei14]), though a larger magnetic field broadens the transmission function which leads to a reduced sensitivity.
5. adiabaticity. The motion of a signal electrons through the main spectrometer has to be adiabatic and therefore is the guidance completely reversible. Adiabatic transport

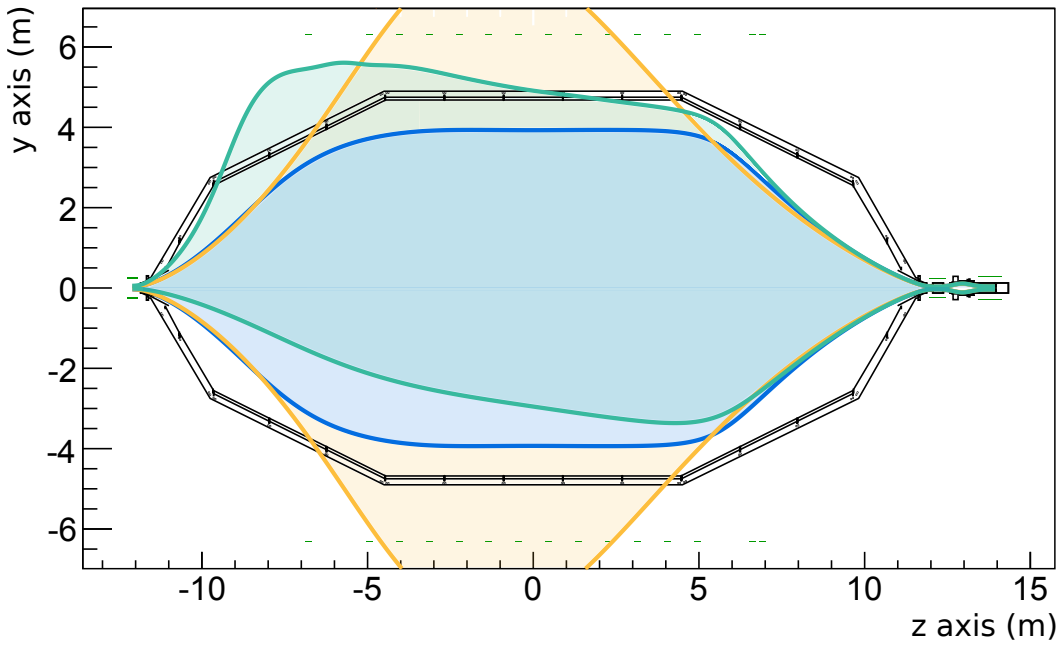

Figure 2.6: Influence of the air-coil system on the magnetic flux tube. In black the main spectrometer vessel and the inner electrodes are drawn. The magnetic field generating superconducting solenoids and the low field correction system (LFCS) are drawn in green (the earth magnetic-field compensation system (EMCS) is not shown here). The field lines correspond to a magnetic flux of 191 Tcm^2 on the detector waver. In case of the green line, the magnetic field is composed of the superconducting solenoids and the earth magnetic field only. For the yellow line the earth magnetic-field is fully compensated by the EMCS. When both air-coils systems (EMCS and LFCS) are combined, the resulting blue line is in agreement with all electromagnetic requirements.

can be assumed when the magnetic field changes only slightly within one cyclotron revolution (chapter 2.1). Non-adiabatic effects occur typically for high-energy electrons (ref. [Wan13b]).

To meet all the requirements stated above, an sophisticated air-coil system was installed at the KATRIN experiment. This large volume air-coil system allows for adjustment and fine tuning of the magnetic field shape in the main-spectrometer volume. It consists of two different types of coils, the low field correction system (LFCS) to define the magnetic field strength along the spectrometer axis and the earth magnetic field compensation system (EMCS) to ensure axial symmetry. Here only a brief introduction to the basic functionality of the air-coil system is given, advanced information is given in section 3.1.3 and chapter 4.

In the central part of the main spectrometer is the low-magnetic field region of the KATRIN setup located. To ensure axial symmetry in this region, the background field needs to be compensated, where the most prominent contribution is the earth magnetic field of about 50 µT. If not corrected for, the magnetic flux tube would be considerably deformed and non of the requirements as stated above would be fulfilled (figure 2.6). The EMCS generates a

constant and homogeneous magnetic field in the central part of the main spectrometer.

When only the EMCS is used, still several requirements are not satisfied, in particular the first and second. Therefore, the LFCS system is a necessary versatile design-element that allows to correct for the remaining electromagnetic requirements. A detailed description of technical realization of the air-coil system can be found in section 3.1.3.

Further adjustment of the electromagnetic design and parameter constraints are based on studies of other possible background processes, e.g. penning traps, field electron emission and hydrogen anions (ref. [Frä14], [Lei14], [Sch14b]). A discussion of those processes is beyond the scope of this thesis and the reader is addressed to the corresponding publications.

2.2 Main components

The experimental aperture of the KATRIN experiment is currently assembled at the KIT Campus North, where the Tritium Laboratory Karlsruhe (TLK) provides the necessary large throughput of gaseous molecular tritium. All components and sub systems of the 70 m-long main beam-line are on-site since summer 2015 and about to be commissioned. An overview of the KATRIN setup is given in fig. 2.7. Major sub-components are discussed in this section.

2.2.1 Tritium source and rear section

For the KATRIN setup a windowless gaseous tritium source (WGTS) is deployed as an emitter of β-decay electrons (fig. 2.8). The technical challenges are to ensure a high luminosity and stability simultaneously. Therefore, the WGTS is housed in a rather complex cryostat, to control the inlet pressure, the gas temperature and the tritium purity.

Gaseous molecular tritium is injected with a pressure of $p_i \approx 10^{-3}$ mbar and a temperature of $T = 30\,\mathrm{K}$. Thereby, a total of 5×10^{19} tritium molecules per second enter the source

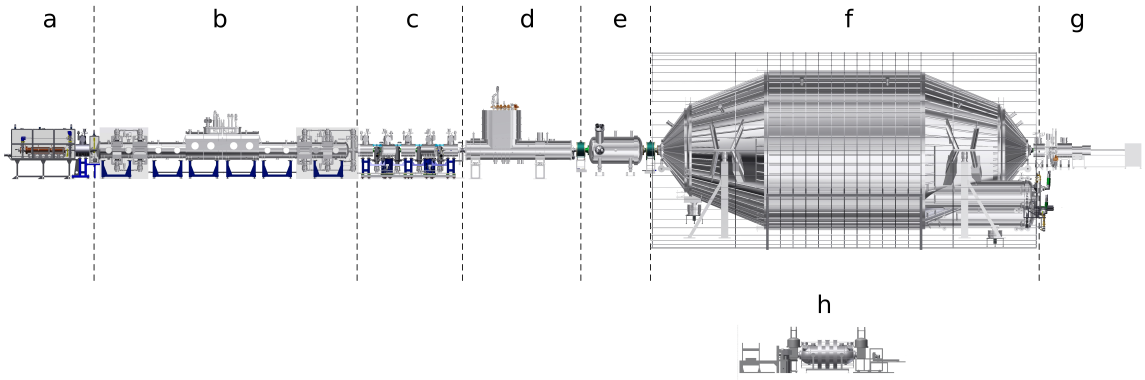

Figure 2.7: The KATRIN experiment has a 70 m-long beam line that consists of several sub components, indicated by dotted lines. The rear section (a), used for calibration of the experiment and monitoring of the WGTS (b), a windowless gaseous tritium source. The transport section is split in a differential (c) and cryogenic pumping section (d) and is supposed to reduce the gaseous tritium flow and to guide signal electrons magnetically to the spectrometers. In the pre-spectrometer (e) low-energy electrons are rejected and in the large main spectrometer (f) the energy of signal electrons is precisely analyzed. Finally the electrons are detected by the focal plane detector (g). The monitor spectrometer (h) is a component of the system to monitor the retarding-potential of the main spectrometer.

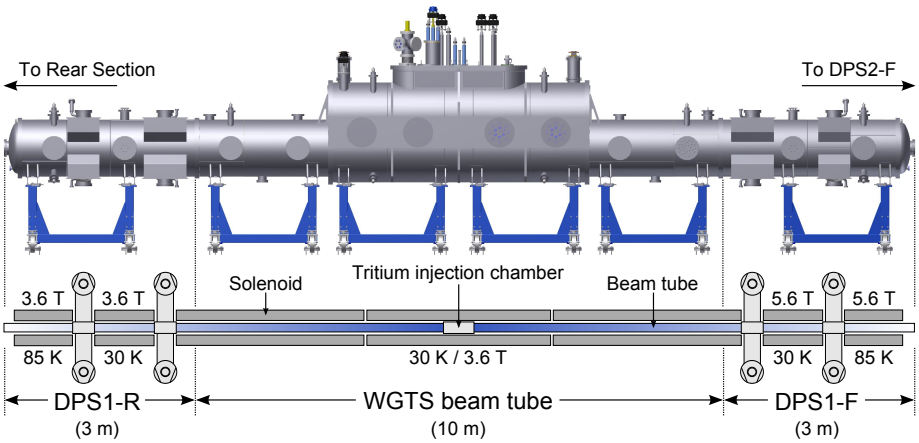

Figure 2.8: Windowless gaseous tritium source (WGTS) of the KATRIN experiment. A central beam tube of 10 m length is temperature-stabilized to 30 K. In its center highly-pure molecular tritium is injected via a set of capillaries. Two 3 m-long differential pumping systems (DPS1-R and DPS1-F) pump-out the injected gas on both ends. The blue gradient indicates the tritium density. A super conducting solenoid generates the source magnetic-field to guide the electrons to the spectrometer. Gaps between the three sections lead to minor magnetic-field variations of ≈1.7 %. Figure adapted from ref. [Höt12].

beam-tube in its center. The beam tube is a cylindrical stainless-steel tube of 10 m in length and 90 mm in diameter. To reduce the gas flow towards the spectrometer by a factor of 10^2, turbo-molecular pumps (TMP)'s are utilized in 3 m long differential pumping sections at both ends. The pumped-out tritium is collected, purified and re-injected via a pressure-controlled buffer, thus forming a closed tritium cycle, the so-called inner loop (ref. [Stu10], [Pri15]).

The beam tube is kept stable at a temperature of (30.0 ± 0.3) K by a novel cooling concept based on a two-phase liquid neon thermosiphon (ref. [Bod11], [Gro11]). The benefit of such a low temperature is to minimize the tritium throughput and to limit the effect of thermal Doppler broadening of the electron energies due to molecular motion, but it is also big enough to suppress the effects of clustering and condensation of hydrogen isotopologues. Extensive tests at the WGTS demonstrator revealed the temperature fluctuations to be of one order of magnitude smaller than the requirements (ref. [Höt12], [Gro13]).

For the injected gas, at least a tritium fraction of >95 % is required. The gas composition is monitored by a dedicated in-line Laser-Raman spectroscopy setup, the LARA system (ref. [Sch13], [Fis14]).

With this setup, a stable column density of $\rho d = 5 \cdot 10^{17} \mathrm{cm}^{-2}$ is achieved, which corresponds to an activity of the source of $A \approx 10^{11}$Bq (ref. [Bab12]). Three large superconducting solenoids, coaxially arranged around the beam tube, provide a nearly homogeneous start magnetic field of $B_S = 3.6$ T to guide the signal electrons out of the source. Either in forward direction towards the spectrometer or backwards to the rear section.

The rear section contains several control- and monitor devices to

- monitor the source activity by a β-induced X-ray spectroscopy (BIXS) ref. [Röl13],
- define the electrostatic potential of rear wall and the tritium plasma in the source (ref. [Sch16]),

- measure the source column density in regular intervals via the inelastic scattering of electrons in the source by the use of an angular-resolved electron gun (ref. [Bab14])

This electron gun is also used for various test measurements during the commissioning phase of the beam line, e.g. to measure the energy-loss function and the cross sections for inelastic scattering of 18.6 keV electrons of with molecular tritium molecules (ref. [Gro15]). The final assembly of the Rear Section currently takes place in the TLK and is expected to be finished in 2016 (ref. [Mon15]).

2.2.2 Transport section

The transport section connects the WGTS, where gaseous tritium is injected at a pressure of the mbar-regime, with the ultra-high vacuum (UHV) spectrometer section. Tritium partial pressure must be lower than $p_T < 10^{-20}$ mbar to keep the background below the upper design limit (ref. [Mer12]). Hence, a reduction of the tritium flow by 14 orders of magnitude within the transport section is required. Two different approaches are utilized in the transport section to pump tritium molecules in the differential pumping section (DPS) and the Cryogenic Pumping Section (CPS). Just as important is the adiabatic transport of the signal electrons to prevent energy losses.

Differential pumping section

In the first part of the transport section is the differential pumping section (DPS) located. It is 7 m-long that is split in five segments, each equipped with a superconducting solenoid that generate a 5.6 T field in its center to guide the electrons. The beam tubes of the individual segments are tilted by 20° against each other to suppress the molecular beaming effect by a direct line-of-sight (ref. [Luo06]). Between the beam-tube segments are TMP's with a pump

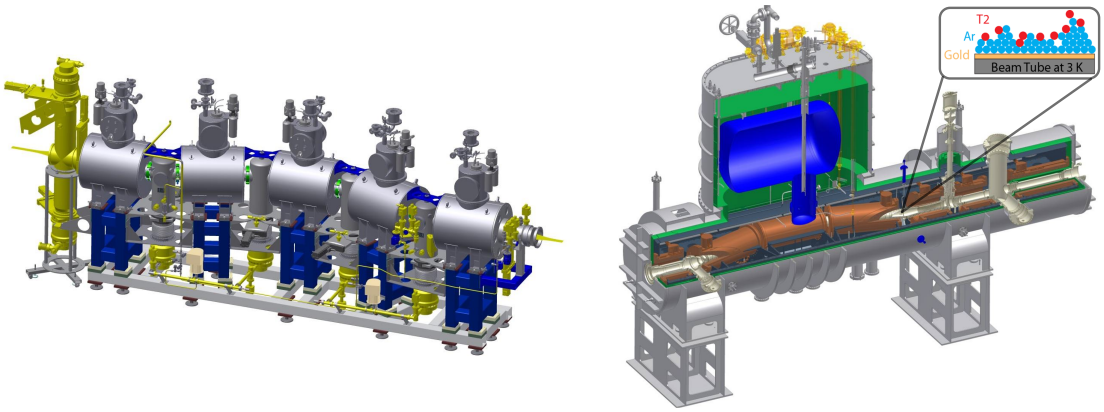

Figure 2.9: Technical design of the KATRIN transport section. On the left, the differential pumping section DPS is shown, consisting of five superconducting solenoids (silver) to guide the β-electrons magnetic-adiabatically through the bent beam-tube. Four turbo-molecular pumps (yellow) are placed in between to reduce the tritium gas flow by four to five orders of magnitude. Figure inspired by ref. [Hac15]. The cryogenic pumping section CPS on the right utilize seven superconducting coils to guide signal electrons trough a bent beam-tube. Here, a passive pumping system is deployed, where tritium molecules are adsorbed on a 3 K-cold gold-plated surface that is covered by an argon frost. Thereby, a reduction of tritium flux by another seven orders of magnitude is achieved. Figure adapted from ref. [Wan13b].

capacity of 2400 l/s installed that reduce the gas flow up to five orders of magnitude (ref. [Luk12], [Jan15]).

However, positive ions are produced in the large number of β-decays in the WGTS as well, and those are not effectively reduced by the differential pumping and guided magnetically towards the spectrometers. As these ions would introduce a large background, they must be restrained from entering the spectrometers. A so-called Fourier Transform-Ion Cyclotron Resonance (FT-ICR) unit is installed to identify ions (ref. [Ubi09], [Día11]). A ring-shaped blocking electrode at the downstream side of the DPS is operated with a positive potential of $U_{\text{block}} = 100\,\text{V}$ to block the ions (ref. [Sac15]). Three dipole electrodes are deployed to remove ions via a $\vec{E} \times \vec{B}$ drift from the active magnetic flux-tube (ref. [Rei09], [Win11]). Additional information on the commissioning process can be found in ref. [Jan15], [Hac15].

Cryogenic pumping section

The remaining tritium flow has to be reduced by another seven orders of magnitude in the cryogenic pumping section (CPS). In contrast to the DPS, a passive pumping technique is deployed (ref. [Luo08], [Eic08]). For cryosorption of T_2 molecules, the beam tube is cooled to a temperature of 3 K. Efficiency of the gas adsorption is increased by a tilting of the beam tubes by 15° against each other in combination with a thin argon frost-layer on a gold-coated surface. A continuous operation of three months until the argon frost is saturated with 1 % tritium is expected and a regeneration is required.

To guide electrons, the CPS elements are surrounded by seven superconducting solenoids that provide a magnetic field of 5.6 T. Furthermore, the CPS houses the so-called forward beam monitoring detector. This is an electron detector, positioned in the outer flux-tube region, which is used to determine the WGTS activity in real time without interfering with a neutrino-mass measurement (ref. [Bab10], [Bes11]). Additional calibration measurements are possible with a condensed krypton source that provides mono-energetic conversion electrons that can be deployed in the active flux tube (ref. [Bot12], [Bau13a]).

For further information the reader is referred to [Gil10] and [Luo08].

2.2.3 Spectrometer section

A tandem setup of MAC-E filter based spectrometers is used for the energy analysis of the β-decay electrons, the pre-spectrometer and the main spectrometer (fig. 2.10). A UHV vacuum in the regime of 10^{-11} mbar is required for a sufficiently low background level.

Pre-spectrometer

The 3.4 m long and 1.7 m width pre-spectrometer is the first spectrometer that electrons from the transport section enter. It is located in between two superconducting solenoids, called PS 1 and PS 2, and each magnet generate a field of 4.5 T. Thereby it serves the purpose of a pre-filter to reject signal electrons well below the tritium endpoint-energy $E_0 = 18.6\,\text{keV}$ and when operated at a retarding potential of $U_{\text{pre}} = 18.3\,\text{kV}$ it features an energy resolution of $\Delta E \approx 70\,\text{eV}$ (ref. [Pra11]). A reduced electron rate in the main spectrometer is in favor, as it reduces additional background introduced by scattering with residual gas. However, it is discouraged to apply such large potentials as a this creates a penning trap between the pre- and main spectrometer (ref. [Pra12]). Therefore, an ideal setting for an operation of the pre spectrometer remains an open issue that will be addressed in an upcoming measurement campaign when the entire KATRIN beam line can be utilized.

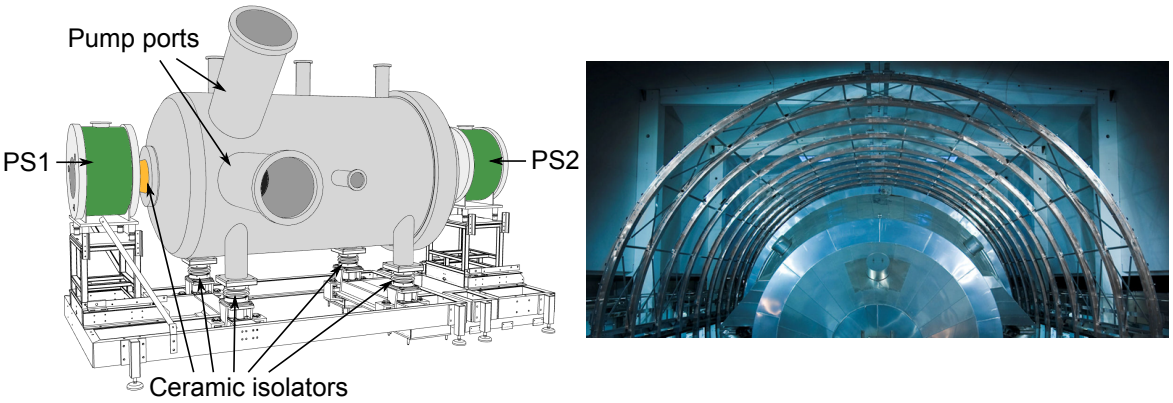

Figure 2.10: The KATRIN pre- and main spectrometer. On the left, a sketch of the pre-spectrometer is shown with the two superconducting solenoids pre-spectrometer magnet 1 (PS 1) and pre-spectrometer magnet 2 (PS 2). Ceramic insulators ensure a potential setting autonomic from the main retarding potential to filter-out low-energetic β-electrons. Figure adapted from ref. [Frä10]. On the right side is picture of the main spectrometer from the pre-spectrometer side, surrounded by the air-coil system (photo by KIT,2009).

Previously to the most recent measurement campaigns, the pre-spectrometer was used as a stand-alone test facility to study transmission properties and background (ref. [Hab09], [Gör10], [Gro10], [Frä11], [Wan13b]). Based on these results the main-spectrometer design was further improved.

Main spectrometer

The main spectrometer is the most outstanding component of the KATRIN experiment by its dimensions alone. With a length of 23.3 m and a maximal diameter of 10 m, it encloses a volume of 1240 m^3. This size is a direct consequence of the electromagnetic design requirements for an adiabatic transport and a precise energy-analysis (section 2.1.2). The retarding potential in generated by applying high-voltage to the vessel itself and to the inner-electrode system of thin wires in addition (ref. [Kra12], [Bau13b], [Res14], [Wac15] and [Kra16]). The advantage of the inner electrode system is a fine-tuning of the potential shape in the analyzing plane and a reduction of the background by a blockage of charged particle from the vessel hull (ref. [Hug08], [Zac09], [Val09], [Val10], [Pra11]). Common settings used in this thesis can be found in (section 3.1.1).

The magnetic field for a MAC-E filter operation is of main interest in this theses. On both ends, a high magnetic-field of several Tesla is generated by the superconducting pre-spectrometer and FPD solenoids (section 2.2.4). Especially the magnetic field that is generated by the air-coil system to fine-tune the magnetic field is thoroughly studied in 4 and chapter 5. These results are the foundation of an elaborated investigation of the transmission properties in chapter 6 and the sensitivity studies in chapter 7.

The background level is further improved by maintaining excellent vacuum conditions, which is accomplished by a sophisticated pumping system (ref. [Are16], [Gör14], [Har15b]).

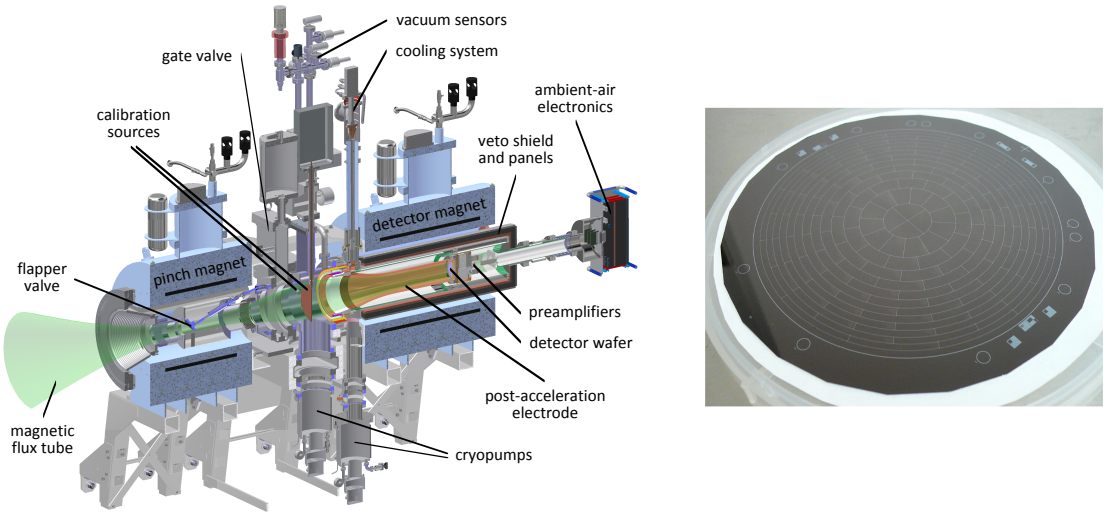

Figure 2.11: Setup of the focal plane detector-system (left side). Electrons that are transmitted trough the main spectrometer are magnetically guided by two superconducting solenoids (pinch magnet (PCH) and detector magnet (DET)) to the detector. To reduce back scattering and to shift the energy of the electrons to a region of superior signal-to-background ratio, a post-acceleration electrode is deployed. Finally, the electrons are recorded by a segmented silicon PIN-diode detector wafer (right side). Figure adapted from ref. [Ams15] and [Wal13].

2.2.4 Focal plane detector

Electrons that pass the main spectrometer retarding potential are counted with the focal-plane detector system (FPD), where they are guided to by two superconducting solenoids, PCH and DET. In the nominal setup, the magnets generate a fields of 6 T and 3.6 T respectively. The detector wafer is a monolithic silicon PIN-diode array (fig. 2.11), where its backside is segmented in 148 pixels and thereby offers a sensitive diameter of 9 cm, of thickness 500 µm. For a low intrinsic background, the wafer is enclosed by lead and copper for a passive shielding and an active veto-system based on plastic scintillators to discriminate against signals from incident cosmic rays. To reduce back scattering of electrons on the detector surface, the wafer is located in the center of the DET magnet for a perpendicular impinging of the magnetic-field. Back scattering is further reduced by a post-acceleration electrode (PAE) that allows to accelerate electrons up to 10 kV (ref. [Ren11], [Erh15e]). Secondly, does the PAE shift the electrons to a high energy level, where a more favorable intrinsic detector background-rate is observed (ref. [Sch14b]). For all measurements presented in this work, the PAE was set to $U_{\mathrm{PAE}} = 10\,\mathrm{kV}$).

Further information on the detector operation parameter and performance can be found in ref. [Ams15], [Har12], [Wal13], [Sch14b] and [Har15b].

2.2.5 Monitor spectrometer

The monitor spectrometer is a major component of the high-voltage monitoring concept (ref. [Erh14d]). By measuring mono-energetic conversion electrons of $^{83\mathrm{m}}$Kr, conclusions about the stability of the applied retarding potential can be made. It also serves as a test facility for the e-gun prior to the most resent measurement campaign (ref. [Beh14]).

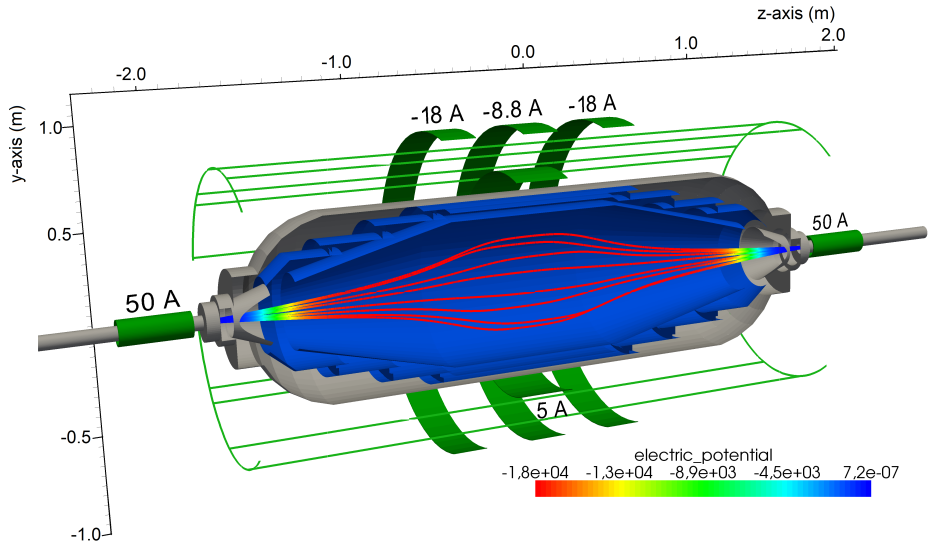

Figure 2.12: The monitor spectrometer at KATRIN is operated as a MAC-E filter. Two superconducting solenoids on both sides generate a magnetic field of $B_{\mathrm{MoS}} = 6\,\mathrm{T}$ in their center. Four air-coils and an earth magnetic-field compensation system are used to fine-tune the magnetic field in the spectrometer center. An inner electrode system provides the retarding potential. Figure adapted from ref. [Erh14d].

Just as the main spectrometer, the monitor spectrometer is based on the MAC-E filter principle and is operated with the same energy-resolution of $\Delta E = 0.93\,\mathrm{eV}$. It has a length of 4 m, a maximal diameter of 1 m and is located parallel to the main spectrometer in a separate building. The main magnetic-field is provided by two superconducting solenoids of 6 T, located on the spectrometer entrance and exit at $\pm 2.01\,\mathrm{m}$. In addition, an air-coil system for fine-tuning of the magnetic field in the analyzing plane is deployed (ref. [Gou10], [Sch11]). A galvanic connection to the main spectrometer supplies the monitor spectrometer with the identical retarding potential[1].

A measurement of mono-energetic electrons is used to continually monitor the retarding potential. Such electrons are found in a solid-state krypton source, emitting conversion electrons from the K-shell by the 32 kV γ-transition with an energy of 17.8 keV (ref. [Zbo11]). These sources are produced by implanting the mother isotope ^{83}Rb in a substrate, such as platinum or highly ordered pyrolytic graphic (HOPG) (ref. [Erh12], [Sle13]). As the line energy is about 800 eV below the tritium end point, an potential has to be applied to the sources. This additional sources potential also allows for an individual measurement schedule, even when operated in parallel mode with the main spectrometer. The observed drift and fluctuation of the energy and width of the K-32 conversion electrons are then used to evaluate the high-voltage stability on the sub-ppm scale (ref. [Sle16]).

1 The monitor spectrometer can be decoupled from the main spectrometer and operated with an independent power supply. This separated setup is typically used in test measurements.

2.3 Sensitivity for a neutrino mass discovery

The measurement with a MAC-E filter results in an integrated spectrum of the tritium-decay electrons (section 2.1). In the minimal five parameter fit configuration, the observed total count-rate depends on the applied retarding potential U_i, the background rate R_{bgd}, the tritium endpoint energy E_0, an amplitude C and the measurement observable of a neutrino mass $m^2_{\bar{\nu}e}$ (ref. [KAT05]). At any given retarding potential U_i the theoretical count rate is

$$R_{\mathrm{theo}}(U_i, C, R_{\mathrm{bgd}}, E_0, m^2_{\bar{\nu}e}) = R_{\mathrm{sign}}(U_i, C, E_0, m^2_{\bar{\nu}e}) + R_{\mathrm{bgd}}, \tag{2.13}$$

where R_{bgd} is assumed to be constant and Poisson distributed in the tritium endpoint-energy region. From eq. (2.8), a signal rate is derived

$$R_{\mathrm{sign}}(qU_i,E_0,m^2_{\bar{\nu}e}) = C \cdot N_{\mathrm{tot}} \cdot \varepsilon_{\mathrm{det}} \frac{\Omega}{4\pi} \int_{qU_i}^{E_0} \frac{\mathrm{d}^2 N}{\mathrm{d}E\mathrm{d}t}(E_0,m^2_{\bar{\nu}e}) \cdot R(E,qU_i)\mathrm{d}E, \tag{2.14}$$

where the total number of observable electrons from the source is given by $N_{\mathrm{tot}} = AS \cdot \rho d \cdot \varepsilon_{\mathrm{tot}}$, the detector efficiency is identified with $\varepsilon_{\mathrm{det}}$, the solid angle $\Omega = 2\pi\,(1 - \cos\,(\Theta_{\mathrm{max}}))$ of the transmitted electrons and $R(E, qU_i)$ is the response function[1] of KATRIN.

When the theoretical and experimental (measured or simulated) count rates are compared, the four parameters C, R_{b}, E_0 and m^2_ν are used to minimize the difference

$$\chi^2(R_{\mathrm{exp}},R_{\mathrm{bgd}},E_0,m^2_{\bar{\nu}e}) = \sum_i \left(\frac{R_{\mathrm{exp}}(qU_i) - R_{\mathrm{theo}}(qU_i,R_{\mathrm{s}},R_{\mathrm{bgd}},E_0,m^2_{\bar{\nu}e})}{\sigma_{\mathrm{theo}}(U_i)} \right)^2, \tag{2.15}$$

where $\sigma_{\mathrm{theo}}(U_i)$ is the expected statistical fluctuation $\sigma_{\mathrm{th}}(U) = \sqrt{(R_{\mathrm{sign}} + R_{\mathrm{bgd}})}$ of the count rate. The resulting statistical-uncertainty strongly depends on the selected measurement time distribution for each retarding potential $t(U_i)$.

Based on the design parameters of the KATRIN experiment, for the neutrino mass $m^2_{\bar{\nu}e}$ a statistical uncertainty of

$$\sigma_{\mathrm{stat}} = 0.017\,\mathrm{eV}^2 \tag{2.16}$$

is obtained after a three year long measurement-period. In a conservative estimation, regarding the parameters in the KATRIN design-report, the systematic uncertainty is of the same order of magnitude and the total error budget is calculated by

$$\sigma_{\mathrm{tot}} = 0.025\,\mathrm{eV}^2. \tag{2.17}$$

1 The response function combines the transmission function with additional energy-modification and energy-losses due to a variety of effect such as final state distribution, a thermal Doppler effect and more. The responds function starts to differ from the transmission function about 10 eV below the tritium endpoint.

Such conditions allow for a measurement of a 5σ significance for a neutrino mass $m^2_{\tilde{\nu}e}$ down to $350\,\mathrm{meV/c^2}$ or a new upper limit of

$$m^2_{\tilde{\nu}e} < \sqrt{1.64 \cdot \sigma_{\mathrm{tot}}(m^2_{\tilde{\nu}e})} = 200\,\mathrm{meV/c^2} \quad (90\,\%\,\mathrm{C.L.}) \tag{2.18}$$

is derived, improving the current upper limit of the neutrino mass by one order of magnitude.

The magnetic-field uncertainty has an impact on the neutrino-mass sensitivity in various aspects, as it directly influences the width of the transmission function, the accuracy of the analyzing plane position and the observed background rate. Based on the magnetic field studies in this thesis, ensemble test are performed in chapter 7 to estimate the influence of the magnetic field and to identify a setting for an optimal neutrino-mass measurement.

CHAPTER 3

Measurements of the spectrometer and detector section

In the context of the commissioning measurements, the utilized hardware setup comprises the main- and monitor spectrometer, together with their magnet systems as well as the FPD system (see chapter 2) and is referred to as the spectrometer and detector section (SDS). To confirm the operation readiness for a neutrino mass measurement, the SDS sub-components were tested together in an extended measurement campaign to check the overall hardware integrity, to develop and refine background models and to test analysis methods as well as the involved simulation framework.

The first commissioning measurement phase of the spectrometer and detector section (SDS 1) revealed insight to the properties and respective background processes of the system which were detail in ref. [Thu], [Are16], [Lei14], [Sch14b], [Gro15]. The thesis at hand is based on results obtained during the second commissioning measurement phase (SDS 2), where extensive hardware and software updates were implemented to operate the electromagnetic setup very close to its nominal regime. The SDS 2 measurement campaign is split in two phases A and B, reflecting the bake-out phase in between. Results of the thesis at hand were almost exclusively obtained during the phase SDS 2 A.

Section 3.1 is focused on the hardware setup of the SDS 2 campaign and the specific operation ranges of the individual sub-components. A key focus is put on upgrades of the hardware. These are directly coupled to the refinements of the analysis software and measurement infrastructure, particular with respect to measuring and control technology applications in the periphery of SDS (section 3.2).

The monitoring of the magnetic field relies on several sensor systems and is a key example of hardware related progress, where the installation of the high-precision magnetometers has improved the magnetic-field monitoring considerably (section 3.3). In this section the utilized magnetometer types and their implementation in the magnetic field analysis framework are introduced.

To tap the full potential of the SDS apparatus, extensive alignment measurements were necessary (section 3.4). A key aspect here was to obtain a correct magnetic-field mapping by measurements which then were compared to simulations to generate a realistic magnetic-field model.

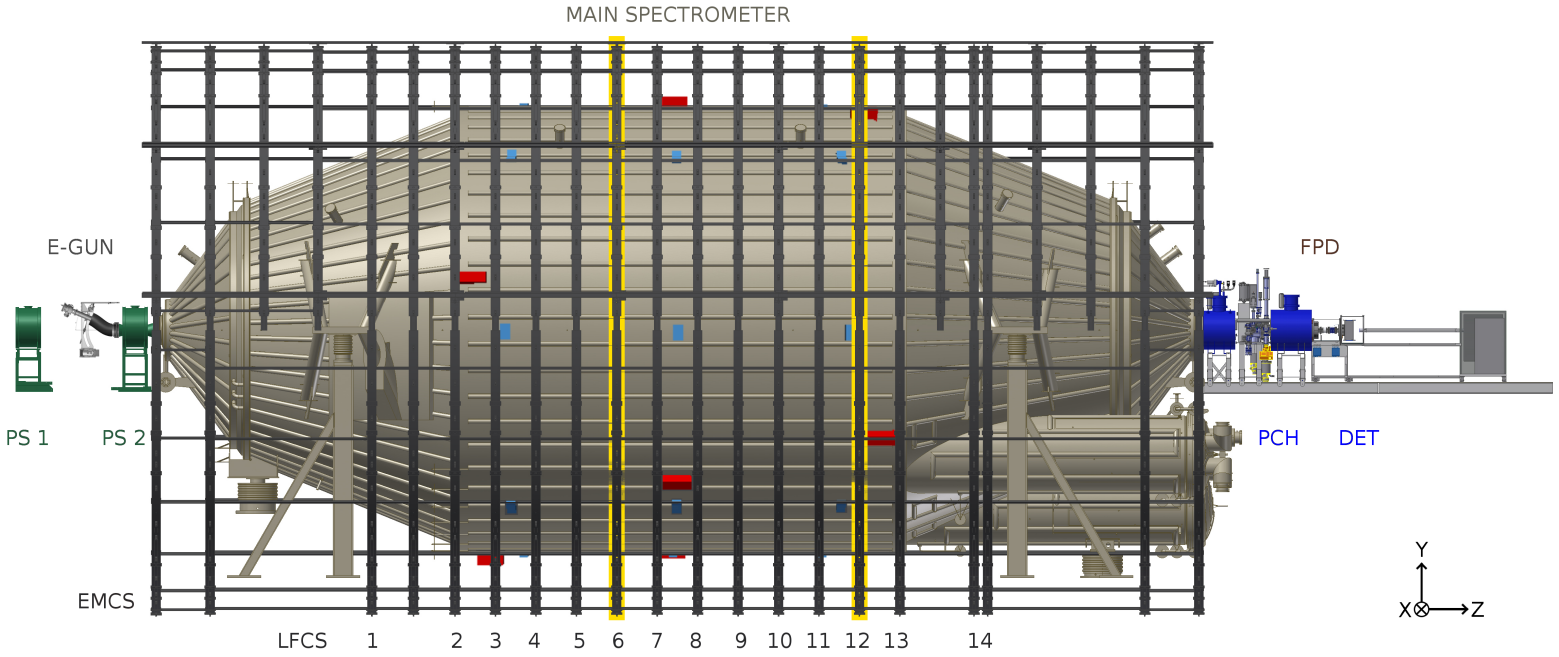

Figure 3.1: Hardware setup of the second commissioning measurement phase of the source and detector section. The 30 m long beam line consists of the main spectrometer vessel in the center, an electron gun (E-Gun) attached on the upstream side (left) and the focal plane detector system (FPD) on the downstream side (right), consisting of a silicon wafer with 148 pixels. The magnet system is formed by two pairs of superconducting solenoids, the pre-spectrometer magnets 1 and 2 (PS1 and PS2), as well as the pinch (PCH) and detector (DET) magnets. The large volume air-coil system surrounding the vessel is shown in dark grey. The individual coils of the low field correction system (LFCS) are enumerated in increasing numbers from upstream to downstream. The non axial-symmetric earth magnetic field compensation system (EMCS) consists of parallel bars along the beam axis and circular cabling on the two outer most rings of the air-coil system. The red and light-blue boxes indicate the positions of the two installed magnetometer types. The two LFCS rings 6 and 12 (highlighted in yellow) are equipped with a mobile magnetic-sensor unit (MobSU). The monitor spectrometer is not included.

3.1 Hardware configuration

The entire KATRIN experimental hall contains several reference points which allow to measure a position relative to the KATRIN coordinate system. The right-handed KATRIN coordinate system has its origin in the center of the main spectrometer vessels. The z-axis points axially to the detector, the y-axis describes the vertical (pointing to the top) and the x-axis is the horizontal alignment directions (pointing to the west). Positions that are closer to the WGTS are referred to as upstream while those closer to the FPD reflect the downstream side. A object in the KATRIN coordinate system is described with its three spatial coordinates and three Euler angles, usually a z-x′-z″ rotation convention is used.

An overview of all components of SDS 2 can be found in fig. 3.1.

3.1.1 Main spectrometer vessel

The main spectrometer allows precision electron-energy filtering close to the β-decay endpoint. This requires

- ultra-high vacuum in the 10^{-11} mbar regime to reduce electron scattering off residual gas. With a length of 23.3 m and an inner diameter of 9.8 m at maximum, the UHV recipient has a volume of 1240 m^3 and an inner surface of 690 m^2, making it the world's largest ultra high-vacuum. To reach the operational pressure a cascaded pumping system in three huge pump ports on the downstream side of the spectrometer (right side off fig. 3.1) equipped with a total of six TMP of type Leybold MAG-2800 and SAES St707 non-evaporable getter (NEG) strips of 1 km length have been implemented.

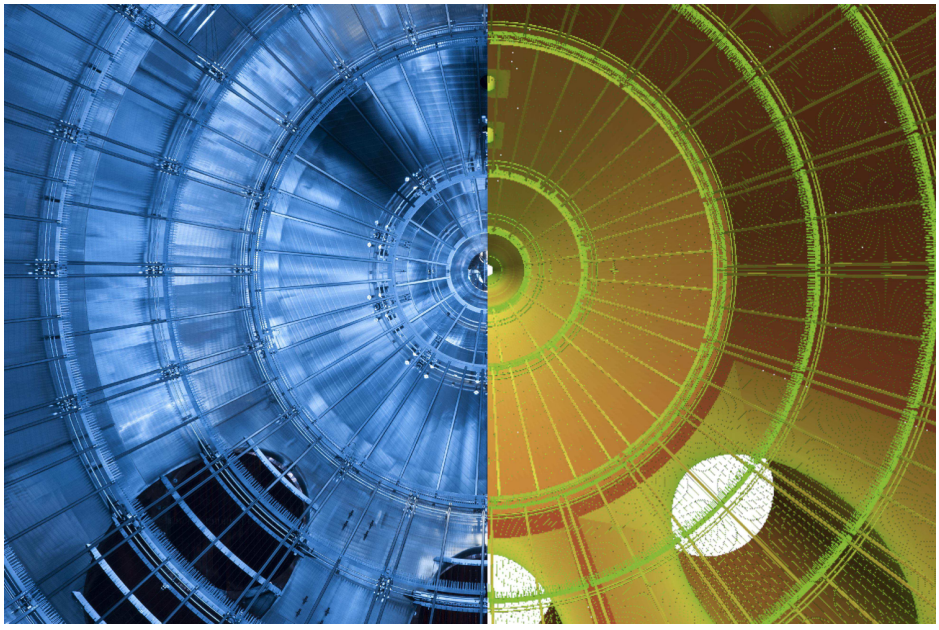

Figure 3.2: Inner surface of the KATRIN main spectrometer. The figure compare a photograph of the inner surface of the main spectrometer and its inner electrode-system (left) with the corresponding representation in the simulation package (right) allowing a detailed three dimensional potential simulation. Picture by KIT, figure adapted from [Cor14].

The discussion of a pressure dependency of the background in the main spectrometer is beyond the scope of this thesis. The reader is referred to ref. [Are16] for technical details on the vacuum performance and the composition of the residual gas, whereas and the impact of the UHV conditions on the observed background is discussed in ref. [Har15b].

- precise retarding potential for the MAC-E filter. The vessel it is insulated against ground potential to allow continuous high voltage (HV) operation in the range of up to −35 kV (ref. [Kra16]). A key element for precision filtering is the inner wire electrode-system that is used to define the shape of the retarding potential. In particular, this major component corrects the non-cylindrical shape of the vessel hull (ref. [Hug08], [Zac09], [Val10]) and allows electrostatic shielding against low-energy electrons from the vessel surface up to −1 kV (ref. [Val09], [Pra11]) by applying additional potential offsets.

In fig. 3.2 the downstream side of the inner KATRIN main-spectrometer is shown both as a photograph and its representation in the simulation package of KATRIN. The three pump ports and the ring-shaped support structure of the inner electrode-system are clearly visible. In section 3.1.2 the technical realization and characteristics of the KATRIN electrode system are presented, while the corresponding implementation in the simulation package is detailed in section 3.2.3.

3.1.2 High voltage system

The inner wire-electrode system consists of a total of 248 modules, which are sub-divided into 15 rings along the spectrometer axis. A total of 23 000 wires are installed with an diameter of 300 µm. In the central and flat-cone parts of the spectrometer the wires are organized in a double-layer structure were the inner wires have a diameter of 200 µm only. The HV routing is such, that different potentials can be applied to the two wire layers. In addition, these modules are also split in a west and east side to allow a dipole configuration. In the high electric-field regions on both ends of the spectrometer, a so-called anti-Penning electrode and ground electrode are installed for field shaping (ref. [Zac09],[Bau13a]).

The HV distribution system (fig. 3.3) allows to apply potential differences of several hundred volts between electrode units (ref. [Bau13a]) and thereby to adjust the electric field for requirements of a specific measurement. Several short-circuits in the HV distribution inside the spectrometer occurred during the initial bake-out of the spectrometer prior to SDS

Table 3.1: Standard potential settings for transmission function measurements. A global vessel voltage plus an offset to the inner electrode (IE) (ring 02 to 16 in fig. 3.3) define the overall setting, while a further offset voltage is added to the steep cones (ring 02,03 and 15,16) to prevent early retardation. Acceleration and dipole voltages applied to the electron gun (e-gun) are explained in section 3.1.4.

setting	vessel (kV)	IE (V)	steep (V)	accel. (kV)	dipole (kV)
HV	−18.4	−200	100	5.0	3.0
LV	0.0	−200	100	0.1	3.0

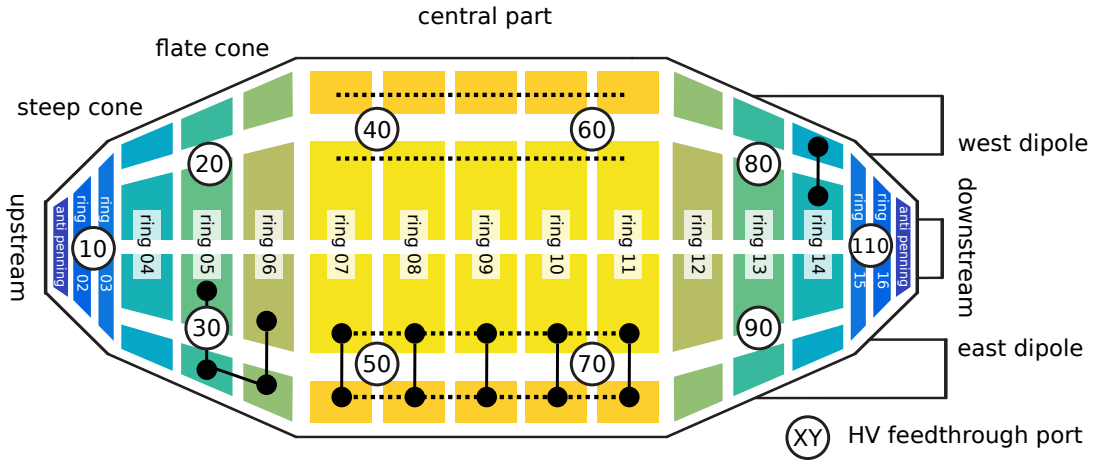

Figure 3.3: High voltage distribution in the KATRIN main spectrometer. The inner electrode system consists of 15 wire-module rings plus an additional solid anti-Penning electrode on each end. Vertical and horizontal segmentation indicate modules on a common potential, in the central part and flat cones they are double layered and split in an west and an east dipole half. A potential is applied via the ten HV feedthrough ports. Intentionally (unintentionally) short-circuited modules are indicated by a dashed (solid) line. Fig. inspired by [Han13a].

1 (ref. [Han13a], [Dyb14]). Up to now this has prevented to operate the system in a double layer mode.

The electron-transport properties of the main spectrometer during a later neutrino-mass measurement require an axial-symmetric potential distribution. Also, the HV system has to be reliable and stable. In the context of the presented works, two HV configurations were used for transmission function studies, referred to as HV-setting and LV-setting (table 3.1) that are discussed in greater detail in section 6.3. There, the rings 04-14 were short-circuited to a common potential to guarantee radial and axial symmetry and usually ring 02,03 and 15,16 were short-circuited as well. In case of the individual set points of steep cone rings, the minor potential fluctuations of a few mV can be neglected (ref. [Kra16]). The electric-field layout used in this thesis is based on only three parameters: A common HV level applied to the main spectrometer, a negative potential offset for the inner electrode, plus an additional positive offset for both steep cones.

3.1.3 Magnet system

During SDS 2 campaign, the magnetic field was generated by four superconducting solenoids as well as the large volume air-coil system that comprises normally conducting coils, 14 of the LFCS and 2 of the EMCS (ref. [Erh16]). The general direction of the magnetic flux tube points from the detector to the source and is thereby anti-parallel to the earth magnetic field and the spectrometer. Individual magnetic-field direction of a specific magnet is associated with the current sign. A positive (negative) sign indicates that the generated magnetic field in the coil center is parallel (anti-parallel) to the z-axis. The magnetic-field strength of a magnet refers always to the value in its center.

The four superconducting solenoids are grouped as follows: The PCH and DET are located on the downstream side of the main spectrometer while the PS 1 and PS 2 units are placed on the upstream side, in the final setup the pre-spectrometer will be located between the latter two. All solenoids are arranged co-axially to the beam line with the beam tube located in the axis of the warm bores.

- The PS 1 and PS 2 units were manufactured by *Cryogenic Ltd.* (ref. [Cry03]) and thoroughly tested during the SDS 1 phase and earlier measurement campaigns with the stand alone the pre-spectrometer setup. A user manual was compiled in ref. [Gör14]. Both magnets can generate a maximal magnetic field of $B_{\text{max}} = 4.5\,\text{T}$ for a current of $I_{\text{max}} = 157\,\text{A}$. For SDS 2 they were operated in the driven mode[1] with *FuG NTS 800-5* power supplies providing stable operation with a high setting resolution of a few mA (ref.[FUG15]). While position and current of the PS 2 unit correspond to the nominal operating parameters, the non-standard setting for PS 1 were were chosen to optimize the e-gun operation.
- The recondenser-type solenoid magnets PCH, DET by *Cryomagnetics Inc.* (ref.[Cry11]) were characterized in ref. [Sch14b], [Ams15]. For the SDS 2 campaign they were operated in persistent mode. Both magnets can generate a maximal magnetic field of $B_{\text{max}} = 6\,\text{T}$ at a current of $I_{\text{max}} = 87.15\,\text{A}$ ($I_{\text{max}} = 93.59\,\text{A}$ for DET). Due to technical limitations, the PCH could only be operated at a maximal field of $B_{\text{max, SDS 2}} = 5\,\text{T}$. To maintain the design magnetic-field ratio $B_{\text{DET}}/B_{\text{PCH}}$ between the PCH and the DET unit, the current of the latter coil was lowered accordingly. At the center of the PCH coil the maximal magnetic-field strength B_{PCH} of the total SDS setup is reached.

  A larger magnetic-field strength in the solenoids on the detector side is favored, as charged background particles then are more likely to leave the spectrometer at the upstream side.

The key operating parameters for the solenoids during the SDS 2 campaign are summarized in table 3.2. All z-positions refer to the as-planned values. The real z-positions with respect

Table 3.2: Current settings and z-positions of the coil senters used in the SDS campaign of the four solenoids. Due to magnet safety the nominal PCH field of 6 T had to be lowered. To retain the magnetic-field ratio between the PCH and DET units, the current of DET had do be lowered respectively.

solenoid	z (m)	I (A)	B (T)
PS 1	-15.470	-104.0	3.0
PS 2	-12.104	-156.0	4.5
PCH	12.1835	-72.625	5.0
DET	13.7835	-46.795	3.0

1 Superconducting solenoids can be operated in two modes. In driven mode, the superconducting coil is powered continuously by the magnet power-supply unit. While in persistent mode, the windings of the superconductor are short-circuited once the magnet has reached its nominal field

to the KATRIN coordinate system were determined by careful alignment measurements (section 3.4). Based on the two operation modes of the magnets, uncertainty estimations vary accordingly (fig. 5.7). For the PCH and DET unit in persistent mode, the generated magnetic fields is expected to be stable and featuring a negligible decrease over time (ref. [Sch14b]), while for the PS 1 (PS 2) unit in driven mode, the uncertainties are dominated by the power supply fluctuations of 14 mA (16 mA).

Mechanical layout of the air-coil system

The LFCS and EMCS coils are both mounted on a common support structure. The overall layout of the air-coil system can be seen in fig. 3.1. It consists of 25 rings, coaxially aligned along the main spectrometer over a total length of 23.4 m. To enhance its mechanical stiffness, a single ring has a double-T beam design with an inner (outer) radius of $r_{\mathrm{si}} = 6.155\,\mathrm{m}$ ($r_{\mathrm{sa}} = 6.305\,\mathrm{m}$). For weight reduction aluminum was chosen.

On the outside of the rings 205 mm wide combs are mounted to guide the individual turns of the wires of the LFCS system. The guiding tubes of the EMCS system are fixed with spacers to these rings as well (fig. 3.4). Cables of the EMCS system feature an average bending radius of $r_{\mathrm{we}} = 6.375\,\mathrm{m}$. For both air-coil systems, the cables feature an average diameter of 12.8 mm, with the conducting wire having a diameter of 9.8 mm (ref. [Bay09]).

Due to imperfections of the bending of the support structure elements and weight-induced deformations, the radius of the support structure shows variations of up to ±5 cm (ref. [Gum13]). At an azimuth positions with negative deviations from the design radius, wooden spacers were introduced to adjust the cable position, while the positive deviations remain.

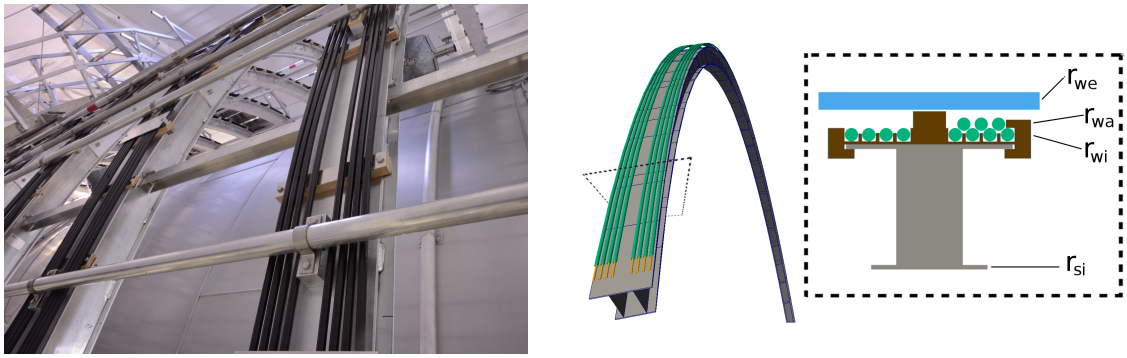

(a) Photo of the aircoil systems

(b) Simulation model of the aircoil systems

Figure 3.4: Mechanical layout of the air-coil system, shown in a photograph (3.4(a)) and in the realistic Kassiopeia representation (3.4(b)). Figure 3.4(b) shows a close up of the air-coil support structure where the black cables of the LFCS, shimmed with wooden spacers, intersect with the aluminum tube of the EMCS. In fig. 3.4(b) is the support structure of the air coil system shown in grey. The winding of a LFCS is modeled with individual rings that incorporate corrections of the inner support structure $r_{\mathrm{si}} = 6.155\,\mathrm{m}$ deformations (the wooden shims are not plotted). LFCS cables are on a radius of $r_{\mathrm{wi}} = 6.317\,\mathrm{m}$ (conducting wire in yellow, insulation in green). In the cross section plot, the comb-like structures guiding the LFCS are shown cables in brown. The right half of the T-structure shows the winding structure for a double layer ring at $r_{\mathrm{wa}} = 6.324\,\mathrm{m}$. The EMCS guiding tube at $r_{\mathrm{we}} = 6.375\,\mathrm{m}$ is shown in light blue. In a magnetic field simulation only the conducting wires of the LFCS and EMCS are relevant

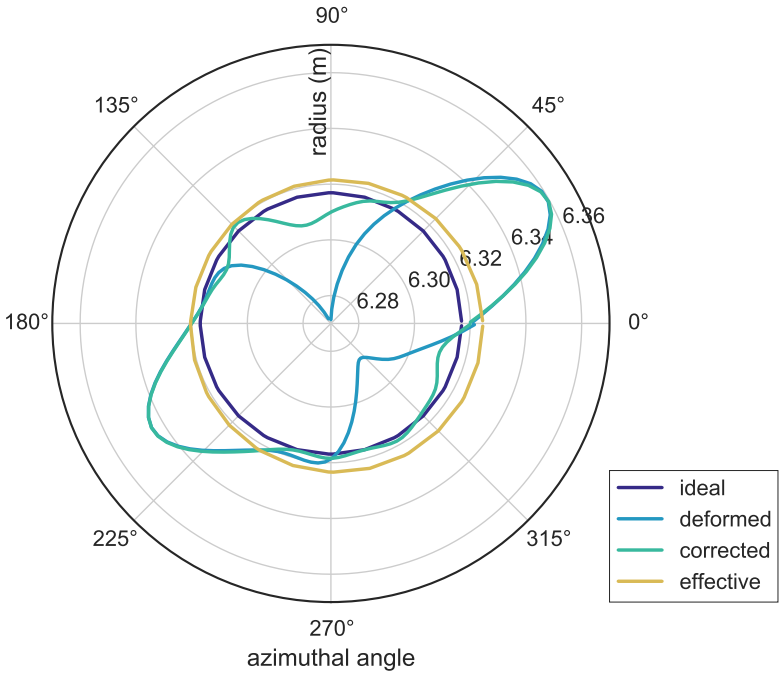

Figure 3.5: Radius of LFCS 6 coil for different levels of discretization. An azimuthal angle of 0° corresponds to the x-axis of the KATRIN coordinate system. View direction is in upstream direction. The "Ideal" circle correspond to the design value of the inner wire radius $r_{\mathrm{wi}} = 6.317\,\mathrm{m}$. The measured deformations of the holding structure by weight is labeled "deformed". The measured positions after the installation of the correction spacers, is referred to as "corrected". Finally, the approximated circle with an effective radius is labeled as "effective".

A highly realistic most realistic representation of the cable shape can be achieved by performing a cubic spline (fig. 3.5). In long-term tracking simulations this representation of the LFCS coils would increase the computation time drastically. Therefore, each deformed LFCS ring deformation was fitted to a circle with an effective radius and ring center and implemented as magnetic-field calculation option. This approximation is almost as fast in computation as the original coaxial model. Although the deformed any longer relevant for magnetic field simulation, the azimuthal variation is required as a correction of the radius of the mobile sensor units (section 3.3.2).

Low field correction system

The purpose of the LFCS system serves two key tasks. On the on hand it has to define the magnetic field strength in the analyzing plain and on the other hand, it has to ensure a smooth and symmetric gradient of the magnetic field along the spectrometer axis as well as radially within the analyzing plain. Thereby the magnetic flux tube is also confined within the main spectrometer vessel and allows to fulfill the transmission condition for signal electrons together with the other electromagnetic design features.

The magnetic field of all LFCS coils point in the same direction as the solenoids of the KATRIN beam-line. The single exception is the LFCS coil located closest to the PCH which

Table 3.3: Technical parameters of the air-coil power-supplies. The LFCS ring numbers follows fig. 3.1 and EMCS directions from fig. 3.6. The power supply unit (PSU)s are units form the SM 3000 series from Delta Elektronika [Del12].

system	ring/direct.	turns	module	max. current
LFCS	3 to 11	8	SM 15-200 D	200 A
LFCS	1,2 and 12,13	14	SM 30-100 D	100 A
LFCS	14	14+14	SM 45-70 D	70 A
EMCS	X	$2 \cdot 5$	SM 30-100 D	200 A
EMCS	Y	$2 \cdot 8$	SM 45-70 D	70 A

acts as a counter measure against the asymmetric stray fields of the PS 2 and PCH units. Each of the 14 coils is equipped with its own PSU of the SM 3000 series from Delta Elektronika (ref. [Del12]). With this measure, the LFCS layout allows to generate a huge variety of different magnetic-field settings with strengths of up to 1 mT (table 3.3). A high-precision measurement of the applied currents is achieved by using the by Current Transducer IT 200-S from LEM [LEM14].

The standard current settings during the SDS 2 campaign can be found in table A.1.

Earth magnetic field compensation system

The most significant contribution to the magnetic background field of the KATRIN experiment is the earth magnetic-field with an absolute field of about 50 µT. To ensure axial symmetry, it has to be compensated (fig. 2.6). Based on the magnetic-field of ref. [GFZ15] and the known orientation of the KATRIN spectrometer, the earth-magnetic field components can be transformed into KATRIN coordinates (table 3.4).

To compensate the earth magnetic-field, a homogeneous field is generated by two coil sets,

Table 3.4: Earth magnetic field values for Karlsruhe. Values are calculated for the SDS-2 period from November 2014 to March 2015 (ref. [GFZ15]). Negative values denote western and positive eastern declination. The magnetic field values are given in KATRIN coordinates. This implies a rotation about 15.7 degree in the horizontal plane (ref. [Her10]).

component	value	secular variation
declination	1°56′	8.5 arcmin/a
inclination	64°46′	0.1 arcmin/a
total Intensity	(48 333.8 ± 4.4) nT	28.7 nT/a
north-component	(20 599.3 ± 1.6) nT	12.3 nT/a
east-component	(695.1 ± 7.9) nT	51.3 nT/a
vertical-component	(43 719.1 ± 4.4) nT	25.1 nT/a
$B_{\text{earth,X}}$	4.90 µT	
$B_{\text{earth,Y}}$	−43.72 µT	
$B_{\text{earth,Z}}$	20.02 µT	

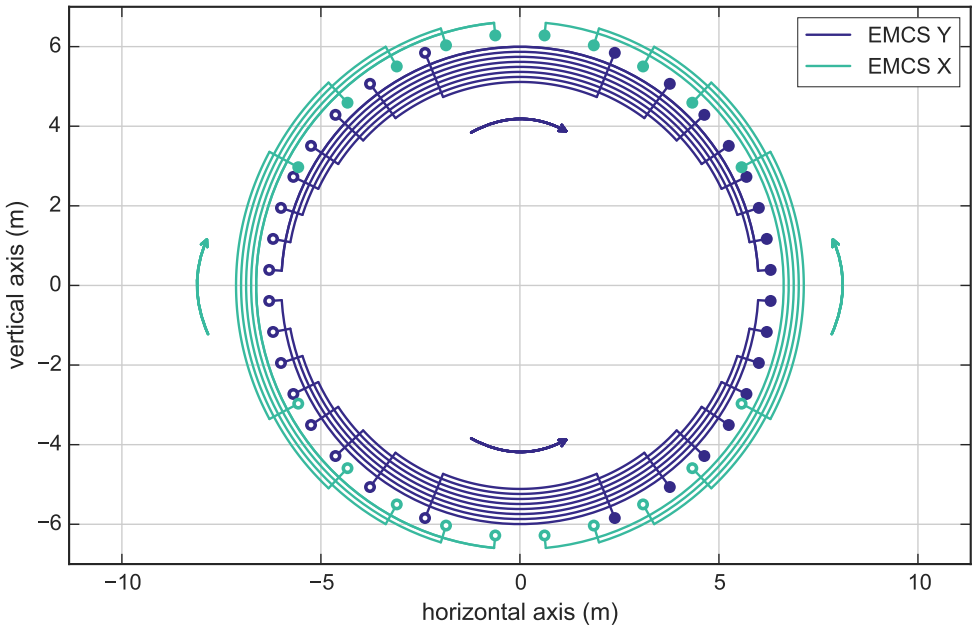

Figure 3.6: Wiring of the earth magnetic field compensation system (EMCS), here shown for the downstream end, facing upstream from the detector side. The radius $r_{\mathrm{we}} = 6.375\,\mathrm{m}$ of the coil tubes along the spectrometer axis are shown with hollow (full) markers where the current flow points in negative (positive) z-direction. On the end caps, a wiring layout is chosen according to a current pattern of a cosine distribution, signified by intersections. The effective direction of the generated field is indicated by the corresponding arrows.

which are aligned perpendicular to the spectrometer axis. A spherical winding geometry is chosen to follow a cosine distributed current-pattern (ref. [Her10], [Erh16]), with eight horizontal (five vertical) oriented coils to compensate for the magnetic background field component in y- (x-) direction (fig. 3.6). Magnetic-field inhomogeneity resulting from the discretisation of the spherical current shape by the chosen wire layout inside the main spectrometer vessel can be neglected (ref. [Rei13]).

Both EMCS coils are operated with PSUs of the SM 3000 series (ref. [Del12]) while current measurements are done by IT 200-S Current Transducers (ref. [LEM14]). The currents to compensate for the earth magnetic field are calculated based on the given geometry and the known strength of the earth magnetic field. The EMCS X (Y) is operated with 9 A (50 A).

3.1.4 Electron-Gun

A key element to characterize the transmission properties of the spectrometer MAC-E filter during the SDS 2 measurement phase was the e-gun with a well-defined energy and angular distribution, developed for this purpose (ref. [Han13b], [Zac14]). Compared to the initial SDS 1 configuration, the e-gun was overhauled to improve its reliability and stability, and its operation readiness was demonstrated prior to SDS 2 (ref. [Beh14]). Here a brief introduction to the system is given, detailed hardware specifications can be found in ref. [Beh16].

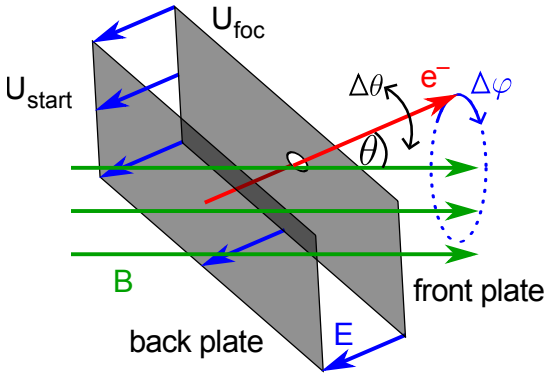

(a) e-gun setup for an angular selectivity

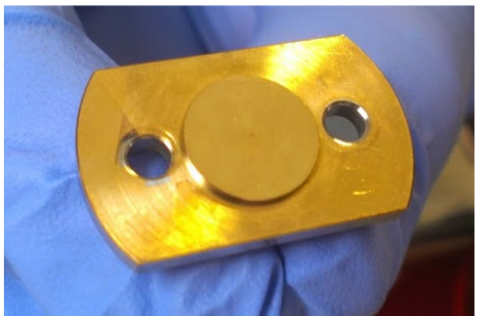

(b) gold coated fiber

Figure 3.7: In fig. 3.7(a), the e-gun principle is illustrated (ref. [Wan13b]). Electrons are emitted from the back plate and focused on a defined path by a strong electrostatic field between the back and the front plate. The polar angle relative to the magnetic field is selected by rotating the e-gun-chamber. Electrons are generated by the photoelectric effect when a 20 nm golden layer on the back plate is illuminated by an UV light from behind (fig. 3.7(b)). The actual spot size is about 200 µm wide, corresponding to the diameter of the optical fiber (ref. [Beh14]).

Initially are low-energy electrons generated by the photoelectric effect generated via UV light. To ensure a narrow energy spread of $\sigma = 200\,\text{meV}$, a gold layer of 20 nm width is illuminated by laser light with a wave-length of $\lambda = 266\,\text{nm}$ (fig. 3.7). Light pulses of 20 ns enable time-of-flight measurements. The electron rate is adjustable by tuning the frequency from 20 kHz to 100 kHz and regulation of the laser intensity. To obtain a constant light yield, the laser is water cooled to a temperature of 25 °C.

To focus the electron beam on a path with a well defined polar angle relative to the magnetic field, the emitted electrons are accelerated non-adiabatically by an electrostatic field (fig. 3.7), which is generated by a potential U_{foc} <5 kV of the customized *HCN 35M - 5000* power supply (ref. [FuG15a]). To select a specific angle θ_{EGun} the plates, mounted inside a housing, can be rotated by pneumatic motors with an angular precision relative to the magnetic field of 0.05°.

To cover the entire magnetic flux-tube projected on the FPD detector, the e-gun is mounted on an UHV manipulator (ref. [Frä10]). The UHV manipulator can be rotated by ±23° in vertical and horizontal direction and allows positioning of the e-gun with a precision of 0.1° on a specific field line (fig. 3.8). To prohibit voltage flash overs and energy losses of the electrons, the e-gun is operated in high vacuum. To allow maintenance the e-gun can be disconnected from the main spectrometer by valves.

During the SDS 2 phase all e-gun related sensors and controllers were integrated into the slow-control framework. This feature allowed fully automatized measurements and later offline precision analyses. Also, the hardware integrity was improved by dedicated safety scripts, in particular the control of the applied high voltages is crucial for a reliable and an effective operation of the e-gun. When the e-gun is operated in blocking mode, a Penning

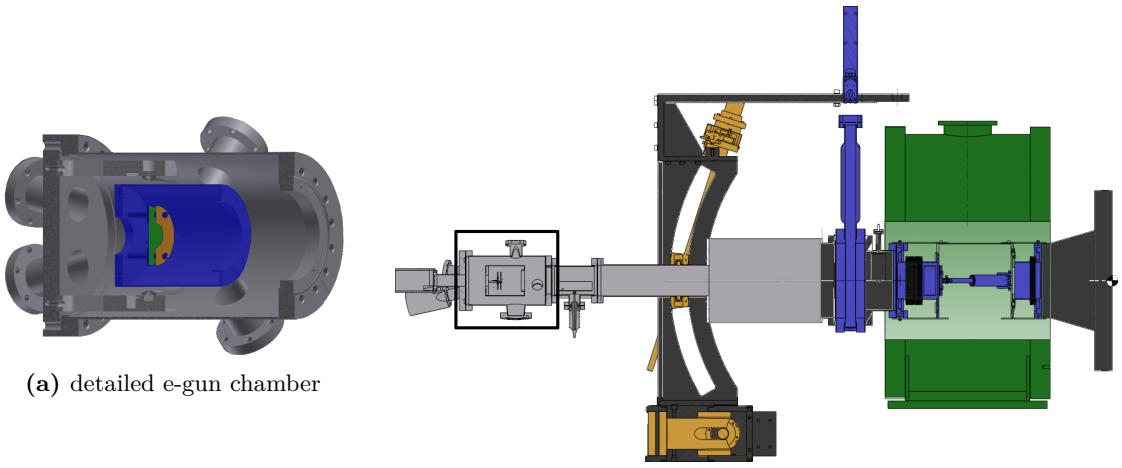

(a) detailed e-gun chamber

(b)

Figure 3.8: CAD drawing of the e-gun setup implementation during the SDS 2 campaign (ref. [Erh15a]). In fig. 3.8(b), the PS 2 magnet (green) and the e-gun (light grey) are aligned coaxially to the beam line (dark grey). The e-gun can be moved by the manipulator (yellow) and be separated from the main spectrometer by valves (blue). Details of the e-gun are shown in fig. 3.8(a) (see also fig. 3.7), where the back plate (green) and the front plate (yellow) are elevated on high voltage inside the movable inner chamber (blue).

trap[1] is created between the analyzing plane and the e-gun back plate. To break the storage condition for charged particles in the Penning trap, a dipole electrode is installed between the e-gun chamber and the PS 2 unit. The dipole electrode is operated with a potential of 3 kV, which is a compromise between a efficient particle extraction of the stored electrons and a small deflection of the signal electrons.

To obtain a well-defined surplus energy of the electrons relative to the retarding potential of the main spectrometer, the e-gun back plate has a galvanic connection to the inner electrode system. This allows a precise adjustment of the voltage and also suppresses high-voltage fluctuations. To vary the start potential U_{start} in the range[2] from 90 V to −900 V, a combination of a battery pack providing 90 V U_{bat} and a *MCP 14-1250* power supply, generating the acceleration potential U_{acc} (ref. [FuG15b]), is used. Readout of the voltage difference is done with a DVM *8846A* by Fluke (ref [Flu06]). Further details e-gun voltage can be found in section 6.1.2 and ref. [Res15].

1 An electromagnetic field configuration where charged particles are confined within a magnetic flux-tube according to eq. (2.3) and reflected by two potential maxima or minima (depending on the particle charge) is called a penning trap. In the KATRIN setup, a magnetic reflection according to eq. (2.6) is also possible. In the specific case of measurements with the e-gun, such an setting is achieved when the energy of signal electrons is below the transmission energy (see section 6.1).

2 Due to the negative charge of electrons, a more negative value of U_{start} corresponds to higher surplus energies and vice versa.

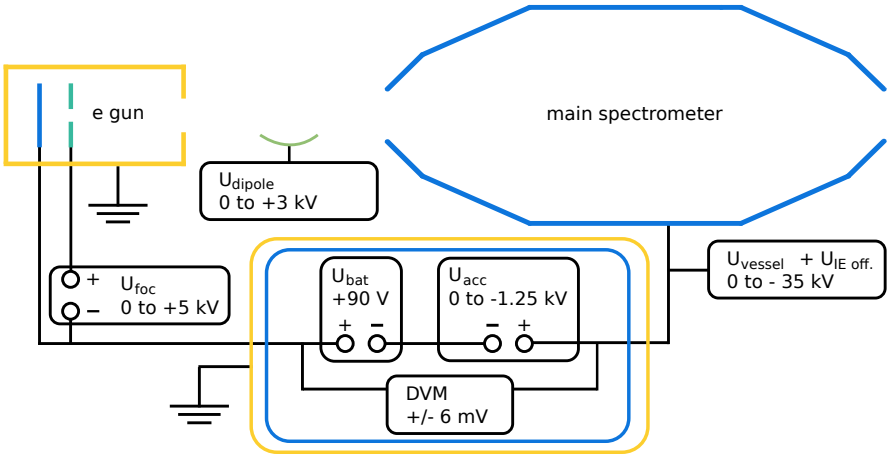

Figure 3.9: Integration of the e-gun in the high-voltage system. The potentials of the e-gun back- and front-plates are defined by the central inner electrode potential to suppress voltage fluctuations. The start potential $U_{\text{start}} = U_{\text{bat}} + U_{\text{acc}}$ is monitored with a 5.5-digit digital voltmeter (DVM). A dipole field with U_{dipole} is applied to prevent Penning discharges.

3.2 Software and analysis tools

During the commissioning of the SDS setup an array of thousands of sensor channels had to be handled. Depending on the scope of duty data formats, the recording intervals and precision requirements differ. The vast majority is automatically processed and linked to calibration data (ref. [Kle14]). The entire data stream organized in two groups.

On the one hand, there is the fast and high-precision data stream that originates from the detection of signal electrons by the FPD system. To obtain adequate a spatial resolution, the backside of the detector wafer is segmented into 148 pixel (px) elements (fig. 3.10) which are processed as individual channels in the data-acquisition (DAQ) chain (section 3.2.1). All pixels of the detector were operational during SDS 2. However, close to the end of the SDS 2 phase, when e-gun measurements were performed, a pre-amplifier card was damaged so that pixels $10, 34, 58, 82, 106$ and 130 on the horizontal axis were excluded from the analysis.

The second data stream arises from the sensor readouts, used to monitor relevant parameters of a measurement and to control safety-related components to protect operators and the apparatus. This heterogeneous system is commonly referred to as the slow-control system (section 3.2.2).

3.2.1 Data acquisition

The hardware used for data-acquisition of the FPD was initially developed for the Pierre Auger Cosmic-Ray Observatory and is provided by the Institute for Data Processing and Electronics (IPE) of KIT. It consists of 8 first-level trigger (FLT) cards and one second-level trigger (SLT) card, all housed in a single IPE v4 crate. Additional FLT cards are used to read out external pulsers or synchronization signals from other subcomponents of KATRIN such as magnetic pulse triggers and an e-gun time-of-flight reference signal. On each FLT card, the analog inputs of up to 24 detector channels are digitized without further shaping via serial ADCs with 12-bit precision and a sampling rate of 20 MHz. The single SLT card handels the FLT cards and communicates via Ethernet-TCP/IP with the DAQ computer,

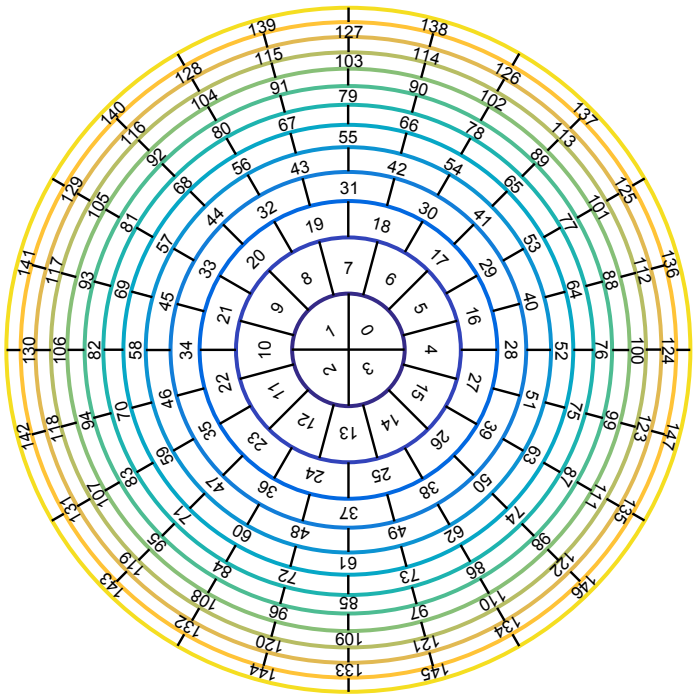

Figure 3.10: Segmentation of the focal-plain detector in 148 pixels. Four pixels form the central bulls-eye, with 12 rings with 12 pixels each being placed around it. The color pattern shown here is used throughout this thesis for the visualization of field line simulations. See for example fig. 3.17.

delivering either digital traces of the signals and digital amplitudes or histograms of amplitude distributions (ref. [Kop08],[Phi10],[Ber12]).

A software for object-oriented real-time control and acquisition (ORCA) is deployed to access the detector hardware and to enable a low-level on-line visualization (ref. [How04], [How14]). ORCA provides a fully automatized run-control via ORCA-scripts for all key measurement parameters such as run time, potentials and magnetic-field settings (ref. [Hau13]). A completed run is processed to a ROOT file and transferred to a KATRIN database (ref. [Bru97], [Kle14]). During the SDS 2 campaign, also a scintillator based muon-detection system and the monitor spectrometer (MoS) were making use of ORCA.

More details of the FPD DAQ chain see ref. [Ams15] and [Sch14b].

3.2.2 Slow control system

Recording of sensors are referred to as slow control data and are organized in so-called log-groups. Sensors within a log-group feature a common time stamp and measurement interval and usually belong to a common KATRIN sub-system or task.

To ensure safe and reliable hardware operation also for tritium-containing components the well-established PCS7 control system by Siemens Inc. is deployed throughout the experiment. These units control the vacuum, heating and cryogenic system. A feature of the PCS7 environment is the rather time-consuming implementation of additional devices and the

limited support of many common interfaces. To communicate with a variety of devices with different interfaces and protocols, so-called field controllers (compact Field Point (cFP) and cRio by National Instruments Inc.) are used in addition. This is used in particular for units serving HV and air-coil control, magnetic-field monitoring, as well as dedicated positioning devices and others. In the following the air-coil control is used as example of the hardware involved.

A main core of the KATRIN air-coil control system is a cFP bank, which is based on the latest generation *cFP-2220* real-time controller allowing readout intervals up to 200 ms. The communication with the measurement devices comprises:

- Two single ended *cFP-AO-210* voltage-output digital analog converters (DAC). With 12-bit precision they transfer the current set values to the PSU analog interfaces.
- Two *cFP-AI-118* isolated voltage input analog digital converters (ADC). With 16-bit precision they are used to readout the LEM current transducer (ref. [LEM14]).
- Two *cFP-AI-112* single ended voltage input ADCs with 16-bit precision. One unit is used for the PSU output voltage and the other for monitoring the temperature and polarity status of the flip-boxes (ref. [Erh16]).
- A *cFP-DI-304* 32-channel digital input module, used to read the status of all power supplies and current transducers.
- A *cFP-DO-401* 16-channel digital output module is used to set the output polarity of the flip boxes.

The performance of this setup during long-term measurements is discussed in chapter 4.

All slow-control data are collected and archived in a central SQL database for later analysis. Convenient access to slow-control data is possible through the software package Kasper (section 3.2.3) and the ADEI-web interface (Advanced Data Extraction Infrastructure) (ref. [Kop15]). A sketch of the data chain at KATRIN can be found in fig. 3.11.

The current status of the slow control system is described in ref. [Kop14] and [Beg14], for a detailed overview of the data processing and storage infrastructure see ref. [Kle14].

3.2.3 Kasper software framework

The strategy of the KATRIN collaboration to organize the analysis and simulation tools is to combine existing code into a modular `C++` framework called Kasper. It compiles on Linux and Mac OS and facilitates open-software packages such as the boost libraries and the root framework (ref. [Sch14a], [Bru97]). This unifies common tasks, eases introduction of new users and ensures comparability and reliability during the development process (ref. [Gro], [Gro15], [Fur15]).

In the thesis at hand, all simulations are based on the Kasper3 release that comprises 12 modules. Most important for this work were the KaLi (data access), KemField (magnetic and electric field calculation) and Kassiopeia (particle tracking) parts that have facilitated the development of the field-line monitor tool (fig. 3.16).

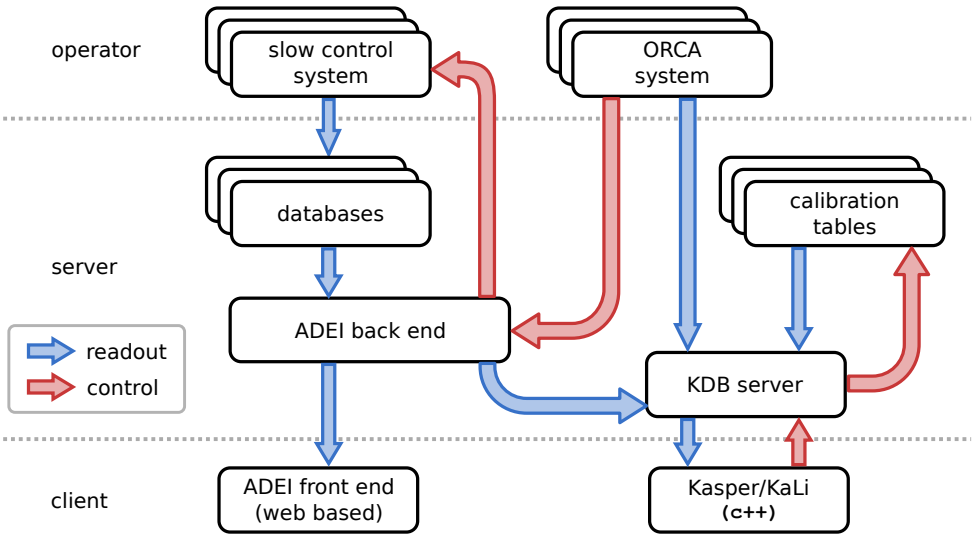

Figure 3.11: Schematic overview of the KATRIN data-management structure. A measurement is organized by an operator via an ORCA-script to control the detector and the slow control system. Acquired data is automatically stored, processed and linked to a calibration on a server. Client access is via a web-based ADEI front-end or via the KaLi C++ library of the Kasper software package. Image inspired by ref. [Har15b].

3.3 Magnetic field monitoring

To perform a neutrino-mass measurement with the reference sensitivity, a precise knowledge of the strength and the shape of the magnetic-field in the active volume is essential, hence continuous monitoring of local magnetic field values over a large volume is mandatory. Evidently, during neutrino-mass measurement campaigns it is not possible to measure the magnetic field inside the flux-tube of the main spectrometer. The strategy is thus to determine the magnetic field condition relying on an accurate and precise magnetic field model. The input data for this model stem from a magnetometer grid around the main spectrometer vessel. The key goal of the magnetic field monitoring system of KATRIN is to obtain a sensitivity to deviations from axial symmetry on the 0.5 % level along the beam axis ([Glü09]).

The overall magnetometer grid comprises several different sensor types, pursing basically two approaches. A certain number of magnetometers is installed stationary on the main spectrometer vessel to facilitate continuous magnetic field measurements closest to the active magnetic flux tube. For those magnetometer, high precision and a well known orientation of the sensor is of key importance. A different type of magnetometers is mounted on small robots that move automatized around the spectrometer to obtain magnetic-field mapping over a large volume. These robots however require extended maintenance and measure only in intervals of several minutes.

Over the course of this thesis the commissioning of the stationary sensor grid was completed and tested for the first time. In the following sections, the individual sensor units and their implementation into a magnetic field monitoring system is presented.

3.3.1 Stationary magnetic-field measurement

The magnetic-field sensor grid comprises 38 stationary sensor units. A sensor unit consists of a triaxial magnetometer with customized electronics. The sensor units are subdivided based on the magnetometer type; there is a total of 14 high-precision magnetometers of type *Mag-03MSB1000* produced by Bartington (ref. [Bar13b]), and a further 24 magnetoresistive magnetometers developed and installed by the IPE. All sensors are mounted on the main spectrometer.

To obtain spatial resolution, all magnetometers are distributed over the outer vessel surface in the central part of the main spectrometer. In the very center, were the analyzing plane is located, a distortion of the magnetic-field would have the biggest impact on the neutrino mass sensitivity, therefore a total of 14 sensors is installed at this position alone.

The magnetometer mounting is based on steel robes wrapped around the vessel hull and tightened by steel springs. Consequently, several magnetometers are located on one common axial position, referred to as magnetometer rings. A total of six magnetometer rings are installed, three are equipped with high-precision magnetometers at $z = -4.5, -0.14, 4.3\,\mathrm{m}$ and three of them with magnetoresistive sensors at $z = -3.6, 0.0, 3.6\,\mathrm{m}$. Identification is provide by the magnetometer type (Bartington B or IPE I), their position (upstream U, middle M and downstream D rings) together with a clockwise assigned number (fig. 3.12).

An orientation of the sensor axis is chosen that corresponds to the cylindrical shape of the spectrometer and the magnetic field, one points along the spectrometer axis, in radial direction and a third component running tangential to the spectrometer surface. The ring positions given above represent average values, the correct positions of the individual sensors are stored in a KATRIN database[1] as a parameter of a sensor.

Magnetoresistive sensor units

The first magnetic-field sensor units were developed and install by IPE (ref. [Wüs07], [Har09b]). Magneto-resistive magnetometers were chosen for their high sensitivity-to-cost ratio with a measuring range of 2 mT. In the center of the main-spectrometer hull, close to the analyzing plain, magnetometers of type *KMZ10B* were installed (ref. [Phi98]), for the later mounted rings on the up- and downstream side of the cylindrical part of the spectrometer hull at $z \approx 4.5$ m, successor sensors *KMZ20M* were chosen (ref. [Mea08]). Due to a known temperature dependency of these magnetometers, a temperature sensor is included in sensors unit (ref. [Ana04]). A description of the layout of a sensor unit can be found in ref. [Ada15].

Beside a low price, these magnetometer allow for an adequate precise magnetic-field measurement, but require a comprehensive calibration to achieve a reasonable accuracy. Several important calibration steps were performed during the assembly of the sensor units, such as the pre-magnetization, an offset determination and a correction for an angular uncertainty and an orthogonality error between the three axis. ([Har09a]).

The magnetometers were magnetized by placing a suitable magnet close to the individual magnetometer axis when they were already mounted on a circuit board. The circuit board was installed in an aluminum box that serves as housing for a magnetometer and as a reference for the sensor coordinate system (fig. 3.13). A magnetic-field measurement offset and angular

1 Internal KATRIN database: http://katrin.kit.edu/katrin-ng/kdb-admin.fcgi/positions/

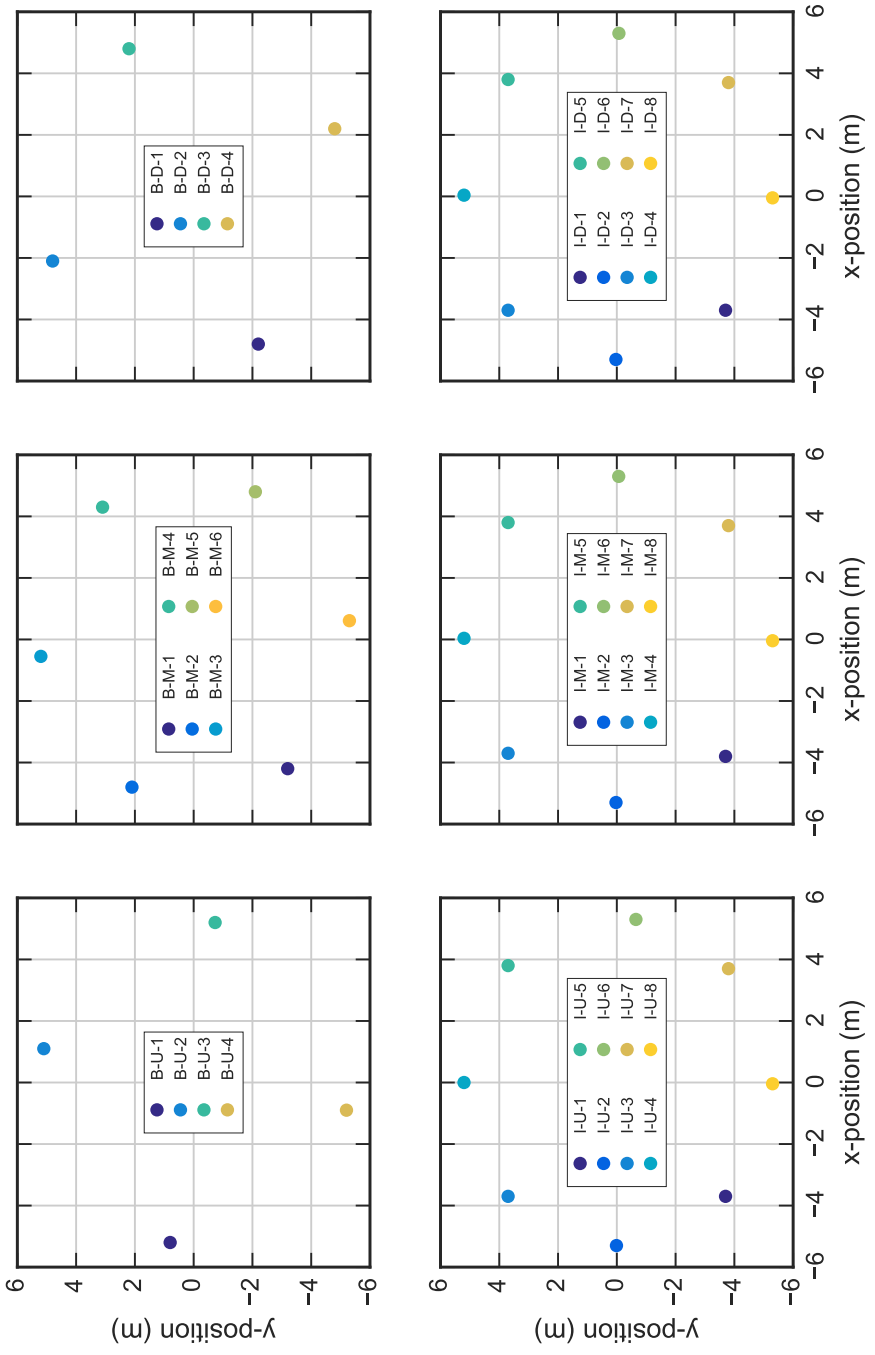

Figure 3.12: Positions of all permanently installed magnetometers of the main spectrometer. The upper row shows the azimuthal positions of the precise Bartington magnetometers and the lower row the magneto-restive magnetometers, installed by the IPE. The average radius of a sensor is about 5.28 m. From left to right, the individual upstream-, middle- and downstream-rings of the Bartington (IPE) sensors at $z = -4.5, -0.14, 4.3\,\mathrm{m}$ ($z = -3.6, 0.0, 3.6\,\mathrm{m}$) are shown. A name of a magnetometer consists of its type, axial position and a clockwise assigned number. Due to finite size of a sensor unit the position of the z-axis sensor is here given, the other components are within a range of 3.0 mm.

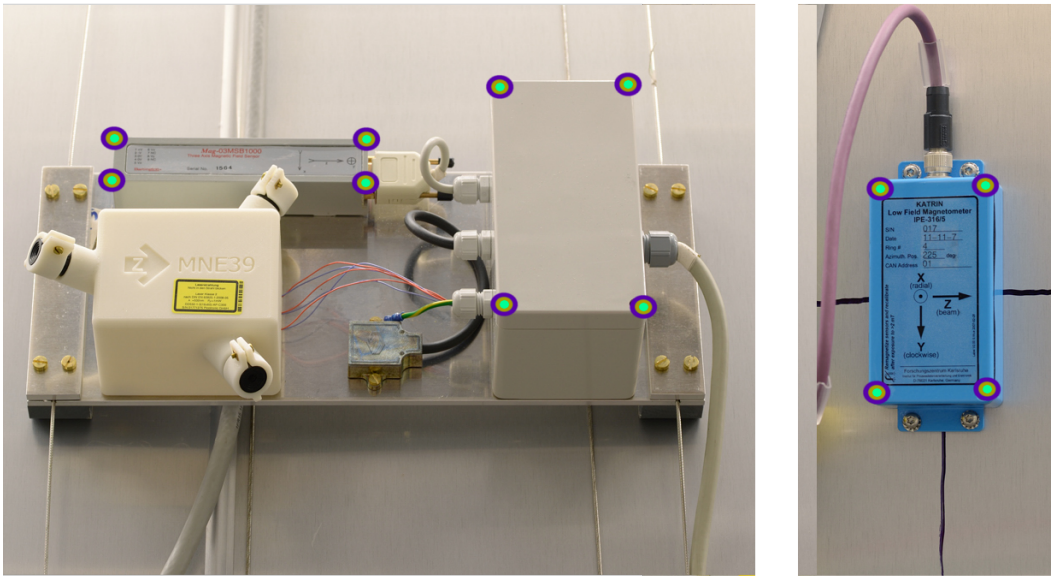

Figure 3.13: Alignment measurement of a magnetometer, here shown for sensor B-M-5 and I-D-7. Based on accessibility, either a sensor or an electronic box surface was measured. The distance measurement of the four points to the defined the surface orientation and the angular measurement the position in KATRIN coordinates.

uncertainty was determined when a sensor was placed in a non-magnetic, rectangular box relative to the homogeneous earth magnetic-field. By means of a high-precision magnetometer the box was carefully aligned. Measurements in all orientations and the respective inverse orientation allow to determine all elements of a correction matrix

$$C \cdot \vec{B}_{\text{raw}} = \begin{pmatrix} c_{xx} & c_{xy} & c_{xz} \\ c_{yx} & c_{yy} & c_{yz} \\ c_{zx} & c_{zy} & c_{zz} \end{pmatrix} \cdot \vec{B}_{\text{raw}} = \vec{B}_{\text{meas}} \tag{3.1}$$

were $c_{ij} = (b_{ij} + b_{ij}^{-1})/2$ is an offset corrected matrix element. The resulting magnetometer-axis readout $\vec{B}_{\text{meas}}$ is saved to a KATRIN database. A calibration within 5 % of the earth magnetic-field was achieved. Calibration matrices are embedded in the cFP software for magnetometer readout.

When the sensors were mounted on the vessel, their location and orientation was measured (section 3.4.3), as well as a scaling factor and a temperature coefficient determined. By applying different currents to the air coils a magnetometer scaling factor was determined. Especially extreme settings in combination with the magnetic pulse of the flip boxes were used for a full magnetic field range coverage. These calibrations are stored in the KATRIN calibration database.

A temperature correction coefficient of a magnetometer was determined during the bake-out phase of the main spectrometer. Over the time period from 2015-5-1 to 2015-6-10, no magnetic field was applied at any of the air-coils, as well as the DPS-, the main- and

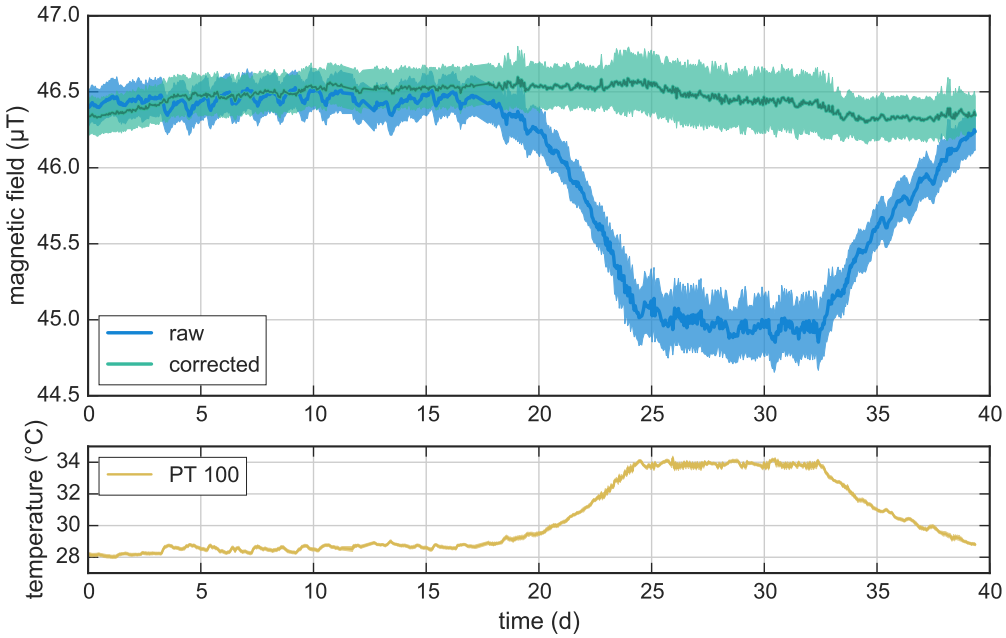

Figure 3.14: Temperature corrected magnetic-field measurement of a IPE sensor, here shown for the x-axis of the sensor unit on top and in the middle of the spectrometer. In the upper plot, the time development of the measured magnetic-field value with a 1σ uncertainty is shown when all KATRIN magnets and solenoids were turned off. With an applied temperature correction, the magnetic field output is flattened while the fluctuations are not artificially altered. The temperature correction is based on the internal temperature measurement shown in the lower plot.

monitor-spectrometer solenoids were turned off[1] (fig. 3.14). A temperature increase in the second half of the period is due to the bake-out of the main spectrometer vessel. On the outside of the insulation a temperature increase up to 7 °C was detected by the thermometers of the IPE sensors. The observed magnetic field variations are purely temperature related. The applied calibration flattens the mean of a magnetic field measurement by correcting for temperature variations of the ambient air temperature, but does not alter a measurement artificially as the standard variation is constant within hours (see 5 d to 10 d in fig. 3.14).

High-precision sensor units

A high-precision sensor-unit consist of four main components that are mounted on a 16.5 cm × 36 cm aluminum plate, which is fixed with two stainless-steel wires to the main spectrometer vessel (ref. [Ant13]). The most important component is the *Mag-03MSB1000* magnetometer by Bartington (ref. [Bar13b]). It is manufactured with an offset of <50 nT, a linearity uncertainty of <0.0015 % and a neglect-able temperature dependence of 200 ppm/°C.

1 From 2015-5-12 5:00 to 2015-5-13 16:00 and 2015-5-18 5:00 to 2015-5-18 17:00 quench tests were performed with the DPS solenoids. Magnetic field values during that time period were excluded.

Combined with an orthogonality uncertainty <0.5°, this magnetometer meets all requirements for a precise magnetic field monitoring of KATRIN. To exploit their full potential, a precise position and orientation measurement is absolutely necessary. Therefore an inclinometer and a laser-based position measurement system are installed on a sensor unit as well.

Inclinometer of type SCA121T-D05 allow for a two-axial orientation measurement (ref. [Mur12]). An advantage of these inclinometer are a continuous, easy and save orientation monitoring, but are non sensitive to rotations along the gravitation axis. Unfortunately the inclinometer were not calibrated before the sensors units were installed on the main spectrometer vessel and a later calibration was impossible, due to time and safety restrictions.

Not only an orientation, but a position measurement of a sensor unit is possible with the installed laser boxes. A laser box is a custom made fixture for three laser with known relative angles and a common center. When the laser-beam spots are measured, the KATRIN coordinates of a sensor unit can be determined with an sensitivity of $\pm 0.23°$ and $\pm 1.0\,\mathrm{mm}$ as an upper limit (ref. [Ant13]). However, this measurement proceeding requires an extensive initial sensor-unit alignment to hit laser targets that are known within KATRIN coordinates. Due to time limitations, the implementation of this position orientation was postponed. An external position and orientation measurement was therefore used for SDS 2 (section 3.4.3).

The forth component of the sensor-unit is a housing for a DC-DC transformer, that provides the 12 V and 5 V supply voltages for the magnetometer, inclinometer and lasers. It also serves as a tension relief for the cable that connects a sensor unit with the cFP and as reference for the alignment measurement when the magnetometer it self could not be used (fig. 3.13).

3.3.2 Mobile sensor units

A mobile magnetic sensor unit (MobSU) is an automatized robot that is mounted on the inside of an air-coil ring support-structure. It carries two custom made flux-gate sensors *FL3-500* that measure the magnetic field on 2×36 positions per cycle with a precision of $\pm 0.5\,\%$ (ref. [Osi12b], [Let15], [Let11], [Sel13]). Currently two units have been build and the rings of LFCS 6 and LFCS 12 have been prepared for a MobSU operation. After one revolution, the batteries are charged in a docking station, the measurement data is extracted and analyzed on a local computer. Therefore the magnetic field must not change within a measurement cycle of about 360 s for an unbiased analysis.

The mechanical setup of a MobSU consists of a drive unit, a tower to increase the distance between the magnetometers and the air-coil cables and a crossbar on the end of which, the magnetometers are installed (fig. 3.15). A MobSU is moved with a gear drive drive and is supported by a tooth belt that is glued on an air-coil ring-structure to secure traction and reliable positioning at point along a track. The magnetometers are positioned on an effective radius of $(5.876 \pm 0.003)\,\mathrm{m}$ and thereby 441 mm away from the air-coil cables. Due to the deformation of the air-coil ring structure and the correction spacers for the air-coil cables, the radius and distance to the cables variate, which is inevitable to be accounted for in the analysis of the field. Based on the alignment of the magnetometers on a crossbar that is parallel to the KATRIN z-axis, the two magnetometers are referred to as a downstream and an upstream sensor. On the crossbar also an inclinometer installed for a precise orientation measurement and a thermometer to correct for a temperature dependence of the magnetometer. To suppress a disturbance of the field by the MobSU itself, aluminum and other non-magnetic materials is used in the frame structure.

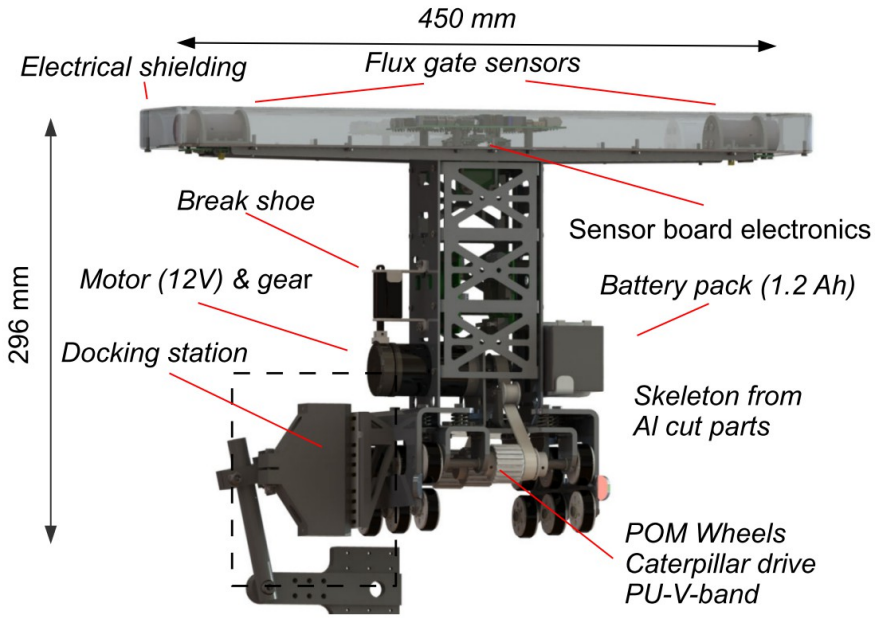

Figure 3.15: Setup of a mobile sensor unit. The magnetometers are installed in the upper crossbar. When a MobSU is moved along the inside of an air-coil support structure, the magnetometers are on an effective radius of (5.876 ± 0.003) m. Figure adapted from [Osi14].

3.3.3 Kasper implementation of the magnetic-field monitoring

The magnetic-field monitor is integrated in the Kassiopeia software package of the Kasper framework and is used for both, a near time magnetic-field monitoring and for a substantial magnetic-field analysis. In the control room it is used for a visualization of the magnetic flux tube. Thereby it can be verified, that the selected magnetic-field setting works as expected and all currents are stable. For a later analysis of the magnetic field, all SDS current and magnetometer related sensor data are saved to a ROOT file. To solve this task, the magnetic-field monitor is split in three components (ref. [Erh15b]).

Within a given time frame, the actual set and readout values of all SDS related currents are retrieved by the KaLi package and a mean and a standard deviation is calculated for the individual magnets. Based on a difference between a set and readout value as well as limits on their standard deviations, the status of SDS magnet-system is analyzed by the *sds currents painter* module. The algorithm of this module determines whether a magnet current is stable, its field is fluctuating or ramping, and stores its status in a state indicator. For the air-coils, additional status bits are analyzed to identify a reversed polarity and a possible pulse mode. All 20 magnets of the SDS setup are shown with their names, a state indicator and its readout current. A frame of a magnet is colored in a traffic-light scheme to indicate its current state.

Based on the known geometry of the SDS setup and current readout values, a magnetic field is calculated. Corresponding to the FPD detector rings (fig. 3.10), magnetic-field lines area plotted in the x-z and y-z plain utilizing the *root track painter* of Kassiopeia. The

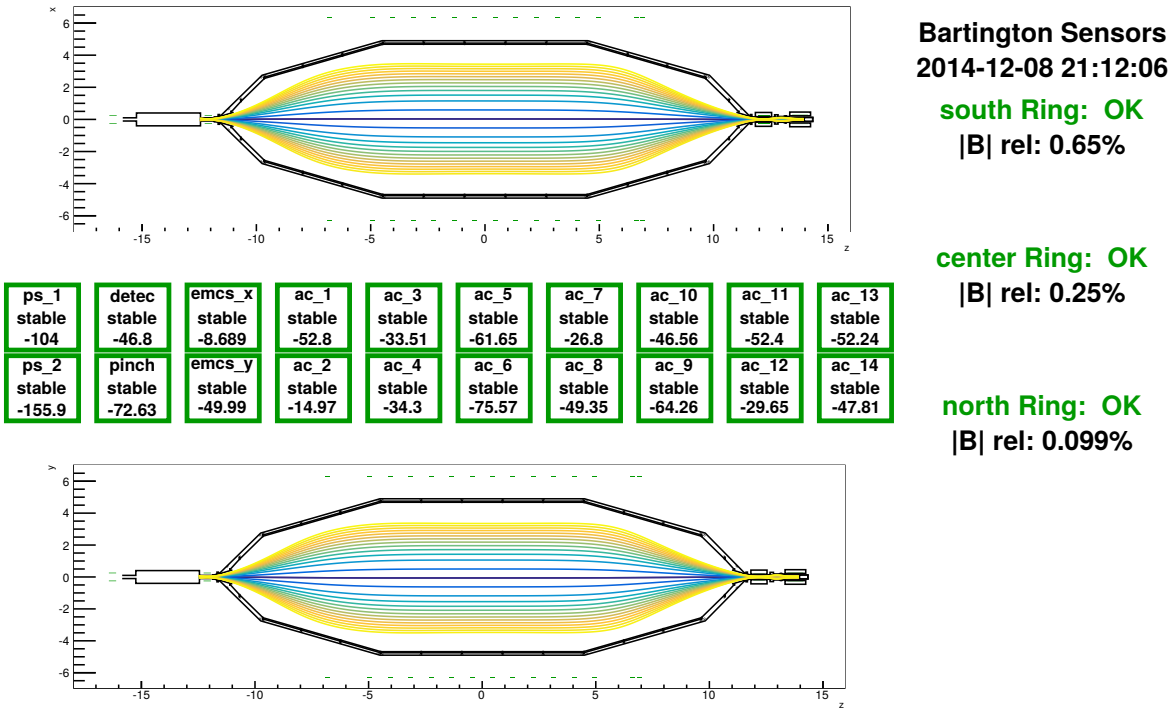

Figure 3.16: Visual output of the magnetic-field monitoring with Kassiopeia. The actual currents of all coils are read from the database and a field line simulation is executed. In the upper (lower) part is the magnetic flux-tube shown in the x-z (y-z) plain. The central tile structure shows the status of all SDS power supplies in a traffic-light style manner (green=stable, yellow=ramping, red=discrepancy). Additionally, all magnet sensors are read out and the values are compared to a calculations of the magnetic-field based on the actual values of the currents (right). Both, magnetometer values and current readout values are saved to ROOT files.

same magnetic field is used to evaluate the magnetic field at the positions of the stationary magnetometers of the main spectrometer. The measured magnetic field of the individual sensors is linked to a calibration (table A.3) and rotated in the KATRIN coordinate system (section 3.4.3). Based on the z-component and the absolute magnetic-field value in axial direction, the absolute and relative deviation is examined for the individual magnetometer positions[1] by the *root magnetometer painter* of Kasper. A user can selected magnetometers for a analysis, either only IPE, high-precision or all magnetometers.

Requirements on the precision of a magnetic-field setting depend on the effective field strength in the center of the main spectrometer (ref. [Kle15]). Therefore, constrains on allowed fluctuations and offsets of the currents and magnetic field analysis can be defined by the user in the configuration file of the magnetic-field monitor. An example of the magnetic-field monitor is given in fig. 3.16, in this case all currents are stable at their nominal values and deviations of a magnetic-field simulation to the corresponding measurement are within limits.

1 The south, center and north ring are usually notated as upstream, middle and downstream position

3.4 Alignment of sub-components

The hardware setup of the KATRIN experiment is axially-symmetric, thereby an axially-symmetric electromagnetic field is generated that is utilized for a background reduction and for a precise calculation of an electron trajectory. Therefore, it is crucial to carefully align all component of the KATRIN beam-line and to implement any geometrical deviation from their respective design value in a sophisticated electromagnetic-field model.

The main-spectrometer vessel, that incorporates the electrode system, is fixed to the support-beam structure in the foundation of the experimental hall and represents the reference frame for the alignment of the magnet- and the FPD-system. In case of the SDS 2 phase, also the e-gun system needs to be aligned relative to the main-spectrometer.

Alignment measurements in preparation of SDS 2 comprise measurements with a FaroArm (ref. [FAR14]) during the mechanical assembly of a sub-component, magnetic-field measurements with a hall probe (ref. [Lak15]) to determine the position and orientation of a solenoid in its cryostat, and the verification by dedicated measurements with the FPD system.

3.4.1 Alignment of the FPD system

The scheme for the conjunction of the FPD system with the main spectrometer requires first the assembly of the FPD system, followed by the alignment relative to main spectrometer and finally the joint integration. Due to the limited mechanical flexibility of the inner components of the FPD system and the lack of possibilities to adjust the setup once it is arranged, a highly accurate assemblage is required.

The position of the magnets inside their cryostat housings was determined by magnetic-field measurements ([Mue14]). The vacuum chamber that contains the PAE and the detector wafer is positioned between the magnets. Based on the known positions of the detector wafer relative to the vacuum chamber, the alignment of the wafer is optimized relative to the magnetic flux tube. Remaining positioning and orientation imperfections lead to a shift of the magnetic flux-tube center of $\Delta x_{\mathrm{sim}} = -0.34\,\mathrm{mm}$, $\Delta y_{\mathrm{sim}} = -0.84\,\mathrm{mm}$. This procedure

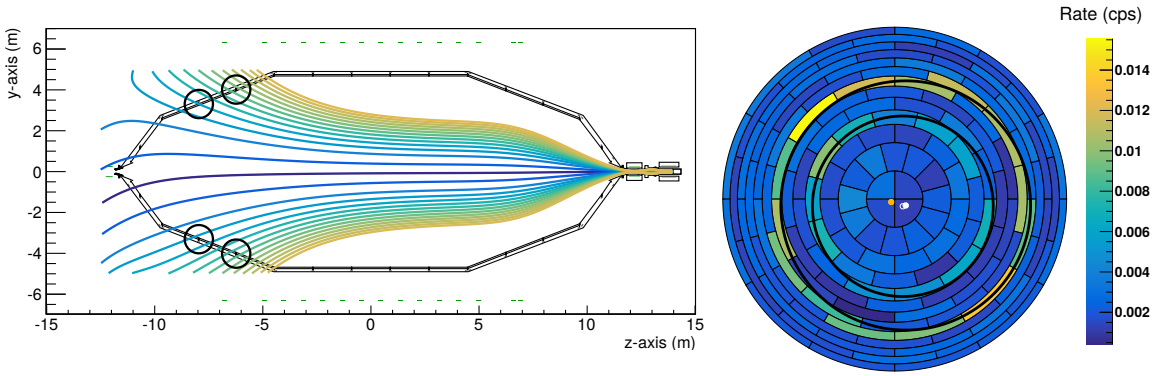

Figure 3.17: FPD alignment verification. When an asymmetric magnetic-field configuration is applied, the magnetic flux-tube projected on the FPD is connected to the vessel wall. In a magnetic field-line simulation (left), the positions where electrons are emitted are identified with the comb structures. The two resulting ring patterns in the measurement are fitted (right), where the white bullet corresponds to the outer ring and the circle to the inner ring. By a golden bullet, the simulated center is shown which takes the available alignment information into account.

was introduced in ref. [Sch14b] and improved in ref. [Har15b] for the SDS 2 measurements.

The alignment of the FPD system in its final position is tested, relative to the main spectrometer, with an asymmetric magnetic-field setting (table A.1) and a potential offset of −300 V is applied to the inner electrode relative to the vessel (ref. [Nte14]). Magnetic field-lines thereby penetrate the main spectrometer vessel and low-energy electrons emitted from the inner-electrode ring-structures[1] are mapped on the detector wafer. As the position of the inner electrode system is determined with a precision of ≤1 mm (ref. [Hil11]), any additional deviation is associated with an unrecognized alignment uncertainty. The center of the electron ring pattern in fig. 3.17 is determined to $\Delta x_{\mathrm{mes}} = (-2.5 \pm 1.0)\,\mathrm{mm}$, $\Delta y_{\mathrm{mes}} = (-1.88 \pm 1.00)\,\mathrm{mm}$. As the observed offset does not lead to any collisions of the magnetic flux-tube with vacuum components, the slight deviation of between the alignment simulation and measurement is of no concern. The additional introduced misalignment is interpreted as a wafer offset in simulations within this thesis.

3.4.2 Alignment of the electron gun

The alignment of the e-gun and the associated PS magnets follows the alignment principle of the FPD system, with a magnet position and orientation measurement at first, a FaroArm measurement to determine the position of the sub components relative to each other, and a verification with a dedicated electron optic measurement.

As the pre-spectrometer vessel can be detached from the magnets it is possible access both magnets from both sides for alignment measurements. By an elaborated magnetic-field measurement campaign, it was possible to determine the position and orientation of the magnets inside the cryostats (ref. [Ada15]). A displacement solely along the z-axis of $(-1.09 \pm 0.11)\,\mathrm{mm}$ ($(2.94 \pm 0.14)\,\mathrm{mm}$) for PS 1 (PS 2) was verified, the other axes are compatible with zero within uncertainty. For the orientation of the coils, relative to the cryostats, an incline of $(0.23 \pm 0.14)°$ ($(0.30 \pm 0.17)°$) is detected for PS 1 (PS 2).

When all components were mounted in their final positions, the location of various surfaces were measured with a FaroArm (fig. 3.18) relative to the upstream main-spectrometer flange (ref. [Erh15a]). The positions of the solenoid cryostats are within a distances of 0.05 mm to their design values and the position of the e-gun is within 0.2 mm. These values are in the order of the FaroArm precision. Combined with CAD drawings, also the effective center of rotation and radius of the UHV manipulator was determined. When the manipulator is in its central position, the resulting position of the e-gun back plate is $\vec{x}^{\top} = (0.19, 0.19, -13\,702.294)\,\mathrm{mm}$ with a tilt of 0.08° and the rotation radius is 1359 mm.

To verify the e-gun alignment and the relative position to the detector wafer, an electron optical measurement was performed, a method that was successfully tested during SDS 1 (ref. [Sta13]). e-gun electrons with a sufficient surplus energy of ≈50 eV relative to retarding potential were measured along the vertical and horizontal axis when the UHV manipulator was rotated with a constant speed. To cover the entire diameter of the wafer, the full angle range of ±20° was utilized. The resulting cross-shaped count rate distribution is shown in fig. 3.19 (left side).

1 The origin of the emitted electrons are the comb like holding structures as visualized in fig. 3.2, the wires are too thin.

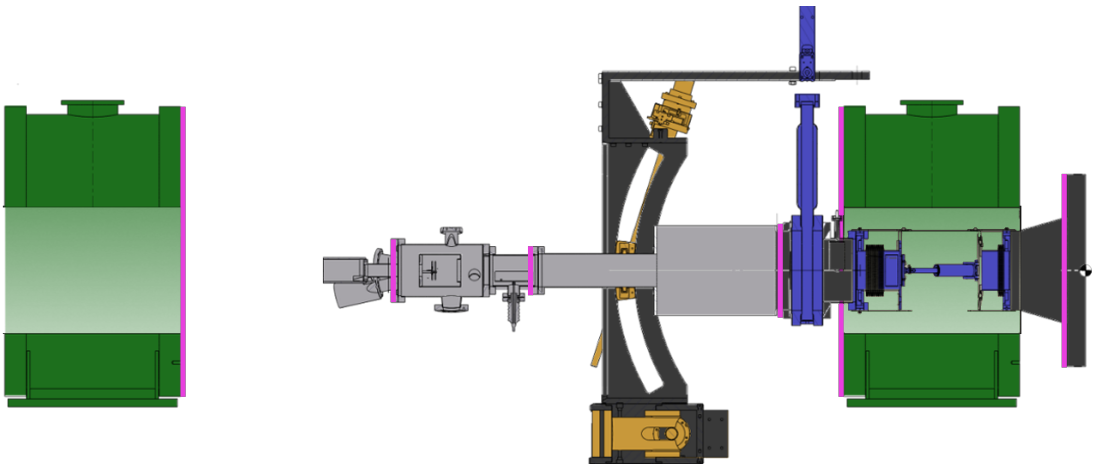

Figure 3.18: Alignment of the e-gun and the PS magnets. The position and orientation of the magnets in their cryostats was determined by magnetic-field measurements (ref. [Ada15]). The final positions were determined at pink highlighted surfaces by FaroArm measurements relative to the a main spectrometer flange (on the far right).

Due to the finite size of the electron beam of 20 µm on the detector wafer, electrons were detected by two neighboring pixels when the e-gun hit the border. Based on the characteristic shape of the FPD pixels and the assumption of a constant rotation speed, the count rate distribution on ring 1 is used to calculate the intersection of the vertical and horizontal rotation scan. Hence, the center of the electron beam on pixel 2 is determent to $x = -0.82\,\text{mm}$ and $y = -2.82\,\text{mm}$ when the UHV-manipulator is in the neutral position. Considering the FPD misalignment as stated in section 3.4.1 and the conservation of the magnetic flux, an offset of $x = 13.6\,\text{mm}$ and $y = 1.0\,\text{mm}$ is included in the simulations additionally.

Based on the fully implemented alignment information of the e-gun and the magnetic field, the observed count rate distribution is reproduced in a simulation (fig. 3.19). As in the measurement, the e-gun was positioned at different field lines by rotating the UHV manipulator from $-20°$ to $20°$ in $0.1°$ steps, where field lines from the back plate to the FPD wafer are calculated. Not only is the correct target-pixel distribution, but the correct event rate reproduced as well. Differences to the measurement are the result of the rotation speed of the UHV manipulator[1] and the magnetic-reflection effect due to an uncorrected zero angle on outer radii (section 6.4.3). The deviation at the bottom pixel may result form an $\vec{E} \times \vec{B}$ drift due to an applied voltage on the dipole electrode (section 6.2.2). Overall, a great level of alignment accuracy and an excellent agreement with simulations is achieved.

It is important to note, that these alignment values are effective values of the full beam line (from the e-gun to the detector). Especially the FPD alignment introduces a large positioning uncertainty, which was measured in stand alone mode without liquid nitrogen cooling of the PAE where the wafer is located. The thermal stress can lead to a mechanical deformation and thereby to a tilting of the wafer position of a few mm.

1 The vertical axis of the UHV manipulator has only half of the horizontal rotation speed due to the additional torque of the e-gun chamber.

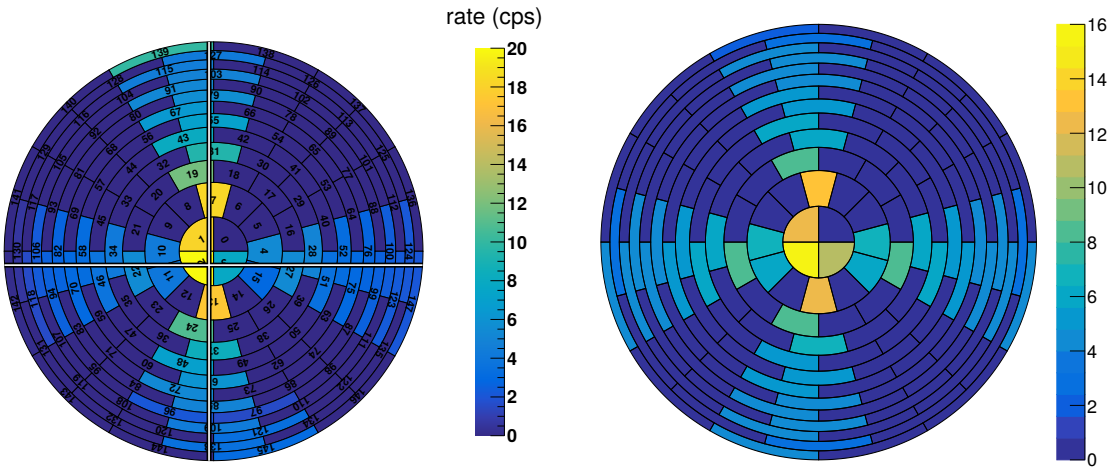

(a) measurement **(b)** simulation

Figure 3.19: e-gun alignment verification. The e-gun was moved along the horizontal and vertical axis with constant speed of the UHV manipulator. Based on the count rate distribution the e-gun center was calculated (white cross). When a realistic magnetic field and e-gun alignment information are included, field-line simulations can reproduce the observed tracks.

3.4.3 Alignment of the magnetometer system

A tachymeter was used to determine the position of a magnetometer in the KATRIN coordinate system. First, the tachymeter position was measured relative to reference points installed in the main spectrometer hall. A reference point is a fixed position where a prism can be magnetically mounted, which allows for a high precision position measurement of the tachymeter of about 0.3 mm relative to the KATRIN coordinate system. Second, the position of a sensor relative to the tachymeter was measured. Since non-magnetic materials were used exclusively for a sensor unit, a different, non standardized approach was deployed to determine the position off a sensor unit that combines the laser distance measurement and the highly accurate angular sensitivity of the tachymeter (fig. 3.13).

The distances of four points on the surface of a sensor unit were used to define the orientation of a sensor relative to the KATRIN coordinate system. In most cases, the measurements were performed with a low incidence angle of $\rho = (14 \pm 15)°$ that lead to an distance uncertainty δ_{surface} of about 0.5 mm. With the length l_{i} of a sensor surface, the effective length

$$l_{\text{eff i}} = l_{\text{i}} \cdot \cos(\rho) \cdot (1 + \delta_{\text{surface}}) \tag{3.2}$$

of a geometry axis can be calculated, where the uncertainties of the three rotation angles

$$\delta\Omega_{\text{i}} = \arcsin\left(\frac{\delta_{\text{surface}}}{l_{\text{eff i}}/2}\right) \tag{3.3}$$

can thereby be estimated to $\delta\Omega_{1,2,3} = [2.9°, 0.7°, 2.9°]$ for a Bartington magnetometer and $\delta\Omega_{1,2,3} = [2.3°, 1.5°, 2.3°]$ for a IPE magnetometer, assuming normal distributed measurement uncertainties. These angular uncertainties of the sensor units are upper limits.

A position of a sensor is defined by the edges of its four corners. Due to the finite size of the laser beam, the distance measurement uncertainty increased drastically when the laser was reflected partly on the sensor and the surface in the background of a sensor corner. The angle of the tachymeter at this position was used to calculate the virtual intersection with the previously defined surface. The positioning uncertainty of a sensor unit is for all magnetometers and all axes $\delta x_{\mathrm{i}} = 0.8\,\mathrm{mm}$. In this estimation the very low angular uncertainty of $0.5''$ of the tachymeter is neglected.

Position and orientation uncertainties are incorporated in simulations as uncertainties of the magnetic-field of the sensor units. Utilizing the laser positioning module of a high precision sensor unit, the precision and accuracy of the alignment measurement of a sensor unit can be increased significantly; due to time restrictions this time-consuming and work-intensive procedure was postponed.

3.4.4 Resulting magnetic field disturbances

The geometry properties of all components, their deviations from design values, the positioning and orientation imperfections have an influence on the magnetic field distribution in the main spectrometer vessel and thereby alter the MAC-E filter characteristics. The particular contribution of a magnetic device to the magnetic-field perturbation is locally limited. As the deformations and deviations vary for individual coils, the effective magnetic field is rather inhomogeneous. Consequently, a compensation system, as for the earth magnetic field, is a complex task and would require a sophisticated additional air-coil system (ref. [Glü14]).

All effects listed in this chapter are implemented in the Kasper software framework to estimate their influence on the field in the analyzing plane. As a reference, a purely axially symmetric magnetic-field is chosen, where all magnets are coaxial aligned and no deformations are present. Fifth configurations are selected:

- "EMCS" is the test of the realistic modeling of the coil system. The EMCS system is designed to generate a homogenus magnetic, although on outer radii an azimuthal variation is expected due to a discrete, cosine distributed current.
- "LFCS corrected" is the test of the realistic modeling of the deformed LFCS coils, including the correction spacers. In this case not only azimuthal, but also variations along the beam axis are expected.
- "LFCS effective" is an approximation of the deformed LFCS by an ring coil shifted to a new center coil and with a adjusted coil radius. This is used as a test of the approximation.
- "tilted" considers the measured tilts and displacements of the PS 1, PS 1, PCH and DET solenoid in the simulation.
- "all effects" is the combined simulation of "EMCS", "LFCS corrected" and "tilted".

The resulting difference of the absolute magnetic-field to the ideal configuration is shown in fig. 3.20 along the beam axis with radius $r = 0\,\mathrm{m}$ and along ϕ at $z = 0\,\mathrm{m}$ on a radius $r = 4.5\,\mathrm{m}$. Fortunately, the impact on the magnetic field homogeneity is in the low sub-µT regime. Thus, the contribution to a magnetic-field deviation is subordinate and the inclusion of the computation-time intensive configuration "LFCS corrected" is recommended only for high-precision simulations, especially on outer field lines.

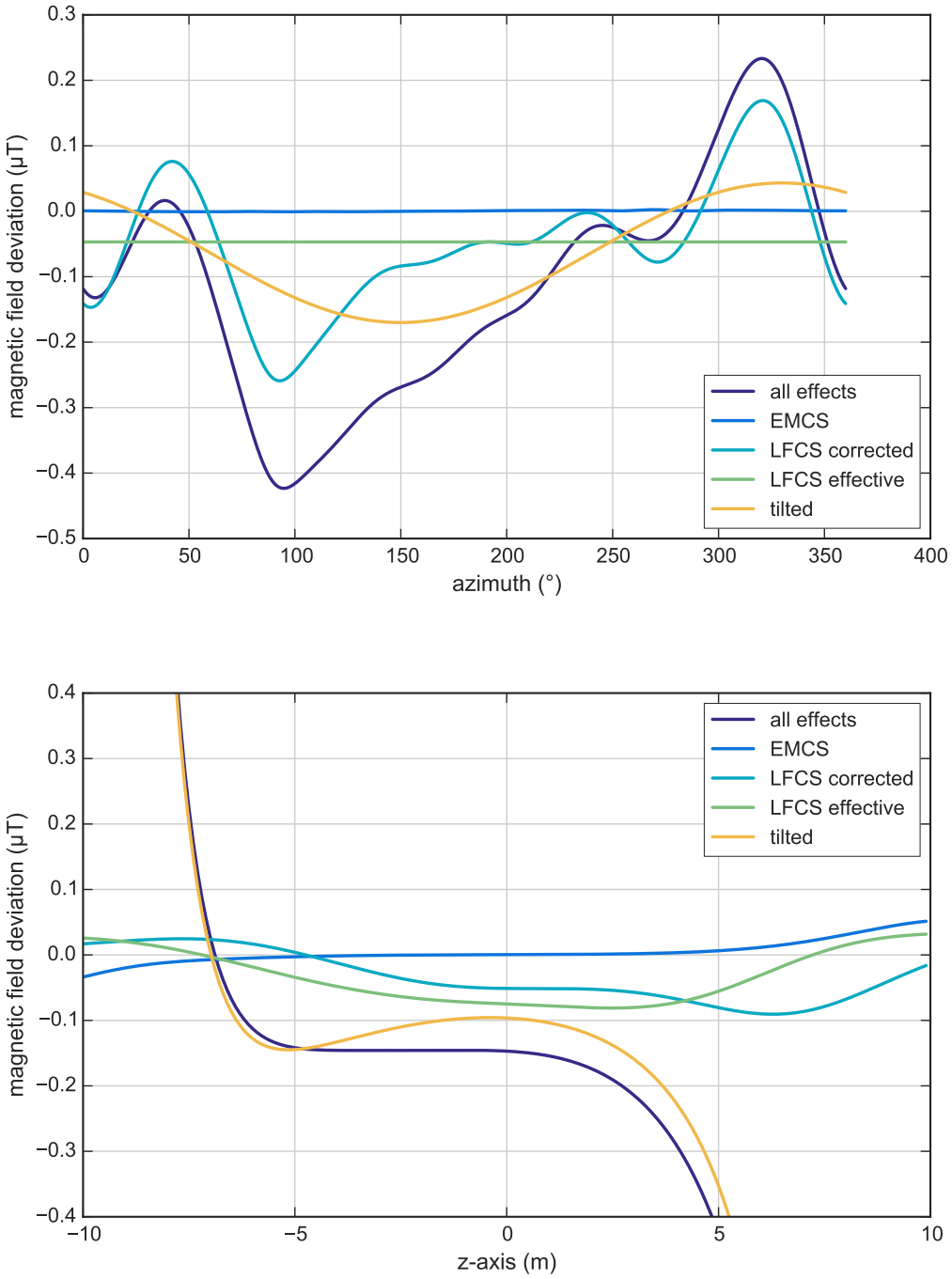

Figure 3.20: Effect of a misalignment of various sub components. All values are given relative to a magnetic-field simulation based on an axial-symmetric system and neglecting the earth magnetic field components perpendicular to the z-axis. EMCS shows the effect of the realistic representation of the "earth magnetic field compensation system" and its misalignment. LFCS corrected and LFCS effective correspond to the different models of the low field correction system as shown in fig. 3.5. In the graph tilted, the results of alignment measurement of the four SDS magnets are shown. Label with "all effects", this simulation combines the influence of the EMCS, the corrected LFCS and the tilting of the SDS solenoids. The upper plot shows the azimuth development of the magnetic field in the analyzing plain on a radius of 4.5 m. The magnetic field along the symmetry axis of the spectrometer is shown in the lower plot.

CHAPTER 4

Settings and performance of the air-coil system during SDS 2

The superconducting solenoids on both sides of the spectrometer are complemented by a system of air-coils to obtain a well-defined magnetic field inside the spectrometer volume. To fulfill the transmission conditions it is necessary that the magnetic and electrostatic field vectors are aligned parallel to each other (section 2.1.2). There are three electromagnetic field configurations to generate a MAC-E filter. Three criteria were defined to optimize the air-coil current setting for an ideal magnetic-field operation during SDS 2 (section 4.1).

The performance of the air-coil system of the KATRIN experiment has been studied by means of simulations and measurements with magnetic-field sensors which were installed temporally in the main-spectrometer building and inside the main spectrometer vessel. These measurement campaigns have verified the basic functionality of the air-coil system and the influence of various distortions on the homogeneity of the magnetic field inside the main-spectrometer was estimated (ref. [Rei13], [Erh16]).

In comparison to previous measurement campaigns such as the SDS 1 phase, the air-coil currents can now be set much faster and with a higher precision due to an overhauled slow-control infrastructure via ORCA-scripts (section 3.2.2). An important goal there is to provide a system to implement magnetic-field layouts on a quasi-online time scale. To achieve this, the air-coil system was thoroughly calibrated. Furthermore, internal and external correlations, such as temperature dependencies were quantified (section 4.2).

A crucial design goal is to avoid or minimize instabilities of the applied magnetic field on different time scales. With a duration of 135 days, the SDS 2 phase exceeded the estimated time of a neutrino-mass measurement-cycle of 60 days by more then a factor 2. The SDS 2 campaign therefore allowed to study issues such as the drift behavior of the air-coil PSUs, long-term effects of the air-coil system and, on a more general level, systematic effects of the magnetic guiding field. Also, on time scales on the ms level the relaxation of the magnetic field generated by the air-coil system could be tested for various magnetic-field settings (section 4.3). In this chapter, long-term time scales are notated relative to the date 2014-12-04, prior to this date air-coil power-supplies were exchanged and smaller adjustments to the air-coil and monitoring system were made.

The tests outlined in this chapter were thus targeted to investigate the air-coil system in its final setup and to check if the reliability, accuracy and precision of the generated magnetic-fields indeed meet the KATRIN requirements.

4.1 Magnetic field settings

The electromagnetic design requirements (section 2.1.2) are an essential prerequisite to operate the main spectrometer as MAC-E filter. There are three different approaches (electrostatic potential distribution, the magnetic field distribution or a combination of both) to locate the analyzing plane, i.e. the area of the minimal longitudinal kinetic energy $E_{\parallel}$ as defined in eq. (2.9), in the center of the spectrometer.

- An inhomogeneous electrostatic potential with its minimum in the center of the spectrometer with a steep increase on both sides (upper plot fig. 4.1). In this case, the minimum of $E_{\parallel}$ is defined by the global potential minimum and only moderate constraints on the shape of the magnetic field are required. However, given the large radius to length ratio of the KATRIN main spectrometer, this setting is disadvantageous. In this geometry, a large axial potential inhomogeneity implies a large radial potential inhomogeneity also. As the energy resolution is proportional to the radial potential inhomogeneity, this setting is strongly disfavored.
- A rather homogeneous electrostatic potential in the central region is implemented together with a magnetic field featuring a global minimum (central plot fig. 4.1). The design of the KATRIN main-spectrometer HV system allows to generate a homogeneous electrostatic potential with minimized radial potential inhomogeneity. However, in this setting the position of the minimum of $E_{\parallel}$ is sensitive to the magnetic-field shape and both fields have to be aligned carefully. While the increase of the electrostatic potential towards the spectrometer center leads to a reduction of $E_{\parallel}$, a reduction of the magnetic field will lead to an increase of $E_{\parallel}$. These two counteracting effects can easily cause a violation of the transmission conditions, especially for larger angles of the momentum of an electron relative to the magnetic field. Therefore this solution is not the preferred option although being feasible.
- A rather homogeneous electrostatic potential in the central region is implemented together with a magnetic field with a local maximum (lower plot fig. 4.1). To prevent a violation of the transmission condition as in the previous setting, the magnetic field has two local minima at positions where the electrostatic potential is rather large. If $E_{\parallel}$ is dominated by the electrostatic potential at the positions of the local magnetic-field minima, an electron is transmitted. In between the two minima both fields cause a reduction of $E_{\parallel}$ to ensure that the position of the minimal $E_{\parallel}$ is located at the center of the spectrometer. In this setting the transmission condition is fulfilled most easily and is therefore the favored setting for the KATRIN main spectrometer. However, this magnetic-field setting could result in an increase of background events, as it enhances a trapping of charged particles in the region of the two magnetic-field minima (ref. [Glü09]). Given the above considerations, only simulations have revealed that at positions of the magnetic-field minima, secondary electrons drift in the active magnetic flux-tube (ref. [Tro15]).

In conclusion, the two latter electromagnetic design solutions are of relevance for KATRIN. In both cases, the magnetic adiabatic collimation of electrons must be sufficiently fast (or the potential setting must be adjusted respectively) to transform $E_{\perp} \rightarrow E_{\parallel}$ and prevent an early retardation (section 2.1).

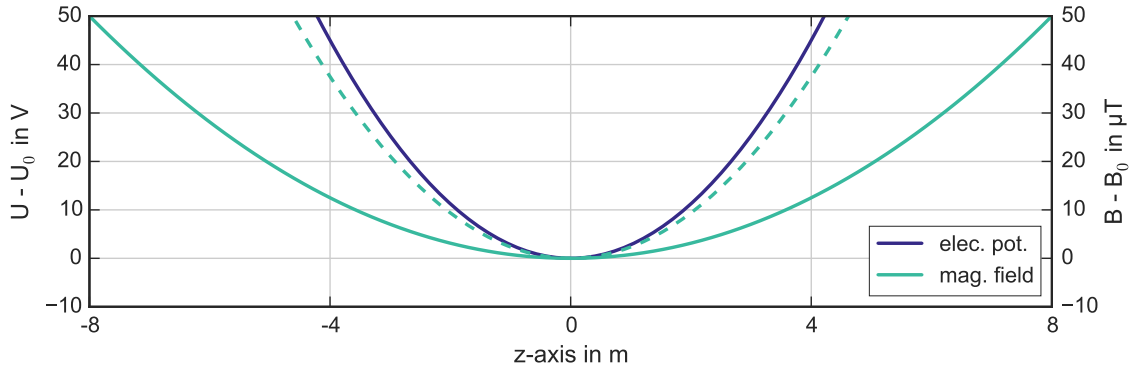

(a)

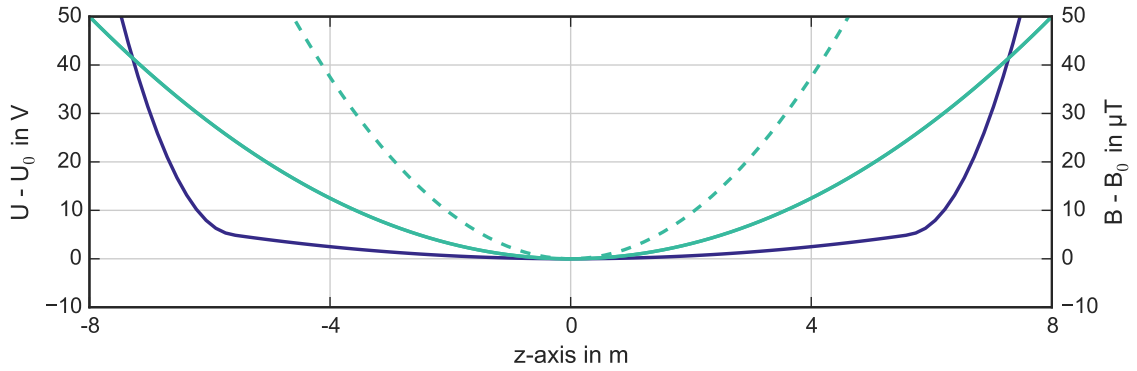

(b)

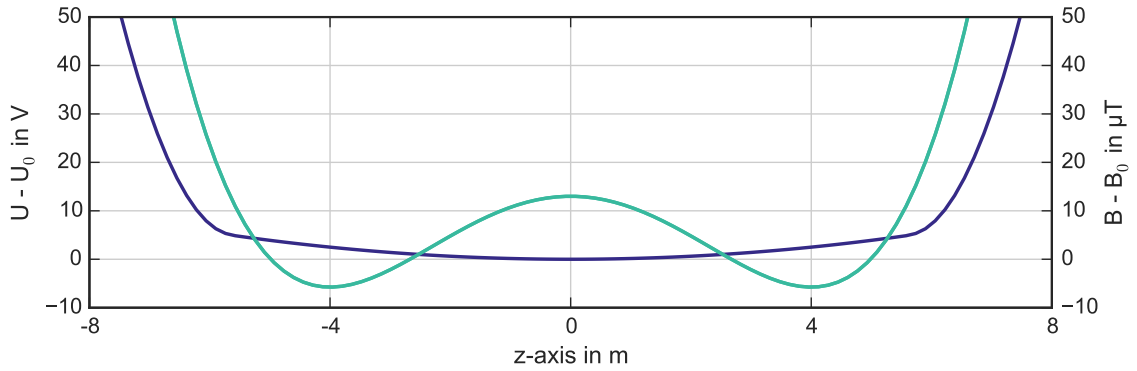

(c)

Figure 4.1: Possible electromagnetic field configurations of a MAC-E filter. Potential (blue) and magnetic (green) field values are plotted relative to global values U_0 and B_0. In (4.1(a)) the transmission conditions are based on an inhomogeneous electrostatic potential and magnetic field which have to reach their minima at exactly the same position. Due to the geometry of the main spectrometer, this solution is disadvantageous and not implemented (see text). In (4.1(b)) a homogeneous electrostatic potential and a magnetic field with a global minimum is chosen. To fulfill the transmission conditions a rather homogeneous magnetic field is required (solid line). In (4.1(c)) a magnetic-field configuration with two local minima is shown. This solution gives the benefits of implementing a homogeneous electrostatic potential largely independent of the magnetic-field shape in the central region. Figure inspired by ref. [Glü09].

4.1.1 Magnetic-field criteria for optimal transmission conditions

The currents of the LFCS system need to be set to level out the upstream-downstream imbalance between the magnetic stray fields of the PCH magnet and the PS 2 unit and to fulfill the transmission conditions. The high flexibility of the LFCS system to shape the magnetic field shape via its 14 coils, each powered by an independent PSU, allows a huge variety of different magnetic-field settings. To find the optimal setting is therefore a complex task where all electromagnetic design constraints have to be included.

Based on three criteria, an algorithm was developed for automated optimization of the LFCS currents (ref. [Gro15]), thoroughly tested (ref. [Sta13]) and successfully applied to implement specific electromagnetic configurations throughout the SDS 1 phase. Later on, the nominal current settings of the SDS solenoids were changed for SDS 2 and so the current setting of the LFCS had to be adjusted accordingly (ref. [Erh14b]). The three optimization criteria for these measurements are identified with respect to these parameters:

1. Absolute magnetic-field strength. Depending on the required energy resolution and the desired background reduction factor (appendix C.1), the absolute value $B_{\mathrm{set}}(z = 0\,\mathrm{m}, r_0 = 0\,\mathrm{m})$ in the center of the main spectrometer can be chosen. The squared difference of the actual value to the pre-set value

$$C_1 = \left(B\left(r_0\right) - B_{\mathrm{set}}\right)^2 \tag{4.1}$$

   is the first criterion to be minimized. It defines the active-volume and the confinement of the magnetic flux-tube inside the spectrometer vessel.

2. Radial magnetic field homogeneity at N positions, which are equally distributed between r_0 and r_{max} in the analyzing plane. Here, the sum of all squared differences

$$C_2 = \frac{1}{N}\sum_{i=1}^{N}\left(B\left(r_{\mathrm{i}}\right) - B_{\mathrm{set}}\right)^2 \tag{4.2}$$

   of the magnetic field values at B_i is the second criterion to be minimized. Typically $N = 10$ is chosen between r_0 and r_{max} to include the full detector flux tube at any time during the optimization process. The maximal radius r_{max} is defined by the outer flux-tube radius of $\Phi = 210\,\mathrm{Tcm}^2$, approximate by previous flux-tube simulations.

3. Axial magnetic-field homogeneity. Here, the gradient in z-direction at N points is used as a third criterion. By minimizing the biggest gradient

$$C_3 = \max\left|\frac{\mathrm{d}B_{\mathrm{actual},p}}{\mathrm{d}z}\right| \tag{4.3}$$

   at the N points, the axial magnetic-field homogeneity is maximized.

For a numerical optimization, the three criteria C_k are combined into the function

$$F = \sum_{k=1}^{3} w_k \cdot C_k \tag{4.4}$$

with individual weight factors w_k. In the optimization routine, the 14 LFCS currents are free parameters within the technical limitations of the PSUs as boundary conditions.

Depending on the desired magnetic-field setting (single or double minimum solution, fig. 4.1) the weights need to be selected. For the optimization of a double setting the relation between the weights is $w_3 \gg w_2 > w_1$. In order to calculate a single setting, the second weight should be neglected as it counteracts the tendency of a single setting with respect to radial homogeneity.

4.1.2 Optimized magnetic field settings for SDS 2

In general, the magnetic-field settings calculated for the SDS 2 measurements can be classified as being symmetric or asymmetric with respect to the spectrometer center. An asymmetric setting is achieved when one or both superconducting magnets on the upstream side are ramped down so that the magnetic flux tube dimension exceeds the main spectrometer radius. Such a setting is chosen for alignment measurements and dedicated background measurements (fig. 3.17). A symmetric magnetic-field setting is implemented when nominal currents are applied to the superconducting solenoids and the spectrometer is operated as a MAC-E filter. A magnetic-field setting is identified and labeled by the magnetic-field value in Gauss that roughly corresponds to the magnetic-field strength in the center of the main spectrometer. Throughout this thesis, magnetic field values are given in Tesla (T) whereas magnetic-field names involve Gauss (G). A field setting with one global minimum has the name suffix "single" or (s) and a setting with two local minima has the name suffix "double" or (d). As the double minimum settings was the configuration by default, the suffix (d) is usually omitted.

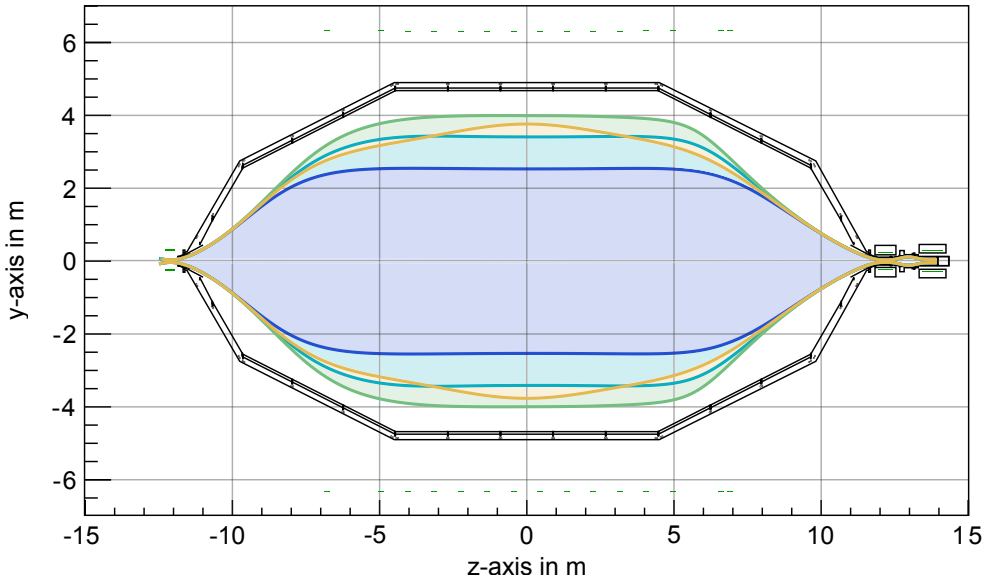

Figure 4.2: Shape of the magnetic flux-tube for various magnetic-field settings. The most frequently used magnetic-field configurations are the 3.8 G(d), 3.8 G(s), 5.0 G(d) and 9.0 G(d) settings shown in green, orange, light and dark blue, respectively. The label (s) refers to a single, the label (d) to a double minimum solution.

The most frequently used magnetic field settings during SDS 2 are shown in fig. 4.2 by their outer-most field line. The magnetic field settings used in this thesis are given in table A.1. For the optimization of the coil settings an axial-symmetric magnetic-field model was used that incorporates the design values of the solenoid and air-coil positions.

Details of the magnetic-field shape of a single and a double 3.8 G-setting are given in fig. 4.3. In case of the double setting, the minima are located at −5 m and 5 m from the analyzing plane[1] and the single setting has one global minimum in the center. The zoom to the inner-most part confirms the axial homogeneity for both settings, but the radial spread is larger by a factor of 6 for the single minimum setting.

The currents of the EMCS system are based on straight-forward calculations of the magnetic field that has to be generated to cancel out the distorting earth magnetic-field components given in table 3.4.

4.2 Basic functionality of the air-coil system and systematic uncertainties

The impact of the stability of the air-coil system on systematics of electron transmission can be investigated when the power-supply characteristics over the full current-range and the influence of possible disturbances are known. The observed current uncertainties are rather complicated combination of individual properties of all involved power-supplies, analog-output cards and cFP characteristics; for simplicity, all air-coil system characteristics will be referred to as air-coil properties.

The entire air-coil system is designed to provide a magnetic-field precision of at least 1 % in the central region of the main spectrometer (ref. [Glü13]). The overhauled and extended slow-control infrastructure enables to study the air-coil system functionality for the first time with such high precision and accuracy.

4.2.1 Linearity of the air-coil system

A fundamental parameter in the assessment of the air-coil reliability is the linearity of all air-coil currents derived from calibration. Since the current read-out electronics is performed independently from the PSUs, the linearity can be studied with a precision of 3 ppm, limited only by the utilized current transducer readings.

To study the linearity of the air-coil system, the currents of all runs with stable conditions during SDS 2 were combined. As data quality criteria for a stability of the magnetic-field, a run has to fulfill the following requirements:

- The set-values of all air-coil currents as well as the currents of the superconducting solenoids have to be constant. Thereby a later comparison of magnetometer data with magnetic field simulations is possible.
- None of the air coils is operated in magnetic-pulse mode and all currents are applied in their nominal direction.
- The total duration of a run is 900 s or longer to suppress the influence of an air coil being in a transient state such as the initial warm-up (section 4.2.3).

1 The minimum at the downstream side is more pronounced due to the influence of the anti-parallel magnetic-field of LFCS coil 14.

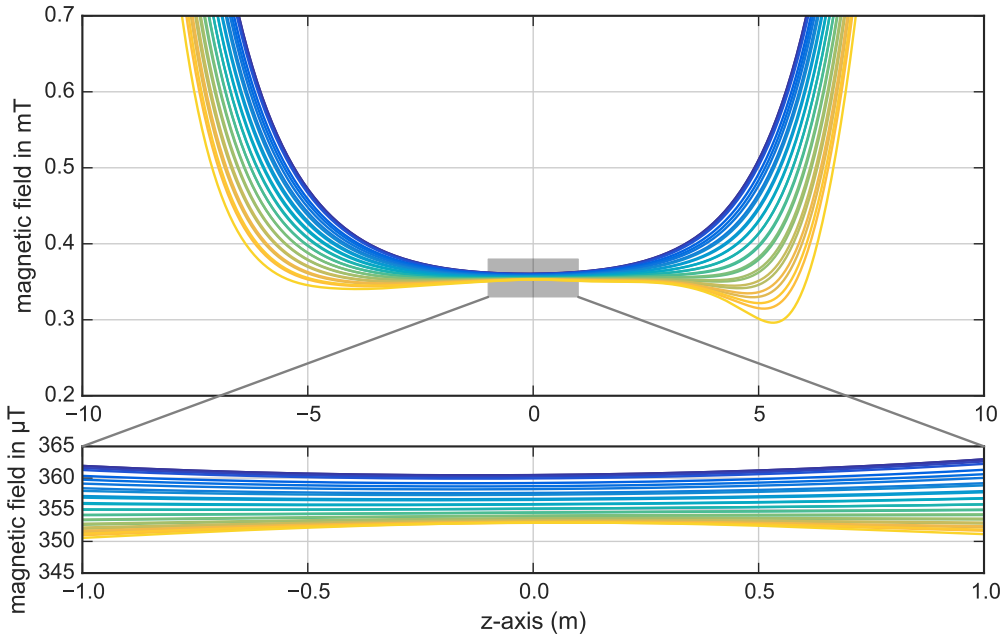

(a)

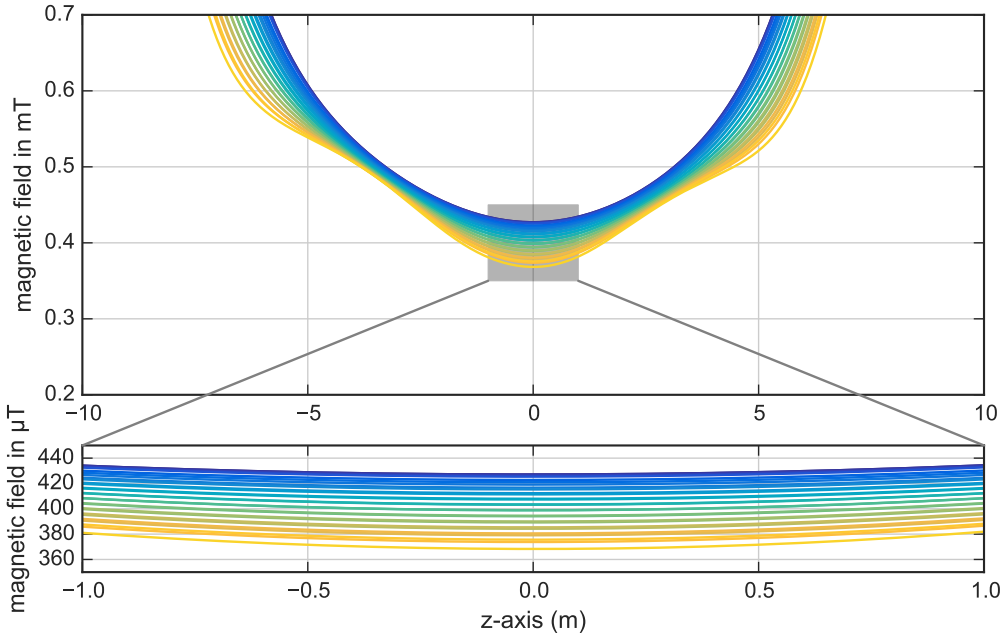

(b)

Figure 4.3: Optimized magnetic field for a 3.8 G-setting. In (4.3(a)) the double minimum setting is shown. The minima are located at $z = -5\,\mathrm{m}$ and 5 m, the different shape is due to the influence of LFCS coil 14. The zoom to the central region reveals a good axial homogeneity and a small radial spread of the magnetic field. In the lower plot the single setting with one minimum in the central region and the overall magnetic field shape is more axial symmetric. In the central region the radial spread of the magnetic field is more pronounced (note the scale). The depict magnetic field lines represent the FPD ring structure as introduced in fig. 3.10.

The observed behavior of all air-coils is largely comparable since all air-coils are operated with PSUs of the SM 3000 series. Therefore, the following results are given for the two LFCS coils closest to the analyzing plane. A more comprehensive summary of the performance of all air coils can be found in appendix A.

In fig. 4.4 the deviation of the current output of the PSU to its set-value is given and the measurement uncertainty was weighted by the duration of a run. In doing so runs are favored where stable currents are more likely. This is due to the fact that the entire air-coil system is in a transient state after a magnetic-field setting is changed and stable currents can not be guaranteed (section 4.2.2). The full current range can be utilized and the observed deviation sufficiently described by a linear function

$$I_{\text{out}} = (1 + \Delta s)\, I_{\text{set}} + \text{c}\,, \tag{4.5}$$

where Δs is the deviation to an ideal slope and c is a constant offset, here shown with a 3σ-uncertainty. With an average slope of $(3.6 \pm 1.1)\,\text{mA/A}$, the air-coils feature only a minor deviation from an ideal linear behavior and below the 0.5 %-limit of the manufacture for the power-supply units. The offset of all air-coils (LFCS 1-14) is non-zero with an average value of $(-290 \pm 79)\,\text{mA}$. Therefore, all applied magnetic fields are slightly smaller than originally intended. In case of a 3.8 G setting this offset corresponds to about 1 %.

4.2.2 Temperature dependence of the air-coil system

The performance of the air-coil system is influenced by external factors, with the temperature being the most prominent one. To simplify the analyses of magnetic-field properties, a temperature dependency has to be suppressed. As the whole air-coil system is temperature stabilized by the air-conditioning of the spectrometer hall only, a small temperature coefficient for all electronic devices of the air-coil system is a requirement. As the temperature coefficient of the PSUs is tiny with a nominal value of $20 \times 10^{-6}\,\text{K}^{-1}$, the fluctuations of the operating temperature of a few Kelvin can be negligible.

Consequently, only the power consumption of the air-coil system fluctuates as a result of an altered resistance of the air-coil wires in case of temperature variations. In thermal equilibrium, this behavior should be given by the resistance temperature-coefficient[1] $\alpha = 3.86 \times 10^{-3}\,\text{K}^{-1}$ of aluminum, the conductor material of the wires (ref. [Bay09], [Hay14]). However, the extended geometry of the air-coil system implies a top-down temperature gradient. A direct calculation based on thermal diffusivity and capacity would require dedicated temperature

Table 4.1: Linearity of the LFCS 7 and LFCS 8 units. The values correspond to the fit parameters of the linear functions shown in fig. 4.4. Comparable results are obtained for all other PSUs.

air coil	Δslope (mA/A)	offset (mA)
LFCS 7	2.408 ± 0.035	-247.0 ± 1.7
LFCS 8	4.448 ± 0.035	-319.4 ± 2.1

1 The temperature coefficient refers to a ambient temperature of 20 °C.

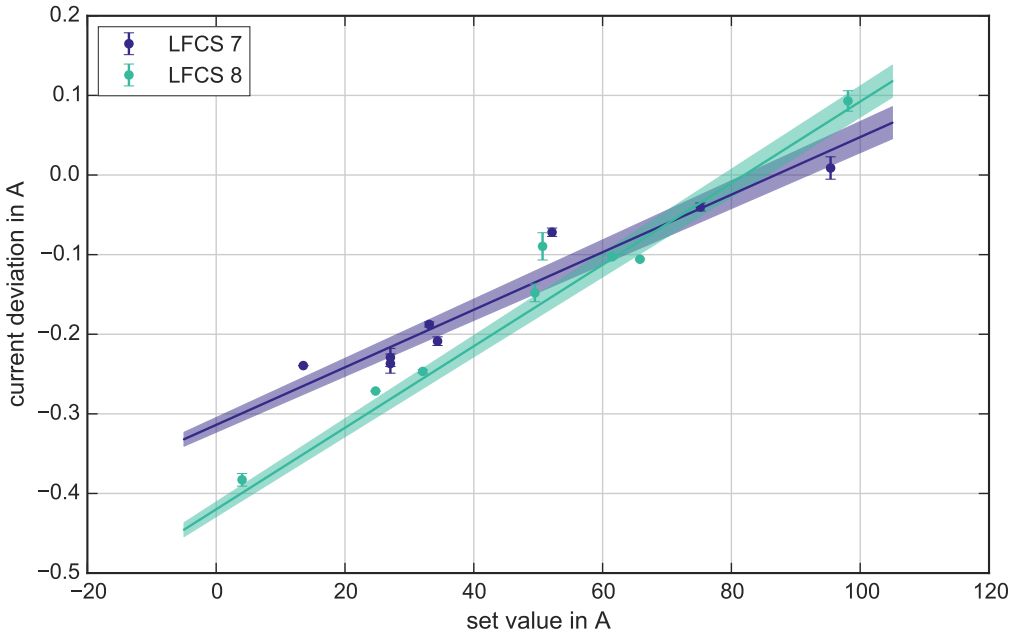

Figure 4.4: Linearity test of the air-coil PSUs of LFCS 7 and LFCS 8 during SDS 2, shown as a difference of the current output of the PSU I_{out} relative to the set value I_{set}. Only runs with stable current set-values and without magnetic pulse are included in this analysis. The data points are weighted with their run-time in the fit. The results of a linear fit are shown together with an 1σ uncertainty band.

sensors being deployed over the entire system. As such a temperature sensor system is not feasible, an analytic description of its temperature characteristics is inhibited.

Instead, to study a temperature dependency, a time period was chosen when the temperature of the spectrometer hall was influenced by the air-conditioning system exclusively. This situation is to favor, as in this case a rather homogeneous temperature of the whole system is expected and the temperature development can be described approximately by a sinusoidal behavior.

Figure 4.5 shows such a situation when thermal equilibrium was reached after 1.2 h of operation with a stable 9 G-setting. To suppress minor individual fluctuations, the current and voltage outputs of all PSUs were combined. In the upper plot the mean difference of the current read-out and set value is shown with a 1σ-uncertainty. During this period the current is constant and a correlation with the temperature can be excluded with a correlation factor of -0.068 ± 0.120.

At the same time, the mean voltage output of the PSU and the air temperature of the main spectrometer hall show specific variations. Both curves can be fitted by a sinusoidal with a frequency of $(0.47 \pm 0.01)\,\text{h}^{-1}$. Shifted and normalized to the voltage trend, the main-spectrometer hall temperature is congruent with the voltage trend at a correlation factor of 0.98. The temperature coefficients $\alpha_{\text{LFCS 7}} = (6.6 \pm 0.2) \times 10^{-3}\,\text{K}^{-1}$ and $\alpha_{\text{LFCS 8}} =$

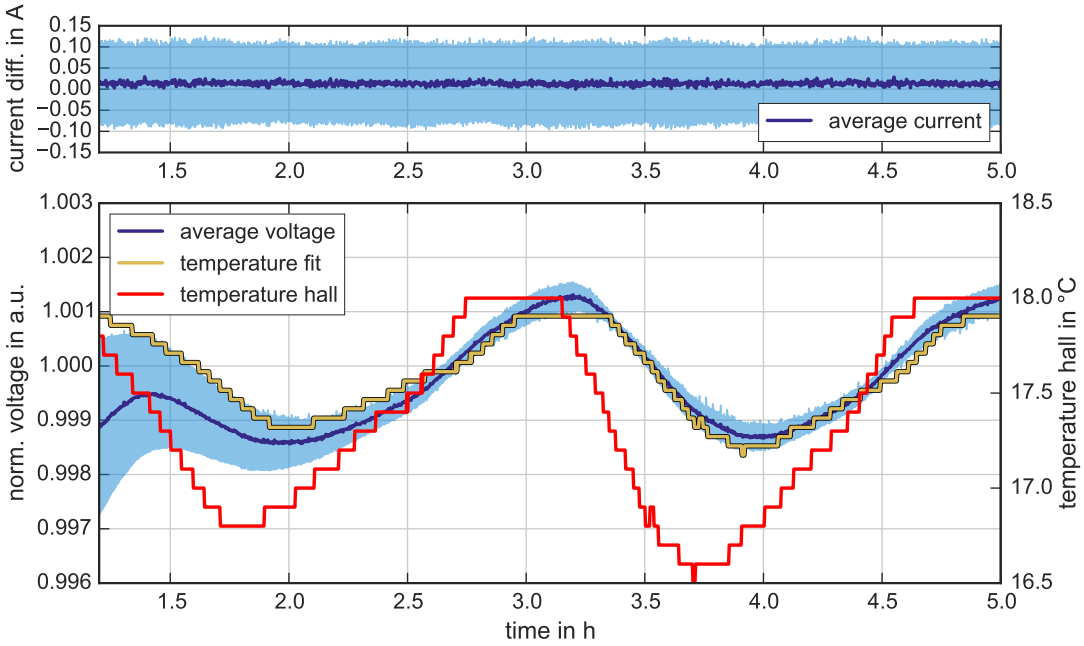

Figure 4.5: Influence of the hall temperature on the air-coil system in a stable 9 G-setting. The upper plot shows the mean difference between the current output and the set value of the power-supply units with a 1σ-uncertainty. In the lower plot the normalized mean voltage output is shown. The voltage fluctuations can be explained by the temperature fluctuations of the main-spectrometer hall with a correlation factor of 0.82. The temperature fit reveals a phase shift of 12 min.

$(4.8 \pm 0.2) \times 10^{-3}\,\mathrm{K}^{-1}$ of the two central coils deviate from the pure aluminum literature value by a factor of 1.45. This deviation most likely originates from the geometry based temperature profile and winding structure of a wire that enhances the temperature coefficients.

A different behavior is observed during the warm-up of the air-coil system. Before the test was started all currents were turned off for about 12 h, therefore the total system was at ambient temperature. About 1.2 h after the start, the temperature of the air-coil system was in equilibrium with the main spectrometer hall temperature. In the first 15 min after the ramp up, the currents are regulated to their final values. A stable magnetic field is observed after 30 min of operation by the six high precision magnetometers close to the analyzing plain. During this transition period, the absolute magnetic-field changes by 0.4 µT.

Despite this rather long ramp up time, this test represents the most extreme case and serves as example to define an upper limit on a possible temperature dependency. The magnetic-field change is below 5×10^{-3} % and thus clearly within the error budget of the magnetic field (see chapter 7).

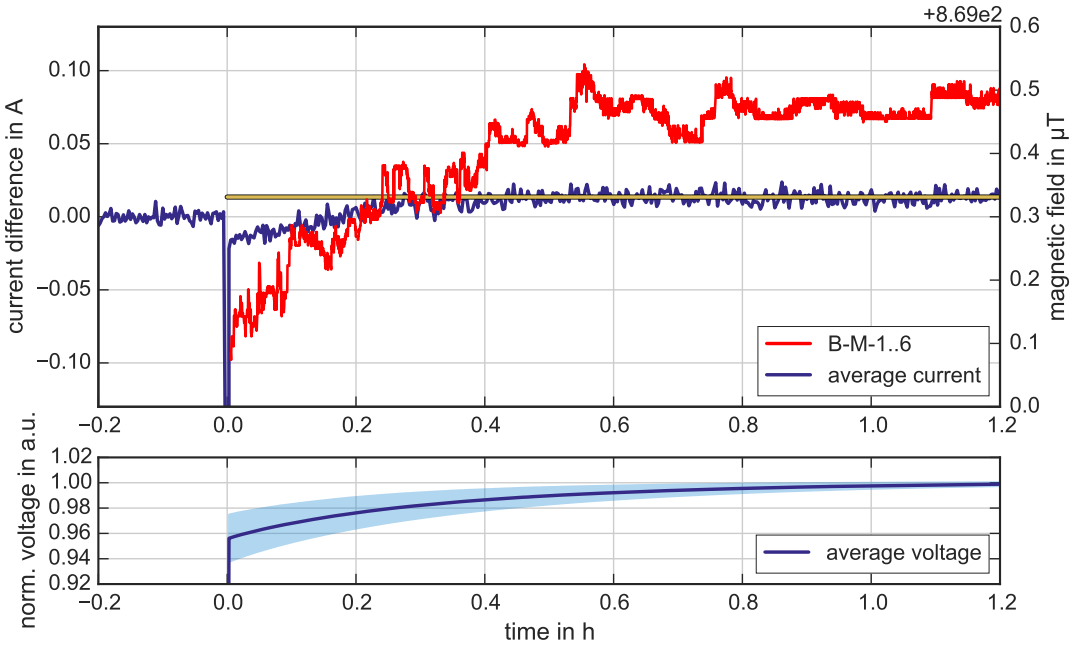

Figure 4.6: Temperature dependence of the air-coil system by ramping the cold PSUs to the 9 G-setting. In the upper plot the mean difference between the current output and set value of all air-coil PSUs is shown with a 1σ uncertainty, in the lower plot the normalized mean voltage output. The yellow line marks the mean current difference when the air-coil system has reached thermal equilibrium. The mean magnetic field of the high precision magnetometers in the central region of the spectrometer are shown in red. It takes about 0.5 h until a stable magnetic field is observed.

4.2.3 Correlated current output of the air-coil power supplies

Originally it was intended to study the linearity of the system and to ensure its operation readiness with dedicated calibration measurements in the first days of SDS 2 campaign. In doing so, a current was applied to a PSU and increased in 5 A steps to cover the full range. The measurements duration per current set value was 60 s to detect a transition state of a PSU. Subsequently this was repeated for each PSU (details in appendix A). In comparision to the final setup, the deviation of the air-coil PSUs was about one order of magnitude larger. Also, an increase of the current set value of one PSU leads to an increase in the current output of about 0.3 % of the PSU right next to it. As a first counter measure to following measurements, a ground loop of the ADC channels was resolved that reduced the observed current correlations significantly. However, these observations triggered a dedicated study of correlations between air-coil currents.

To check for remaining correlations, a measurement with a precision analog isolation-amplifier was performed (ref. [Del13]). Being located at the outer most upstream side, the PSU of EMCS Y is most likely to be sensitive to disturbances by other PSUs. As the

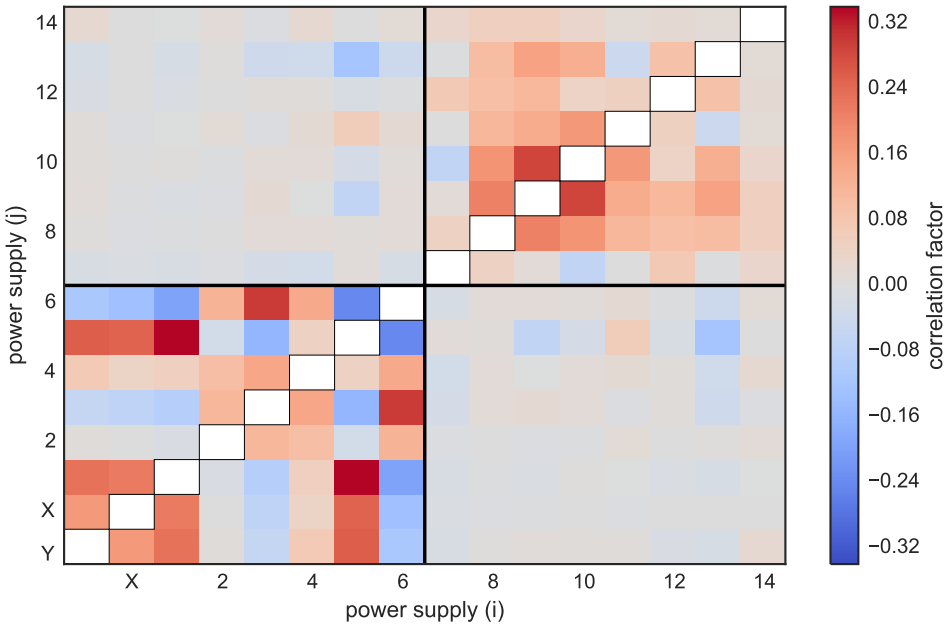

Figure 4.7: Correlations of the PSU outputs during a stable 3.8 G-setting analyzed over 3 days. The first two columns are the PSUs of the EMCS Y and EMCS X, followed by the 14 PSUs of the LFCS system. The uncertainty of all correlations is in the order of 0.02, determined by the bootstrapping method. Controlled by two 8-channel analog I/O cards, only minor correlations are observed on one card of a PSU, the cards are indicated by black lines.

set-values are sent via unshielded cables, the seven other power-supply signals may interfere[1]. However, even in the extreme case that all air-coils were varied over their full current limits, no influence could be detected above the isolation-amplifier precision of 0.1 %. Also no voltage drop was detected between the current distribution cabinet and the PSUs.

Another source of potential correlations is the fact that the eight PSUs are adjoining in the air-coil current-distribution cabinet. The two PSUs of the EMCS and the first 6 LFCS, as well as the LFCS 7 to 14 are connected to one common DAC card. A separation of all PSUs from one another is only possible by an extensive intervention in the hardware setup that had to be postponed due to time restrictions. Consequently, minor correlations among air coils do remain.

To study any remaining correlation of the PSUs, a period with an applied 3.8 G-setting was selected. This measurement continued uninterrupted for nearly two days, so time or temperature variations can be neglected. In fig. 4.7 the correlation of all PSUs between each other are shown. Significant correlations between currents are observed in a pattern that corresponds to the wiring in the current distribution cabinet. Currents of PSUs

1 The air-coil current-distribution cabinet is located in the center of the 16 PSUs. On both sides eight PSUs are located.

mounted on a common DAC are slightly correlated with correlation coefficient up to 0.32. In between different DAC cards the correlations can be neglectable within the experimental uncertainty. Based on the bootstrap method, an uncertainty of about ± 0.02 was estimated for all combinations. The same correlation pattern is observed for other magnetic-field settings also.

Based on these correlation studies the following conclusions can be drawn:

- an applied current does not influence a set-value of another PSU. Therefore, current offset variations beyond the calibration in section 4.2.1 can be excluded.
- within a DAC card the applied currents feature minor correlations. The correlation pattern corresponds to the hardware setup in the air-coil current-distribution cabinet.

The consequences of the remaining correlations are studied in section 4.4.

4.3 Stability of the air-coil system

During long-term neutrino-mass measurements, the applied set values of the air-coil currents will not be altered. However, several effects may influence the stability of individual devices, each with its individual impact on the systematic uncertainty and the effective magnetic field in the analyzing plane. It is reasonable to differentiate between fluctuations and offsets of the absolute magnetic field. When an increase of the total neutrino-mass uncertainty of only 1 % due to magnetic field instabilities is tolerated, an upper limit is found for magnetic field fluctuations of $\sigma_B = 20\,\mu\mathrm{T}$, and for an offset a limit is given by $\Delta B = 2\,\mu\mathrm{T}$ (ref. [Gro15]). Note that those values apply to the analyzing plane. At the positions of the magnetometers outside the spectrometer vessel, the magnetic field uncertainties could increase. Therefore these values should give a fist orientation only, a more detailed discussion of the results of this chapter can be found in chapter 7.

4.3.1 Magnetic field relaxation after magnetic pulse

The generation of a short magnetic pulse is one of the active methods that can be used to reduce background events at the spectrometer. So-called flip boxes were installed in between the PSUs and the air-coil wires, to enable inversion of the direction of the currents generating a magnetic field. During a magnetic pulse the transmission conditions are no longer fulfilled. Any charged particle that is trapped in the volume of the flux tube due to the magnetic-mirror effect will be guided to spectrometer vessel where it is absorbed (ref. [Beh15b], [Beh16]). Considering the magnetic field stability, the only important aspects of a magnetic pulse in this context is the relaxation time, equivalent to the time scale until stable magnetic-field conditions are reached after a magnetic pulse and regular measurements can continue.

During a magnetic pulse the air-coil system can be described as a combination of a resistance and inductance. Based on the known coil geometry, the applied current I and number of turns N, an inductance of

$$L = N/I \cdot \int \vec{B}(r) d\vec{A} \tag{4.6}$$

is calculated with Kassiopeia for a single-layer (double-layer) LFCS-coil of $L_\mathrm{s} = 2.6\,\mathrm{mH}$ ($L_\mathrm{d} = 8.0\,\mathrm{mH}$). The inductance results are inconsistent with measurements presented in

[Sta13], indicating that the actual inductance could be about one order of magnitude larger. Nevertheless, the values as stated above are used for further calculations in this chapter.

Analytically, a current change can be described as

$$I(t) = I_0 \cdot \left(1 - \mathrm{e}^{-(t-t_{\mathrm{pulse}})/\tau}\right), \tag{4.7}$$

where $\tau = L/R$ can be derived from eq. (4.6) and R from a resistances measurement in [Pli10].

The relaxation time $t_{95,\mathrm{i}}$ is defined as the time interval from the current flip until the magnetic field at a magnetometer ring i reaches 95 % of its field value in standard operation mode. This is a reasonable choice as the remaining difference of the absolute magnetic-field value corresponds to $\Delta B \approx 2\,\mu\mathrm{T}$, the upper limit for an offset of the magnetic field with a 3.8 G setting. Based on the air-coil geometry in section 3.1.3, for a single-layer (double-layer) LFCS coil, a time interval of $t_{95,\mathrm{s}} \approx 67\,\mathrm{ms}$ ($t_{95,\mathrm{d}} \approx 120\,\mathrm{ms}$) is expected.

In addition, the value of $t_{95,\mathrm{i}}$ is limited by the maximal power-output of a PSU. As a result, a PSU is either in constant-current operation mode when a current development is described by eq. (4.7), or in constant-voltage operation mode, resulting in a linear current change. Depending on the PSU load, the rise and fall time of the PSUs variate between 7 ms to 58 ms, increasing the relaxation time of the magnetic field accordingly. Furthermore, eddy currents will be induced in an conductive object such as the spectrometer vessel and the superconducting solenoids. Due to the fact that the strength and time development of those eddy current highly depends on the material and geometry of an object, a calculation of the resulting magnetic field is challenging. Therefore the magnetic pulse is studied by means of the high-precision magnetometers only.

To study the relaxation time, a pulse mode was chosen where the coils LFCS 1 to 13 were flipped once for 8 s during a pulse cycle of 25 s. These times are sufficiently long to reach a stable field in both directions. Also, any delay between the pulse trigger signal and the slow control timescale can be accounted for with a high measurement frequency of the precise magnetometers of 5 Hz. Small time delays between magnetometer readouts allow for a time binning of 60 ms by accumulating nearly 5×10^4 pulse cycles[1]. To compare all magnetometer positions and different magnetic-field settings, all field values are normalized. Here, a field value of $B_{\mathrm{norm.}} = 0$ corresponds to a fully flipped and $B_{\mathrm{norm.}} = 1$ to the nominal field direction.

Figure 4.8 shows the relaxation time of the magnetic field for a 3.8 G setting, with the solenoids PS 2, PCH and DET at nominal currents, and PS 1 and all other magnets of the KATRIN setup being turned off. Magnetometer readings on the same sensor ring[2] were combined, and an average absolute field and its standard deviation were calculated, shown by an 1σ uncertainty band. A trigger signal in a DAQ channel of the FPD system indicates a flip of the currents, defining $t_0 = 0.0\,\mathrm{s}$. A delay of the trigger signals of maximal 5 µs was

1 In fact, due to the readout routine a delay of a few ms is expected between individual slow control sensors, even within a common log-group.

2 The precise magnetometers are mounted at three distinct axial positions. On the upstream, middle and downstream position at −4.5 m, −0.14 m and 4.3 m. Details can be found in fig. 3.12.

observed[1].

To analyze the time development of the magnetic-field, the data set was empirically subdivided to two intervals at $t_{\text{cv to cc}} = 610\,\text{ms}$, corresponding to the two operation modes of the PSUs[2]. The time offset between the DAQ and slow-control time stamp fitted here are shown as a vertical line at $t_{\text{start}} = 323\,\text{ms}$. They are derived from a linear fit and in agreement with all magnetometer rings within their uncertainty $\sigma_{t_{\text{start}}} = 8\,\text{ms}$. This indicates that the slow-control log-groups of the magnetometers are synchronized among each other and can be directly compared.

When the PSUs are in constant-current operation, it is observed that

- the time constant τ for all magnetometer rings is much bigger than expected from the calculations above. Even when the time constant τ for a double layer coil is assumed, these values still exceed the theoretical values at least by a factor of 3.
- along the spectrometer axis the time constant τ increases. For the magnetometers at the downstream side, the time constant τ is significantly bigger than for the others.
- the time t_{95} when a 95 %-field is reached variates significantly for all three magnetometer rings. In the center the relaxation time is the smallest and for the downstream position the longest relaxation time is observed. The difference between the center and downstream is about 50 %.

To test a possible dependence of the field trend on the applied LFCS currents, the measurement was repeated with a 5 G-setting (table 4.2). No significant deviation is observed for the t_{95} duration for all three sensor rings and only a slight increase of the time constant τ. The fit results of both measurements are in agreement with the 3σ-uncertainties.

Table 4.2: τ_{i} is the exponential relaxation of the precise magnetometers for the individual downstream-, middle, upstream sensor rings. The time $t_{95,\text{i}}$ corresponds to the time when 95 % of the nominal field value relative to t_{start} is reached. The offset between the DAQ signal and the magnetic pulse is t_{start}. Fit results of magnetic pulse relaxation in fig. 4.8 (measurement with a 5 G setting in fig. A.4).

	3.8 G setting	**5.0 G setting**
τ_{U}	$(405 \pm 2)\,\text{ms}$	$(411 \pm 4)\,\text{ms}$
τ_{M}	$(413 \pm 2)\,\text{ms}$	$(421 \pm 3)\,\text{ms}$
τ_{D}	$(471 \pm 2)\,\text{ms}$	$(472 \pm 3)\,\text{ms}$
$t_{95,\text{U}}$	$(1.217 \pm 0.009)\,\text{s}$	$(1.219 \pm 0.021)\,\text{s}$
$t_{95,\text{M}}$	$(1.075 \pm 0.008)\,\text{s}$	$(1.077 \pm 0.009)\,\text{s}$
$t_{95,\text{D}}$	$(1.507 \pm 0.011)\,\text{s}$	$(1.512 \pm 0.016)\,\text{s}$
t_{start}	$(323 \pm 6)\,\text{ms}$	$(300 \pm 7)\,\text{ms}$

1 Based on measurements that combined a magnetic pulse with the e-gun, a small trigger-signal delay was verified (ref.[Beh16]).

2 Please note this is only a approximation of the transition state leading to inconstancy when actually a superposition of linear and exponential current change of the individual PSUs is observed.

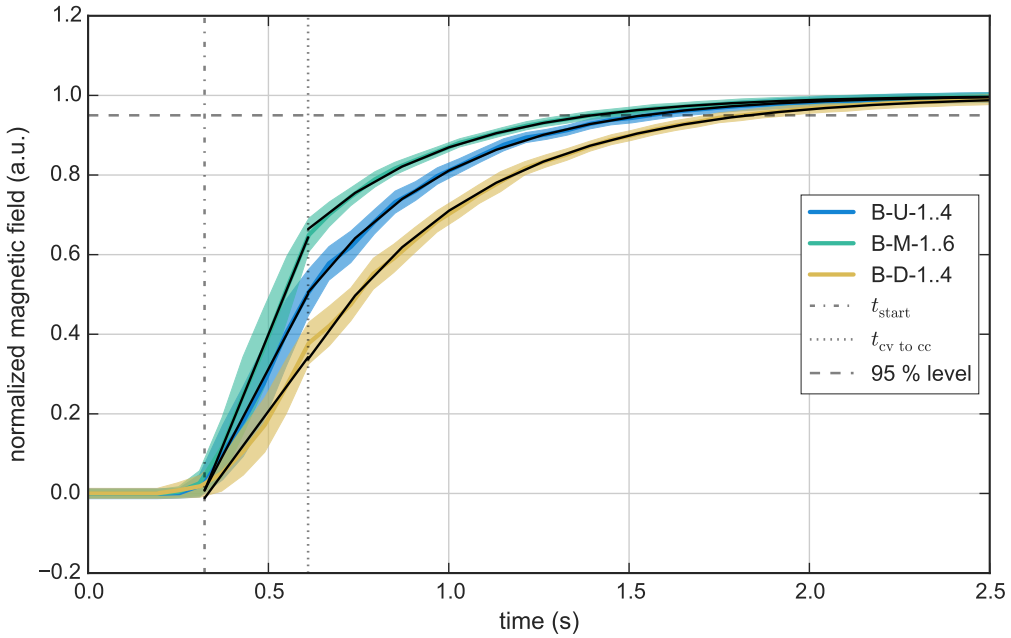

Figure 4.8: Relaxation after application of a magnetic pulse of the LFCS air-coils 1-13 at a 3.8 G setting, as measured with the precision magnetometers. Magnetometer readings on a common ring are combined, the resulting mean values are shown with a 1σ uncertainty. The magnetic field is normalized, where 0.0 corresponds to a reversed and 1.0 the nominal field value. Fits of the relaxation time scales are shown with black lines, divided in two intervals. At first between t_{start} and $t_{\mathrm{cv\ to\ cc}} = 0.6\,\mathrm{s}$ a linear, and after that an exponential function is used (see text). A horizontal line marks the 95.0 % level. Fit results are shown in table 4.2.

This suggests a strong influence of eddy currents, mainly in the spectrometer vessel. The permeability of the vessel is constant along the spectrometer axis, but the geometry does change considerably. Especially the three large pump ports on the downstream side represent a clear disturbance of the axial symmetry of the spectrometer. This fact can explain the observed upstream-downstream increase of the time constant τ.

Given that the smallest relaxation time occurred in the spectrometer center, the solenoids on both sides can be identified as a source of eddy currents. Here, the copper housing of the superconducting wires are of key interest as they are a part of the quench protection of the solenoids. At a temperature of $\approx 4\,\mathrm{K}$ the electrical resistivity of copper is about four orders of magnitude smaller than the values given for stainless steel at ambient temperature[1] (ref. [Haa34]). As a result the induced eddy currents are reduced much slower than in the spectrometer vessel and the resulting magnetic-field is detected at the outer rings. During the measurements the PS 2 unit and the two superconducting solenoids PCH and DET were

1 The electrical resistivity strongly depends on the purity of the material. Nevertheless, a large difference between copper and stainless steel is expected.

evidently operated at nominal 4 K. This asymmetry in the number of cold solenoids could also lead to a longer relaxation time on the downstream side.

For further studies of eddy currents, more varied measurements with different magnetic-field settings and magnetic pulse modii are recommended. Thereby the PSU characteristics can be disentangled from the eddy current development. To verify the influence of the copper housing of the solenoids, measurements with cold and warm solenoid cryostats are required.

4.3.2 Long-term stability and precision of the air-coil system

The current output of the air-coil system has to be stable and reproducible, as any current fluctuations of the power-supplies of the air-coil system will translate to a fluctuation of the generated magnetic field. Although the magnetic-field setting that will be used for a neutrino-mass measurement campaign may differ from the settings used during SDS 2, the standard magnetic-field settings (table A.1) utilize the full current range of the present PSUs. Therefore predictions with respect to the precision of the generated magnetic field for settings with coil currents up to 100 A can be drawn.

Furthermore, as the overall duration of the SDS 2 measurement phase exceeds the expected tritium-measurement phase[1] by about a factor of 2, it is well suited to detect any relevant long-term drift of the air-coil PSUs. As long as such a drift is detected, it can easily be implemented into the analysis chain and thus does not impair the sensitivity to measure the neutrino mass. However, the long-term stability of the generated magnetic field must be known to interpret any drift detected by the magnetometers (section 5.2).

With a total run time of several days each, the three most common field settings (3.8 G, 5 G and 9 G-setting, see section 4.1.2) can be utilized to analyze the PSUs with respect to their long-term stability as well as to the current precision. To evaluate these air-coil PSU properties, only those runs were included in the analysis if being performed under stable magnetic field conditions (section 4.2.1).

The observed behaviors of all PSUs for different field settings are comparable and follow the characteristics described with the PSUs of the LFCS 7 and LFCS 8 coils during the 3.8 G setting.

Figure 4.9 shows the long-term development of the PSUs of LFCS 7 and LFCS 8. The full data set of the current readout values is split into 1 h periods, where the mean value and the standard deviation was calculated. PSU drifts are described by a linear function. The observed slopes are in agreement with a vanishing drift within a 1σ uncertainty. However, this can not be interpreted as a perfect reproducibility of the applied currents, in fact the LFCS 8 PSU features two distinct current values. These two current values are an artifact of the limited precision of the slow-control DAC card of the current set-point[2] (section 3.2.2). The drift behavior of all individual PSUs operated with an 3.8 G-setting is shown in fig. A.1.

To determine the current fluctuation of the ensemble of PSUs, all current read-out values

1 A neutrino-mass measurement campaign will be separated in tritium measurement and maintenance phases. The length of a a single tritium-measurement period is estimated to be defined by the argon-frost regeneration cycle of the CPS of 60 d or more (ref. [KAT05] [Jan15]).

2 During the SDS 2 campaign all current set-values were applied with 12 bit precision. It is planed to upgrade the analog output to 16 bit precision. Also a proportional-integral-derivative (PID) regulation will be tested to minimize the linearity divergence of the set-value (section 4.2.1).

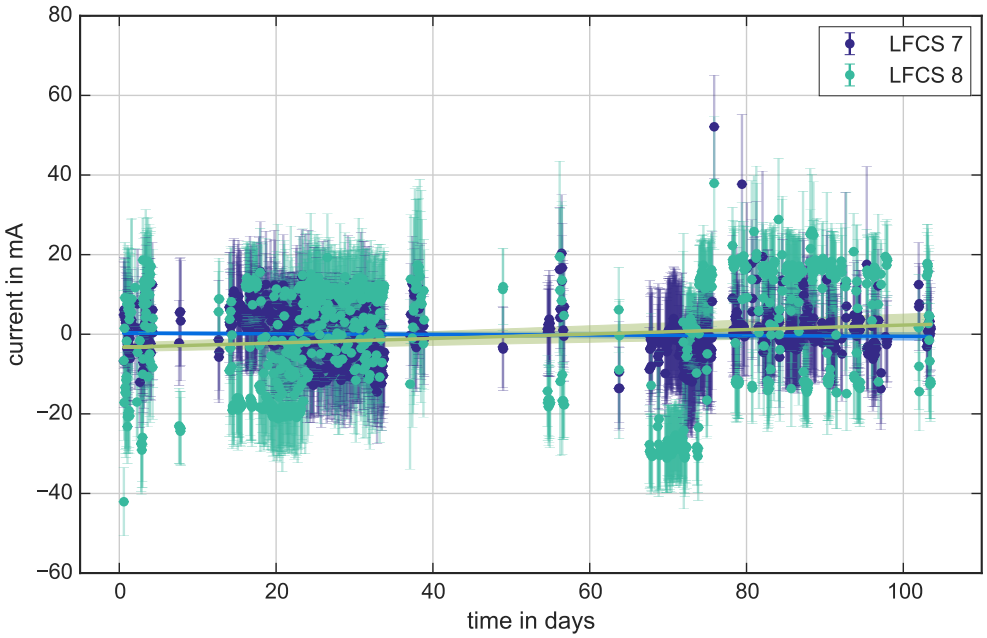

Figure 4.9: Long-term trend of the air-coil PSUs of LFCS 7 and LFCS 8 with the 3.8 G setting during SDS 2. Both data sets were split into 1 h periods and plotted relative to the mean value. The drift of LFCS 7 (LFCS 8) is identified with the slope of a linear fit of (-0.0078 ± 0.0059) mA/day ((0.056 ± 0.017) mA/day). Both drifts are negligible within a 3σ uncertainty.

were combined in one analysis. The normalized current-distributions are shown in figure 4.10, with the mean shifted to $\mu = 0\,\text{mA}$. For the PSU of LFCS 7 the distribution can be described by a Gaussian width of $\sigma_I = 16\,\text{mA}$.

However, LFCS 8 has a rather complicated structure which can be approximated by two Gaussian distributions centered at $\mu_1 = -20\,\text{mA}$ ($\mu_2 = 13\,\text{mA}$) with $\sigma_{I_1} = 9\,\text{mA}$ ($\sigma_{I_2} = 13\,\text{mA}$). This behavior is associated with the above mentioned accuracy of current set-values and temperature coefficients of the used electronics. If a new set-value is applied to the system at the beginning of a run, a shift of 0.07 % relative to its mean value can be observed. Therefore this issue is not only tiny, but it can be easily avoided as well and is of no major concern.

Nevertheless, when this distribution is fitted only with one Gaussian, it yields $\sigma_I = 24\,\text{mA}$, which is still within the specification of $\sigma_I = 25\,\text{mA}$. Albeit this double Gaussian shape was also detected for the PSU of LFCS 5 and LFCS 10, all PSUs of the air-coil system work within their specifications with an average fluctuation of $\sigma_I = 14\,\text{mA}$. The results of all PSUs and field settings can be found in table A.2.

4.4 Simulation of realistic air-coil currents on the magnetic field

An evaluation of the influence of the air-coil system on the magnetic field inside the main spectrometer is to be made by simulations. In these simulations three important air-coil

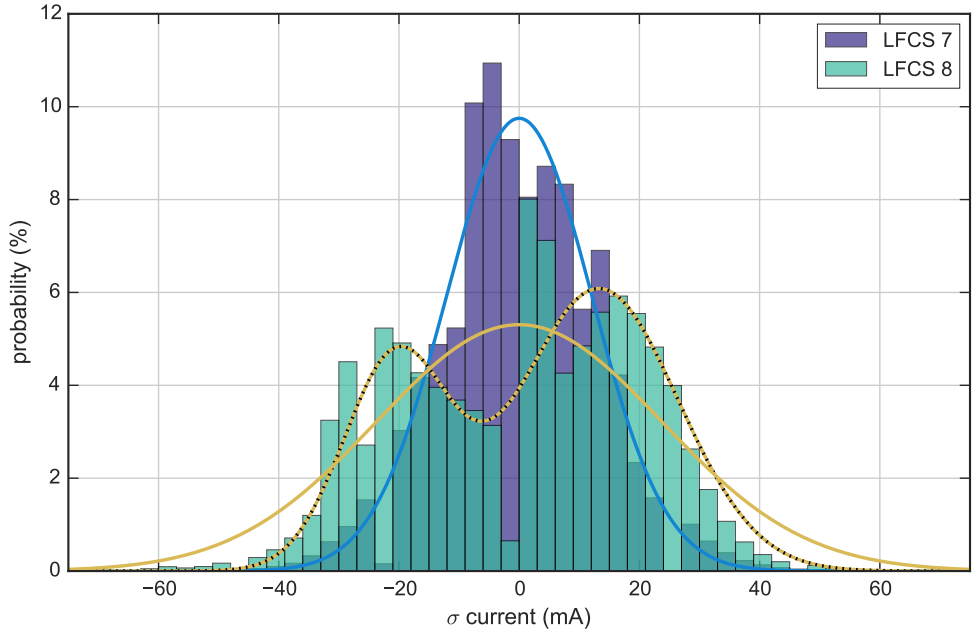

Figure 4.10: Fluctuations of the air-coil currents with an applied 3.8 G-setting. Utilizing all measurements under stable conditions, the normalized current fluctuations of two PSUs relative to their mean values is shown. LFCS 7 (LFCS 8) can be described by a Gaussian with $\sigma_I = 16\,\mathrm{mA}$ ($\sigma_I = 24\,\mathrm{mA}$). Additionally LFCS 8 is fitted with two Gaussians $\sigma_{I_1} = 9\,\mathrm{mA}$ and $\sigma I_2 = 13\,\mathrm{mA}$ (dotted line). Such a double peak structure is the result of the limited precision of the current set points. However, this slow control artifact is no serious issue, as both PSUs operate within their specifications.

properties are included:

1. the calibration of the air-coil system. In section 4.2.1 a minor deviation from the ideal linearity of the current output in the low mA/A regime and a current offset of a few hundred mA was observed.
2. the fluctuation of the current output of the individual PSUs. Based on fig. 4.10, a normal distribution was assumed for the individual fluctuations. (See also fig. A.2).
3. the correlation of the current-output between the PSUs. A longtime analysis of the PSU current output revealed a minor correlation between the devices operated on a common DAC card. The PSUs are thereby split in a upstream and a downstream group.

In the magnetic-field model for this simulation the LFCS, the four SDS solenoids and the EMCS together with the earth magnetic-field are included. The LFCS system is fully discretized, comprising the effect of the mechanical LFCS-deformation and coil position-offsets (fig. 3.5), also the realistic EMCS model is utilized (fig. 3.6). The SDS solenoids (PS 1, PS 2, PCH and DET) are operated with nominal currents (table 3.2) and the correct

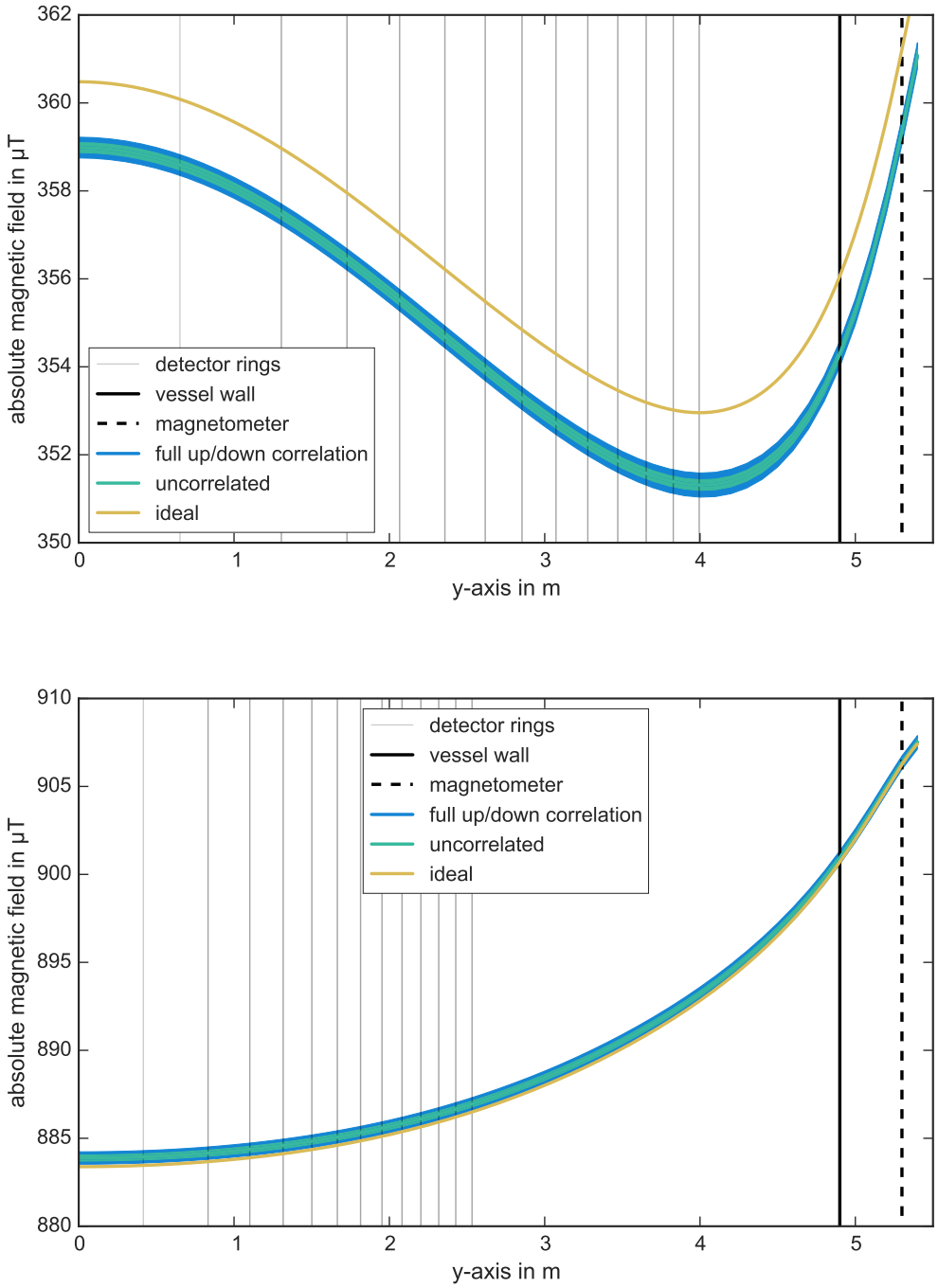

Figure 4.11: Effect of the PSU fluctuations on the magnetic field for the 3.8 G- (upper plot) and 9.0 G-setting (lower plot). Gaussian distribution were assumed for the uncertainties of the power-supply currents. The resulting magnetic field fluctuation is shown for fully uncorrelated fluctuations of the PSUs and a full correlation between the first eight and last eight PSUs respectively (fig. 4.7). Both simulated fluctuations are approximately constant over the active flux tube volume and shown as a 3σ-uncertainty band. The 3σ uncertainties for the 3.8 G- (9.0 G-)setting are 0.14 µT and 0.3 µT (0.18 µT and 0.36 µT) in the uncorrelated and correlated case.

alignment-parameters are used (section 3.4).

In total four simulations were performed (fig. 4.11) with

- the 3.8 G(d) and the 9.0 G(d)-setting to study the influence of the PSU linearity.
- the the current-output of the PSUs fluctuate individually (labeled uncorrelated) or the two power-supplies groups are fully correlated (full up/down correlation).

The magnetic field is simulated radially along the vertical axis in the analyzing plane ($z = 0\,\mathrm{m}$) from $y = 0\,\mathrm{m}$ to $y = 5.4\,\mathrm{m}$ in 0.1 m steps. For every radial position an ensemble test of 100 000 iterations is performed. The resulting fluctuations are shown as an error band of 3σ in comparison to the magnetic-field with the previously calculated currents (section 4.1) for an optimized air coil operation (labeled ideal).

For both magnetic-field settings a constant offset to the ideal currents is observed, but no significant change of the overall shape. In case of the 3.8 G-setting (9.0 G-setting) the magnetic field is reduced in the center by 1.5 µT (0.5 µT). By implementing the air-coil calibration in the slow-control routine of KATRIN, the observed offsets can fully compensated. The current-output of the PSUs is used as an input to simulate the magnetic field in the analyses in the next chapters.

The fluctuations of the air-coil currents result in constant magnetic-field fluctuations along the radius and their absolute value is comparable in both settings. Merely the correlation of power-supply current-output increases the fluctuations. Compared to uncorrelated currents, an increase of the fluctuation by a factor 2 is observed for a full up/down correlation. However, in all cases the observed relative fluctuations are small and do not exceed 0.085 % with a maximal fluctuation of the absolute field of 0.36 µT.

4.5 Conclusion

Two approaches are possible with the KATRIN setup to generate an optimized MAC-E filter configuration. Both of them meet the KATRIN electromagnetic-design requirements and were successfully introduced for the SDS 2 measurements (section 4.1).

To ensure operation readiness for a neutrino-mass measurement campaign, several tests were performed concerning the basic functionality and the systematic uncertainties of the air-coil system. One of the basic demands for the air-coil system is a reliable current adjustment that has been demonstrated in section 4.2.1 and section 4.2.2. Only during phases acting as stress tests, when most extreme conditions occur, minor instabilities became detectable and revealed possibilities for hard- and software upgrades to improve the air-coil system even further (section 4.2.3). An improved regulation of the PSUs is currently under way to minimize the current offset, to enable an automated calibration and reduce correlations of the currents. In standard operation, no short-term or long-term drift behavior of the air-coil system was detected and magnetic field settings were applied in a reliable, stable and reproducible manner over the course of SDS 2 phase (4.3). Fluctuations occured only on the level of a few mA and an offset of about 200 mA was observed. These result in a maximal magnetic-field offset of 1.5 µT and a maximal fluctuation of 0.36 µT. Both effects are well within the limits of the KATRIN requirements.

In conclusion, it has been shown that the air-coil system is ready for long-term neutrino-mass measurements.

CHAPTER 5

Monitoring of the magnetic field at the main spectrometer

During a regular neutrino-mass measurement, information about the magnetic field inside the spectrometer vessel is provided by the read-outs of the air-coil PSUs and the magnetometer sensors only. The condition of the magnetic flux-tube is relevant for the transport of signal electrons and influences several background processes that can only be accessed by simulations. To avoid an increase of the systematic uncertainty of a neutrino-mass measurement by an unrecognized offset or fluctuation of the magnetic field, a precise monitoring-system is essential. Therefore a sophisticated magnetic-field model was developed and incorporated in the monitoring software (section 3.3.3). Components which generate a magnetic-field and their contribution to the effective field are outlined in section 5.1.

When combining the results of the evaluation of the magnetic-field model and the stability analysis of the air-coil system, an analysis of the magnetic field at the main spectrometer over extended periods of time can be made (section 5.2). As a variety of different magnetic-field settings were used over a measurement period of more than 100 days, the SDS 2 campaign gives the unique opportunity to set upper limits on the magnetic-field uncertainties.

The accuracy of the magnetic-field monitoring depends on the alignment precision of the magnetometers and the completeness of the magnetic-field model. In this context, the influence of ferromagnetic materials is expected to be the dominant contribution to the magnetic background field which has not yet been included in the magnetic-field model in a parameterized form. At the KATRIN setup, these materials predominantly come in the form of steel rods in the concrete of the KATRIN buildings. In section 5.3 the remanent component is estimated and the induced magnetic-field is discussed.

In preparation of the SDS 2 campaign a large-scale demagnetization of the steel rods in the concrete walls of the spectrometer hall was performed. It is expected to reduce the remanent magnetic-field and to improve the axial and azimuthal magnetic background field. The MobSU system allows to increase the number of measurement points, thus enabling an evaluation of the symmetry of the magnetic field at the main spectrometer (ref. [Rei13], [Osi12b]). Although the MobSU system is still in a development stage, various test measurements were performed during SDS 2 (section 5.4).

In summary, this chapter investigates the accuracy of the magnetic-field monitoring and points out deviations between measurement and simulation. Based on these results, criteria for an assessment of the magnetic-field quality are developed.

5.1 Evaluation of the magnetic-field model

There are two fundamentally different approaches to determine the magnetic-field within the main-spectrometer volume. One is to solve the Laplace equation

$$\nabla^2 \cdot V\,(x,y,z) = 0 \tag{5.1}$$

where $V(x,y,z,)$ can be identified with the scalar potential in a current-free volume and the relation

$$\vec{B} = \nabla \cdot V\,(\vec{x}) \tag{5.2}$$

is fulfilled. The magnetic-field measured at various points is used in Neumann boundary conditions to solve eq. (5.1) for the magnetic-field components $\partial V/\partial x = B_x$, $\partial V/\partial y = B_y$ and $\partial V/\partial z = B_z$ (ref. [Osi12a]).

To determine a magnetic field distribution within the KATRIN main spectrometer volume by means of measurements, a large number of 7200 measurement points values is required for an accuracy better than 2 % (ref. [Osi12a]). With 48 permanently installed magnetometers on the vessel surface (section 3.3.1), the amount of sensors is far too small to generate a magnetic-field model, even taking into account the full MobSU system.

On the other hand, simulations of the magnetic-field are straightforward and fast to calculate, but they can not reveal unforeseen behavior of the magnetic systems.

The KATRIN strategy to evaluate the magnetic-field is to calculate the field both outside and inside the main-spectrometer vessel and to compare this simulation with data from the magnetic field monitoring system. Therefore, a simulation model has been developed that incorporates the magnetic-field generating components as comprehensive as possible. Based on a precise knowledge of the geometry and the applied currents of the magnet system and a calibrated magnetic-field monitoring system, for a total magnetic-field

$$\vec{B}_{\mathrm{tot}} = \vec{B}_{\mathrm{model}} + \vec{B}_{\mathrm{other}} \tag{5.3}$$

it can be ensured that the relation

$$\|\vec{B}_{\mathrm{model}}\| \gg \|\vec{B}_{\mathrm{other}}\| \tag{5.4}$$

is fulfilled under all circumstances and at any position within the main spectrometer volume.

Besides the fields of the superconducting solenoids and the air-coil system during SDS 2

$$\vec{B}_{\mathrm{SDS}} = \vec{B}_{\mathrm{PS1}} + \vec{B}_{\mathrm{PS2}} + \vec{B}_{\mathrm{PCH}} + \vec{B}_{\mathrm{DET}} + \vec{B}_{\mathrm{LFCS}} + \vec{B}_{\mathrm{EMCS}} \tag{5.5}$$

the earth magnetic-field $\vec{B}_{\mathrm{earth}}$, as well as the following sources are assessed within this thesis with respect to their influence on the magnetic field at the main spectrometer:

- DPS magnet system. In the beginning of 2015, a series of tests concerning the ramping, stability and quenching performance of the DPS superconducting magnets were performed. The stray field of all DPS magnets on full field is at the position of the analyzing plane of the order of the earth magnetic field, decreasing along the beam axis from upstream to downstream. The magnetic field $\vec{B}_{\mathrm{DPS}}$ on axis at $r = 0\,\mathrm{m}$ and at

Table 5.1: Contribution of individual magnetic components to the total magnetic field at the position $z = 0\,\mathrm{m}$ of the analyzing plane. The inner magnetic field values correspond to a radius of $r = 0\,\mathrm{m}$ and the outer magnetic-field to $r = 4.5\,\mathrm{m} \mathrel{\widehat{=}} x = -4.5\,\mathrm{m}$. At both positions the absolute $\|\vec{B}(r_i)\|$ and axial component $\vec{B}_\mathrm{z}(r_i)$ are given. Absolute field values below 10 nT are set to zero. Here the nominal SDS 2 currents were used for the SDS solenoids and the EMCS and a 3.8 G setting for the LFCS. For the magnetic materials only the remanent component is considered in calculations by ref. [Rei13] and [Lei14] based on a model prior to the hall demagnetization. The influence of the auxiliary devices is extrapolated based on measurement results for a scroll pump (ref. [Bar14]).

component	inner magnetic field (µT)		outer magnetic field (µT)	
	abs.	axial	abs.	axial
LFCS	226.66	−226.66	266.12	−265.79
PCH	54.13	−54.13	42.62	−36.63
earth	48.03	20.02	48.03	20.02
PS 2	46.79	−46.79	36.69	−31.42
EMCS	43.47	0.0	43.43	0.0
DET	40.11	−40.11	33.18	−29.47
DPS	17.91	−17.91	16.99	−16.46
PS 1	12.84	−12.84	11.19	−10.28
rem. mag. field	0.62	−0.5	1.87	−1.58
MoS	0.33	−0.30	0.64	−0.54
aux. devices	0.0	0.0	0.18	−0.13

the z positions of the precise magnetometers is calculated to be 26.0 µT, 16.0 µT and 10.5 µT. Due to the off-beamline-axis orientation of the transport section also a small azimuthal magnetic-field variation is introduced. For the magnetometers closest to the analyzing plane, a resulting variation of about $\Delta B = 0.3\,\mu\mathrm{T}$ is expected. This value is based on the realistic geometry of the DPS (ref. [Com15], [Sac15]). The corresponding stray field $\vec{B}_\mathrm{DPS}$ of the DPS is thus included in the model of the magnetic field of the main spectrometer.

- The monitor-spectrometer magnet-system is centered around the position of the monitor spectrometer analyzing plane at (x,y,z) = (−22.42,−2.4,−3.52) m anti-parallel to the main spectrometer. Calculations of the stray field $\vec{B}_\mathrm{MoS}$ of the two 6 T-solenoids of the monitor spectrometer at the main spectrometer magnetometer positions yield a field offsets in the range of 0.18 µT to 0.65 µT. During the SDS 1 phase it was verified that the stray field of these magnets penetrates into the main-spectrometer building and thus is not shielded by the steel rods in the concrete of the building (ref. [Bar14]). A stray field of the monitor spectrometer is included in the model of the magnetic field of the main spectrometer.
- The ferromagnetism of the reinforced concrete of the walls and the outer parts of the foundation of the main spectrometer hall normal steel-rods is of particular importance. A

key issue here is the fact, that they not only introduce a remanent magnetic-background field $\vec{B}_{\text{rem}}$ (ref. [Her10]), but that they are the dominant contribution to the non-axially-symmetric field components. Additionally, an induced magnetic fields $\vec{B}_{\text{ind}}$ has been identified at various positions in the main-spectrometer hall (ref. [Erh14c]). For a 3.8 G-setting the magnitude of B_{ind} is of the same order as B_{rem} (ref. [Ada15]).

The industrial demagnetization of the main-spectrometer structural materials prior to the SDS 2 campaign has reduced the effect significantly and a more homogeneous magnetic background field has been achieved ([Wol14],[Ada14]). However, the model developed in [Rei13] to describe the remanent magnetic-field is thereby obsolete after the demagnetization. Therefore, the order of magnitude of the remanent and induced magnetic field has been re-estimated in this chapter.

- Throughout the commissioning phases several auxiliary devices were introduced at the main-spectrometer setup such as an additional scroll pump (ref. [Bar14]) as well as the µ-metal shieldings of the photo multipliers of the muon detection system (see [Rov13]). These either generate a magnetic-field $\vec{B}_{\text{aux}}$ or contain magnetic materials that cause strong local distortions of the magnetic field. These local disturbances can partly be detected by the stationary installed sensor units. It should be emphasized however, that a significant disturbance of the magnetic field in the active volume of the magnetic flux in the spectrometer can be excluded (ref. [Bar14]).

The relevant magnetic-field model for the SDS 2 setup consists of

$$\vec{B}_{\text{model}} = \vec{B}_{\text{SDS}} + \vec{B}_{\text{earth}} + \vec{B}_{\text{DPS}} + \vec{B}_{\text{MoS}} \tag{5.6}$$

together with the novel field sources not previously represented in the model. The latter are split into three components

$$\vec{B}_{\text{other}} = \vec{B}_{\text{rem}} + \vec{B}_{\text{ind}} + \vec{B}_{\text{aux}}. \tag{5.7}$$

A summary of various magnetic-field sources and their specific stray field at the analyzing plane can be found in table 5.1, where all major contributions to the magnetic-field model are listed. The remanent field of the magnetic materials, that currently is not included in the field model, features a magnetic field of only a faction (0.7 %) of the LFCS field. These values are reduced even further after the demagnetization of the main spectrometer hall. It is thus expected that eq. (5.4) is fulfilled, even though the induced magnetic-fields are neglected.

The purpose of the following analyses is to disentangle the contribution of the individual components to the overall field, to study the influence of their specific field layout and to evaluate if the accuracy of the present magnetometers system is sufficient to serve as a long-term monitoring system. Thereby it is possible to estimate the impact of the fields $\vec{B}_{\text{rem}}$ and $\vec{B}_{\text{ind}}$, and to investigate if additional components $\vec{B}_{\text{add}}$ must be included.

In the following sections a field deviation is defined as the difference $\vec{B}_{\text{dev}} = \vec{B}_{\text{exp}} - \vec{B}_{\text{sim}}$ of a measured and a simulated field. The calculations are based on an axially-symmetric model if not outlined otherwise. In most cases only the z-component of the magnetic field is considered since the alignment uncertainty of the magnetometers is the smallest along the z-axis and it is the dominant contribution to an effective field in the analyzing plane.

5.1.1 Influence of the monitor spectrometer magnets

The monitor spectrometer is anti-placed parallel to the main spectrometer at a central position of $\vec{r}_{\mathrm{mos}} = (-22.42, -2.4, -3.52)^{\mathrm{T}}\,\mathrm{m}$ (fig. 5.1). Its magnetic field is dominated by two superconducting magnets, located at the local coordinates $z' = \pm 2.1\,\mathrm{m}$, with $B_{\mathrm{sol}} = 6\,\mathrm{T}$ in the bore holes (further information in section 2.2.5). This configuration can lead to an azimuthal distortion of the magnetic-field in the analyzing plane of the main spectrometer. With an effective field in the sub-µT, it is the smallest contribution to field in the analyzing plane, and so the analysis of the MoS stray field can be interpreted as a precision test of the monitoring system and magnetic-field model.

When a stable 3.8 G-setting was applied to the air-coil system, a time period of 6 days (before and after the monitor spectrometers started to operate) is selected to calculate a mean variation of the absolute field for the two configurations $\vec{B}_{\mathrm{mos,on}}$ and $\vec{B}_{\mathrm{mos,off}}$. The monitor spectrometer stray field is then obtained by

$$\vec{B}_{\mathrm{mos}} = \vec{B}_{\mathrm{mos,on}} - \vec{B}_{\mathrm{mos,off}}. \tag{5.8}$$

The uncertainty of a magnetometer reading is the quadratic sum of the standard deviations of $B_{\mathrm{mos,on}}$ and $B_{\mathrm{mos,off}}$. The resulting field is shown in the upper plot of fig. 5.2 for the central magnetometers as a function of their distance to the monitor spectrometer center. Clearly an increase of the field is observed towards the monitor spectrometer.

The magnetic moment of the monitor spectrometer can be approximated by $\vec{m} = N \cdot I \cdot \vec{A}$, where N is the sum of the winding number of both MoS solenoids, I is the operation current

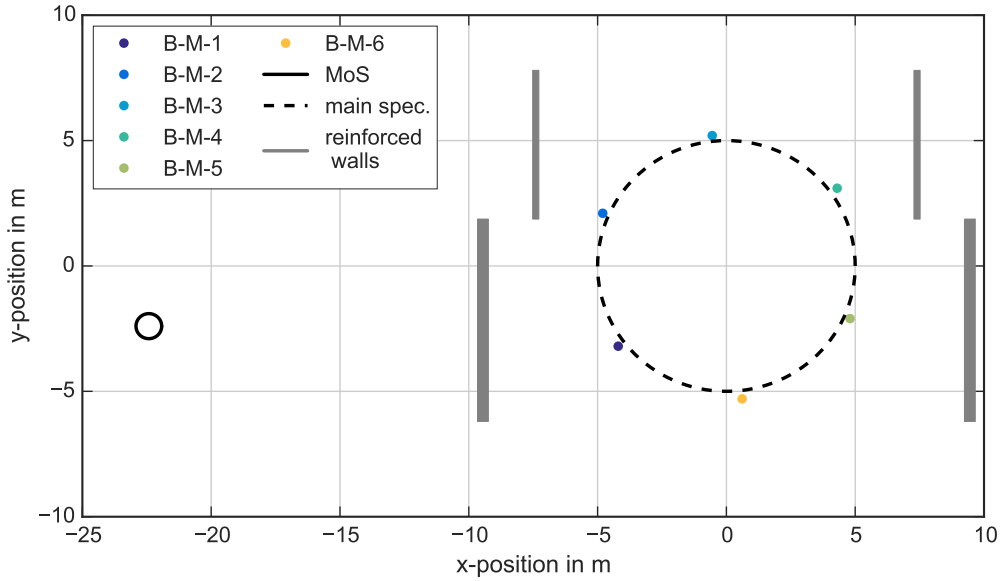

Figure 5.1: Position of the MoS magnet-system (black line) relative to the main-spectrometer vessel (black dashed line) and the central high-precision magnetometers, here shown in the x-y plane at $z = 0\,\mathrm{m}$. The grey lines represent the reinforced concrete walls of the building.

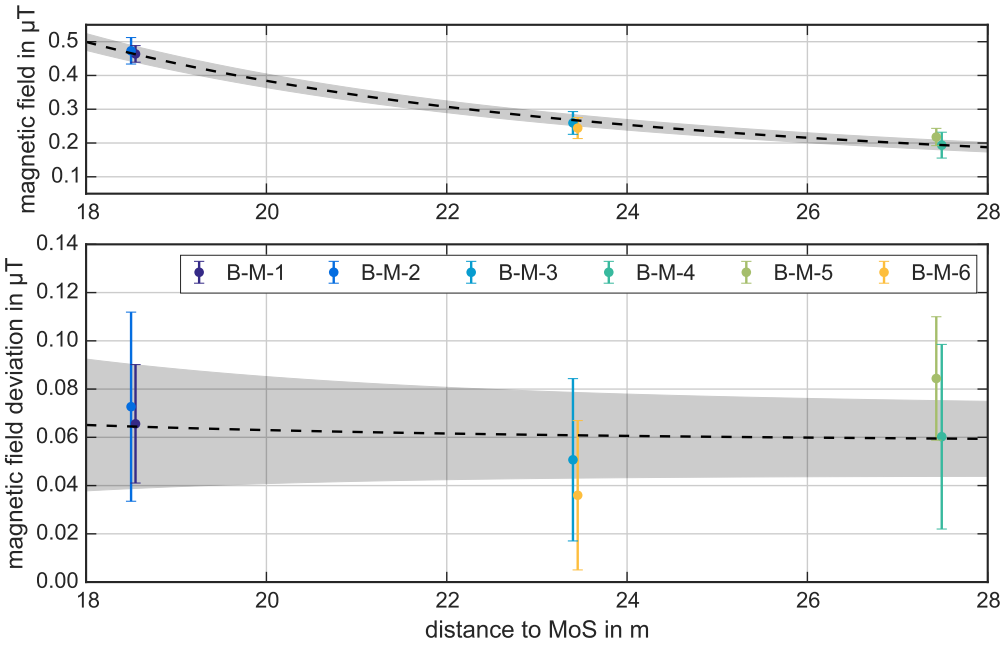

Figure 5.2: Stray field of the MoS magnet-system eq. (5.8) at the analyzing plane and its deviation relative to a calculation $\vec{B}_{\mathrm{dev}} = \vec{B}_{\mathrm{exp}} - \vec{B}_{\mathrm{sim}}$. In the upper plot a time period when the MoS magnet system was operated is used to extract $\vec{B}_{\mathrm{mos}}$. The magnetic field features an r^{-3} dependence as given in eq. (5.9). When the calculated values are subtracted, the r^{-3} dependence is reduced by a factor 98.2 %, showing this to be the dominant contribution.

and $\vec{A}$ the surface area. At a distance r to the main-spectrometer, the stray field is thus

$$\vec{B}_{\mathrm{mos}} = \alpha \frac{\mu_0 \cdot \vec{m}}{4\pi} \cdot \frac{1}{(r - r_0)^3}, \tag{5.9}$$

i.e. the field perpendicular to the magnetization $\vec{m}$ of dipole. A scaling factor α and a position offset r_0 are introduced to account for a minor shielding effect of the magnetic materials in the reinforced concrete of both spectrometer buildings as well as a geometry correction for positioning imperfections. Here eq. (5.9) is used to quantify the accuracy of the field model.

When the magnetic-field of the monitor-spectrometer, simulation with Kassiopeia, is subtracted from $\vec{B}_{\mathrm{mos,on}}$ in eq. (5.8), the r^{-3}-dependence is decreased by a factor of (98.2 ± 0.7) % (fig. 5.2, lower plot). In addition, a homogeneous systematic offset of 57 nT is observed. If the offset would be purely due to a shielding effect of the magnetic materials, a negative offset is expected. The positive sign of the offset indicates a shift of the MoS to an actual position which is (0.89 ± 0.10) m closer to the main spectrometer. This is in agreement with the rough position estimation with an accuracy of ± 0.5 m per axis, based on construction overview-drawings. However, the observed offset is well within the uncertainty budget and thus the magnetic-field of the monitor spectrometer is reproduced with the field model with the shielding of the ferromagnetic materials of the building being marginal.

5.1.2 Influence of the DPS magnets

The stand-alone superconducting magnets of the DPS were the first magnets of the transport section to be installed in the KATRIN beam line. Due to their rather distant positions far away from the analyzing plane, a typical small misalignment only has a minute influence on the magnetic field at the main spectrometer compared to the solenoids of the SDS magnet system. Additionally, the positioning of the DPS magnets was carefully executed by the DPS team and its geometry properties were thoroughly tested. Therefore, the DPS magnets are one of the most accurately parameterized components in the field model.

However, as ferromagnetic steel-rods are used in the reinforced concrete supporting the DPS magnets the field of several Tesla generated in such an environment will cause a magnetization of the steel rods of the order of a few µT (ref. [Ada15]). This fact makes the DPS magnet system an ideal showcase to study variations of the remanent field $\vec{B}_{\text{rem}}$ and the magnitude of an induced magnetic-field $\vec{B}_{\text{ind}}$ at the main-spectrometer.

On March 19th 2015, a stable 3.8 G setting was applied to the main spectrometer[1], while the magnet on position 3 of the DPS (located at $z = -27.24\,\text{m}$) was tested by ramping from 0.0 T to 5.5 T. After a period of 1.2 h on full field DPS-M3 was ramped down and turned off again. The high-precision magnetometers on a common sensor ring were used to observe this ramping process. To do so, they were combined to an average value over a 10 min interval. The data are normalized to the field value prior to the magnet test and are displayed with a 1σ-uncertainty band (fig. 5.3, upper plot). A change of the magnetic field is observed by all three sensor rings while the expected decreasing DPS stray field in downstream direction is clearly observed.

At present, the currents applied to a DPS magnet are not logged. For the calculation of the stray field, the applied current was approximated based on a field measurement close to the DPS magnet 3. The current uncertainty is estimated to 0.16 A (0.2 %) when a stable magnetic-field configuration is reached. However, a 4 % lower field reading is observed for all three magnetometer positions when magnet 3 is operated at a 5.5 T-magnetic field (fig. 5.3, lower plot). This effect is associated with the induced magnetic-field $\vec{B}_{\text{ind}}$ due to the sign of the magnetic-field deviation[2].

In addition, a change of the magnetic background field is detected when the magnet was turned off again. Since this was the first ramp test of this magnet, the observed offset corresponds to a first magnetization of the steel rods in the reinforced concrete. For the three positions this change accounts to $-0.06\,\mu\text{T}$, $-0.01\,\mu\text{T}$ and $0.1\,\mu\text{T}$. With a measurement uncertainty of $0.2\,\mu\text{T}$ a significant magnetic background variation is only observed for the upstream sensors.

However, a similar behavior was identified also for other DPS-magnet tests. Consequently, a significant field variation is possible in the analyzing plane when more magnets are operated or can develop over time. Further tests and an estimate of the influences on $\vec{B}_{\text{rem}}$ can be found in section 5.3.

1 PS 1 was turned off during that run and currents of the air-coil setting are adjusted to fulfill transmission conditions.

2 The direction of the magnetic-field generated by a DPS magnet inside its borehole is anti-parallel to the corresponding field in the surrounding concrete. An induced field in ferromagnetic materials therefore is anti-parallel to the magnetic field orientation of the DPS so that the effective field is reduced.

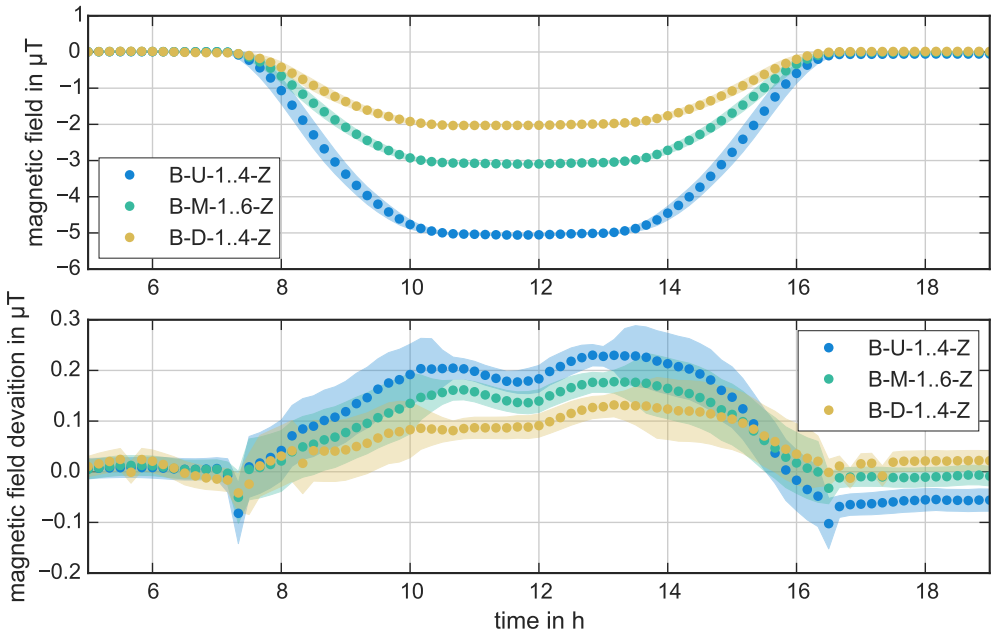

Figure 5.3: Stray-field z-component of the DPS magnet 3 at the main spectrometer. During the time interval displayed magnet 3 was ramped to full field (5.5 T in its bore hole). In the upper plot, the field as measured by the high-precision magnetometer rings is shown, the lower plot gives its deviation to the corresponding simulation $\vec{B}_{\mathrm{dev}} = \vec{B}_{\mathrm{exp}} - \vec{B}_{\mathrm{sim}}$.

The investigations detailed in this section comprise the DPS, in particular the DPS-M3, of a total of 19 superconducting solenoids in the source and transport section. Correspondingly, the commissioning of the remaining components of the KATRIN beam-line (WGTS and in particular the CPS) will result in a substantial change of the magnetic environment that inhibits a concluding assessment of the field influence of the source and transport section at this point. This issue has to be investigated later when all superconducting magnets in the KATRIN beam line are ready for operation.

5.1.3 Influence of the LFCS system

The strength and shape of the field in the central region of the main spectrometer is dominated by the LFCS system. Its mechanical layout (section 3.1.3) as well as geometrical features were thoroughly tested (ref. [Gum13]) and all aspects of this system are implemented in the field model. Test measurements have demonstrated an excellent linearity of the air-coil power supplies (section 4.2.1) and an axially-symmetric field alignment of the LFCS better than 1.0 % (ref. [Rei13]). However, this level of agreement with calculations was only reached once the remanent field of the steel rods in the reinforcement of the main spectrometer walls was implemented. Given this agreement, the analysis of the LFCS field values not only serves to validate the major component of the field model, but also serves as an estimate of the remaining remanent field after the demagnetization. In particular, it allows to deduce the influence of an induced magnetic-field in the walls of the main-spectrometer building.

To study the influence of the LFCS-system, all runs with a stable magnetic-field configuration, as defined in section 4.2.1, are analyzed to cover the entire accessible field range. The currents of the SDS solenoids are at nominal field-setting and all DPS magnets were turned off. The total range of the observed values of the magnetic-field z-component is split in 4 µT-intervals where an average field value together with an uncertainty, the standard deviation of an individual sensor unit, is calculated.

The upper plot of fig. 5.4 displays the deviation of the measured field to the corresponding calculations for the high-precision magnetometers on the central sensor-ring as a function of the field z-component. The resulting field deviations are fitted with a linear function

$$B_{\mathrm{dev}}(B_{\mathrm{z}}) = \alpha\,[B_{\mathrm{exp}}(B_{\mathrm{z}}) - B_{\mathrm{sim}}(B_{\mathrm{z}})] + B_0 \tag{5.10}$$

where the field independent fit parameter is treated as correction factor for $\vec{B}_{\mathrm{rem}}$ and the field dependence is associated with an induced magnetic field $\vec{B}_{\mathrm{ind}}$ in the spectrometer walls.

However, the field cannot be analyzed based on individual high precision magnetometers due to the limited number of sensor units and the relative large uncertainty. A study of the azimuthal field structure is therefore performed with the MobSU in section 5.4, although an asymmetry is already here observed for α in east-west direction (table 5.2). Instead, the overall trend of the individual magnetometers is used in the field analysis of this section, as all sensors show a larger field deviation for larger absolute field values. Readout values of the individual magnetometers within a magnetic-field interval are used, weighted by their respective uncertainties, to calculate a mean value and the standard deviation as the field uncertainty. Therefore, a large uncertainty indicates a large spread of the measured field values and should not be interpreted as an imprecise measurement. The resulting fit of the combined magnetometer readout of the central ring is shown by a black line with an 1σ-uncertainty.

In the lower plot of fig. 5.4 the combined sensor-ring analysis of all three sensor-rings is shown. In addition, three measurements for a 3.8 G, 5.0 G and 9.0 G setting are highlighted.

Table 5.2: Results of magnetic field deviation fir for various LFCS-field settings. The data sets in fig. 5.4 were fitted with eq. (5.10). A fit of an entire sensor ring is based on the combined sensor readings, weighted by the individual uncertainties and labeled with "1 to 4(6)".

sensor ring	sensor number	alpha (µT/mT)	B_0 (µT)
upstream	1 to 4	1.6 ± 0.5	-1.25 ± 0.24
middle	1	3.7 ± 0.9	0.1 ± 0.5
middle	2	2.4 ± 1.2	0.7 ± 0.6
middle	3	4.6 ± 1.0	1.3 ± 0.6
middle	4	2.7 ± 1.0	0.3 ± 0.5
middle	5	3.7 ± 1.3	1.3 ± 0.7
middle	6	0.8 ± 0.8	0.3 ± 0.4
middle	1 to 6	3.9 ± 0.3	1.07 ± 0.17
downstream	1 to 4	-0.5 ± 0.8	1.32 ± 0.32

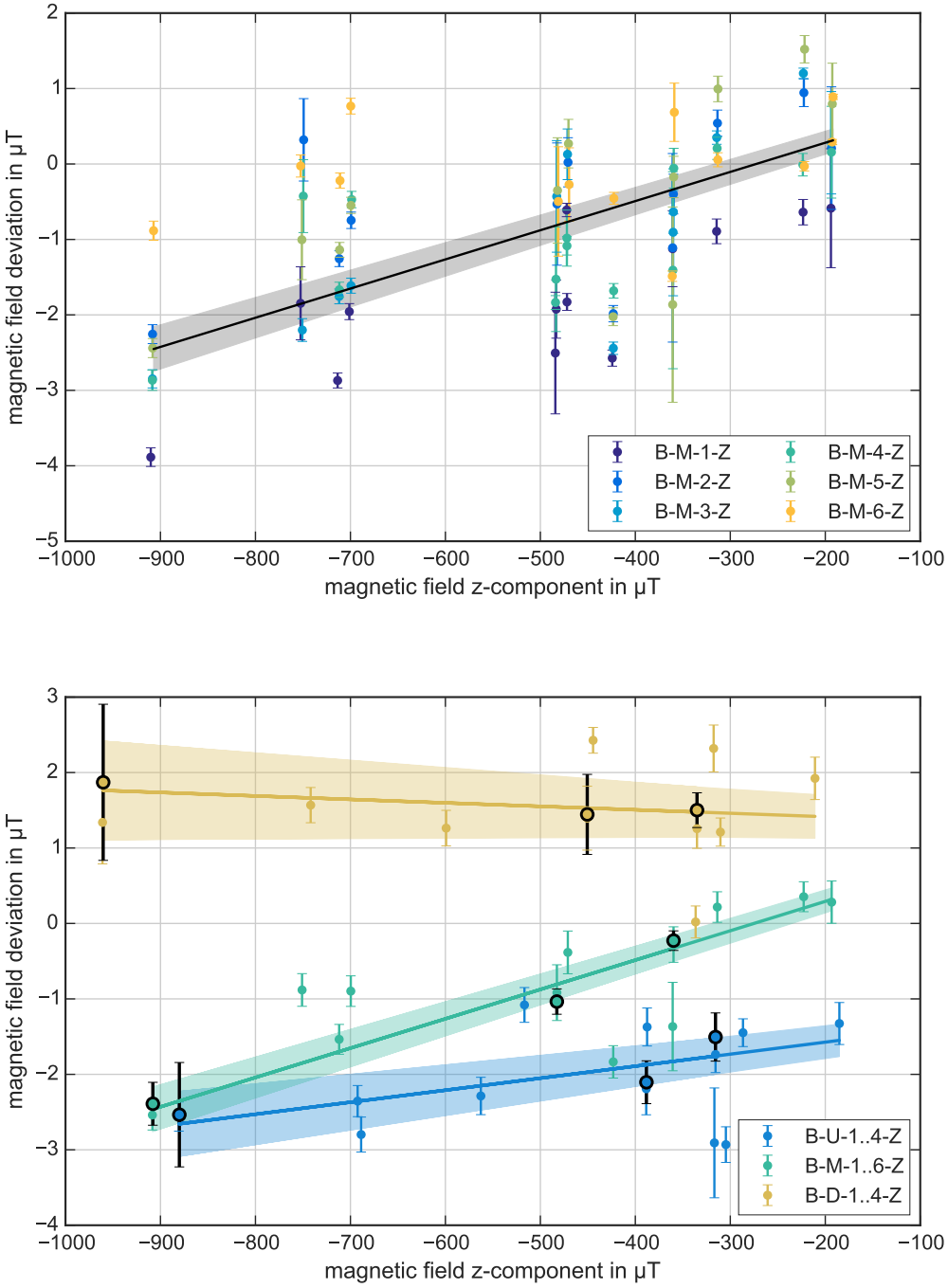

Figure 5.4: Magnetic-field deviation $\vec{B}_{\mathrm{dev}} = \vec{B}_{\mathrm{exp}} - \vec{B}_{\mathrm{sim}}$ for various LFCS-field settings. All runs with stable conditions are split in 4 µT-intervals to investigate the measured z-component dependence on the applied field. Here the SDS solenoids were operated with nominal currents. In the upper plot the central ring of the high-precision magnetometers is shown. A linear-trend of the mean values of all sensors with a 1σ-uncertainty is shown in black. The weighted sum of the field values of all three sensor rings is shown in the lower plot together with a mean linear-trend. Additionally, three measurements with 3.8 G-, 5.0 G- and 9.0 G-settings for ideal conditions are highlighted. The magnetic-field deviation increases towards higher absolute field-values for all three rings, but is most pronounced in the central region. An induced field of the ferromagnetic materials is associated with the observed magnetic-field deviation.

The data here are selected for specific stability during the runs. The magnetic field was stabilized for at least 45 min and measured for more than one hour. Furthermore, all three runs were performed over a single week, therefore long-term dependencies are suppressed. Influences by other field sources can be excluded as only the SDS magnets were in operation.

When fitting the readings with eq. (5.10), the sensor rings (upstream, middle, downstream) display an offset of the low µT range. According to the measurement and simulation results in ref. [Rei13], a remanent field of $\approx 1.5\,\mu T$ was observed at a radius of 4.5 m. The field monitoring system is mounted on a radius of $\approx 5.3\,m$ where larger field variations are expected due to the closer position to the spectrometer walls and the remanent field sources. Considering the fact, that the sensors nonetheless measured a reduced offset, a reduction of the remanent field by at least a factor of 50 % can be concluded.

The fit also reveals a non-vanishing absolute magnetic-field dependence α for all three sensor rings. Especially in the important central region, the effect is most pronounced where the field is dominated by the LFCS. For a 3.8 G setting B_{ind} already exceeds the remanent field-component by 31 % and by 227 % in case of a 9.0 G setting. The consequences of a remanent and induced magnetic-field are further discussed in section 5.3.

The observed field deviations, especially in the central region, could be caused by an incorrect representation of the LFCS in the field model. To investigate whether the field deviation results from an induced field or the LFCS geometry in the simulation, the current and the radius of the LFCS system were studied in detail. The currents of the LFCS system were thoroughly tested in section 4.3 and the resulting deviation is limited to ≈0.7 %. The LFCS radius is therefore the only reasonable parameter to cause the observed field deviation due to its large impact on the magnetic field, especially on the z-component. Simulations were performed in which the radius of the LFCS was varied to match the measured magnetic-field values.

For a vanishing magnetic-field deviation in the central region in case of a 3.8 G-setting (9.0 G-setting) the radius needs to be decreased by about 5 cm (45 cm). These simulation results are unrealistically large, considering that the inner radius of the LFCS system was measured with a precision of 5 mm. In addition, the deviations for the three sensor rings can not be explained by a common radius variation.y The observed magnetic-field deviations can therefore not be explained by an incorrect LFCS geometry.

5.1.4 Influence of the PS 1 and PS 2 magnets

The solenoids of the SDS section have a high impact on the field at the main spectrometer with a stray field of several µT in the analyzing plane (table 5.1). Different effects can lead to an insufficient representation of the solenoid field in the model, either by an inaccurate magnet alignment, or incorrect operation current, or imperfections of the magnet geometry, namely the mean coil radius, as well as an additional induced field in the ferromagnetic components in the spectrometer walls. As the first point is of no concern (see section 5.2), the latter points are studied in this section, based on measurements with different solenoid settings. Key objective is to investigate if a similar field deviation as in section 5.1.3 can be verified also for magnetic field components further away from the analyzing plane.

Throughout SDS 2 only a few measurements were executed when only the solenoid fields were altered. Mainly maintenance breaks when one or both PS magnets were turned off give the opportunity to study their specific impact on the magnetic field. The two solenoids of

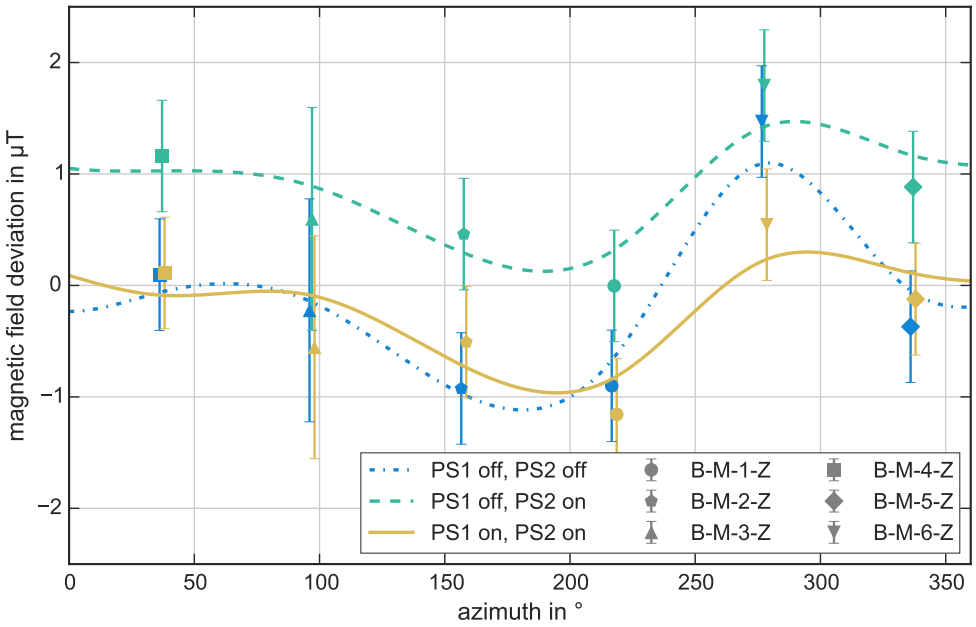

Figure 5.5: Influence of the PS magnets on the magnetic field in the analyzing plane. Three measurements at a stable 3.8 G setting are shown when currents of the PS magnets are variate as a deviation to a simulation $\vec{B}_{\mathrm{dev}} = \vec{B}_{\mathrm{exp}} - \vec{B}_{\mathrm{sim}}$. Azimuthal distribution is described by a cubic spline. Magnet misalignment is incorporated in the simulated field, remaining deviation can not be explained by PS magnet geometry.

the FPD system could not be studied during SDS 2. The FPD system was only once ramped up in the beginning of SDS 2 when the magnetic-field monitoring-system was not yet in operation, and the ramp down procedure coincides with a DPS ramping test. Therefore, the stray field test of the FPD system must be addressed in upcoming measurements.

Three runs were selected when a stable 3.8 G setting was applied and the DPS as well as the monitor spectrometer were not in operation. These runs represent three different settings of the PS magnets, when both magnets are turned off (PS 1-off-PS 2-off), when only PS 2 is on full field (PS 1-off-PS 2) and when both magnets are operating with their nominal setting (PS 1-on-PS 2-on). Analyzed is the field with the high-precision sensors in the central region (fig. 5.5), as this ring is the closest to the analyzing plane.

The field features an azimuthal variation which is comparable in all three cases. As the global azimuthal field trend is identified with the influence of the remanend and induced field of steel rods in the spectrometer walls, only a divergence from the overall trend can be attributed to an influence of the PS solenoids. The measurements PS 1-off-PS 2-off and PS 1-on-PS 2-on are in agreement within measurement uncertainties, featuring a mean field deviation of $(-0.14 \pm 0.81)\,\mu\mathrm{T}$ and $(-0.28 \pm 0.54)\,\mu\mathrm{T}$ respectively. For PS 1-off-PS 2-on the same trend (indicated by a cubic spline) is observed, but significantly shifted by a global offset to a field deviation of $(0.82 \pm 0.57)\,\mu\mathrm{T}$.

As the currents of the solenoids are set manually, a change of the operation current could be a straightforward explanation for the field offset. In fact, there was a difference in applied current for PS 2 with 155.9 A in the PS 1-off-PS 2-on mode compared to 156.1 A in the PS 1-on-PS 2-on mode. However, the resulting field difference of 43 nT is far too low to explain the observed field difference of about 1 µT.

To investigate if the 1 µT-shift in PS 1-off-PS 2-on mode originates from wrong geometry parameters, simulations were performed where the position and the effective coil diameter of PS 1 and PS 2 was variate in 1 mm-steps. Tolerances of both parameters are limited to 5 mm, within those limits no significant improvement of the magnetic field deviation is observed. Due to a misalignment of both magnets, including a tilt of the coils relative to the beam line (section 3.4.3), a minor azimuthal dependence of the stray field is expected. Therefore, the simulation was repeated with a incorporated tilt of the PS magnets resulting in an improved maximum likelihood in both cases ,PS 1-on-PS 2-on and PS 1-off-PS 2-on. However, the small magnetic-field changes and the few measurement points inhibit the quantification of the alignment measurement. More details are given in section 5.4.

Genuinely, the marginal azimuthal magnetic-field changes in the measured magnetic field it self indicates a sufficient alignment of the solenoids and the remaining orientation uncertainty can be accounted for in the magnetic-field model. In conclusion, the magnetic-field offset of 1 µT must be caused by remanent and induced magnetization of the steel rods in the reinforced concrete close to PS 1 and not geometry or alignment imperfection.

Moreover it is important to utilize the MobSUs in upcoming measurements for an in-depth investigation of the solenoid stray fields of all SDS solenoids.

5.1.5 Influence of geometry imperfections

Aside from the tilting of the SDS magnets in the previous section, geometry imperfections introduced in chapter 3 were not considered. Drawback of non-axially symmetric object for a magnetic field calculation is the drastically increased computation time, an important factor especially for elaborated background simulations. The goal is to expand the alignment simulations in section 5.1.4 with all know geometrical deformations of the magnet system (section 3.4) and estimate if a non axial symmetry is necessary to significantly increase the agreement of a magnetic-field simulation with measurement results.

In fig. 3.20 the influence of the geometry approximations and imperfections were calculated. Within the active volume and in the central region of $z = -5.0\,\mathrm{m}$ to 5.0 m, magnetic-field deviations do not exceed 0.1 µT for any given geometry configuration. In fig. 5.6 the same effects are studied based on the PS 1-on-PS 2-on mode measurement in section 5.1.4. The total measurement time was 1 h with a 1 h long waiting time to stabilize the current output of all power supplies (see fig. 4.6). During this measurement, no current was applied to any DPS magnet or the MoS magnet system.

When all geometry imperfections are included in the magnetic-field model, the maximum likelihood is increased but not significantly. These simulations thereby confirm a sufficient alignment of the PS magnets, but for the entire SDS magnet system. Since induced and remanent magnetic-fields are not implemented in the magnetic-field model, and both effects exceed the influences of the geometry imperfection substantially, a final evaluation is prohibited.

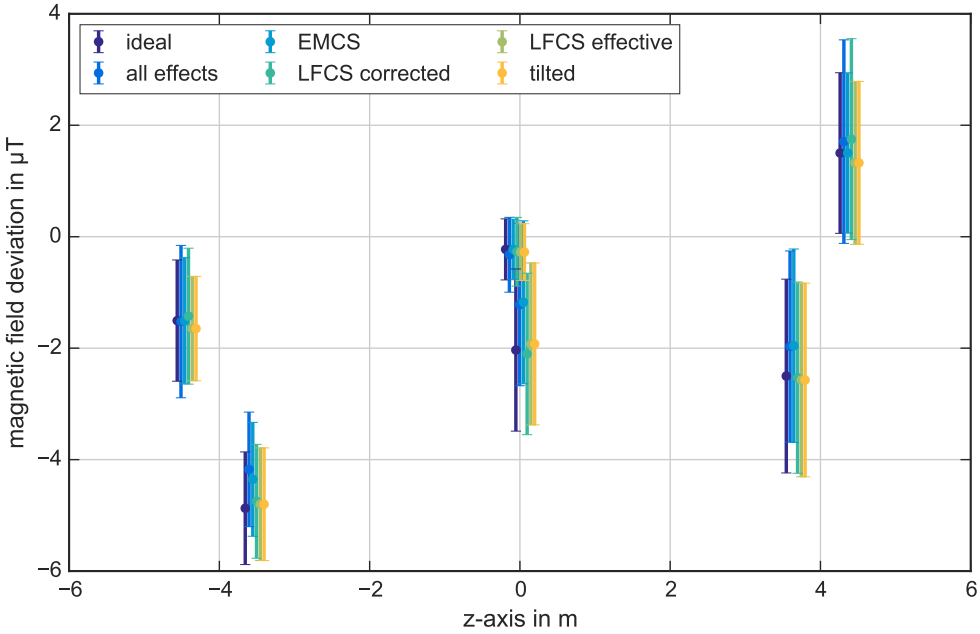

Figure 5.6: Influence of geometry imperfections on magnetic field along the spectrometer axis shown as a magnetic field deviation to a 3.8 G-setting measurement. The magnetometers at a common position were combined (3 high-precision , 3 IPE magnetometers), plotted with some jitters to distinguish individual effect. Although the combination of all effect lead to the best likelihood, no significant difference is observed.

5.2 Long-term measurement of the magnetometer system

An analysis of a long measurement period allows an evaluation of a possible drift behavior of individual magnetic-field sensors or changes in the magnetic environment in the main-spectrometer hall. The 3.8 G-setting is the most common magnetic-field setting during SDS 2 and with an energy resolution close to the KATRIN design value, it is well suited to study a long-term dependence of the magnetic field.

Analyzed are all phases when a 3.8 G-setting was applied and the field fulfills the stability conditions defined in section 4.2.1. Additionally, measurements after ramping processes, especially of the PS magnets, were excluded to inhibit transition state data (section 4.2.3). For every stable phase, the magnetic field deviation of the magnetometers was calculated as the difference between the mean of a measured magnetic-field and the corresponding magnetic-field simulation. Long time periods were re-sampled in 1 h phases to preserve sensitivity for variations on smaller time scales. Magnetic-field deviation of the magnetic z-component of the high-precision magnetometers close to the analyzing plane are shown in the upper plot of fig. 5.7. The error bars are measurement uncertainties which are dominated by the fluctuations of the air-coil currents (section 4.4).

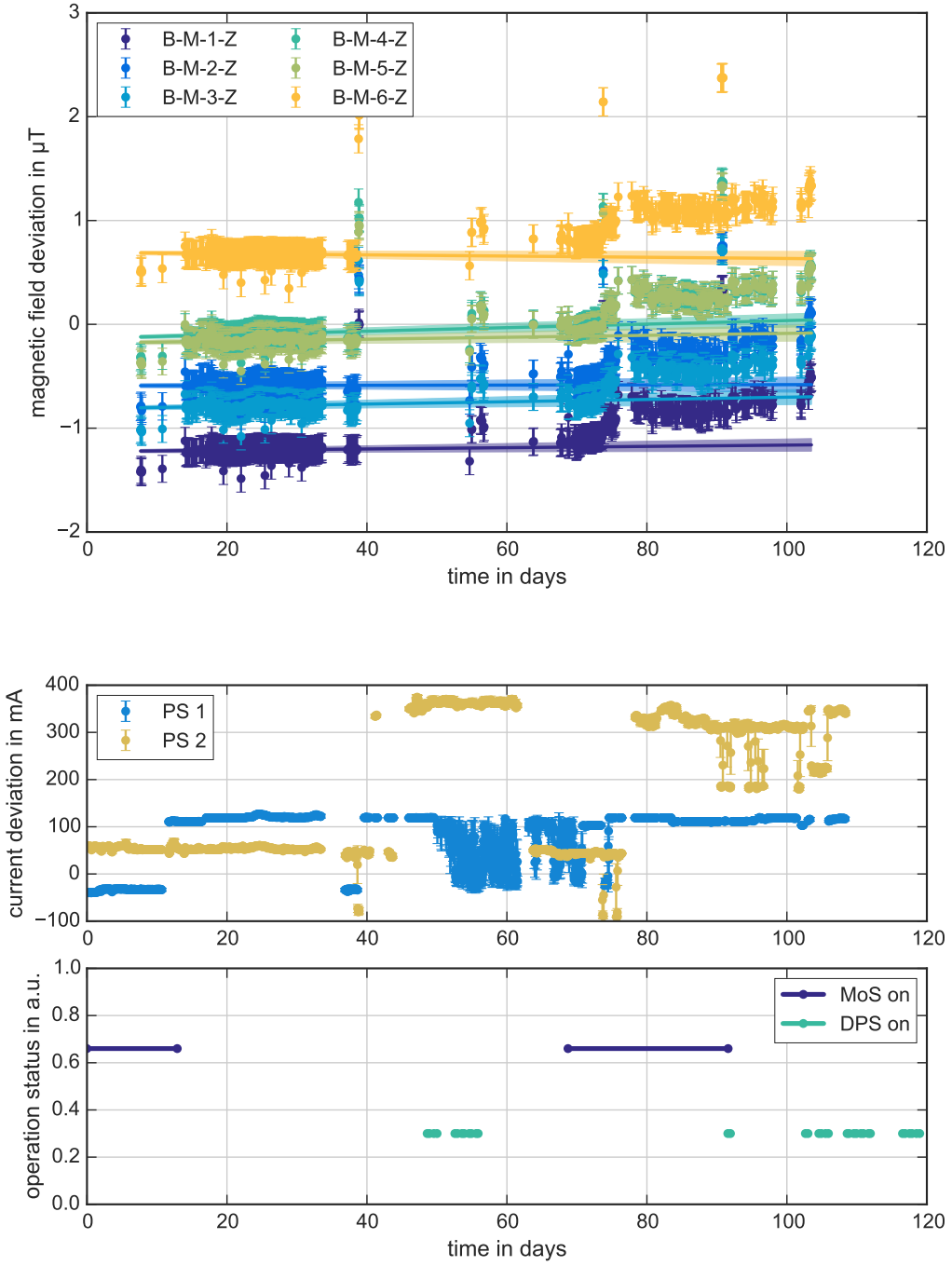

Figure 5.7: Long-term analysis of the 3.8 G-setting with high-precision magnetometer and status of magnetic sub-systems. In the upper plot the z-component of the magnetic field of the central sensor ring is shown as a deviation to the corresponding simulation. Average values of all magnetometers are within requirements of 2 µT. In the range 17 d to 33 d a linear drift below 2 nT is observed, extrapolated for the whole data set. A shift at 77 d is related to a changed current of PS 2 as shown in the central plot for both magnets relative to their nominal current. A larger deviation is observed when PS 1 was turned off at 38 d, 74 d and 92 d. In the lower plot periods are shown when a DPS magnet or the MoS magnet-system is operated with at least 10 % of their full magnetic-field.

In the lower plots the operation status of all super-conducting solenoids[1] in the SDS setup on the course of SDS 2 is shown. The first plot depicts the current variations of both PS magnets as a difference to their nominal currents (table 3.2). Missing data points indicate a period when the applied current was 5 % smaller than the nominal value and therefore excluded from further analyses. The second plot shows the operation status of the DPS magnets and the MoS magnet-system, where 10 % of the nominal magnetic-field of the respective sub-component is considered as an in-operation phase.

A major task of this section is to ensure a reliable functionality of the magnetic-field monitoring system. During the SDS 2-measurement period for none of the magnetometers was an abnormal behavior observed, such as a sudden distinct drift, a significant temperature dependence or even a malfunction. By comparing the simulated field with the individual sensor measurements, the reproducibility of the field can be established. Despite frequent changes of the magnetic-field settings, the observed field deviations of all sensors over the entire SDS 2 are within a 3σ-range of the uncertainties. On average, the observed uncertainty of the z-component of the measured field is $(47.0 \pm 1.1)\,\mathrm{nT}$ throughout SDS 2. Thus, only a long term drift of one or more sensors could impair the monitoring system.

In the range from 17 d to 33 d the currents of all solenoids were constant, so a variation of the induced field as shown in fig. 5.5 is suppressed, and therefore a stable magnetic field can be assumed[2]. Based on the determined air-coil stability in section 4.3.2 a magnetic-field drift for the sensors in the central region can be approximated to $0.5\,\mathrm{nT/d}$. Assuming only a linear dependence, the combined readouts of all magnetometers result in an average magnetic-field drift of $(0.6 \pm 0.8)\,\mathrm{nT/d}$. For a single magnetometer, a drift does not exceed $(1.7 \pm 0.5)\,\mathrm{nT/d}$. Fit results of all individual sensors can be found in table 5.3. The observed field drifts are not only insignificant during the estimated KATRIN measurement interval of 60 d, but are also well in agreement with the verified air-coil current drift. The remaining long-term magnetic-field changes can therefore already be explained by a variation of the earth magnetic-field.

Using the drift results of the high precision magnetometers as a reference for field deviations during the entire SDS 2 data set, four distinct field modifications are observed that originate from two causes. First, there are three distinct peaks detected on the days 38 d, 76 d and 91 d, these measurements coincide with a turned-off current of PS 1. Second, a constant shift at 78 d that can be explained with a changed current of the PS 2 magnet. The resulting field deviations are comparable with the observations in section 5.1.4. A further, minor shift of the observed magnetic-field deviation is detected after a test of a DPS magnet at 92 d.

Based on the simulation result in section 5.1.5, it is unlikely that geometry imperfections can cause the observed field deviations, but rather a change in the magnetic background field. The remaining magnetic-field deviation and offset, as well as the absolute difference between the individual sensors are attributed to a remanent- and induced magnetic-field. Thereby all features of the long-term field trend can be explained with these additional fields.

1 The FPD magnets were ramped up in the beginning of SDS 2 and ramped down when SDS 2 was finished. Hence, the FPD magnets were operated at full magnetic-field at any time and are therefore not explicitly included.

2 During this period, only the LFCS settings were variated. Reproducibility of currents of the air-coil system is demonstrated in fig. 4.10

Table 5.3: Long-term analysis of the high-precision magnetometer with an applied 3.8 G-setting. The sensor names and position are defined as in fig. 3.12. Column "mean uncert." is the average standard deviation of a magnetometer, the uncertainty of these values is well below the nT-regime. The drift slop and offset are the results of a linear fit in fig. 5.7. Column PS 2 shift is the mean field offset when the current of the PS 2 magnet was increased at 77 d.

sensor	mean uncert. (nT)	drift slope (nT/day)	drift offset (nT)	PS 2 shift (nT)
B-U-1	46.2	0.82 ± 0.94	-2338 ± 24	-229 ± 550
B-U-2	46.7	-1.03 ± 0.83	-3251 ± 21	-442 ± 568
B-U-3	47.7	0.56 ± 0.92	-1162 ± 24	-534 ± 551
B-U-4	46.2	-2.14 ± 0.95	202 ± 24	-530 ± 528
B-M-1	46.8	0.63 ± 0.47	-1225 ± 12	-154 ± 101
B-M-2	47.4	0.11 ± 0.57	-592 ± 15	-113 ± 120
B-M-3	46.7	1.10 ± 0.57	-811 ± 15	-252 ± 109
B-M-4	46.0	1.70 ± 0.51	-134 ± 13	-309 ± 100
B-M-5	46.2	0.94 ± 0.60	-181 ± 15	-376 ± 88
B-M-6	48.9	-0.58 ± 0.54	692 ± 14	-310 ± 86
B-D-1	47.7	-0.03 ± 0.98	1512 ± 25	-184 ± 171
B-D-2	46.7	0.33 ± 1.01	-915 ± 26	-145 ± 173
B-D-3	45.2	1.13 ± 0.94	3194 ± 24	-214 ± 168
B-D-4	46.7	-0.48 ± 0.88	1256 ± 23	-188 ± 171

The second sensor system installed on the main spectrometer vessel to continuously monitor the magnetic field is equipped with the IPE sensors. These magnetometers are used as a backup system as they are not as accurate as the Bartigton sensors. An average drift of $(3.0 \pm 1.5)\,\mathrm{nT/d}$ is observed in the same time interval and with the same applied data cuts as for the precision magnetometers (fig. A.5). Drift values of both sensor types match within uncertainties. However, the large drift uncertainty of IPE sensors is a result of the high susceptibility to calibration imperfections of this sensor type[1]. Considering the IPE sensor specifications and properties, especially the insufficient magnetometer accuracy, a magnetic-field analysis based on the IPE sensors alone can only verify relative field changes. However, as the operation range extends to $\pm 2\,\mathrm{mT}$ and hence exceeds the operation range of the other sensor systems by a factor 2, the IPE sensors can be used to monitor the field stability above 1 mT. For more details see appendix A.3.

Fortunately, no significant drifts are observed with both systems. Under stable field conditions, deviations are of $1.5\,\mu\mathrm{T}$ or below for every high-precision sensor close to the analyzing plane. Conclusively, the installed magnetic sensor system is sufficient for a long-term field monitoring during a KATRIN tritium spectrum measurement.

1 Especially in the later measurements from 75 d when the magnetic-field setting was changed often, magnetic-field deviations as measured by the IPE sensors reveal a shift. This is due to uncertainties of the angular and orthogonality calibration of the three measurement axis.

5.3 Estimation of the magnetic background field

A magnetic background field consists of all field components that can not be controlled by an operator. The most prominent component is the earth magnetic-field that is uniform within the entire KATRIN setup and so, it can be compensated by a homogeneous field of the EMCS. Unfortunately, a much more complex remanent (table 5.1) and induced magnetic-field of ferromagnetic steel rods in the reinforced concrete of the KATRIN buildings needs to be considered also, as verified within this thesis.

A remanent magnetic-field of a ferromagnetic material

$$\vec{B} = \frac{\mu_0}{4\pi} \frac{3\vec{r}(\vec{m}\vec{r}) - \vec{m}r^2}{r^5} \tag{5.11}$$

depends on its magnetization

$$\vec{M} = \frac{\sum \vec{m}}{V}, \tag{5.12}$$

which is the sum of all magnetic dipole-moments within a given volume (ref. [Glü05]). To simulate a magnetization distribution along the spectrometer based on eq. (5.11) many fit parameters are necessary to represent the large amount of steel rods in the concrete. To incorporate also an induced magnetic-field eq. (5.12) has to be rewritten to

$$\vec{M} = \frac{\chi}{\mu_0 (1 + \chi)} \vec{B_{\text{in}}} \tag{5.13}$$

where $\chi = \mu_\text{r} - 1$ is the susceptibility, $\mu_\text{r} = \mu/\mu_0$ is the relative permeability and $\vec{B_{\text{in}}}$ denotes the magnetic field inside the magnetic material. The relative permeability depends on the properties of the magnetic material that can be easily altered by impurities. Hence, to calculate the magnetization, every magnetic dipole-moment is associated with a specific relative permeability and the field model becomes rather complex.

This additional contribution to the magnetic background field was already expected during the design phase of the main spectrometer building and non-magnetic, stainless steel rods were used in the reinforced concrete to reduce the effect whenever possible. Due to cost constrains, stainless steel was used for the sidewalks, directly beneath the main spectrometer, the pre-spectrometer and close to the FPD system only (ref. [Glü14]). In the walls of the main-spectrometer building normal steel was used, with a density of $6\,\text{kg/m}^2$ in the top walls and $25\,\text{kg/m}^2$ in the bottom walls (fig. 5.1). The positioning of the walls in a y-z plane on both sides of the spectrometer provides the orientation of the steel rods. It is expected that the transport section influences the magnetic background field in a similar way (section 5.1.2). This issue will be addressed later when all STS magnets are ready for operation.

The evidence for an induced magnetic-field in the previous sections and a demagnetization of large parts of the main-spectrometer building (ref. [Wol14]) make a former model of the remanent magnetic-field obsolete. Since more than 2000 measurement positions were needed to develop the remanent magnetic-field model (ref. [Rei13]), the remanent and induced magnetic-field can only be estimated. In a first approach $\partial\vec{M}/\partial V$ is assumed to be constant.

5.3.1 Remanent magnetic-field of magnetic materials

To estimate an absolute value and a related variation of the magnetic field due to a remanent magnetization of the KATRIN building, time periods are selected when all magnets of the KATRIN setup are turned off. In this case, the magnetic background field consists of the earth magnetic-field and a remanent magnetic-field of the magnetic materials only. The direction and intensity of the earth magnetic-field is well known and annual variations do not exceed 50 nT. Thereby it is possible to estimate the average remanent magnetic-field with the precision of ≈0.1 µT and to qualitatively evaluate the demagnetization.

Figure 5.8 shows the z-component of the magnetic field measured with the high-precision magnetometers close to the analyzing plane as a deviation to the earth magnetic-field. The data was obtained prior and subsequent to the two large measurement phases SDS 2 and SDS 2b[1]. Grey shaded areas in the second panel indicate tests of the DPS magnets and the commissioning of a new pinch magnet. (ref. [Fra15]). The magnetic background-field values of the individual sensors are given in table 5.4 along a sensor-ring average.

Table 5.4: Development of the magnetic background field B_z. The column numbers correspond to the numbers of the high-precision magnetometers in the central region and the respective mean value. The rows correspond to measurements before the demagnetization, before SDS 2, after SDS 2a and after SDS 2b. All values are given in µT.

#1	#2	#3	#4	#5	#6	mean
-1.93 ± 0.15	0.08 ± 0.16	-0.11 ± 0.16	1.01 ± 0.12	1.44 ± 0.12	1.45 ± 0.12	0.44 ± 0.02
-0.98 ± 0.06	1.04 ± 0.07	-0.36 ± 0.07	-0.09 ± 0.07	-0.18 ± 0.07	0.72 ± 0.07	0.00 ± 0.01
-0.39 ± 0.02	1.68 ± 0.02	0.30 ± 0.02	0.51 ± 0.01	0.44 ± 0.01	1.25 ± 0.01	0.67 ± 0.01
-0.95 ± 0.26	1.28 ± 0.11	-0.92 ± 0.13	0.79 ± 0.21	0.06 ± 0.11	0.83 ± 0.28	0.22 ± 0.03

The field variations between individual sensors can be interpreted as an upper limit of the field uncertainty in the analyzing plane. Due to the demagnetization of the building, a ΔB_z is reduced by 57 % from 1.2 µT to 0.74 µT. Changes of the magnetic background field occur as global, sharp offset shifts[2, 3] and correlate with the tests of the PCH and DPS magnets, these changes originate from an altered $\vec{B}_{\text{rem}}$ of the ferromagnetic materials in the KATRIN building of the source and transport section.

During an extended measurement campaign, the magnetic background field cannot be measured. Any chance of the remanent magnetic-field $\vec{B}_{\text{rem}}$ can only be determined in retrospective. To reduce the possibility of changes in the magnetic background field, changes of the current setting, especially of the KATRIN solenoids, should be avoided. Based on the observed changes between measurement campaigns, an upper limit on the uncertainty of the magnetic background field is estimated to 0.67 µT.

1 A large maintenance break divides SDS2 in phase A and B. During the shut down the main spectrometer was beaked out and a new PCH was installed. So not only interfered this procedure with the magnetic-field monitoring, but chanced the magnetic environment. To avoid additional uncertainties the phase B is usually neglected. Only for the analysis of a remanent magnetization Phase B is considered.

2 A similar trend is observed for the sensors on the upstream and downstream position

3 The field change on 150 d feature a different signature, when only sensor B-M-1 and B-M-2, mounted on the spectrometer west-side, and B-M-6 beneath the spectrometer show a significant variation. At this time, several ferromagnetic trolleys were moved in the west side basement of the spectrometer hall.

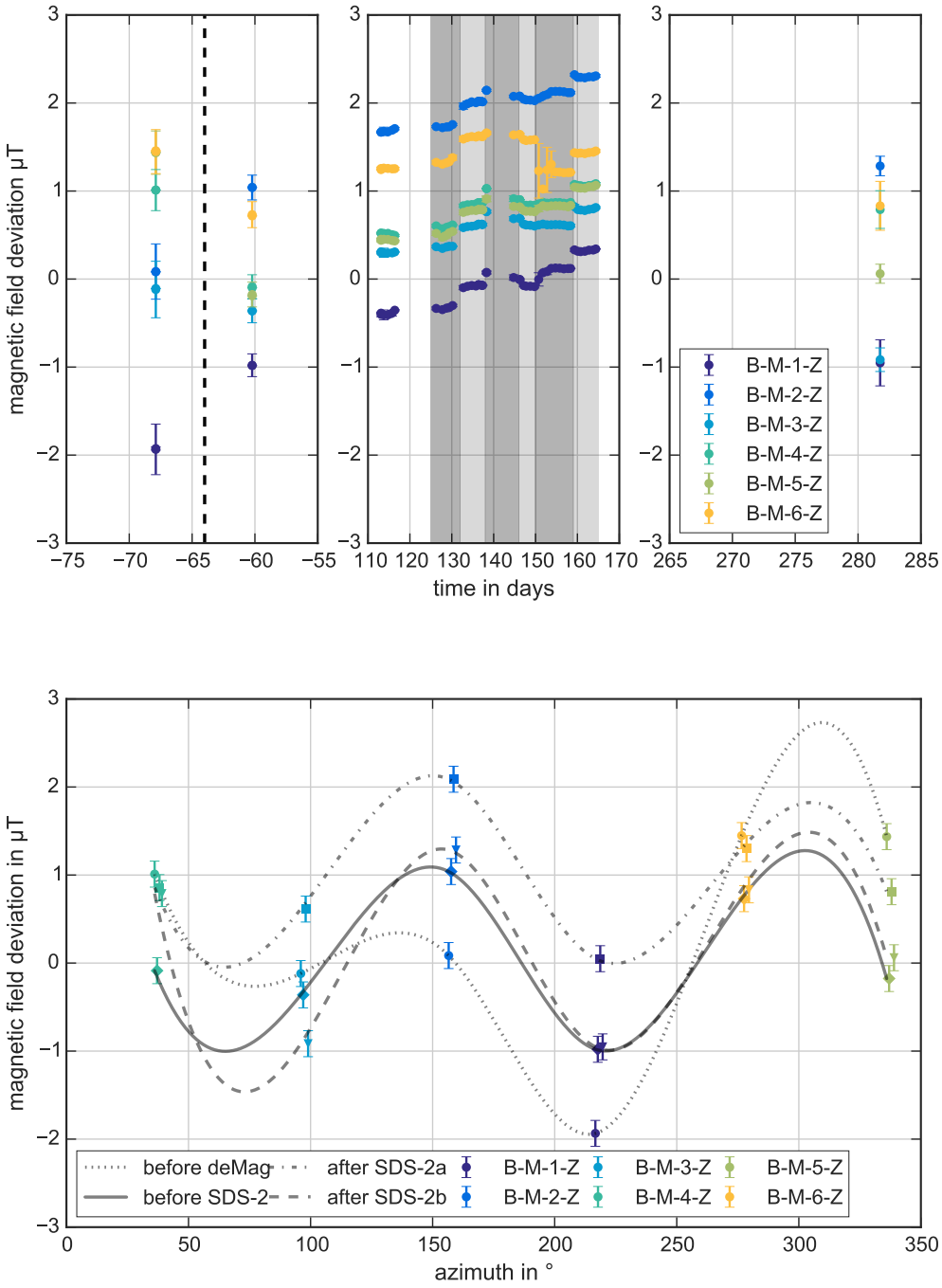

Figure 5.8: Measurement of the z-component of the magnetic background field as a deviation of $\vec{B}_{\mathrm{exp}} - \vec{B}_{\mathrm{earth}}$. All SDS solenoids, the main-spectrometer air-coil system and DPS magnets are turned off. The plot is separated in three time frames corresponding to the phases before SDS 2, after SDS 2a and after SDS 2b. The first phase is also divided in measurements before and after the demagnetization of the main spectrometer hall resulting in a 57 %-reduction of the remanent field. In the second panel, a global shift in the background field is observed, but no variation increase. Further field shifts coincide with tests of the DPS and PCH magnets, represented by grey shaded areas. In the lower plot the azimuthal distribution is shown. The data points are connected with a cubic spline.

5.3.2 Induced magnetic-field of magnetic materials

The analyses of the magnetic background field revealed a magnetization of steel rods in the concrete of the KATRIN buildings. By this means only the remanent field component is accessible, however the permeability of steel rods is needed to develop a realistic field model of the magnetic materials (ref. [Ada15], [Sud15]). Hence, only a rough estimation of the induced magnetic-field is possible due to the unknown permeability and the limited measurement positions of the available sensor system.

Non-vanishing magnetic-moments are expected in y-z planes on both sides of the spectrometer, corresponding to the orientation of the steel rods in the concrete. This assumption is based on the observations of significant offsets when a field is applied to the DPS-, PS-, or LFCS, which are oriented in z-direction (see section 5.1.2 to section 5.1.4). At the same time, this assumption is consistent with the absent of a shielding effect of the MoS field that is primarily in x-direction at the main spectrometer (see section 5.1.1). As the largest contribution to an induced field in the steel rods is made by the LFCS, its influence is here studied at the lower wall of the spectrometer building where the steel density is the highest.

The field of the SDS magnets is simulated with the 3.8 G- and 9.0 G-setting and analyzed for the z- and y-field component(fig. 5.9). The analysis model is based on the assumption of a constant susceptibility χ of the steel rods in the concrete and a uniform pre-magnetization due to the demagnetization of the hall.For both field settings, the magnetic z-component features variations only along the z-axis, but is homogeneous in y-direction. At a given z position, only minor variations of an induced magnetic-field are expected in a plane perpendicular to the z-axis. When the two magnetic-field settings are compared, it needs to be to distinguished between the central region from $-4.5\,\mathrm{m}$ to $4.5\,\mathrm{m}$ and the outer parts closer to the SDS solenoids. In the central region the field nearly vanishes for a 3.8 G-setting and therefore no additional magnetic-field is induced. This is consistent with comparable observations of minor field deviations in case of 3.8 G-setting (fig. 5.4, upper plot) and for the magnetic background field (fig. 5.8). In case of the 9.0 G-setting, there is a field of $\approx 80\,\mu\mathrm{T}$ at the walls. The resulting induced magnetic-field of the magnetic materials causes a reduction of the effective magnetic-field at the main spectrometer, corresponding to a lower value of the observed magnetic-field deviation as in fig. 5.4.

On the other hand, the magnetic field by the SDS apparatus is nearly constant and non-vanishing for different magnetic-field settings at the outer positions $> \pm 5\,\mathrm{m}$, especially on the downstream side close to the FPD system. This observation is reflected by the fact that the dependency of the induced magnetic-field on the absolute magnetic-field is reduced for the outer sensor-rings and features a significant offset to the magnetic-field model (section 5.1.3).

The y-component of the SDS magnetic-field shows a more complex structure that completely changes for the different magnetic-field settings, and it is in the same order of magnitude as the z-component. The result is a non-axially symmetric magnetic-field that does not only change the resolution of the MAC-E filter, but can also lead to an increase of background events as well. When the considerations for the z-components are applicable to y-component, an induced magnetic-field at the main spectrometer from $0.5\,\mu\mathrm{T}$ to $1.5\,\mu\mathrm{T}$ is expected.

Therefore, in any magnetic-field setting, an induced magnetic-field in the ferromagnetic steel of the reinforced concrete is expected. The absolute value of an effective field at the analyzing plane is thereby in the order of the remanent field of $0.7\,\mu\mathrm{T}$ at the outer radii.

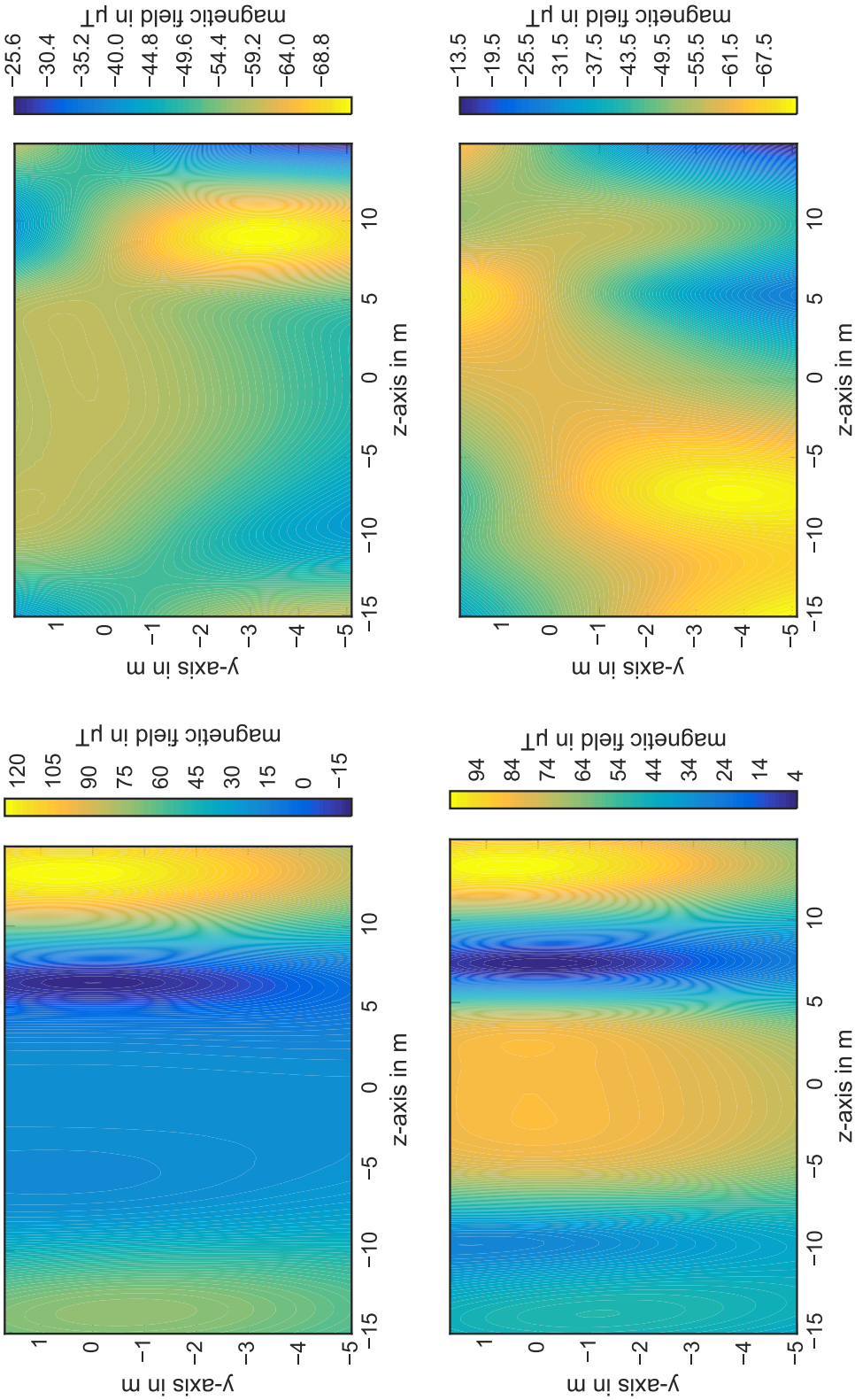

Figure 5.9: Magnetic field at the western wall of the main spectrometer hall at position x = 9.37 m. Upper plots for a 3.8 G-setting and lower plots for a 9.0 G-setting. On the left (right) side is the B_z (B_y) component plotted. Please note that the color code is inverted for the two magnetic-field components so that yellow always corresponds to the largest magnitude.

5.4 Evaluation of the magnetic-field symmetry

An axial symmetry of the magnetic field is an essential requirement to ensure an optimal energy resolution of the MAC-E filter and background reduction of secondary electrons emitted from the vessel hull. In the KATRIN setup axial symmetry is guaranteed by axial alignment of the LFCS coils relative to the main spectrometer hull, and more importantly, the field can be fine tuned by an adjustment of the EMCS currents. The MobSU system is designed to provide a magnetic-field measurement with a 10°-azimuthal resolution to solve eq. (5.1) and is thereby well suited to study the axial symmetry of the SDS magnetic-field, although the MobSU system is still in a commissioning stage.

During SDS 2 a few measurement runs were performed on the LFCS coil 6 and 12 when the 3.8 G- and 9.0 G-setting were applied. The label of a MobSU measurement consists of the LFCS ring-number and the axial (upstream or downstream) position of magnetometer. Therefore it is possible to evaluate the distribution of the remanent and induced magnetic-field (section 5.3) and their disturbance of the axially symmetry.

As described for the other magnetic-field sensors, it is necessary to calibrate the magnetometers (as in section 3.3.1) and to determine the position and orientation of the magnetometer (as in section 3.4.3) in order to analyze the magnetic-field measurements and compare it to a magnetic-field simulation. A position and orientation of a MobSU is determined based on the distance traveled and a measurement of an inclinometer. The position uncertainty is ±9 mm. The orientation uncertainty is between −0.7° to 1.6°, as a result of a torque on a MobSU at the respective position and consequently affects mostly the x- and y- component of the magnetic-field measurement. The measurement uncertainty of the sensor is about 0.5 % and a maximal offset by the amplifier of 0.35 µT (ref. [Let11], [Osi12b]).

After one revolution around a LFCS ring the MobSU is stopped at a docking station, the data is extracted and analyzed on a local computer. An user is then provided with a calibrated field measurement that is transformed and rotated to match the KATRIN coordinate-system. Since the position of a MobSU is close to the air-coil cables, its measurement is already sensitive to minor variations of the distance between a magnetometer and a current-carrying conductor. To use the MobSU data in a comparison with the SDS magnetic-field model, the position of a MobSU must be corrected for the deformation of the respective LFCS ring and the realistic discretisation of the LFCS and EMCS system must be utilized (see fig. 3.5). That the parameterization of the deformations is correct can be seen by the corresponding shape of the simulated magnetic z-component to the measurement (fig. 5.10).

Even then it remains difficult to analyze the individual components of the magnetic-field when a current is applied to the EMCS. The position of a MobSU magnetometer close to the EMCS cables leads to a strong variation of the observed magnetic field; combined with angular uncertainty up to 1.6° and a position uncertainty of about 1 cm can cause a deviation between the magnetic-field measurement and simulation of several µT. Unfortunately, the EMCS was in operation during all MobSU measurements.

Therefore, the magnetic-field is analyzed as a deviation of the z-component of a measured magnetic-field to a simulation result $\vec{B}_{\mathrm{dev}} = \vec{B}_{\mathrm{exp}} - \vec{B}_{\mathrm{sim}}$. The results of the MobSU measurements are then compared to the results obtained with the high-precision magnetometers. The MobSU measurements in the following section were all performed on 2014-12-16 and correspond to the measurements of day 12 of the high-precision magnetometers in fig. 5.7.

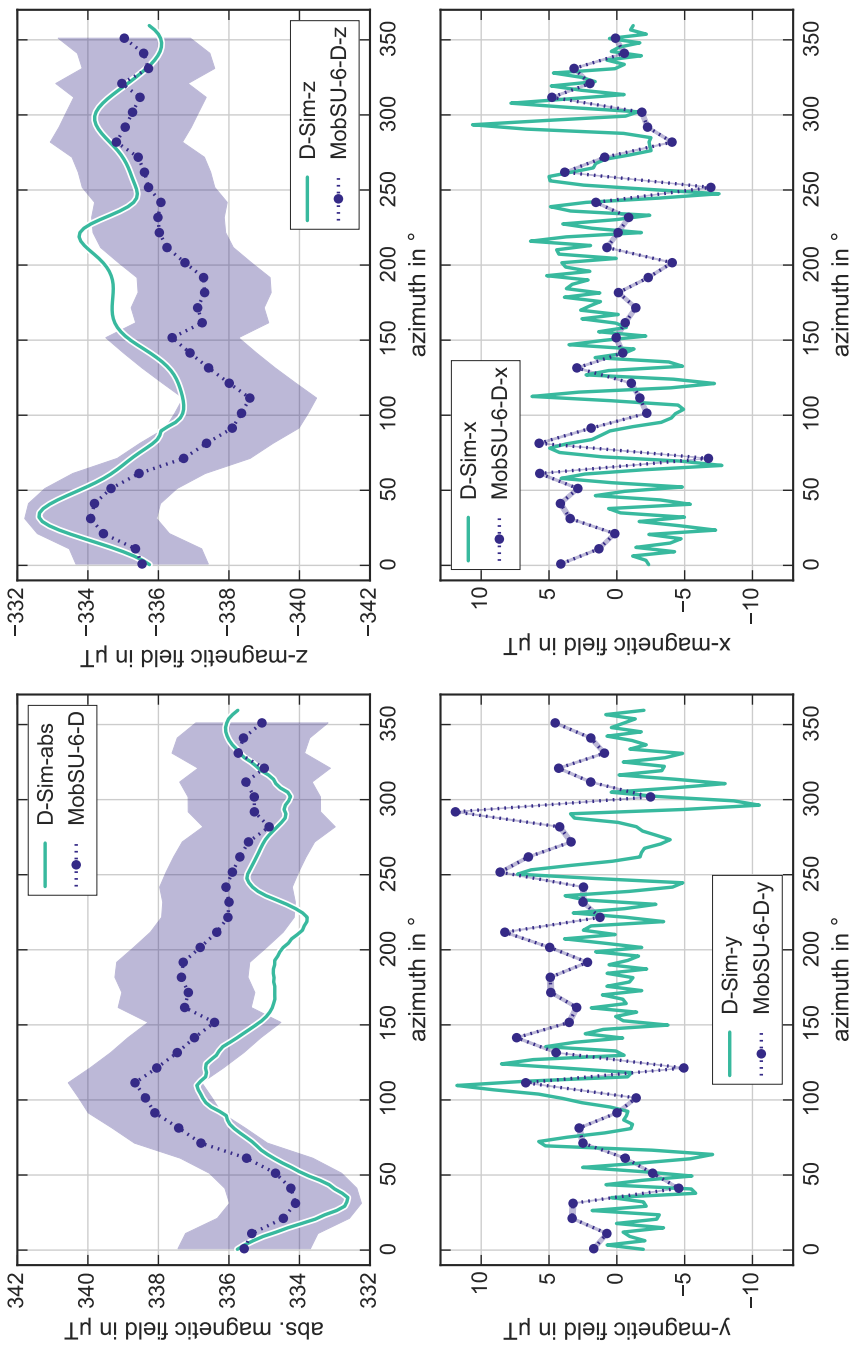

Figure 5.10: Magnetic-field components of a MobSU measurement. Here a measurement is shown of the downstream magnetometer of a MobSU mounted on LFCS 6 at a z-position of about $-1.56\,\mathrm{m}$ with an 1σ-uncertainty band. For the measurement a $3.8\,\mathrm{G}$-setting was applied, EMCS and SDS magnets were operated with nominal currents. Also included is a simulation of the magnetic-field based on the realistic discretized air-coil model. The asymmetric variation of the z-component is caused by the LFCS deformation and the x- and y-components are dominated by the non-uniform magnetic field of the EMCS system on outer radii. Large deviations for the x- and y-components are the result of the angular uncertainty of the magnetometer.

5.4.1 Azimuthal symmetry of the magnetic-field at various axial positions

When a stable 3.8 G setting was applied and the LFCS and EMCS was set to their nominal currents, a measurement run with a MobSU on LFCS ring 6 and 12 was performed. The four magnetometers are at an axial position of −1.56 m, −1.11 m, 3.83 m and 4.28 m, where the first two can roughly be compared to the central magnetometer-ring at −0.14 m and the two later correspond to the position of the downstream high-precision magnetometers at 4.3 m.

Magnetometers mounted on a common MobSU give similar results within uncertainty (fig. 5.11). The observed magnetic-field variation of MobSU-6 (MobSU-12) features a mean magnetic-field deviation of −0.5 µT (1.4 µT) and a maximal spread of 2.6 µT (4.3 µT) and thus are comparable with the associated high-precision magnetometers (fig. 5.4), but are slightly enhanced due to the larger radial position. Therefore, no variation of the magnetic background field along the z-axis is observed within a 0.45 m-range with the given sensitivity.

In a simplistic model of the magnetic background field, the magnetization of the steel rods in the bottom (top) wall from $y_0 = -6.2\,\mathrm{m}$ to $y_1 = 1.9\,\mathrm{m}$ at $x_{\mathrm{bot}} = \pm 9.4\,\mathrm{m}$ ($y_0 = 1.9\,\mathrm{m}$ to $y_1 = 7.8\,\mathrm{m}$ at $x_{\mathrm{top}} = \pm 7.4\,\mathrm{m}$) is approximated by one magnetic dipole each. A resulting magnetic-field deviation can be expressed by a superposition of the modified eq. (5.9) at the MobSU position with

$$B_{\mathrm{dev}}(\phi) = \sum_{i=0}^{3} \frac{-\mu_0 m_{\mathrm{z,i}}}{4\pi} \left(r_i - r_{\mathrm{MobSU}} \cos(\phi - \phi_i)\right)^{-3}, \tag{5.14}$$

where a wall has a magnetic moment m_{z} along the z-axis in a distance r_i to the spectrometer center and ϕ_i is the corresponding angle (fig. 5.1). Due to the similar demagnetization of the top walls, the same magnetic moment is assumed. That leads to only three fit parameters to an avoid overfitting.

Assuming a homogeneous magnetization and constant material properties, the steel density differences between the top and bottom walls predicts a magnetization ratio of 4.3 that is in agreement with the observed ratio of 4.15. A change of sign of the magnetization is observed for the top-wall component, that is plausible based on fig. 5.9.

Although the presented fit model can not reliably describe the magnetic background field inside the spectrometer volume, it provides the evidence that azimuthal distortions originate from a magnetization of the main spectrometer walls and B_{rem} is rather homogeneous.

Table 5.5: Fit results of MobSU measurements based on function eq. (5.14). First four rows refer to fig. 5.11 and last two an fig. 5.12. All magnetic moments are given in units of $1.0 \times 10^6\,\mathrm{Am}^2$. Small reduced χ^2 values due to large measurement uncertainties.

magnetometer	top	bottom east	bottom west	reduced χ^2
MobSU-6-U	37 ± 6	-37 ± 26	206 ± 26	0.43
MobSU-6-D	15 ± 6	-111 ± 20	139 ± 26	0.42
MobSU-12-U	-59 ± 9	-207 ± 37	44 ± 37	0.89
MobSU-12-D	-67 ± 10	-257 ± 43	102 ± 43	1.17
MobSU-6-U	103 ± 21	242 ± 88	551 ± 89	5.05
MobSU-6-U	69 ± 15	93 ± 65	436 ± 66	2.75

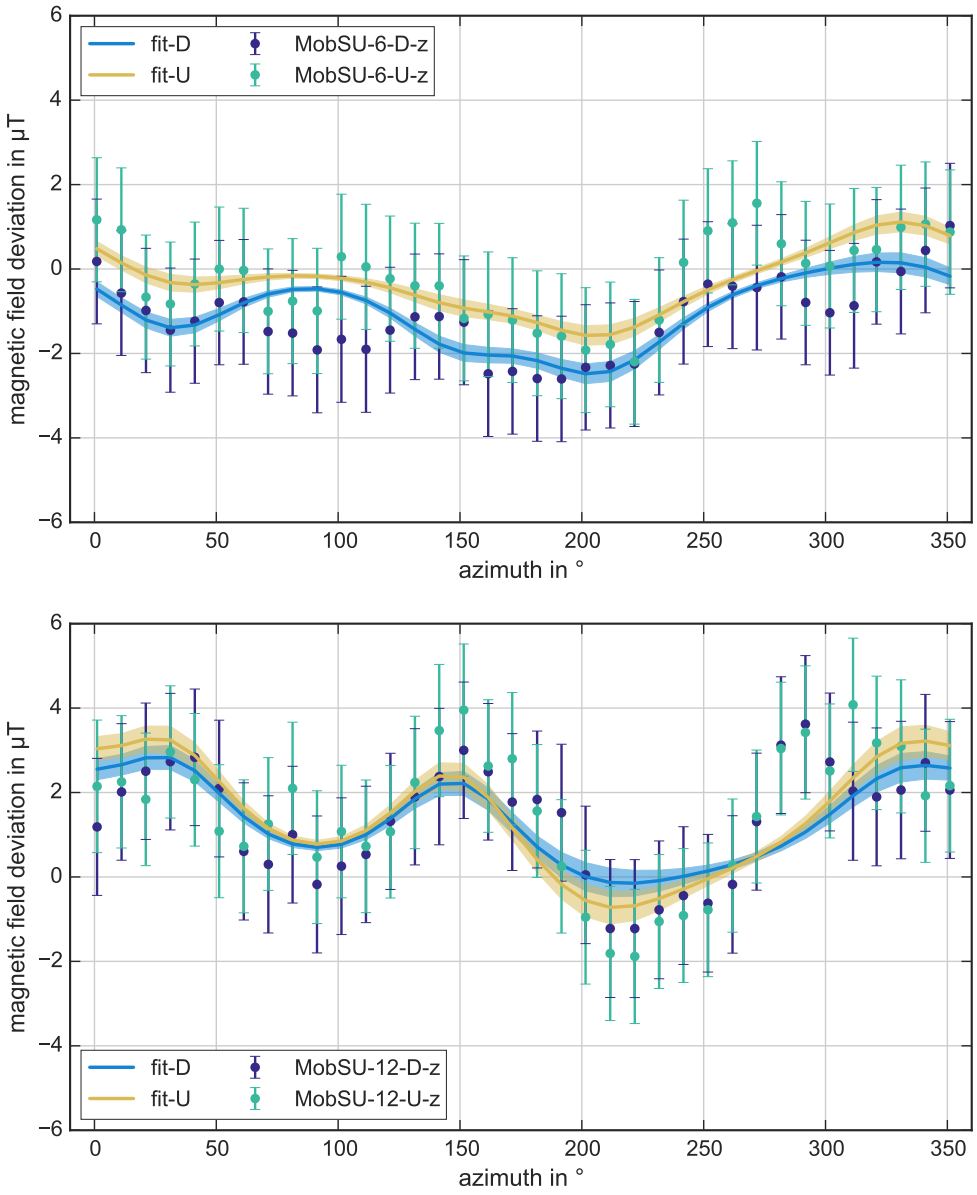

Figure 5.11: Azimuthal symmetry of the magnetic-field at various axial positions along the main spectrometer. The LFCS is set to a 3.8 G-setting, the SDS solenoids and the EMCS to their nominal currents. In the upper (lower) plot the magnetic-field deviation $\vec{B}_{\mathrm{dev}} = \vec{B}_{\mathrm{exp}} - \vec{B}_{\mathrm{sim}}$ of the upstream and downstream magnetometers (U and D) is shown at an axial position of $-1.563\,\mathrm{m}$ and $-1.113\,\mathrm{m}$ ($3.833\,\mathrm{m}$ and $4.283\,\mathrm{m}$). An error band corresponds to the 1σ-uncertainty of the $\vec{B}_{\mathrm{dev}}$ fit.

5.4.2 Azimuthal symmetry of the magnetic-field for different settings

A change of the induced magnetic-field by the magnetic materials is most pronounced in the central region when the LFCS currents are changed (fig. 5.9). Therefore, another MobSU measurement was performed on LFCS 6 when a stable 9.0 G-setting was applied; other magnetic-field components are unaltered.

An enhanced magnetic-field deviation and variation of $(-4.3 \pm 1.9)\,\mu\mathrm{T}$ is observed on average (fig. 5.12, lower plot). A similar tendency was observed for the high-precision magnetometers when the two magnetic-field settings are compared (fig. 5.4). Their linear dependence on the absolute magnetic field of $(3.9 \pm 0.3)\,\mu\mathrm{T\,mT^{-1}}$ is confirmed by the MobSU with $(3.2 \pm 1.2)\,\mu\mathrm{T\,mT^{-1}}$. As the pattern of the downstream/upstream side measurement show no significant deviation from each other, as well as a 3.8-ratio of the top and bottom magnetization, rather uniform properties of the magnetic material are expected. Namely a homogeneous distribution of magnetization within the walls and a rather uniform relative permeability μ_r. However, eq. (5.14) describes the differences of the two magnetic-field variations insufficiently (fig. 5.12, lower plot). The fit features an increased χ^2 compared to the 3.8 G results, revealing the limitation of the approximation of the magnetic materials. Further, profound investigations on the magnetic background field are needed, based on MobSU measurements and additional magnetometers (ref. [Let]), to develop a realistic model.

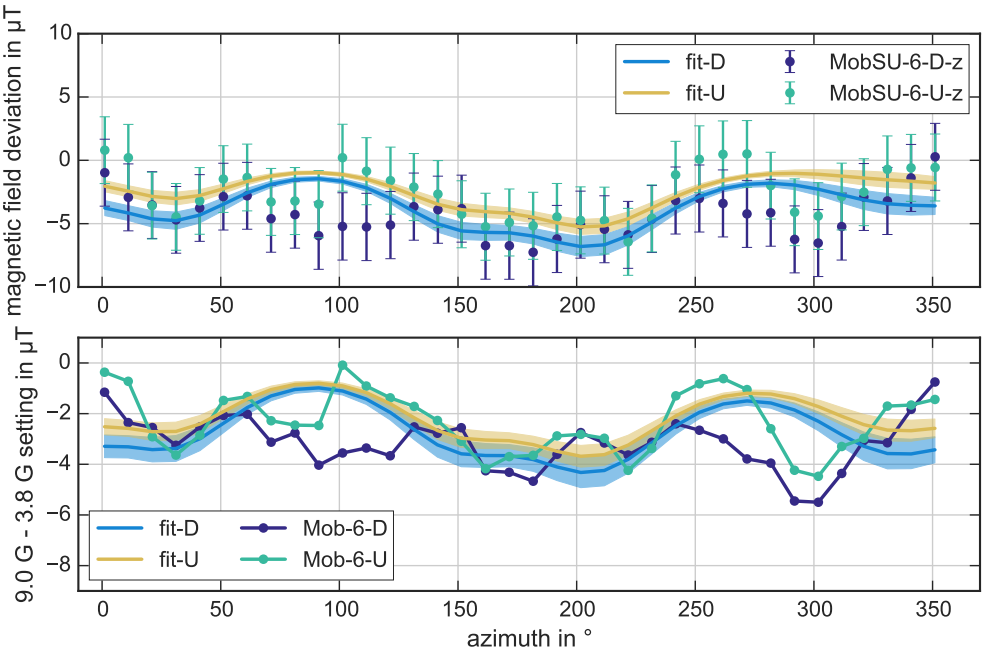

Figure 5.12: Azimuthal symmetry of a 9.0 G-setting and the difference to a 3.8 G-setting. In the upper plot the LFCS is set to a 9.0 G-setting and the magnetic-field deviation $\vec{B}_\mathrm{dev} = \vec{B}_\mathrm{exp} - \vec{B}_\mathrm{sim}$ of the upstream and downstream magnetometers (U and D) of a MobSU mounted on LFCS 6 are fitted with eq. (5.14). In the lower plot the difference to the fit result with a 3.8 G-setting (fig. 5.11) is shown.

5.5 Asymmetry correction with the EMCS

The azimuthal field asymmetry is the dominant contribution to the overall field uncertainty. The preferred strategy to handle the observed asymmetric field structure is to extend the existing field model for a remanent and induced field component. To do so, the entire ferromagnetic materials of the experimental hall have to be parametrized. It is expected that the required additional magnetic-dipole elements are of the order of 10^2 to 10^3. Consequently also way more magnetometers are needed to measure the magnetic-field at various positions and field configuration. Only then a reliable and realistic field model can be generated. Possibilities for an extension of the magnetometer sensor-grid are currently evaluated.

In this thesis, an alternative approach is adopted. The azimuthal asymmetry of a field setting is parametrized by a polinom of n-th order where the constant term can be compensated by an adjustment of the currents of the EMCS. By this means, a reduction of about 50 % of the observed magnetic-field deviation is expected in the center region of the spectrometer for a 3.8 G setting (fig. 5.11). For higher magnetic-field strengths and other axial positions, the reduction factor is slightly reduced (fig. 5.4 and fig. 5.12).

Optimal currents for the EMCS system are found when the absolute field in the central region of main-spectrometer is minimal. In the center of the main-spectrometer, the average absolute field

$$B_{\mathrm{abs}}\left(I_{\mathrm{EMCS}}\right) = \sum_{i=0}^{6} \frac{1}{6} \|\vec{B}_{\mathrm{i}}\|, \tag{5.15}$$

is the sum of the absolute fields of the high-precision magnetometers on the central sensor-ring. The uncertainty of a measurement B_{abs} is the quadratic sum of the individual sensor uncertainties. To determine the optimal current-setting of the EMCS, the horizontal and vertical coils were individually varied in 1 A-steps about ± 20 A around their nominal current set-values. For a reliable empirical model, the SDS solenoids were operated with their nominal field setting.

In fig. 5.13, B_{abs} is shown in dependence of the applied EMCS current and compared to a simulated magnetic field $B_{\mathrm{abs,sim}}$ where only the earth magnetic-field contributes to the azimuthal asymmetry. While for the x-axis only a minor magnetic-field deviation is observed, it is much more pronounced along the y-direction. This result is in agreement with previous result, where a vanishing magnetic-field deviation is observed along the x-axis (fig. 5.2). Fitted with a parabolic function, the optimized current are determined to $I_{\mathrm{EMCS-X}} = (7.197 \pm 0.039)\,\mathrm{A}$ ($I_{\mathrm{EMCS-Y}}(46.448 \pm 0.009)\,\mathrm{A}$). These results refer to a measurement when the LFCS system was turned-off. In this case, the magnetic-field variation is most pronounced due to the absence of field fluctuations of the LFCS coils (see fig. 4.10). Larger uncertainties of single data points are the result of network issues that disturb the communication between slow-control devices and cause a decisive reduction of the utilizable measurement time[1].

1 The sampling frequency of slow control data is usually 0.1 Hz. As most measurements had a duration of 120 s per current set-value, a loss of a few samples results in a substantial reduction of the measurement precision. The slow-control upgrade that enables a readout frequency of 5 Hz as used for the measurement of the magnetic field relaxation (section 4.3.1) was not available for the tests of this section.

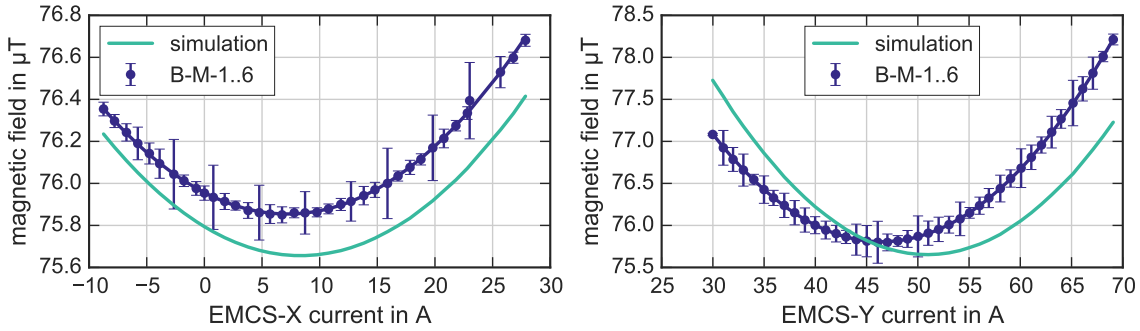

Figure 5.13: Empirical optimization of the EMCS currents. When one EMCS current was set to its nominal value, the other current was variate by ±20 A in 1 A-steps. The sum of absolute magnetic-field value is minimal when the magnetic background field is compensated (see text). A large deviation is observed for the vertical direction and a minor in horizontal direction. Here shown for a measurement with turned-off LFCS coils. An offest of 2 µT is added to the simulation results to account for remant magnetic fields.

The empirical optimization of the EMCS currents was repeated for various settings of the LFCS to cover the full range of the possible absolute field in the analyzing plane. The results of the parabolic fit (see fig. 5.13) to identify an optimal EMCS current setting are visualized in fig. 5.14. Uncertainties of measurements with applied currents to the LFCS system are larger due to the current fluctuation of the power supplies and the described slow-control issues. Additionally, transition state effects (see fig. 4.6) after ramping to another field setting can not be excluded. A linear fit is used to approximate the observed optimal EMCS currents for any absolute field in the analyzing plane (table 5.6).

Along both axes a significant offset to the nominal current settings is observed where a relative current deviation of about 22 % (7.1 %) is determined in x-direction (y-direction). The offset is predominantly defined by the measurement with a turned off LFCS where on average an uncertainty of only 24 mV on the optimal EMCS current was observed. This result is comparable with the air-coil fluctuations (table A.2) and another clear evidence for a remanent magnetization of the steel rods in the reinforced concrete.

However, the influence of an additional field is more pronounced in x-direction than in y-direction, although the opposite was expected. This is most noticeable by comparing the two slopes of the linear fit that nearly vanishes for the y-component. On the one hand, this result originates from much increased uncertainties on the optimal EMCS currents with an applied current on the LFCS by a factor of 27. On the other hand, the large χ^2 of 5.5 is a sign for a systematic effect that compromises the measurement precision significantly. It is expected that the slow control issues and especially the transition state effect are causing these issues. For a more accurate determination field dependence at higher absolute field values, these measurements should be repeated with an overhauled slow-control system that allows for a faster and more reliable readout as well as a longer overall measurement duration.

To verify that the optimized EMCS settings do in fact improve the symmetry of the magnetic-field, it was applied in various tests. The most straight forward test is a measurement with an asymmetric magnetic-field (table A.1) as in the alignment study of the FPD system

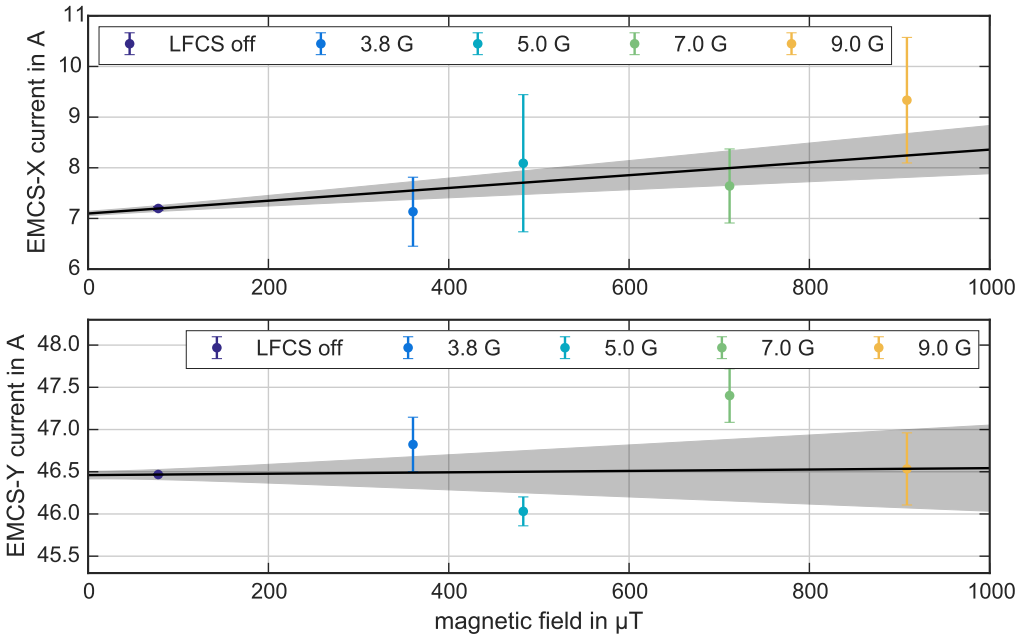

Figure 5.14: Fit results of the empirical EMCS optimization. For various magnetic field settings the minimum of a parabolic (see fig. 5.13) is shown. A linear fit is shown in black with a 1σ uncertainty band. For all magnetic field settings the magnetic background field is slightly over compensated. These results are in agreement with a remanent and induced field of the reinforced concrete walls.

(section 3.4). In the original analysis, a symmetric magnetic-field is assumed to calculate the alignment of the FPD system relative to the main-spectrometer. By repeating the alignment measurement with optimized EMCS currents, an improved agreement between the simulated and measured alignment is expected.

Already by eye a more symmetric ring-structure is observed in fig. 5.15 that is confirmed by a ring-fit analysis. With optimized EMCS currents, the deviations of the mean ring centers to the simulated value is reduced by 41 %. Thereby the EMCS system can be used to optimize the magnetic-field symmetry and partly compensate for an additional remanent and induced magnetic-field of ferromagnetic materials.

Table 5.6: Linear fit results of the optimal EMCS currents. The name of the coil system is in the first column, where X and Y correspond to the resulting field directions. Based on the results in fig. 5.14 an empirical model for an optimal EMCS operation can be identified. Thereby approximately 50 % of the additional remanent and induced fields can be compensated.

system	slope (mA/µT)	offset (A)
EMCS-X	1.26 ± 0.58	7.097 ± 0.055
EMCS-Y	0.08 ± 0.62	46.460 ± 0.055

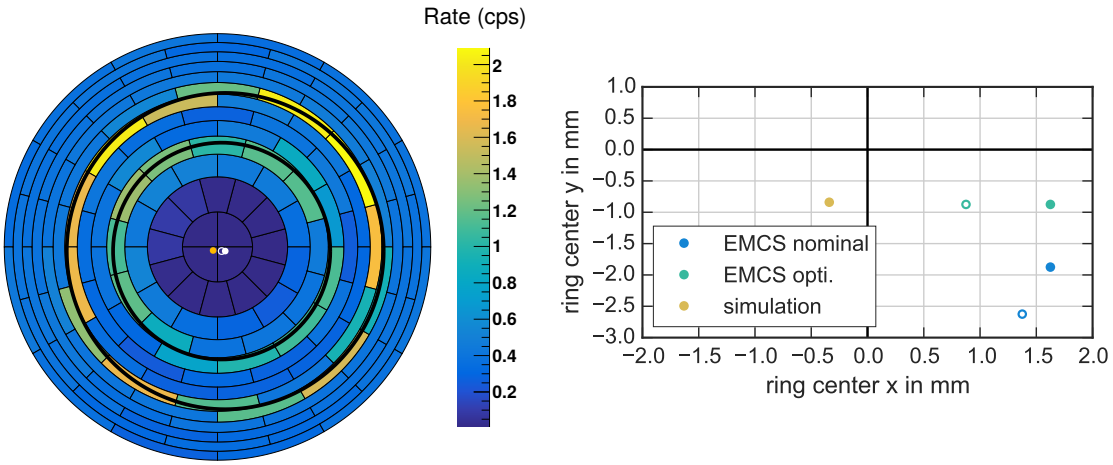

Figure 5.15: Ring fit analysis for optimized EMCS setting. In an asymmetric magnetic-field setting the comb holding-structure of the inner electrode is projected on the detector. On the left, two rings are fitted to the count rate distribution of the FPD. The outer ring center is marked with a white bullet, the inner with a circle. The simulated ring center based on the known misalignment is shown as golden bullet. On the right, a zoom to the FPD bulls-eye is shown together with ring fits for the original EMCS setting. The outer ring center is marked with bullet and the inner ring with a circle. A 50 % improved agreement of the alignment was accomplished.

Moreover, this result is also close to the expected 50 %-reduction from the MobSU measurements, proving the consistency between the field monitoring devices. Tests of the field symmetry inside the spectrometer vessel can be found in section 6.5 based on the studies of the transmission properties and in appendix C based on the observed background rate.

5.6 Conclusion

In this chapter the strategy of the KATRIN experiment to monitor the magnetic field was explained and the accuracy of the magnetic-field model was tested. Based on those results, the long-term stability of the applied magnetic field was determined, the influence of a remanent and induced magnetic-field of magnetic materials in the main spectrometer building estimated, the azimuthal symmetry of the magnetic field evaluated and a countermeasure introduced to account for the observed asymmetry in the magnetic field.

To determine the neutrino mass with the KATRIN experiment, precise knowledge of the magnetic field is essential, especially in the central region of the main spectrometer where the position of the analyzing plane is defined, and consequently also the energy resolution. During a tritium measurement the magnetic field is not directly accessible via measurements inside the spectrometer, but a combination of a precise field measurement outside of the vessel and an accurate field simulation is deployed to determine the magnetic field at any point in the active volume. As this method relies only on a few magnetometers, an elaborate and thorough acquisition of the alignment information is required of all components that generated a field (section 3.4) and so form a detailed magnetic-field model.

For the first time all magnetic field components, as they were present during SDS 2, were

studied with the newly installed high-precision magnetometers. It was demonstrated that even tiny magnetic-field deviations in the sub-µT regime can now be determined (section 5.1.1). Utilizing this precision, it is proven that

- the stray field of magnets at any distance to the main spectrometer can be detected and reproduced within the KATRIN setup. (section 5.1.2 and section 5.1.4).
- the magnetic field monitoring is reliable in the full magnetic field range of the LFCS (section 5.1.3).
- the procedures to align magnetic-field components are sufficient and any further unaccounted misalignment is below the sensitivity limit (section 5.1.5).

Based on those results the properties of the magnetic field at the KATRIN main spectrometer are characterized.

A long-term analysis of the magnetic field relieved a negligible magnetic-field drift of $(0.6 \pm 0.8)\,\mathrm{nT/d}$ that is in agreement with a fluctuation of the earth magnetic field and the precision of a field measurement is about 37 nT (section 5.2). In the most important 3.8 G-setting, an accuracy of 2 µT is reached that fulfills all previous defined requirements of the magnetic-field monitoring.

Most measurements featured a deviation to simulation values due to an inadequate representation of the magnetic background field. This is associated with a remanent magnetic-field of magnetic materials in the concrete of the KATRIN buildings. The remanent component was reduced prior to SDS 2 by a demagnetization of the main spectrometer building. Also, the magnetic-field deviation depends on the absolute magnetic-field that is associated with an induced magnetic-field (section 5.3.2). In the central region it amounts to $(3.9 \pm 0.3)\,\mu\mathrm{T\,mT^{-1}}$. However, the magnetic background field features a time dependency, as every test of a DPS magnet causes a change of the magnetic background field (section 5.3.1). Further shifts are expected when the full transport section is in operation, especially a more severe impact is expected from the CPS solenoids. Based on the DPS measurements, an uncertainty of the magnetic background field of 0.67 µT is estimated.

Fortunately, the observed magnetic-field deviations are rather homogeneous. Measurement of the magnetic-field with the MobSU system have a high angular-resolution and revealed that the azimuthal asymmetries can already be explained by a simplistic model of the ferromagnetic materials (section 5.4). Therefore it is reasonable to assume that a realistic model can be developed based on measurements with a fully functioning MobSU system and an additional sensor grid of magnetometers that is currently commissioned.

As a first countermeasure, the constant fraction of the asymmetric magnetic-field can be corrected with adjusted currents of the EMCS system. By this means, an improvement of 41 % is already accomplished.

CHAPTER 6

Determination of the transmission characteristics of the spectrometer

The sophisticated interplay between an electrostatic potential and magnetic field of a MAC-E filter defines the transmission properties for electrons along various paths trough the spectrometer, referred to as the transmission function. As outlined in section 2.1, the integral shape of a transmission function depends on the angular- and energy-distribution of the electron source. Molecular tritium is utilized in KATRIN, where the energy can be described by Fermi's Golden Rule eq. (1.24) with an isotropic angular distribution. The transmission function used in the analysis of the neutrino mass-measurement is either calculated analytically or obtained by Monte Carlo simulations, in both cases a precise knowledge of the radial distribution of the electrostatic potential and magnetic field in the analyzing plane are crucial input parameters. The electromagnetic properties of the main spectrometer are evaluated by transmission-function measurements with a quasi mono-energetic and angular selective e-gun presented in this chapter.

The geometric and electromagnetic setup of the full SDS apparatus is incorporated in the analyses of e-gun measurements to extract and disentangle the characteristics of the e-gun and in particular of the spectrometer. The applied methodologies were introduced during SDS 1 (ref. [Gro15], [Zac14]). Based on the SDS 1 results, hardware improvements were implemented for SDS 2 (ref. [Beh16]), an advanced measurement strategy introduced in the course of the thesis at hand and significant extensions in the handling of statistical measurement-uncertainties are utilized (ref. [Kra16]).

This chapter will reproduce the simulated radial dependence of the retarding potential and magnetic-field in the analyzing plane (fig. 2.5) and study the agreement of the observed magnetic-field uncertainties and deviations between the high-precision magnetometers and e-gun measurements. First underlying formulas of calculation of the transmission function are given, followed by the extraction of the transmission probability information form measurements and finally the measurement campaign to map the electric and magnetic-field in the analyzing plane are presented.

6.1 Theoretical aspects of the determination of the transmission function

When the transmission conditions (section 2.1.2) are fulfilled, the transmission function can be calculated analytically. The following section represents a summary of the calculations given in ref. [Gro15]. The description of the e-gun properties are extended and adjusted to the SDS 2 setup.

6.1.1 Analytic calculation of the transmission function

An electron is transmitted trough a MAC-E filter when its starting kinetic energy E_S is above the transmission energy E_tr. The transmission energy

$$E_\mathrm{tr} = \frac{q(U_\mathrm{A} - U_\mathrm{S})}{1 - \sin^2(\theta_\mathrm{S}) \cdot \frac{B_\mathrm{A} \cdot (\gamma_\mathrm{S}+1)}{B_\mathrm{S} \cdot (\gamma_\mathrm{A}+1)}} \tag{6.1}$$

is based on the spectrometer properties, the electrostatic potential U_A and the magnetic field B_A at the analyzing point, as well as the source properties, the initial potential U_S and initial angle θ_S of the electron momentum relative to the magnetic field. For mono-energetic electrons with a discrete angle, the transmission function $T(U_\mathrm{A})$ becomes a Heaviside step function

$$T(U_\mathrm{A}) = \Theta(E_\mathrm{S} - E_\mathrm{tr}(U_\mathrm{A})), \tag{6.2}$$

that is 0 for $E_\mathrm{S} < E_\mathrm{tr}$ and 1 for $E_\mathrm{S} \geq E_\mathrm{tr}$. When an energy distribution is introduced, the transmission function is smeared out to

$$T(U_\mathrm{A}) = \int_{E_\mathrm{tr}(U_\mathrm{A})}^{\infty} F(E_\mathrm{S})\mathrm{d}E_\mathrm{S}, \tag{6.3}$$

where only the fraction of electron above the transmission energy E_tr can be detected.

An additional angular distribution requires a further extension of the transmission function. For a given transmission energy in eq. (6.1) the sinusoidal term defines the transmission probability when the potential difference $(U_\mathrm{A} - U_\mathrm{S})$ and magnetic-field ratio $B_\mathrm{A}/B_\mathrm{S}$ are fixed. Mono-angular electrons are transmitted when $0 \leq \theta_{\mathrm{e}^-} \leq \theta_\mathrm{S}$ is fulfilled and the transmission function is expressed by

$$T(\theta_{\mathrm{e}^-}) = \Theta\left(\theta_{\mathrm{e}^-} - \theta_\mathrm{S}\right). \tag{6.4}$$

Therefore are electrons transmitted with an initial angle below a maximum

$$\theta_\mathrm{tr}(E_\mathrm{S}) = \arcsin\left(\sqrt{\frac{E_\mathrm{S} - q(U_\mathrm{A} - U_\mathrm{S})}{E_\mathrm{S}} \cdot \frac{B_\mathrm{S}}{B_\mathrm{A}} \cdot \frac{(\gamma_\mathrm{A}+1)}{(\gamma_\mathrm{S}+1)}}\right) \tag{6.5}$$

that is found by inverting eq. (6.1).

In the generalized case of an source with an arbitrary angular distribution $\omega(\theta)$ and energy distribution $F(E_\mathrm{S})$, the transmission function is a double integral

$$T(U_\mathrm{A}) = \int_{E_\mathrm{tr}(U_\mathrm{A})}^{\infty} \int_{0}^{\theta_\mathrm{tr}(E_\mathrm{S})} \omega(\theta)\mathrm{d}\theta \cdot F(E_\mathrm{S})\mathrm{d}E_\mathrm{S}. \tag{6.6}$$

The inner angular-distribution integral can be interpreted as a weighting factor of the individual initial-energies in E_S.

6.1.2 Transmission function adapted to SDS 2 conditions

For a single transmission-function measurement, a fixed e-gun position and back plate angle is selected and only the potential difference $U_A - U_S$ is varied to determine the transmission energy E_{tr}. These two potentials are abstract observables that need to be linked to measured quantities. Therefore, the transmission equations (section 6.1.1) are adjusted to reflect the operation mode of the e-gun, the integration concept of thee-gun in the voltage distribution and the spectrometer properties.

The electron emission in the e-gun is based on the photoelectric effect. Laser UV light of 266 nm is suitable to release electrons from a gold layer with a low kinetic energy in the sub-eV regime. As the gold layer is embedded in the e-gun back plate, electrons are accelerated by its negative potential U_S, so the resulting kinetic energy at the start point is

$$E_S = qU_S + E_{kin}. \tag{6.7}$$

Due to the finite size of the spectrometer, the electrostatic potential features a radial inhomogeneity (fig. 2.5). The analyzing potential for a given a magnetic field line

$$U_A = U_{IE} + \Delta U_r \tag{6.8}$$

varies relative to the potential of the inner electrode $U_{IE} = U_{vessel} + U_{IEoffset}$, that is the sum of the potentials of two power supplies (section 3.1.2). As the inner electrode and the e-gun are galvanically connected, a battery pack and a power supply are utilized to obtain an offset to U_{IE} (fig. 3.9) as a relative e-gun potential

$$\Delta U_{EGun} = U_{bat} - U_{acc} \tag{6.9}$$

and thereby the potential difference of U_A and U_S. The relative e-gun potential ΔU_{EGun} is measured with a precision of 6 mV (ref. [Kra16], [Wac15]). To apply a potential difference by separate PSUs is disfavored as this setup introduces a much larger measurement uncertainty. E.g. the standard deviation of U_{IE} without a post-regulation is with ± 1 V already much larger (ref. [Kra16]). Finally, the potential difference[1]

$$\begin{aligned} U_A - U_S &= (U_{IE} + \Delta U_r) - (U_{IE} - \Delta U_{EGun} + E_{kin}/q) \\ &= \Delta U_r + \Delta U_{EGun} + E_{kin}/q \end{aligned} \tag{6.10}$$

can be rewritten, where ΔU_{EGun} is a measured quantity, and ΔU_r and E_{kin}/q are properties of the spectrometer or the e-gun respectively.

To determine the magnetic field B_A in the analyzing plane with eq. (6.6), the field B_S and the angular distribution $\omega(\Theta)$ must be known a priori. Unfortunately, these values are fully correlated. Therefore is the angular distribution $\omega(\Theta)$ only accessible via comprehensive electromagnetic field simulations and B_S by an independent field measurement.

1 Actually, an additional global offset is introduced when the work functions of the e-gun gold layer and the inner electrode system are considered. As long as ϕ_{eff} is constant during the measurement campaign the determination of ΔU_r is not affected and is therefore here neglected. Otherwise, when ϕ_{EGun} is determined by a dedicated measurement, ϕ_{spec} can be obtained from transmission function measurements.

6.2 Disentanglement of spectrometer- and e-gun-properties

A goal of the transmission function studies is to determine the potential inhomogeneity ΔU_r precisely and to reproduce the radial distribution accurately by simulations. Once ΔU_r has been established, the magnetic field ratio $B_\mathrm{A}/B_\mathrm{S}$ can also be determined based on transmission function measurements for a full description of the electromagnetic properties of the spectrometer. However, the spectrometer properties and e-gun properties are correlated, and so a set of sophisticated transmission-function measurements is required to disentangle the characteristics of these two components. The following examples are inspired by ref. [Gro15] and extended to the SDS 2 conditions to demonstrate how the spectrometer properties and e-gun properties manifests themselves in transmission-function measurements.

6.2.1 Electron gun characteristics

The two major parameters which define the e-gun characteristic, the energy and angular distribution, are discussed in this section. In first order, both distributions are sufficiently described by a normal distribution

$$f(x) = \frac{1}{\sigma\sqrt{2}\pi} \exp\left[-\frac{1}{2}\left(\frac{x-\mu}{\sigma}\right)^2\right] \tag{6.11}$$

To discuss specific features in the transmission function measurements. To emphasize certain phenomena mono-energetic or mono-angular distributions are shown in addition. Other parameters such as the electron-rate stability, the gold layer work function and voltage stability are assumed to be constant and are discussed in section 6.3.2. The potential inhomogeneity ΔU_r is set to 0 V in this section to suppress the spectrometer influence.

Energy distribution

The initial kinetic-energy of the electrons emitted from the e-gun gold layer, is referred to as the energy distribution of the e-gun.

In first order, the initial kinetic-energy is described by the difference of the photon energy and the binding energy in gold (fig. 6.1). As a result, electrons are released with some kinetic-energy or not at all. In the ideal case, electrons are released with no additional kinetic-energy (dark blue line). The transmission function becomes a Heaviside function and electrons are transmitted trough the spectrometer when the start potential is just above the spectrometer potential. An initial kinetic-energy results in a transmission at lower start potentials which is proportional to the initial kinetic-energy (light blue line).

An additional energy uncertainty will lead to a smeared out energy distribution and the transmission function is described by an error function (yellow graphs). However, this can lead to a significant amount of electrons in the low energetic tail below 0 eV that are not released from the e-gun back plate (green graphs). This effect becomes noticeable in the error function as a kink on the high transmission rate side. To represent the transmission probability, the integrated energy distribution is renormalized.

Therefore, two additional parameters need to be introduced to describe an energy distribution. A cut parameter to include the edge at $E_\mathrm{kin} = 0\,\mathrm{eV}$, and an amplitude that represents the renormalization.

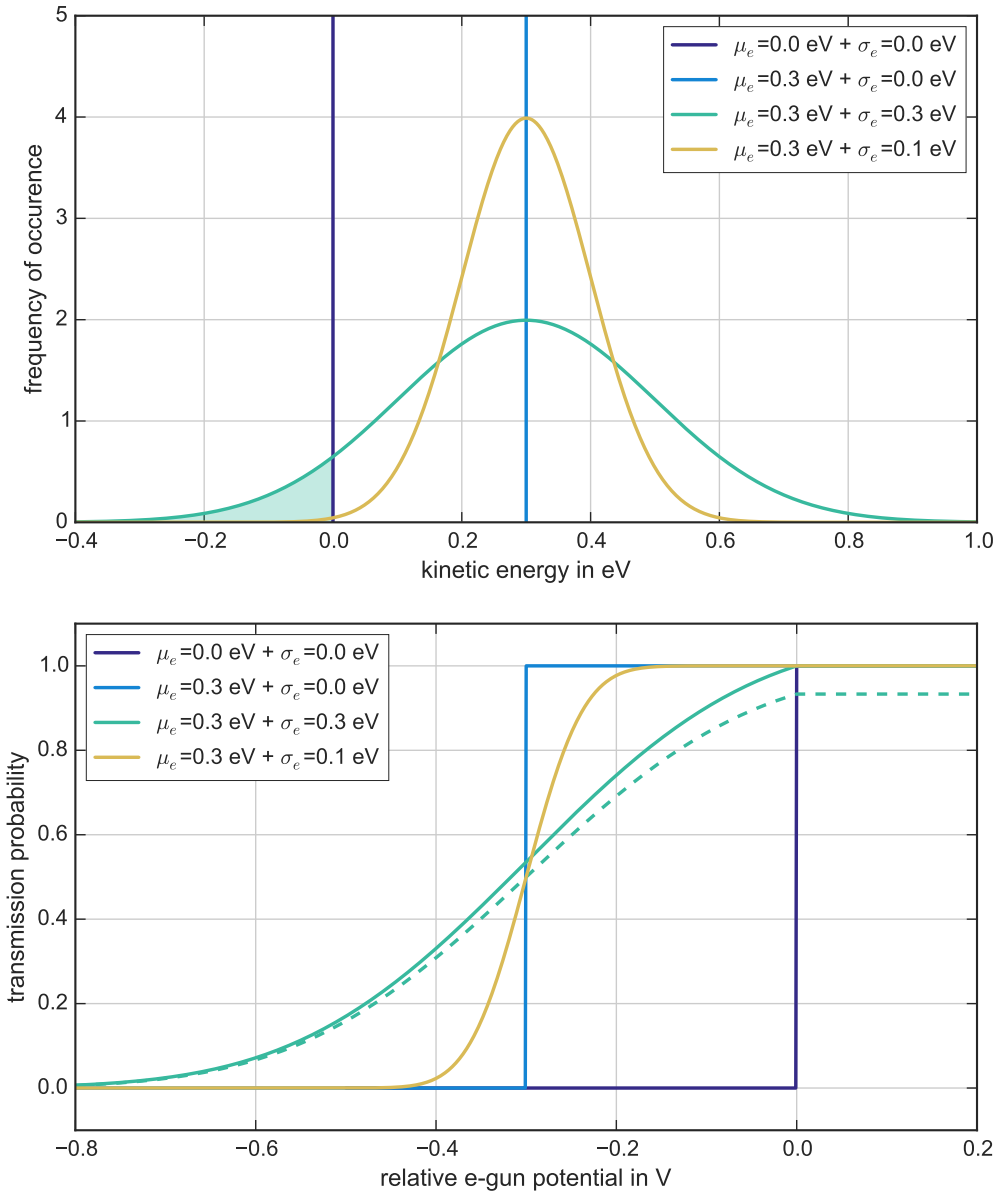

Figure 6.1: Example for transmission probability of various energy distributions of the e-gun. In the upper plot the differential energy-distributions and in the lower plot the integrated transmission functions are shown. The transport of mono-energetic electrons is described by a sharp Heaviside function, while a normal distribution of the initial energy result in an error function. Negative initial energies are suppressed as such electrons remain in the e-gun surface (filled area). A restrained energy distribution usually leads to a tail in the integrated spectrum at lower acceleration voltages and needs to be re-normalized (dashed line). An initial kinetic energy E_{kin} is an additional offset to the start energy $E_{\mathrm{s}} = qU_{\mathrm{egun}} + E_{\mathrm{kin}}$ and will therefore lead to a transmission at a lower relative e-gun potential ΔU_{EGun}. In all calculations a sharp polar angle of $\Theta = 0°$ is used and the potential inhomogeneity is neglected $\Delta U_{\mathrm{r}} = 0\,\mathrm{V}$.

Angular selectivity and distribution

The possible angles of electron momenta emitted from the e-gun relative to the magnetic field is referred to as the angular distribution $\omega(\Theta)$. The complicated interplay between the e-gun geometry and the applied electromagnetic field inhibit an analytic calculation, neither is a measurement quantity identified that is solely sensitive to the angular distribution. Thereby is a valid angular-distribution in the adiabatic-transport region, between the exit of the e-gun chamber and the PCH magnet, only accessible via elaborated simulations. In the thesis at hand, the center of the PS 2 magnet is defined as the start position where the magnetic field $B_\mathrm{S} = 4.514\,\mathrm{T}$ is rather homogeneous and accurate. To demonstrate the influence of $\omega(\Theta)$ alone, the initial kinetic-energy $E_\mathrm{kin} = 0\,\mathrm{eV}$ is neglected, the magnetic field in the analyzing plane is fixed to $B_\mathrm{A} = 360\,\mu\mathrm{T}$ and the spectrometer potential is set to $U_\mathrm{A} = 18.6\,\mathrm{kV}$.

From eq. (6.1) it appears that the transmission energy E_tr is shifted to higher values for larger electron angles Θ. The shift is proportional to $\sin^2(\Theta)$ and therefore non linear. This effect is demonstrated by mono-angular distributions in fig. 6.2 where three angles $\Theta = 0°$, 22.5°, 45° are equidistant, but the resulting energy differences ΔE_tr are not.

Equation (6.6) is integrated to calculate the transmission function. In case of a mono-angular distribution the resulting transmission function is described by a Heaviside step function. However, considering a normal distribution (eq. (6.11)) for $\omega(\Theta)$, the resulting transmission function can not be described by an error function. Due to the non-linear shift for larger initial angles a skewness is introduced. This effect is more pronounced for large σ_a.

Another asymmetry arises from the fact that the polar angle Θ is defined from 0° to 180°. Therefore, only positive values are used to describe an angular distribution. In the upper plots of fig. 6.2 the shaded areas indicate the negative polar angles "flipped" to positive values. The largest asymmetry in the resulting transmission function is introduced for an angular distribution with $\mu_\mathrm{a} = 0°$.

Please note that this description of an angular distribution is only valid for $\Theta \ll \Theta_\mathrm{max}$. Close to Θ_max a transmission shift is reduced asymptotically to a maximal value, comparable to the transmission function close to ΔE_full in fig. 2.4. In addition, the observed e-gun rate is reduced for electron angles $\Theta \approx \Theta_\mathrm{max}$ due to the magnetic mirror effect eq. (2.6). Therefore are too large electron angles avoided in this thesis.

Combined effect an angular- and energy distribution

The combined effect of an energy-distribution with various angular distributions is shown in the upper panel of fig. 6.3. In this example an normal distribution with $\mu_\mathrm{e} = 0.3\,\mathrm{eV}$ and $\sigma_\mathrm{e} = 0.3\,\mathrm{eV}$ is chosen for the energy distribution (fig. 6.1, green function). The same angular distributions as in fig. 6.2 are selected. The functions in the darkest colors represent the effect of an energy distribution alone for distinct angles. An additional broadening is introduced by an normal distributed polar angle which is more pronounced for larger polar angles. The lighter color indicate larger σ_a.

6.2.2 Spectrometer characteristics

When the e-gun properties are determined, the radial dependencies of electromagnetic properties of the KATRIN main-spectrometer are accessible via transmission function measurements. The individual panels in fig. 6.3 demonstrate the individual effect of the radial inhomogeneity of the electric-potential and the magnetic field.

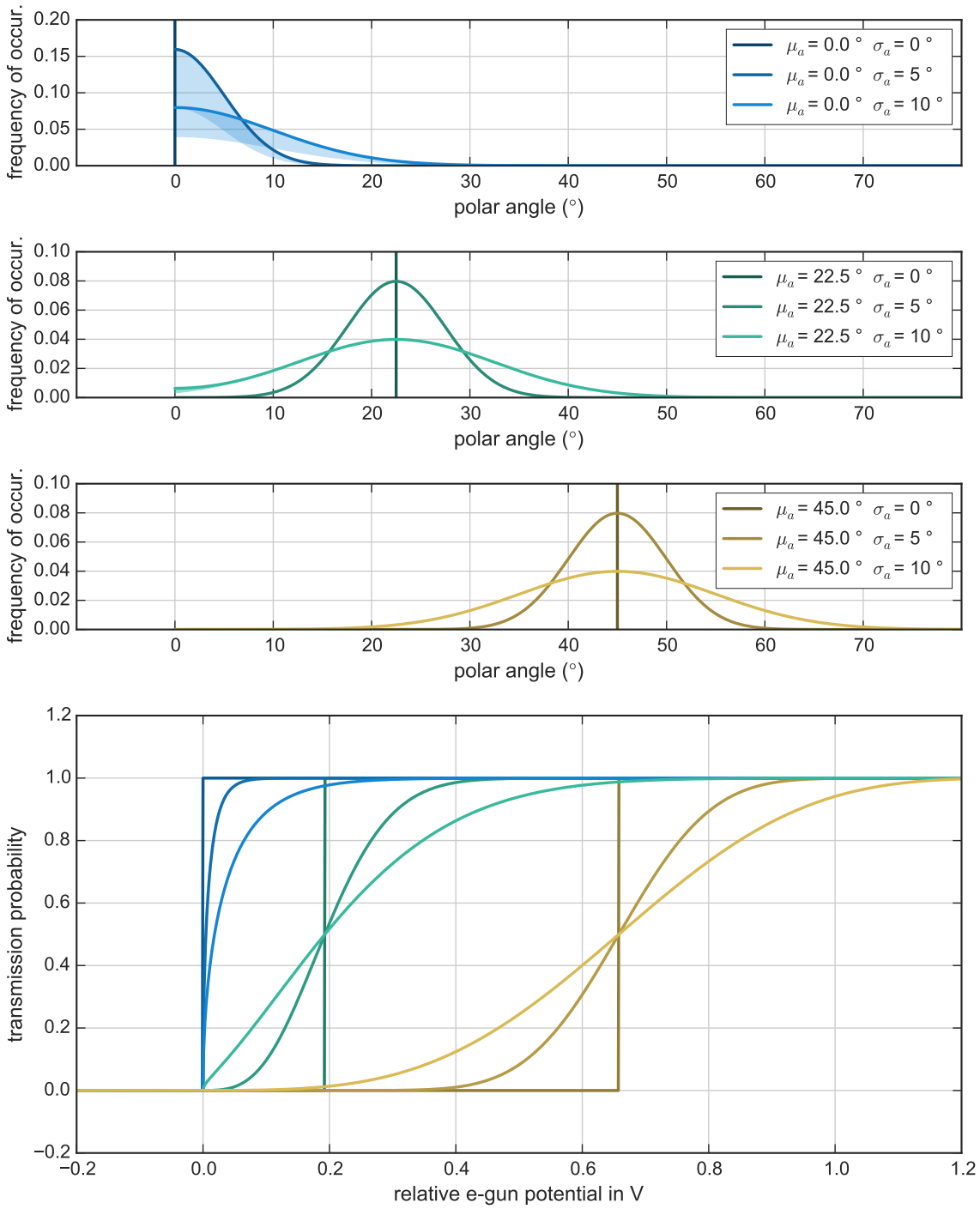

Figure 6.2: Example for transmission probability of various angular distributions of the e-gun. In the upper plot the differential angular-distributions and in the lower plot the integrated transmission functions are shown. Three polar angles Θ are selected with three associated angle distributions. For larger polar angles, additional acceleration voltage is needed to transmit electrons. This is a non linear relation where angles up to 45° are shifted more compared to smaller angles, leading to an asymmetric transmission function with a tail for higher acceleration voltages. As negative polar angles are not defined, those values are mirrored at $\Theta = 0°$, indicated by filled areas in the upper plot indicated by the filled areas. All calculations are performed with mono-energetic electron of $E_{\mathrm{kin}} = 0\,\mathrm{eV}$ and $E_{\mathrm{s}} = 18.6\,\mathrm{keV}$, a magnetic field ratio of $B_{\mathrm{s}}/B_{\mathrm{a}} \approx 1.2 \times 10^5$ ($B_{\mathrm{a}} = 360\,\mu\mathrm{T}$) and a potential inhomogeneity is neglected ($\Delta U_{\mathrm{r}} = 0\,\mathrm{V}$).

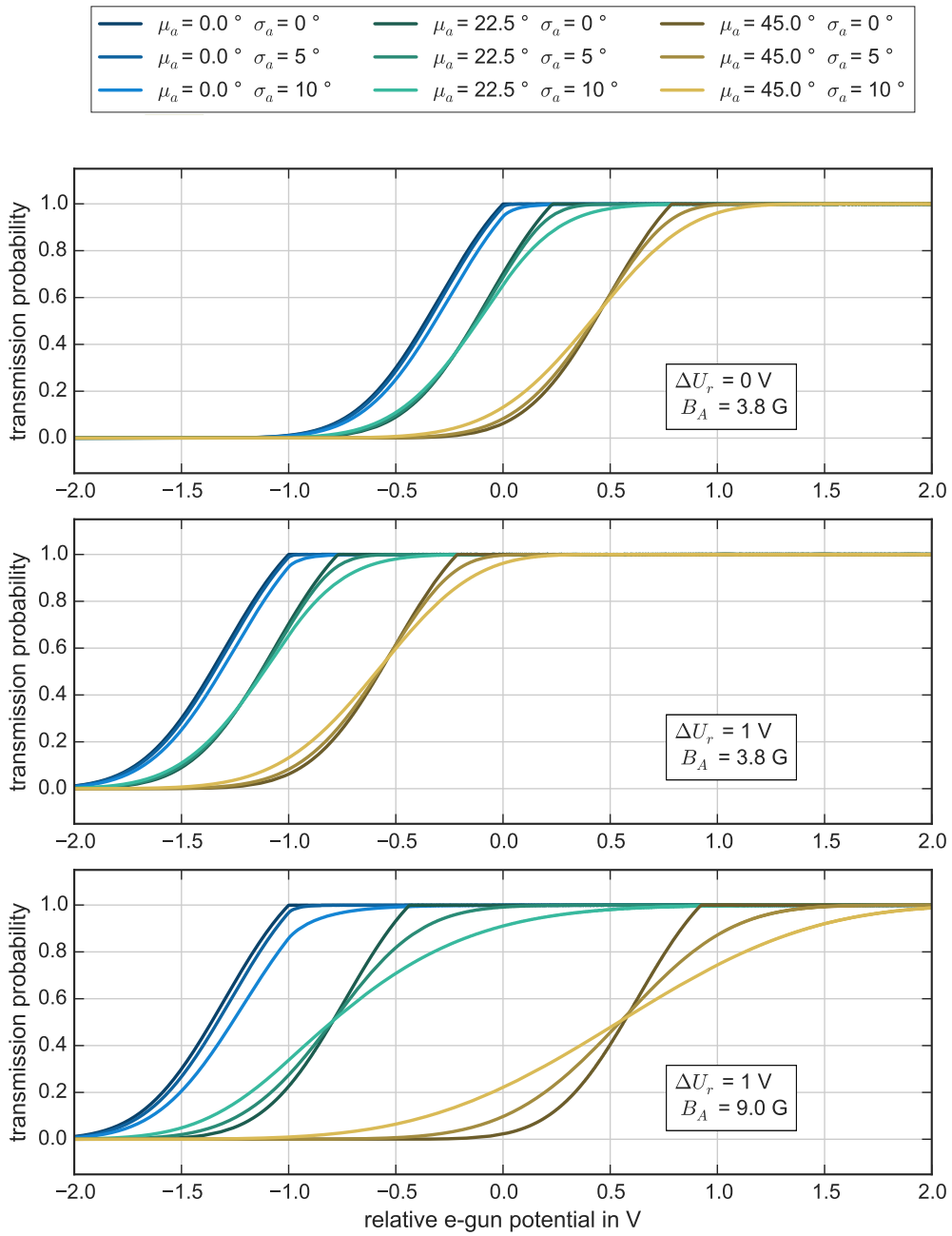

Figure 6.3: Example of spectrometer properties on the transmission probability for various e-gun properties. In the upper (center, lower) plot a potential inhomogeneity of $\Delta U_\mathrm{r} = 0\,\mathrm{V}$ (1 V, 1 V) and a magnetic field in the analyzing plane of $B_\mathrm{a} = 360\,\mu\mathrm{T}$ (360 µT, 880 µT) is selected. In all cases a Gaussian energy-distribution of $\mu_\mathrm{e} = 0.3\,\mathrm{eV}$ and $\sigma_\mathrm{e} = 0.3\,\mathrm{eV}$ and angular-distributions as in fig. 6.2 are used to describe the e-gun properties. It becomes evident that a potential inhomogeneity of ΔU_r lead to a constant shift of the transmission function in all configurations and the shape is unchanged (comparison upper and central plot). A lager magnetic field in the analyzing plane introduces a shift and a widening of the transmission function that increases for larger μ_a (comparison central and lower plot).

Radial potential inhomogeneity

The potential difference between the grounded beam tubes at the spectrometer entrances and the HV of the central vessel causes a radial inhomogeneity of the potential ΔU_r in the analyzing plane, as defined in eq. (6.8). As the transmission energy E_tr is directly proportional to the retarding potential, a change of the potential in the analyzing plane leads to a shift of the transmission function for any e-gun configuration, but does not change the shape of a transmission function (fig. 6.3, first and second panel). The sign of ΔU_r is positive, therefore leads a higher (lower) value to a shift to lower (higher) transmission energies E_kin.

Thereby it becomes obvious, that the initial kinetic energy E_kin of the e-gun and the radial potential inhomogeneity ΔU_r are fully correlated. Consequently, a determination of E_kin prior to an analysis of ΔU_r is mandatory.

Influence of magnetic field strength

From eq. (6.1) and eq. (6.6) it becomes evident that the ratio $B_\mathrm{A}/B_\mathrm{S}$ amplifies any shift and leads to biased shape of the transmission function due to an angular distribution. Therefore, a variation of B_A has only a minor influence on the transmission energy for small angles, but leads to a significant shift for larger angles (fig. 6.3, second and third panel). The examples are based on the 3.8 G- and 9 G-setting of SDS 2 where E_tr variates up to 1 eV for $\mu_\mathrm{a} = 45°$.

Thereby, are the polar angle μ_a of the e-gun and the magnetic field in the analyzing plane B_A highly correlated. A determination of μ_a and σ_a prior to an analysis of B_A is mandatory. As the influence of the field B_A is damped for low absolute fields and small angles, a set of measurements is required with different mean angles but on a common field line.

6.3 Extraction of the transmission probability from a measurement

A e-gun measurement is organized in a run with a set of sub-runs. During a run and especially during a sub-run, all e-gun and spectrometer properties are stabilized. Solely between sub-runs, the relative e-gun potential ΔU_EGun is varied to scan the transmission function close to the transmission energy E_tr. In this section the necessary steps are presented to reconstruct the transmission probability $P\left(\Delta U_\mathrm{eff}\right)$ in dependence of the effective potential ΔU_eff, which combines the applied voltages and e-gun properties as defined in this chapter.

6.3.1 Stability of the spectrometer properties

In section 6.1.2 it has been shown that, only the relative potential ΔU_EGun between the e-gun and the main spectrometer is the only relevant parameter to generate the potential difference $U_\mathrm{A} - U_\mathrm{S}$. As a result, a transmission function measurement is not influenced by global HV fluctuations or potential offsets. Any undetected potential can lead to a significant distortion of the potential distribution by introducing an electric dipole field (ref. [Gro15]). The potential setup for a transmission-function measurement run is selected to guarantee an axial-symmetric electric-field (section 3.1.2). Merely, a symmetric potential offset is applied to the steep cones to prevent early retardation (section 2.1). However, the power supplies to set additional potentials on the inner wire electrode (fig. 3.3) are not included in the presented model. But the potential variations σU_steep are below 6 mV throughout transmission-function measurements and can therefore be neglected. This result is confirmed by dedicated measurements (ref. [Ren14]). For all transmission-function measurements, stable magnetic-fields for B_S and B_A are applied (chapter 4).

6.3.2 Stability of the e-gun properties

The e-gun parameters that are stabilized during a transmission function measurement are the e-gun potential ΔU_{EGun}, the electron rate, the manipulator and back plate angle.

The later two are of no concern, as the e-gun is positioned prior to a measurement. Solely, a systematic uncertainty due to the angular uncertainty of the manipulator and the e-gun back plate needs to be considered in the analysis.

The relative potential of the e-gun ΔU_{EGun} to the inner electrode-system of the main spectrometer is monitored with a high precision DVM with five digits. However, a typical length of a sub-run is about 30 s and thereby only a few voltage measurements per sub-run are available. Thus a meaningful standard deviation can not be calculated and an average voltage uncertainty of 6 mV was assumed for all sub-runs. The estimation is based on long-term measurement where the potential stability of the e-gun power supply was determined (e.g. run #22450 of 70 min). The 6 mV correspond to a 5σ standard deviation of these measurements.

For an estimation of the electron rate stability, the voltage was set to 150 V and thereby well above the transmission energy E_{tr} where a constant electron rate from the e-gun is expected. Any rate fluctuation or drift behavior maybe due to a unstable photon emission from the UV laser or a surface effect of the gold layer. With a relative rate fluctuation of $\Delta R/R = 7 \times 10^{-3}$ and an observed of drift of 2×10^{-6} cps, an electron rate instability can be neglected for transmission-function run. In parallel to all transmission function measurements, the photon beam of the laser was monitored via a beam splitter and a photo diode. The observed photon rate drift of 6×10^{-7} V/s confirms the determined electron rate stability.

Therefore, no additional uncertainty is introduced by the stated properties to a transmission function measurement of a typical duration[1] of 15 min. More details in ref. [Beh16].

6.3.3 Calculation of the transmission probability

The calculation of the transmission probability is split in two stages. First, the correct signal electron-rate of the e-gun is determined for every sub-run and secondly, the actual probability of the transmission function with its uncertainty is calculated, based on a statistical model introduced in ref. [Kra16].

From the raw energy spectrum the electron rate is determined (fig. 6.4, embedded plot). The main peak of signal electrons from the e-gun is in the region of interest (ROI) from -3 kV to 2 kV around an energy of $q(U_{\mathrm{vessel}} + U_{\mathrm{IE}} + U_{\mathrm{PAE}} + U_{\mathrm{Det}}) \approx 28.6$ kV (blue). Multiple signal electrons may arrive at the FPD, which results in an energy pile-up peak equivalent to the number of detected electrons. A first pile-up peak can be found at the double ROI energy, where every entry corresponds to two electrons (green). These pile-up events amount for at least a few percent of the absolute count rate and are therefore included in the transmission-probability calculation. Depending on the UV laser configuration further pile-up peaks may occur, but in the selected Laser operation mode these can be neglected.

Furthermore, the sub-run duration is life-time corrected for a true rate calculation. The life time is monitored with an additional pulser signal in the spectrum at an energy[2] of 10 keV at

1 The duration of a sub-run in the transmission function measurements was below 60 s and an entire run lasted between 15 min to 40 min.

2 The pulser energy is shifted to 40 keV for measurements with low vessel voltages to prevent an overlap between e-gun and pulser signal.

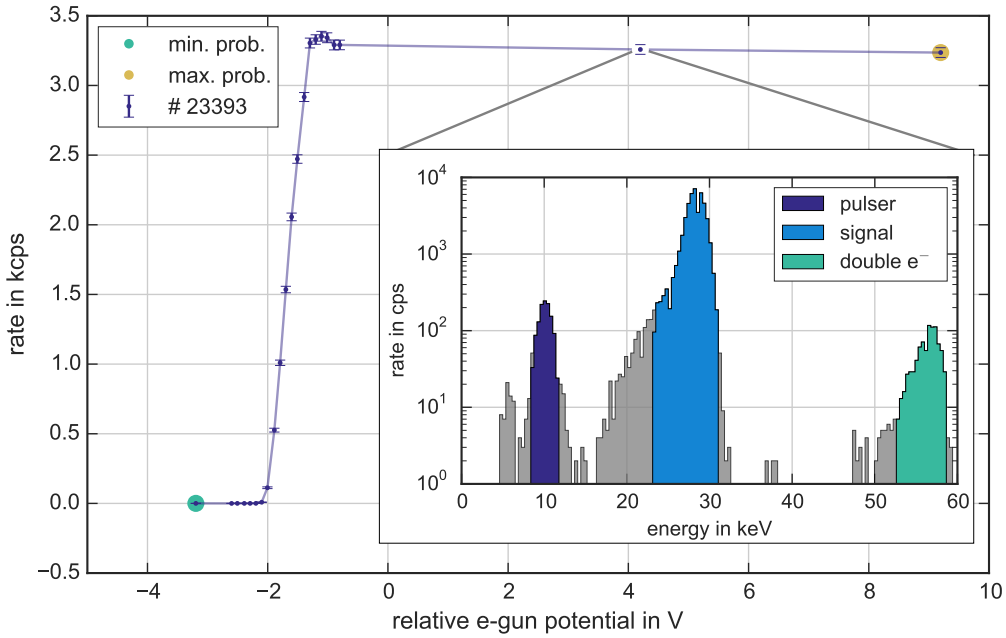

Figure 6.4: Extracting the transmission probability from a measurement. A transmission-function measurement run is split in sub-runs, where ΔU_r is varied. The electron rate of a sub-run is calculate based on eq. (6.12) divided for the sub-run duration. At twice the signal electron energy, the double-electron emission peak is located that is incorporated in the signal rate. A pulser signal is used for a life time correction (embedded plot). The highlighted points (green and yellow) are used to calculate the measurement uncertainties based on eq. (6.13). Measurement uncertainties were multiplied by a factor of 2 for a better viability.

a rate of 100 Hz (violet).

Two points are highlighted in the resulting count rate graph (fig. 6.4, main plot) for their special role to determine the transmission probability. In green is the sub-run shown for which the lowest transmission probability is expected. The absence of e-gun electrons is used to determine the background level and to calibrate the pulser signal. In orange is the sub-run shown with the highest transmission-probability due to the large surplus energy. Thereby, this point defines the mean value ν of the absolute electron counts. When the electron emission of the e-gun is assumed to be Poisson distributed and the spectrometer is treated as an binomial process where electrons are either transmitted or reflected at the transmission energy (described by a Heaviside function), a generalized formulation for the transmission probability ε is given by

$$\varepsilon = \frac{1 - \mathrm{e}^{-\nu}\mathrm{e}_{k+1}(\nu)}{1 - \mathrm{e}^{-\nu}\mathrm{e}_{k}(\nu)} \cdot \frac{k+1}{\nu}, \tag{6.12}$$

with the series expansion $\mathrm{e}_m(x) = \sum_{i=0}^{m} x^i/i!$ and the count rate k. The variance is given by

$$V[\varepsilon] = \left(\frac{1-\mathrm{e}^{-\nu}\mathrm{e}_{k+2}(\nu)}{1-\mathrm{e}^{-\nu}\mathrm{e}_k(\nu)} \cdot \frac{(k+1)(k+2)}{\nu^2}\right) - \left(\frac{1-\mathrm{e}^{-\nu}\mathrm{e}_{k+1}(\nu)}{1-\mathrm{e}^{-\nu}\mathrm{e}_k(\nu)} \cdot \frac{k+1}{\nu}\right)^2. \tag{6.13}$$

Due to the rather high electron rates of the e-gun the approximation $\nu \to \infty$ is justified and thereby the transmission probability and variance is simplified to

$$\varepsilon_{\nu\to\infty} = \frac{k+1}{\nu} \quad \text{and} \quad V[\varepsilon]_{\nu\to\infty} = \frac{k+1}{\nu^2}. \tag{6.14}$$

These calculations apply not only for e-gun measurements but for the tritium measurements as well. More information on this topic can be found in ref. [Kra16].

6.4 Determination of the electron gun properties

In the previous section it has been shown that transmission probabilities can be extracted from e-gun measurements. To disentangle spectrometer- and e-gun properties it is necessary to parametrize the e-gun energy- and angular distribution. Both quantities are a priori unknown and need to be determined by dedicated measurements.

6.4.1 An energy distribution model

A general description of the initial energy-distribution of electrons emitted from the e-gun is rather complex. It depends on several parameters such as the initial photon energy-distribution, the properties of the thin gold layer like thickness and lattice structure, the e-gun geometry and environmental influences such as temperature, the electric- and magnetic-field (ref. [Kna73], [Rei05], [Hec12], [DiS70]). To implement all these effect in a model to describe the energy resolution of the e-gun is not only extremely challenging, but inefficient due to the large number of required parameters. In addition, the initial electron energy-distribution is biased and smeared out by the non-adiabatic energy transformation by the applied focus potential U_{foc} (ref. [Zac14], [Beh16]). Consequently, a parametrization of the energy distribution by a minimal set of parameters needs to be found. A purely empirical model (e.g. a cubic spline or a polinom of n-th order) is disfavored as a meaningful comparison between different measurements is inhibit. Instead, the individual parameters should be loosely identify with a physical quantity.

The approach to describe the energy distribution in this thesis is a normal-distribution with an additional energy cut as introduced in section 6.2.1. The mean value of the initial kinetic-energy arise from the photon effect (ref. [Ein05])

$$\overline{E}_{\mathrm{kin}} = h\nu - (\phi_{\mathrm{gold}} + \delta\phi_{\mathrm{var}}) \tag{6.15}$$

with an work function ϕ that is split in a constant value ϕ_{gold}, defined by the binding energy of electrons in gold, and an variable term ϕ_{var} due to surface effects, e.g. a contamination with residual gases that vary over time. A stable energy is assumed for photons from the UV laser and any variation of the energy distribution is linked to a work function variation. By introducing an additional cut-off parameter, the absolute scale

$$E_{\mathrm{cut}} = qU_{\mathrm{cut}} = 0\,\mathrm{eV} \tag{6.16}$$

of the kinetic energy is defined. Consequently, a work-function correction is defined by the energy difference

$$\Delta E_{\mathrm{corr}} = \phi_1 - \phi_0 = (\mu_{\mathrm{e},1} - E_{\mathrm{cut},1}) - (\mu_{\mathrm{e},0} - E_{\mathrm{cut},0}) \tag{6.17}$$

of two fit parameters, the mean value of the energy distribution $\overline{E}_{\mathrm{kin}}$ and the energy cut E_{cut}. Note that E_{cut} is expected to be constant for a given e-gun configuration of the UHV manipulator and back plate angle.

The width of the energy distribution σ_{e} corresponds to a intrinsic property of the e-gun due to a smeared out photon energy, energy losses by scattering processes within the gold layer and variation of the work-function on the beam spot. Therefore no distinct property is linked to σ_{e}, but a constant value indicates the stability of the overall experimental setup.

Finally, the initial energy distribution is biased due to the e-gun geometry and the prevailing conditions of the electromagnetic field at the beam spot of the e-gun. To account for this additional skewness, a generalized description of the normal distribution is applied (ref. [Nad05]), where a shape parameter α is introduced. For an energy distribution $\psi(E)$ a probability density function is then found in

$$\psi(E) = C_{\mathrm{cut}} \frac{f(\eta)}{\sigma_{\mathrm{e}} - \alpha(E - \overline{E}_{\mathrm{kin}})}, \tag{6.18}$$

where C_{cut} is a normalization and $f(\eta)$ a normal distribution eq. (6.11) in dependence of

$$\eta = \begin{cases} -\frac{1}{\alpha} \log\left[1 - \frac{\alpha(E-\overline{E}_{\mathrm{kin}})}{\sigma}\right] & \alpha \neq 0, \\ \frac{E-\overline{E}_{\mathrm{kin}}}{\sigma_{\mathrm{e}}} & \alpha = 0. \end{cases} \tag{6.19}$$

Based on the energy cut E_{cut} parameter and the shape factor α, the scope of definition for eq. (6.18) is expanded to

$$\eta \in \begin{cases} (-\infty, E_{\mathrm{cut}}) & \text{if } \alpha > 0 \quad \text{and} \quad E_{\mathrm{cut}} < \xi \\ (-\infty, \xi) & \text{if } \alpha > 0 \\ (-\infty, \infty) & \text{if } \alpha = 0 \\ (\xi, \infty) & \text{if } \alpha < 0, \end{cases} \tag{6.20}$$

where $\xi = \overline{E}_{\mathrm{kin}} + \sigma/\alpha$ defines the limit. For a shape factor $\alpha < 0$ ($\alpha > 0$) the probability is $\psi(E < \xi) = 0$ ($\psi(E < \xi) = 1$). In case of $\alpha > 0$ a renormalization is applied with

$$C_{\mathrm{cut}} = \begin{cases} 1./\psi(E_{\mathrm{cut}}) & \text{if } E_{\mathrm{cut}} < \xi \\ 1 & \text{else .} \end{cases} \tag{6.21}$$

The cumulative distribution function of a generalized normal distribution is given by

$$\Psi(E) = C_{\mathrm{cut}} \cdot \frac{1}{2}\left[1 + \mathrm{erf}\left(\frac{\eta - \overline{E}_{\mathrm{kin}}}{\sqrt{2}\sigma_{\mathrm{e}}}\right)\right], \tag{6.22}$$

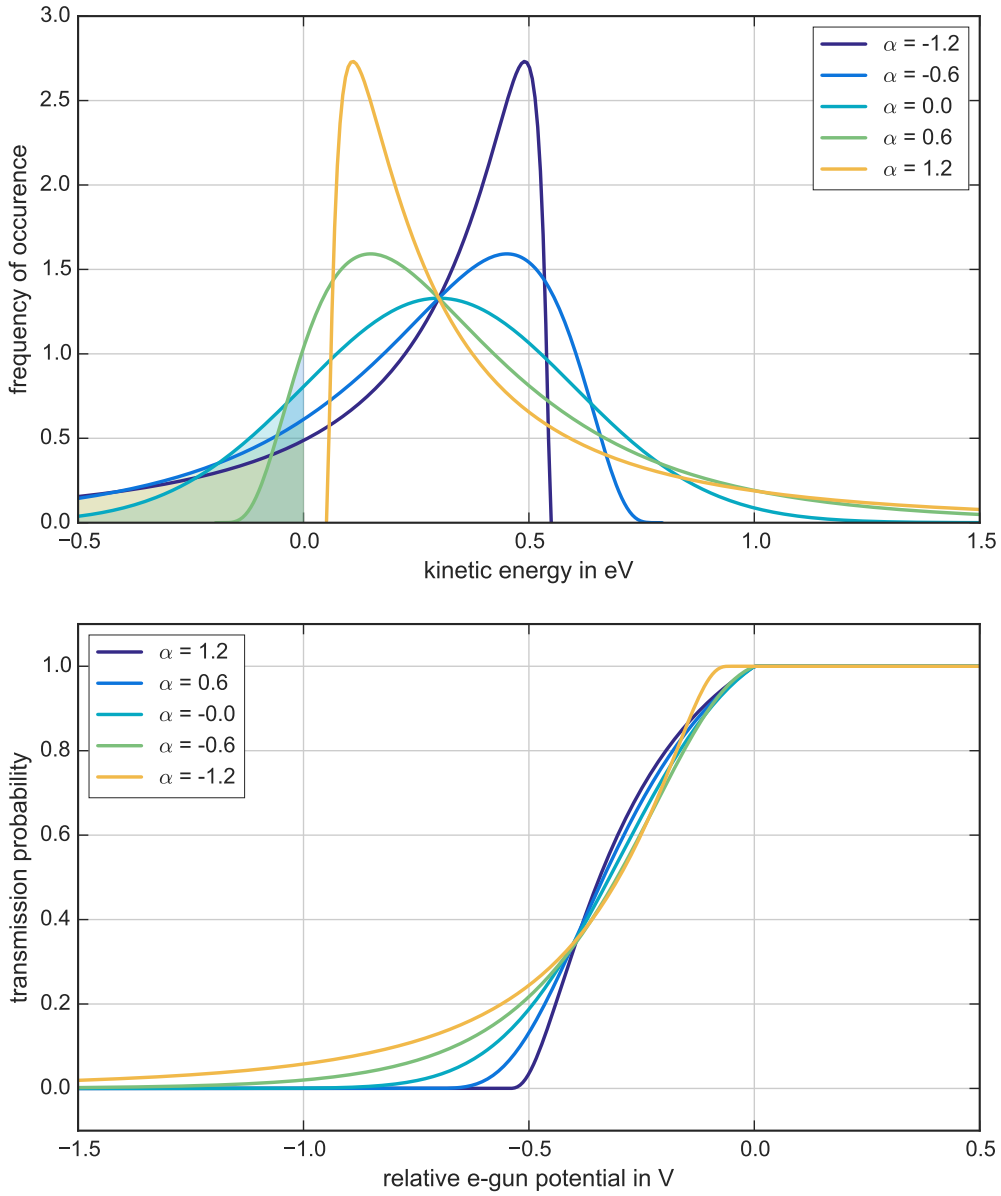

Figure 6.5: Influence of the skewness parameter on the shape of an energy distribution. Lines of same color belong to a common energy distribution. A change of sign is due to a unit change on the x-axis. Shaded areas corresponds to electron energies that are not emitted from the e-gun this leads to a sharp edge in the energy distribution at 0 eV and a kink in the transmission probability at 0 V.

where erf is the error function. Equation (6.22) is used to extract the energy distribution from e-gun measurements. In the analysis of the transmission-function measurements α is expected to have values which lead to a low energetic tail in the energy distribution (ref. [Kna73], [Rei05], [Hec12], [DiS70]).

Based on the energy distribution examples given in fig. 6.1, the influence of a shape factor on an energy distribution is visualized (fig. 6.5). In the given examples the mean kinetic $\overline{E}_{\mathrm{kin}} = 0.3\,\mathrm{eV}$ and energy width $\sigma_{\mathrm{e}} = 0.3\,\mathrm{eV}$ are fixed and spectrometer properties are neglected. For positive values of α a high energetic tail (fig. 6.5, upper plot) is observed that leads to an early rise of the transmission probability at low values of ΔU_{EGun} (fig. 6.5, lower plot). The energy cut E_{cut} suppress nonphysical electron energies below 0 eV and leads to a global upper-edge of the transmission probability at $\Delta U_{\mathrm{EGun}} = U_{\mathrm{cut}} = 0\,\mathrm{V}$ as indicated by the shaded areas in the upper plot. All functions are normalized based on eq. (6.21).

6.4.2 Extraction of the e-gun energy distribution

To extract an energy distribution from a transmission-function measurement, an experimental setup must be found where the influences of the angular distribution and the spectrometer properties are minimized. Here an electromagnetic configuration is chosen where

- the magnetic field in the analyzing plane is minimal, therefore a 3.8 G-setting is selected (table A.1). Thereby, the widening of a transmission function due to a finite angular-distribution is minimized.
- the electrons emitted from the e-gun have an angular distribution with a mean value of about $\mu_{\mathrm{a}} = 0°$. This is accomplished by a low focus potential U_{foc} and the e-gun back plate in a neutral position according to the selected UHV-manipulator position (section 6.4.3). Thereby the mean momentum of the electrons is parallel to the magnetic field and the widening of a transmission function is further reduced.
- a low retarding voltage is applied (table 3.1). This is the most crucial parameter as it improves the energy resolution tremendously. Based on the LV setting (table 3.1), an energy shift due to an angular uncertainty is calculated to $\Delta E = 14\,\mathrm{meV}$ (eq. (2.7)) for an isotropic source. However, for the e-gun is maximal an angular variation $\Delta\Theta$ expected between 0° to 5° (ref. [Beh14]), which leads in the worst case scenario to a maximal energy shift $\Delta E(\Theta)$ of 0.1 meV.

With such an excellent energy resolution and a vanishing influence of an angular uncertainty, the energy distribution of the e-gun is determined. For a high measurement accuracy, the relative e-gun potential ΔU_{EGun} was varied only in 20 mV steps.

In total, five dedicated measurements of the energy resolution were recorded throughout SDS 2 (table 6.1). All of these measurements represent individual measurement cycles where in between the e-gun valve to the main-spectrometer was closed to enable background measurements. Thereby the vacuum in the e-gun chamber was increased significantly by several orders of magnitude. In these vacuum conditions is a change of the residual-gas composition on the e-gun gold surface possible and consequently of the e-gun work function ϕ. An outstanding role in the energy-distribution measurements has the last one, which was recorded after an extensive maintenance break where the e-gun was fully dismantled and therefore in contact with ambient air.

Table 6.1: E-Gun energy-distribution fit results. Measurements with a LV setting were performed to extract the e-gun energy distribution from transmission function measurements. The fit model is a skewed normal-distribution with cut-off parameter (eq. (6.22)). All measurements, except run #22870 were recorded, before a maintenance break. Note that the combined analysis of the first runs is an additional fit, not average values.

run	pixel	mean kin. energy (meV)	sigma (meV)	alpha (10^{-3})
22622	13	328 ± 12	287 ± 13	-437 ± 28
22654	4	305 ± 12	308 ± 14	-493 ± 29
22672	100	316 ± 14	303 ± 15	-469 ± 30
22703	58	317 ± 12	297 ± 14	-463 ± 29
combined	–	330 ± 6	290 ± 7	-451 ± 15
22870	2	288 ± 11	367 ± 13	-532 ± 22

The measured transmission probability eq. (6.14) was fitted with a generalized normal distribution eq. (6.22) with an energy cut parameter, the energy-distribution model described in the previous section (section 6.2.1). For all measurements prior to a maintenance break, the fit parameters are comparable within their uncertainties. Although all energy-distribution measurements were performed along various field lines on different detector pixels, the shape of the energy distribution is not affected significantly. However, as expected a global shift is observed due to the spectrometer-potential inhomogeneity (section 6.2.2). This is an indication largely stable vacuum and surface conditions of the e-gun during the SDS 2 measurement campaign. Therefore it is expected that not only consecutive measurements, but also different measurement cycles can be directly compared.

To reduce the influence of fluctuations and systematic uncertainties, the energy distribution is determined in a combined analysis of the measurements prior to the maintenance break. A linear fit in the central probability region from $p = 0.33$ to $p = 0.66$ was used to shift 50 % transmission probability of the measurements to a common radial potential-inhomogeneity $\Delta U_{\mathrm{r,shifted}} = 0\,\mathrm{V}$ (fig. 6.6). Fitted with a generalized normal distribution eq. (6.22) with a reduced $\chi^2 = 1.56$, no structure in the residuals outside the 2σ range is observed. The row "combined" in table 6.1 represent the fit result of this analysis.

The broad consistency between measurement results and the energy distribution model is best visualized in a differential from (fig. 6.7). This form of the energy distribution is used as $F(E_{\mathrm{S}})$ in eq. (6.6) together with a angular distribution to analyze the following transmission-function measurements.

The "combined" measurement was resampled with a 20 mV binning and numerically differentiated based on Lagrange's formula implemented in Kasper (ref. [Sch04], [Gro15]). The graph corresponds to 99 % of the full integral. The differentiation algorithm begins on the low transmission probability side (corresponding to the most negative relative e-gun potential ΔU_{EGun}). Consequently the uncertainty bars increase for low kinetic energies due to error propagation. However, this routine is superior to a begin on the high transmission probability side as it is more robust and results in overall smaller uncertainties (ref. [Gro15]). Also, the discontinuity at the cutoff parameter $E_{\mathrm{cut}} = 0\,\mathrm{eV}$ is smeared out. In fact, this is the anticipated trend as for the real e-gun work function variations are expected on the beam

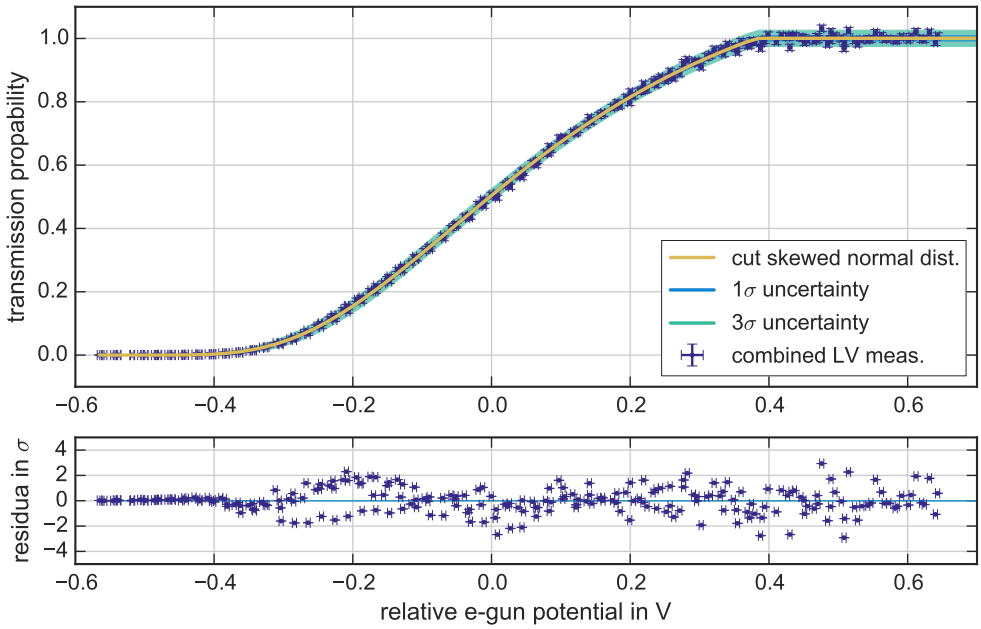

Figure 6.6: Transmission probability for energy distribution measurements were a 3.8 G magnetic-field setting and a low voltage configuration was applied. The plot shows all measurements before the maintenance break, shifted for their individual radial potential-inhomogeneity. Together they are fitted with eq. (6.22), results are given in table 6.1.

spot area which translate to variations of E_{cut}.

The graph is shown together with the analytic function 6.18 as a solid line where the fit parameters of "combined" measurement are applied. Based on the parameter uncertainties the uncertainty belt is calculated. All parameter combinations with their original value or variated by $\pm 1\sigma$ ($\pm 3\sigma$) are used to calculate a set of 6.18 and the resulting standard deviation correspond to the respective uncertainty belt. In the full energy range the numerical differentiation and the analytic function are in agreement within 3σ and predominantly also within 1σ. The only exception is the low energy region close to $E_{\mathrm{cut}} = 0\,\mathrm{eV}$ where a discrepancy is observed. This effect is associated with the work-function variations on the beam spot area which are not incorporated in the effective energy distribution model. Nevertheless, this test demonstrates the capability of the energy distribution model.

The measurement after the maintenance break turned out to be of great importance as it shows a significant deviation to all previous results. This is probability not only due to a contamination with ambient air, but also the e-gun geometry might has been slightly changed on a mm-level after the reassembling and thereby the shape, position and orientation of the electron beam-spot (section 6.4.3). By this measurement a reduced mean kinetic-energy E_{kin} of 42 meV was detected that is used as a correction to compare measurements before and after the maintenance break (table 6.3). In later e-gun measurements should these energy distribution measurements repeated after every maintenance break.

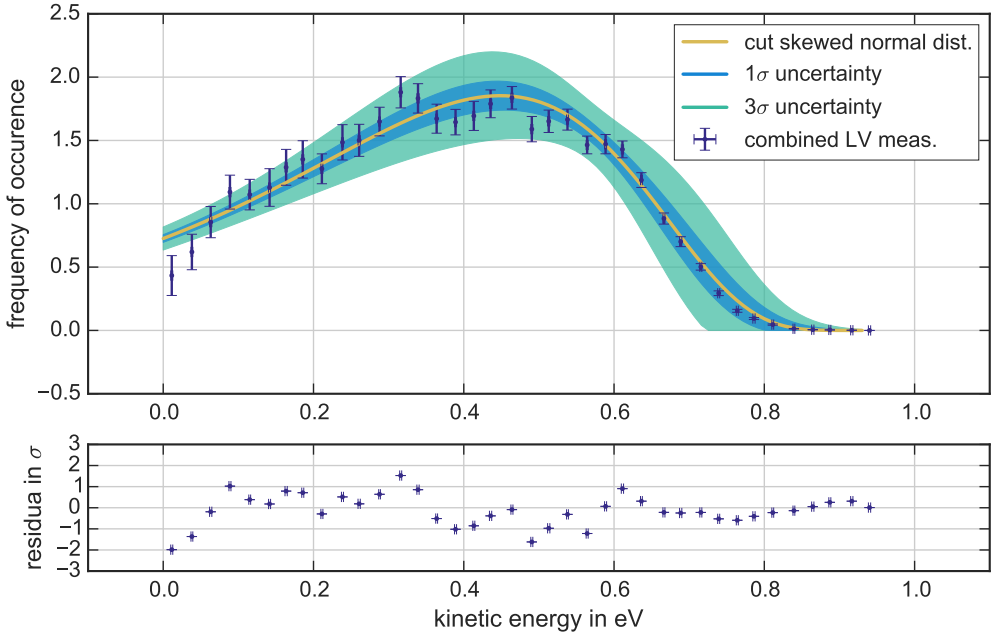

Figure 6.7: Differential energy distribution of combined measurements. The resampled and numerically differentiated low voltage measurements are shown in dark blue. "Combined" fit results (table 6.1) are applied to the analytic function eq. (6.22) in yellow, along with a 1σ (3σ) fit uncertainty in blue (green).

6.4.3 Verification of the angular selectivity

The possibility to manipulate and control the angular distribution of the e-gun is referred to as the angular selectivity. It is a crucial requirement as only by this means it is possible to determine the magnetic field in the analyzing plane. The angular selectivity comprises the following aspects of:

- a clear dependence between an e-gun back-plate angle to an electron polar-angle. In particular this means, that a given e-gun back-plate angle Θ_{EGun} is assigned to exactly one mean electron polar-angle μ_{a} relative to the magnetic field. The functional relation between these two quantities is only accessible via comprehensive simulations (ref. [Zac14]). Simulation results regarding the SDS 2 setup are given in section 6.6.2 and a detailed discussion can be found in ref. [Beh16].
- the unimportance of further parameters on the shape of an angular distribution. In other word, solely the electromagnetic setup defines the angular distribution and an electron blocking by structural components is precluded. This property is also verified in extensive magnetic-reflection measurements[1] in ref. [Beh14].

1 The magnetic reflection or magnetic mirror effect is a direct consequence of eq. (6.5), where electrons with polar-angle above θ_{max} are not transmitted to the detector. Is the electron rate recovered by lowering the focus voltage U_{foc} or an adjustment of the magnetic fields B_{S} and B_{max}, the magnetic reflection is verified.

Are these requirement fulfilled, the electron energy and angular distribution can be simulated (section 6.6.2) and measured (section 6.4.4). Via transmission-function measurements two mean polar-angles μ_a are directly accessible, the minimal angle by a zero-angle measurement and the maximal angle by a magnetic-reflection measurement.

The minimal polar-angle is the reference angle to all other e-gun back-plate angles and is used to measure the radial potential-inhomogeneity. It is therefore the most important angle for transmission-function measurements and needs to be carefully determined. Due to the rotation principle of the UHV-manipulator and the magnetic-field distribution, the minimal polar-angle has to be determined individually for every UHV-manipulator position. A minimal electron polar-angle is identified with the orientation of the e-gun where the minimal transmission energy E_{tr} is obtained. The fact that the transmission energy E_{tr} is shifted in dependence of an electron polar angle eq. (6.1) can be exploited to determine the minimal polar angel.

Prior to a zero-angle measurement, a relative e-gun potential is selected where roughly 50 % of the maximal electron rate is observed (comparable to $\Delta U_{EGun} = -1.8\,V$ in fig. 6.4). An increase (decrease) of the observed rate is thereby identified with a smaller (larger) polar angle of the electrons. By a variation of both rotation angle of the e-gun axes an optimal setting is found (fig. 6.8) where the angles with the maximal rate are derived from a parabolic fit. In the presented case for a zero-angle measurement on pixel 109, the optimal angle for the horizontal-axis (vertical-axis) of the e-gun is $(2.612 \pm 0.011)°$ ($(-8.494 \pm 0.011)°$). The observed fit uncertainties are about the size of the positioning uncertainty of the e-gun chamber and comparable for all recorded zero-angle measurements (ref. [Erh15d]).

To verify the angular selectivity and a correct e-gun positioning relative to the determined minimal polar-angle, transmission-function measurements were performed with the minimal and also with larger polar-angles. Relative to the minimal angle position, the e-gun was rotated with the same step size in opposite directions where a shift of the transmission function to higher transmission-energies E_{tr} is expected. If a symmetric shift is observed in both directions and the values of E_{tr} coincide for measurements with equal polar angles, the requirements as specified above for a reliable angular selectivity are fulfilled.

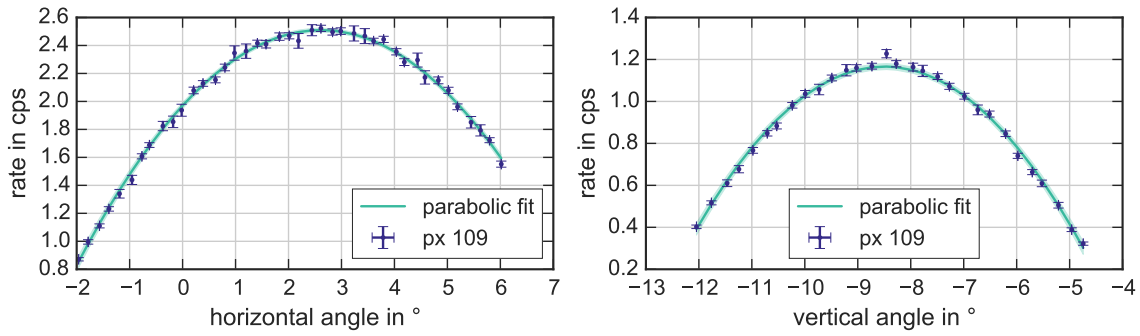

Figure 6.8: Determination of the minimal angle of the e-gun angular distribution. By a rotation of the e-gun back-plate a shift of the transmission function is expected (fig. 6.2). Consequently is the maximal observed rate identified with a minimal polar angle of electrons relative to a magnetic field. The observed rate is fitted to a parabolic function.

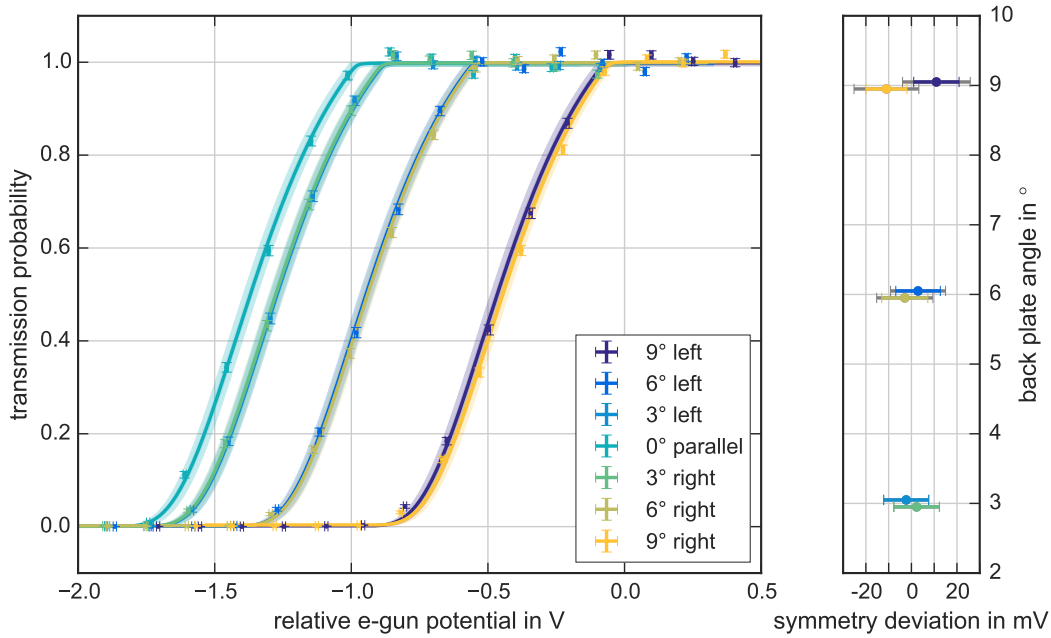

Figure 6.9: Verification of the zero angle by e-gun measurements. The transmission function shifts according to the e-gun back plate-angles relative to the magnetic field. As expected, the zero angle configuration leads to the lowest transmission energy and higher plate angles result in higher transmission energies. A symmetric setup is verified by the differences of the transmission energies of measurements with the same polar angle (right side). The uncertainty of the transmission energy is the quadratic sum of the fit uncertainty (in color) and the angular uncertainty (grey). Polar angles were applied with an azimuth angle of $\phi = 0.0°$ and 180.0° (horizontally, left and right).

Seven transmission function-measurements were performed on pixel 109, where the back-plate angle was varied up to 9° in 3°-steps[1] (fig. 6.9, left plot). The obtained transmission probabilities were fitted with the previously determined energy-distribution eq. (6.22). Clearly, the transmission-function with a polar-angle $\Theta = 0°$ has the lowest transmission energy E_{tr} and for larger polar-angles an increasing shift of the transmission energies is observed (compare to fig. 6.2). Measurements with the same respective polar angle are in agreement within uncertainty, except for the largest angle of 9° where a minor discrepancy is observed.

As the transmission-energy is determined by using only an energy distribution, an additional shift due to an finite angular-distribution is neglected. As the selected polar angles are symmetric relative to the minimal angle, this fact is no major problem, but nevertheless an systematic uncertainty is introduced. The e-gun-axis adjustment precision of 0.05° combined with the maximal transmission angle at $\theta_{\mathrm{EGun,max}} = 12°$ are used to estimate the uncertainty

1 The target pixel 109 is on the bottom of the FPD wafer. Therefore the UHV-manipulator is rotated downwards relative to the spectrometer axis. For a correct magnetic reflection, the e-gun must be rotated perpendicular in left/right direction. More details below.

of the transmission energy. Simulations revealed a nearly linear dependence between back-plate angle and electron polar-angle for angles well below $\Theta_{\max}$ (ref. [Zac14], [Beh16]). For the given back-plate angles of 0°, 3°, 6° and 9° the transmission-energy uncertainty is estimated to $\Delta E_{\mathrm{tr,sys}}$ =0.7 meV, 17.8 meV, 27.1 meV and 42.0 meV in case of a 3.8 G-setting. The additional systematic uncertainties are indicated by grey error bars in the right plot of fig. 6.9 and the increased uncertainties indicate an agreement within 1σ is reached even for the 9°-measurements. Thereby the angular selectivity is confirmed. Further studies on the influences of transmission-energy uncertainty can be found in section 6.5.2. In the following analyses of the transmission-function measurements the additional systematic uncertainties are always implemented.

On average, magnetic reflection is reached for back-plate angles of $\Theta_{\mathrm{EGun}} = 12°$ relative to the minimal-angle position when a HV setting and a focus voltage of $U_{\mathrm{foc}} = 5\,\mathrm{kV}$ is applied. However, measurements on outer pixels revealed, that the magnetic reflection can not be assured for all azimuthal angles. So the magnetic reflection is not reached when the e-gun chamber is rotated towards the spectrometer center due to mechanical limitations and when rotated away from the spectrometer axis, electrons are partly blocked by the e-gun front-plate (ref. [Beh15a]). Since these two issues are purely connected to mechanical limitations of the e-gun, unpredicted electromagnetic design effects can be dismissed. Moreover, any interference by these issues can essentially avoided by a rotation of the e-gun chamber perpendicular to the UHV-manipulator exclusively.

6.4.4 Extraction of the e-gun angular distribution width

The initial angular distribution at the e-gun surface is a result of the photon beam and gold layer properties, which define the initial kinetic-energy and the angular distribution of the electrons at the e-gun surface(ref. [Pei02]). The initial angular distribution is smeared out at the exit of the e-gun chamber, induced by the non-adiabatic acceleration due to the applied focus voltage U_{foc}. In the adiabatic region, the angular distribution can be approximated by a normal distribution (ref. [Zac14]). However, the mean μ_{a} and width σ_{a} of the normal distribution are only accessible via comprehensive simulations. Nonetheless can an effective normal distribution be extracted directly from transmission function measurements as demonstrated in this section. Such an empirical angular distribution can be applied in the analysis of measurements with angular distribution of the same mean μ_{a} angle, e.g. measurements only with a minimal electron polar angle as for the potential mapping (section 6.5).

Assuming a well-known energy distribution and a defined polar angle of the electrons on a given field line, an additional broadening of the transmission function is associated with a finite width of the angular distribution (fig. 6.2). The width can be measure with an electromagnetic setting where

- the magnetic field in the analyzing plane is maximal, here a 9.0 G-setting is used (table A.1). Thereby the widening of a transmission function due to a finite angular-distribution is maximized.
- the electrons are emitted with a mean value of $\mu_{\mathrm{a}} = 0°$. The minimal angel is selected as it can be directly derived from measurements and its significant role.

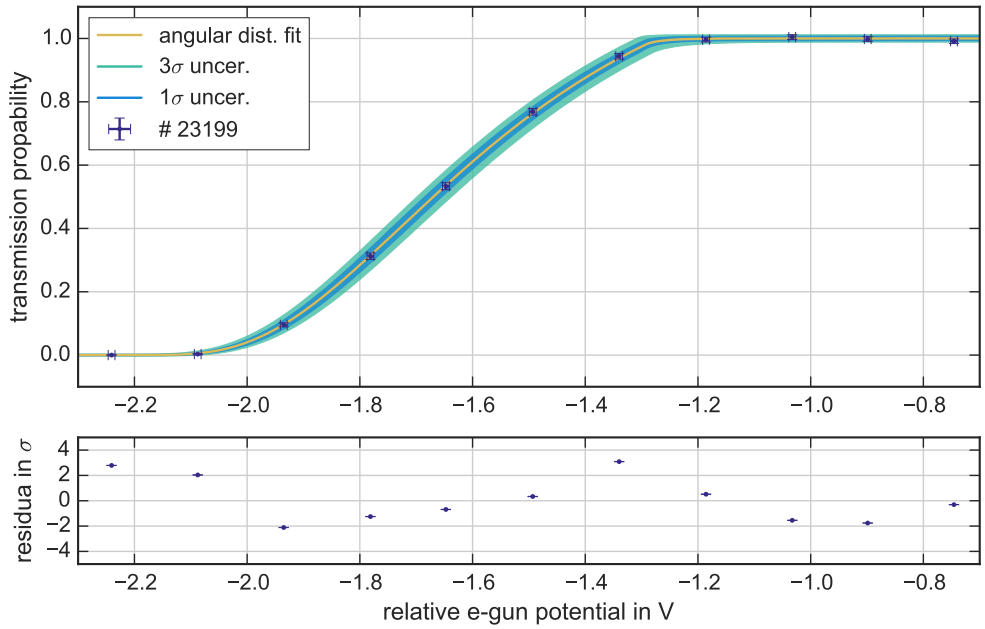

Figure 6.10: Transmission probability for angular-distribution measurement were a 9.0 G magnetic-field setting and a high-voltage configuration was applied. The data points are fitted with a double integral eq. (6.6), where $\omega(\Theta)$ is identified with eq. (6.11) and $F(E_S)$ with eq. (6.18) and the parameters from table 6.1. The fit reveals $\mu_a = (4.84 \pm 0.98)°$ for the width of the angular distribution.

- The focus potential U_{foc} is set to its maximal value (table 3.1). Thereby the comparability for later transmission-function measurements is ensured.

A step size of 150 mV for the relative e-gun potential ΔU_{EGun} is sufficient to determine the width of an angular distribution.

The angular distribution width is determined with eq. (6.6) as a fit function, where the angular distribution $\omega(\Theta)$ is identified with a normal distribution eq. (6.11) and the energy distribution $F(E_S)$ is a generalized normal-distribution eq. (6.18) based on the "combined" parameters (table 6.1). Due to the large correlation between μ_a and ΔU_r, μ_a is fixed to the expected value of 0° in the distribution fit. Similar reasons require a fixed magnetic-field in the analyzing plane B_A in a fit as well. This value is derived from simulations only and may vary do to the unknown additional fields of the ferromagnetic materials in the experimental hall (section 5.3). Therefore, a measurement on a path close to the spectrometer axis is chosen where the influence of unaccounted fields is minimized, the central target pixel 2 with field of $B_A = 903\,\mu T$. The resulting fit of the angular distribution measurement reveals a width of $\sigma_a = (4.84 \pm 0.98)°$ in the center of the PS 2 magnet where a magnetic field of $B_S = 4.5\,T$ is experienced (fig. 6.10). A reduced $\chi^2 = 2.29$ and residuals in the 3σ regime indicate a good agreement between model and measurement. Therefore is the effective angular distribution model sufficient to describe the observed transmission probabilities.

6.5 Radial inhomogeneity of the retarding potential in the analyzing plane

The radial inhomogeneity of the retarding potential in the analyzing plane is one of the major spectrometer-properties that define its transmission characteristics for electrons. By comparing the measured and simulated shape of the potential in the analyzing plane the data analysis chain and the developed software tools are validated. A previous thesis studied the influence of different potential settings on the transmission property of the spectrometer (ref. [Gro15]). In this section these results are not only reproduced, but improved for a potential setting close to the tritium end point (HV setting in table 3.1). For a variety of different positions in the analyzing plane transmission-function measurements are recorded to determine the radial inhomogeneity of the retarding potential. This is accomplished by positioning the e-gun with the UHV-manipulator at various angles and thereby transmitting electrons on different trajectories through the main-spectrometer onto a specific FPD target pixel. With a field-line simulation for every UHV-manipulator position the exact location of the analyzing point is obtained and the associated retarding potential calculated. Correspondingly, these values can also be extracted from transmission-function measurements. To compare both potential values, the systematic uncertainties due to positioning accuracy of the e-gun is included as well.

A variation of the analyzing point location is not only achieved by different UHV-manipulator positions, but also when a different magnetic-field setting is applied to the LFCS. However, a deviation of the magnetic-field between the model and the measurement of the sensor units was verified (section 5.1.3) and a significant azimuthal perturbation of the magnetic field is observed (section 5.4). Consequently, the analysis of the radial-potential inhomogeneity is influenced by the accuracy of the magnetic-field model. For different magnetic-field settings the radial-potential inhomogeneity is analyzed along the y-axis of the spectrometer where a larger magnetic-field deviation was observed (section 5.5).

As an total radial-potential inhomogeneity of 400 mv is expected for the total analyzing plane, the potential inhomogeneity for a single pixel is about 30 mV. This is a straight forward approximation of the required precision for the potential analysis.

6.5.1 Position and shape of the analyzing plane

The analyzing point of an electron eq. (2.9) is the location where its longitudinal kinetic-energy is minimal. The exact location of the analyzing point is somewhere within the main-spectrometer volume and only accessible via simulations. A deterministic and uniquely solution can only be found when an adiabatic transport of the electrons can be assumed. Elaborated simulations of the transport of electrons from the e-gun to the FPD verified an adiabatic transmission within the operation parameters of the e-gun during transmission function measurements (ref. [Gro15], [Bar16b], [Wie16]). Hence it is sufficient to determine an analyzing point by an analytic calculation of the longitudinal energy along an electron trajectory, which is much faster then a full particle-tracking simulation.

In section 2.1.2 the analyzing plane was defined to be perpendicular to the spectrometer, located at $z = 0\,\mathrm{m}$ and it includes all positions where the longitudinal kinetic-energy of electrons is minimal. In other words, the analyzing plane is independent of the electron angle and is perpendicular to the electric field. This is a crucial requirement for an analytic calculation of the transmission probability. Whether these requirements are satisfied is numerically determined based on field-line calculations of the individual analyzing points.

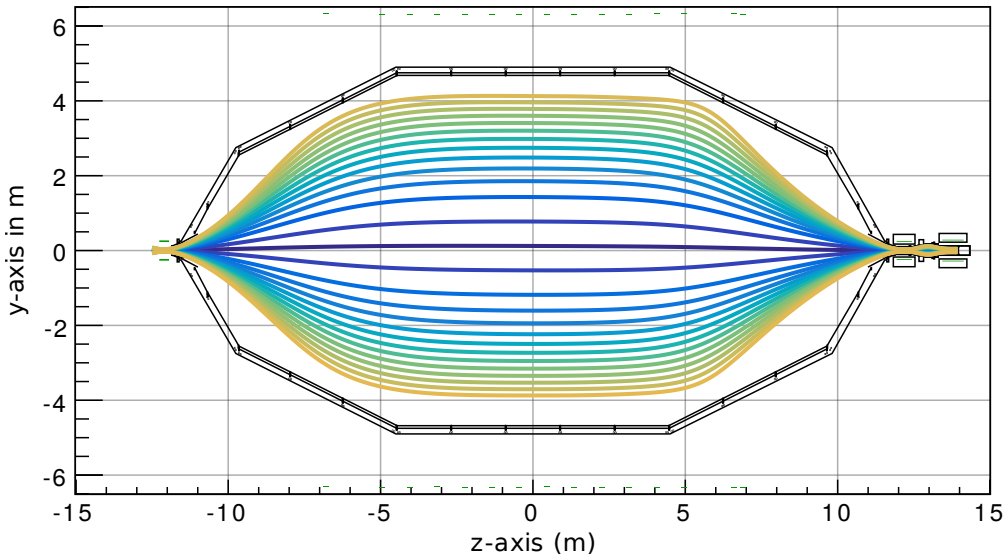

(a)

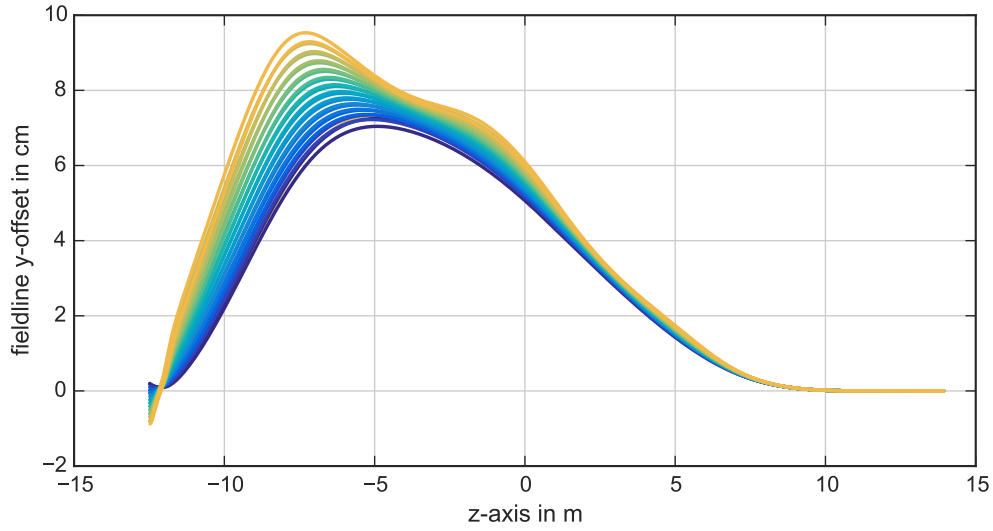

(b)

Figure 6.11: Magnetic fields lines with an empirical offset on the EMCS currents. Figure 6.11(a) shows the magnetic field-lines for a 3.8 G-setting when nominal EMCS currents are applied that lead to a magnetic-field overcompensation, here demonstrated in the y-z plane where the largest deviation is observed. In fig. 6.11(b) the difference between a symmetric and a nominal EMCS setting is shown. The empirical EMCS-current offset not only leads to a shift of the magnetic-field lines (at the analyzing plane at about −6.4 cm), but to a small distortion of the overall shape as well. Since outer rings are more affected, the lower half of the flux tube is compressed and the upper half is dispersed. Such an displacement of the magnetic field effects the overall alignment, position and shape of the analyzing plane.

Based on the realistic geometry of the SDS setup where the complete alignment information is incorporated, an electron trajectory from the e-gun to the FPD is calculated. A starting position of an electron is defined by the selected UHV-manipulator position. Along a magnetic field-line the electrostatic potential is calculated in 1 cm-steps, utilizing a full three-dimensional model of the main-spectrometer. At every step, the kinetic energy is evaluated to determine the position $p_{\mathrm{Ekin,min}}$ of the minimal kinetic energy. For a precision in the sub-cm regime, the longitudinal energy is fitted with a parabolic function in a $\pm 30\,\mathrm{cm}$ range around $p_{\mathrm{Ekin,min}}$. At the new position $p'_{\mathrm{Ekin,min}}$, the electrostatic potential is reevaluated. Thereby an analyzing point is determined with a precision in the sub-mm regime and is limited by the numerical precision of the three dimensional electrostatic-model to a few mV only.

However, the accuracy of an analyzing point determination is defined by the accuracy of the magnetic-field model. In section 5.4 it has been shown, that the magnetic-field is distorted due to the influence of ferromagnetic materials in the main spectrometer build. Although the transmission-function measurements were performed with the originally calculated currents of the EMCS, consequently the magnetic background field is slightly overcompensated by the EMCS and the magnetic flux tube is distorted (fig. 6.11). An empirical adjusted setting can be deployed to account at least for the constant fraction of the additional field asymmetry (section 5.5). The distortion in y-direction of the magnetic flux-tube comprises an overall upward shift, a compression of the lower half and a dispersion of the upper half. As a result, the flux-tube volume is marginally increased (volume ratio symmetric/overcompensated $V_{\mathrm{sym}}/V_{\mathrm{ov.comp.}}$ by about 0.05 %) and the analyzing plane is biased in its location as well as in its shape. Along the x-axis also an overcompensation is observed, but less pronounced (compare with section 5.4.2).

Table 6.2: Radial analyzing positions and radial potential-inhomogeneity relative to the applied voltage on the inner electrode of 18 604 V with a 3.8 G-setting applied. In the simulation of the analyzing-point locations and potential-inhomogeneity a realistic magnetic-field with an overcompensation EMCS is applied. The last column corresponds to the potential difference when the overcompensation of the magnetic-field by the EMCS is neglected and thereby axially symmetry of the magnetic field is assumed. The lines are ordered along the vertical analyzing-position y_{A} from top to bottom.

pixel	run #	x_{A} in mm	y_{A} in mm	z_{A} in mm	ΔU_{r} in V	diff. to sym. in mV
103	23 055	2.0	3558.2	−394.5	1.8	−23.3
55	23 058	3.1	2688.8	28.2	2.0	−20.4
31	22 646	4.0	2106.9	33.5	2.0	−17.1
7	22 641	6.1	1198.6	65.6	2.1	−10.3
2	22 475	6.5	1.8	43.2	2.2	1.3
13	22 623	5.6	−725.5	21.1	2.2	8.6
37	22 630	5.8	−1623.9	−9.2	2.1	17.0
61	22 633	4.1	−2195.3	−11.0	2.0	21.1
85	22 638	4.0	−2656.9	17.0	1.9	24.2
109	22 560	2.2	−3059.2	27.1	1.9	26.1

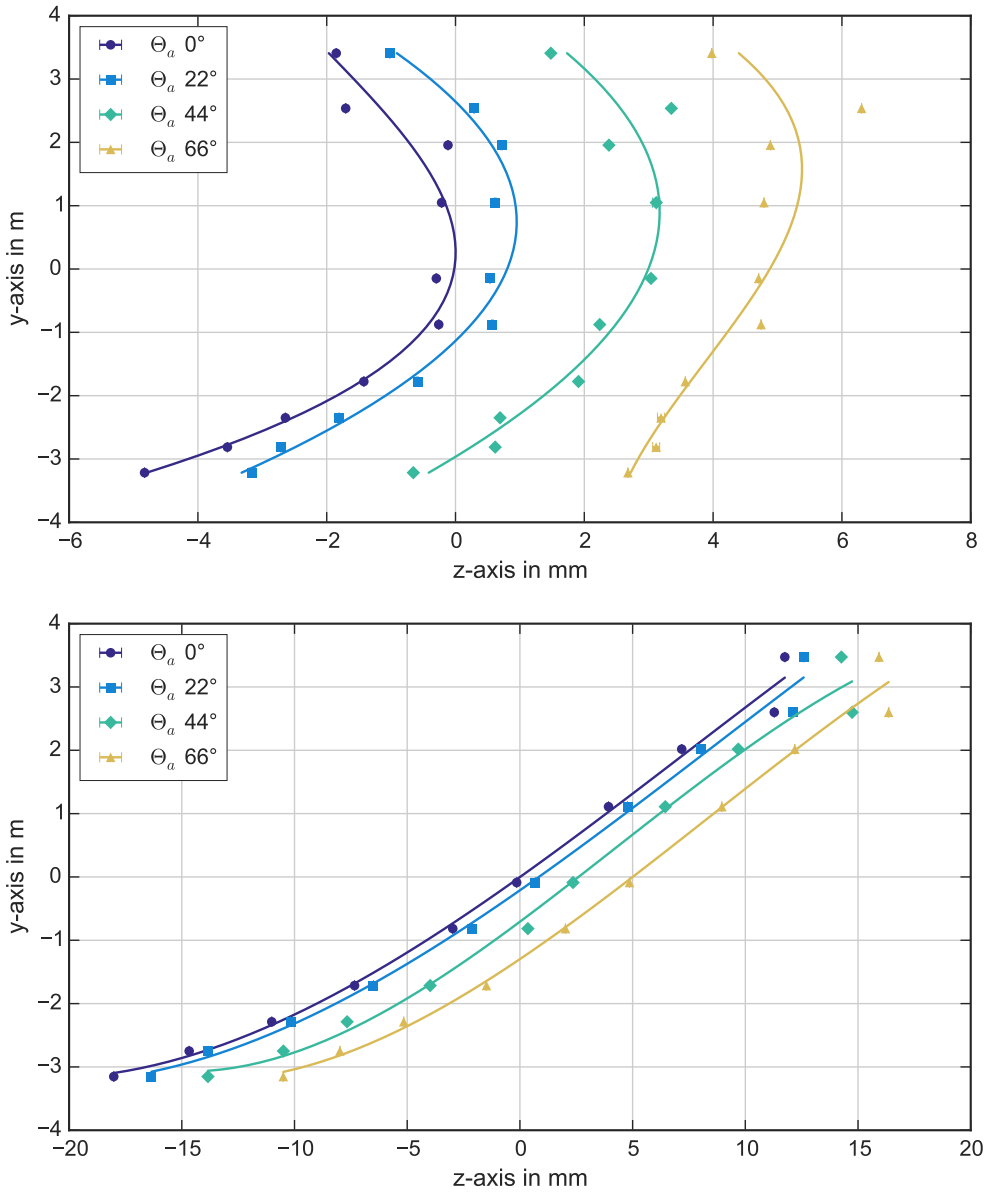

Figure 6.12: Analyzing points of the transmission-function measurements in the y-z plane for a 3.8 G-setting. The position where the longitudinal kinetic-energy is minimal is shown for four different electron angles, a cubic spline indicates the shape of the analyzing plane. In the upper plot the magnetic background field is fully compensated, only the SDS solenoid alignment leads to a minor symmetric perturbation. The lower plot the case for an overcompensation of the magnetic background field is shown that leads to a distortion of the analyzing-plane shape.

In fig. 6.12 the influence of magnetic field distortion on the analyzing plane shape is studied in detail. Magnetic-field lines are selected that correspond to the vertical target-pixels of the transmission-function measurements for a 3.8 G setting (see also section 6.5.3). Polar-angles are selected that roughly correspond to the minimal and maximal electron angles during the e-gun measurements. The calculated analyzing positions are represented by markers and the radial shape is visualized by a cubic spline. For a accurate potential determination, a parabolic fit is performed in a range from −10 cm to 10 cm around the analyzing point (see also section 6.5.2).

The symmetric case (upper plot) features only a minor variation along the z-axis of the analyzing points of a few millimeter is observed for both, the radial and electron angle dependence. The resulting variation of the retarding potential is in the sub-mV regime, thereby negligible as the potential precision is then dominated by the power supply precision of 4 mV to 10 mV (ref. [Wac15]). When the magnetic background field is overcompensated (lower plot), the analyzing plane shows a clear radial dependency of the axial position. However, the radial variation is still in the millimeter regime and the angular dependence is not affected at all. Consequently, analytic functions can still be applied as the introduced retarding-potential uncertainty is in the sub-mV regime.

Finally, the retarding potential that electrons experience in the analyzing plane is affected by the overall flux-tube shift. Depending on the magnetic-field line, the observed retarding potential for an electron variate between 1 mV to 26 mV when a 3.8 G setting is applied (table 6.2) and the magnetic background field is overcompensated. Larger deviations of the retarding potential, close to the systematic uncertainty limit, are observed prevailingly on outer radii where the magnetic-field deviation is more pronounced.

6.5.2 Radial dependence of systematic uncertainties

Systematic uncertainties affect the precision of a potential measurement that arise from several effects. In this section all relevant uncertainties for an analysis of a transmission-function measurement are summarized. Previously mentioned sources of systematic uncertainties are collected and so far unconsidered sources are estimated.

The precision of the determination of the radial potential-inhomogeneity is directly related to the stability of the applied voltages and the readout precision. In this context, the readout precision of the DVM used to measure the relative e-gun voltage ΔU_{EGun} is the dominating parameter, where for every sub-run an uncertainty of 7 mV is assumed (section 3.1.4). The voltages applied to the vessel, the inner-electrode system and an additional step-cone offset define the shape of the radial potential-inhomogeneity. As these voltages are rather stable, all simulations are based on the mean values throughout the e-gun measurement campaign with $U_{\mathrm{vessel}} = -18.404\,\mathrm{kV}$, $U_{\mathrm{IE}} = -200.038\,\mathrm{V}$ and $U_{\mathrm{step}} = 100\,\mathrm{V}$.

In section 6.2 a full correlation was asserted between the radial potential-inhomogeneity ΔU_{r} and the initial kinetic-energy E_{kin} of e-gun electrons. As long as the energy distribution can assumed to be stable, only an additional global offset is introduced. Such an offset is attributed to the work-function difference $\Delta\phi$ between the e-gun and the electrode system (eq. (6.17)) and does not affect the radial potential shape. Variations between measurement cycles can be corrected for based on the individual energy distributions in table 6.1. Then the fit precision of the energy distributions contribute to a systematic uncertainty in a combined analysis of different measurement cycles.

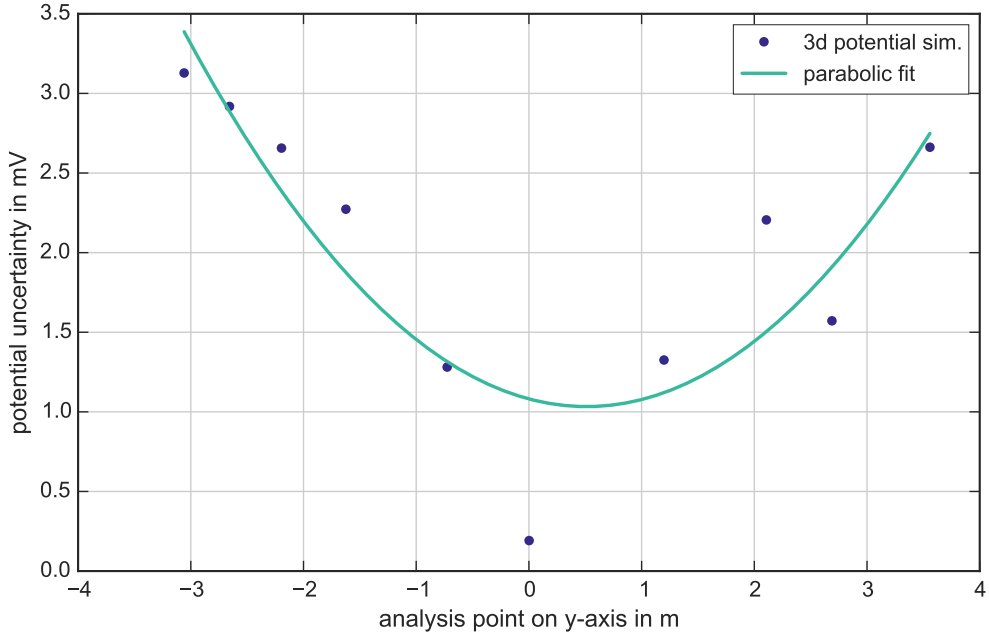

Figure 6.13: Potential uncertainty due to UHV manipulator precision. An uncertainty of the UHV manipulator positioning lead to different electron trajectories that variate in the analyzing plane up to $\Delta r = 2\,\mathrm{cm}$, and due to fig. 2.5 an approximately parabolic shape of the introduced potential uncertainty is expected. Deviation from this shape are due to potential fluctuations in the three-dimensional calculation routine.

The influence of the positioning precision of the e-gun back-plate on a transmission-function measurement was evaluated in section 6.4.3. It could be demonstrated that only for larger angles some uncertainty can be observed, but is of a minor importance for small angles. Therefore is the determination of the radial potential-inhomogeneity measurements performed with the minimal electron-angles of Θ_a. In this case the expected potential uncertainty amounts for $\Delta E_\mathrm{tr,sys} = 0.7\,\mathrm{meV}$ when a 3.8 G-setting is applied and 1.5 meV for a 9.0 G-setting.

Transmission functions of several trajectories are required to measure radial potential-inhomogeneity. Therefore the e-gun is moved by the UHV-manipulator to different positions with a precision of 0.1°. Due to the resulting trajectory uncertainty variate from 1 cm to 2 cm for electrons passing the analyzing plane on different radii, where smaller uncertainties are observed on inner radii. For the individual trajectories the analyzing point variations (as in fig. 6.12) and the corresponding potential uncertainties are calculated to be of the low mV regime (fig. 6.13). Larger uncertainties are observed for outer radii as expected from fig. 2.5. Unfortunately the potential calculation features fluctuations of the order of the potential uncertainty. These fluctuations origin from the utilized cubature in the Kemfield routines to calculate and integrate the charge densities (ref. [Hil16]). A parabolic fit is used to determine the introduced uncertainty by the UHV-manipulator precision to 1 mV to 3 mV.

6.5.3 Determination of the radial potential-inhomogeneity

The radial potential-inhomogeneity is determined by transmission-function measurements for various electron trajectory through the spectrometer. The utilized measurement routine with its selected target pixels and the applied electron angles is referred to as potential mapping. The accuracy of the potential mapping may feature a dependence on the absolute magnetic-field in the analyzing plane, therefore is the potential mapping repeated for different magnetic-field settings (ref. [Erh15d]). This section is focused on potential mapping with a vertical target pixel distribution. On the on hand side is the vertical axis more sensitive to the observed magnetic-field deviations (chapter 5) and on the other hand was a full horizontal potential-mapping inhibited due to a malfunctioning of a pre-amplifier card of the FPD.

The potential mapping for the individual magnet-field settings is split in measurement cycles. A measurement cycle is a set of measurements that consists of consecutive measurements where e-gun parameters, spectrometer- and vacuum conditions are stabilized (section 6.3). Therefore, individual measurements of a measurement cycle can be described by a common energy distribution. A measurement cycles is completed when the valve to the main spectrometer is closed for more than 12 h. When separated from the main spectrometer the e-gun chamber is pumped by a single TMP only and so the vacuum conditions are severely degraded in between measurement cycles. This can lead to a different composition of residual gasses on the e-gun gold layer and thereby to a change of the e-gun work-function (section 6.4.2). A changed work function of the e-gun has two effects. Is the work function lowered (increased), more (less) electrons are released from the e-gun. Therefore is a higher (lower) electron rate observed although the e-gun laser settings are unchanged. More importantly, also the mean initial kinetic-energy of the electrons is increased (decreased) that causes a shift of the observed transmission energy (section 6.2.2). To adapt for such an additional energy shift, the corresponding energy distribution associated with a specific measurement cycle is applied in the analysis (table 6.1).

A change in the e-gun work-function, and thereby electron rate, is best visualized by the observed multi-electron rate where the relative variations are more pronounced. As the e-gun is operated not with a continuous but a pulsed laser beam, the rate variation is even more amplified. In particular is the probability for a multi-electron emission per laser pulse increased. These multi-electrons can not be separated in time by the FPD system and are recorded as one event with twice the energy of the ROI (section 3.1.4 and section 6.3.3).

In fig. 6.14 are the mean multi-electron rates of the potential mappings shown (upper row) together with the a corresponding field-line simulation (lower row), split by their respective field settings. With the field-line simulations, based on the actual e-gun settings, the target pixel distribution as observed in the measurements is reproduced and confirm a correct electromagnetic representation of the e-gun and SDS setup in the Kassiopeia environment (compare with fig. 3.19). The rates are depict with the FPD pixel layout, so that individual pixels represent a single transmission function measurement. The individual measurement cycles can be clearly distinguished, as only comparable rates are observed in a single measurement cycle, e.g. the potential mapping with a 3.8 G(d) setting consists of four cycles, three before the extensive maintenance break and one after on the pixels px55 and px103) where a work-function correction of $\Delta\phi_{\mathrm{EGun,corr}} = 42\,\mathrm{mV}$ is added. The potential mappings with the 9 G- and 3.8 G(s)-setting were recorded after the maintenance break.

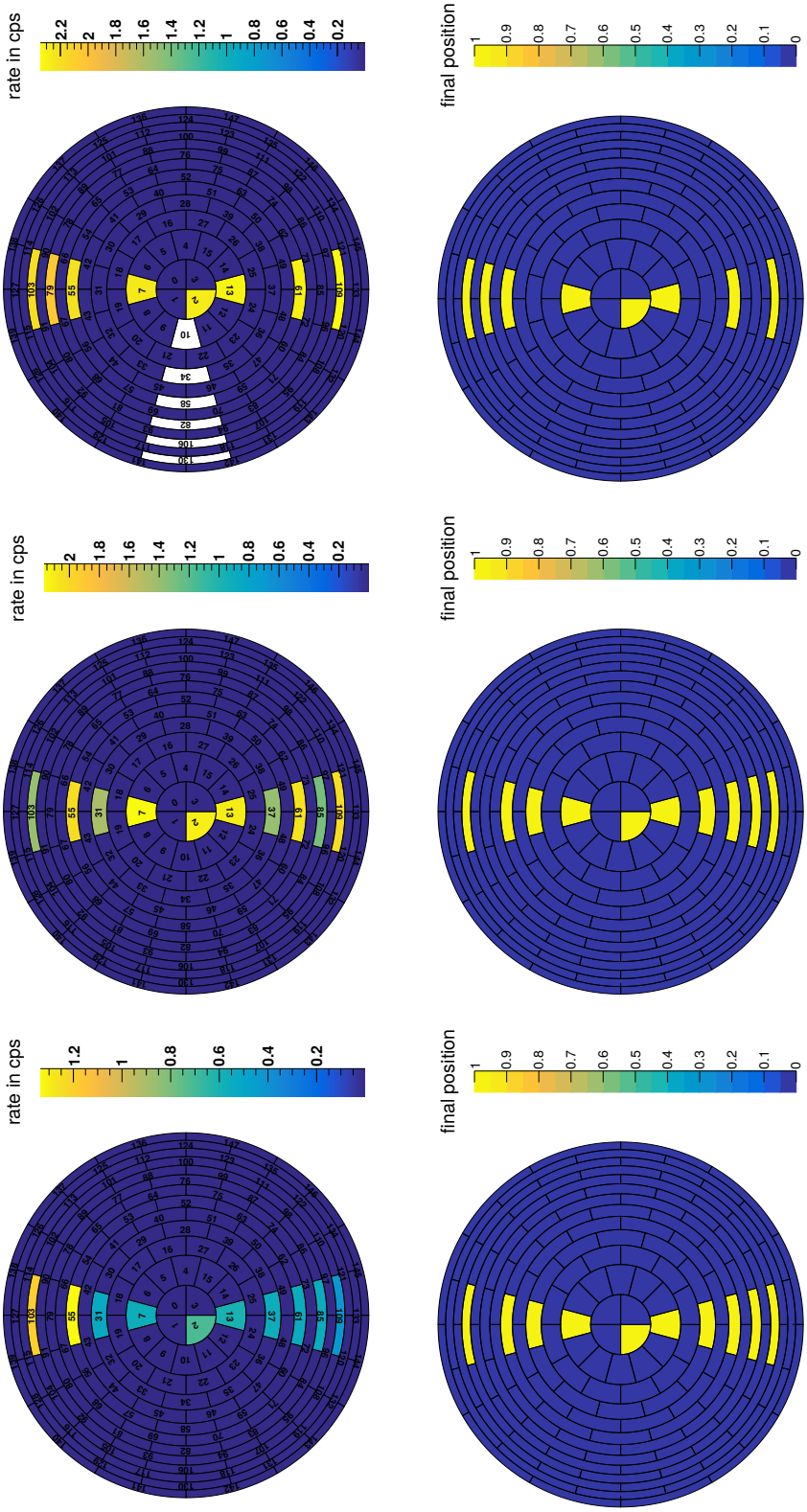

Figure 6.14: Target pixels of the radial scans for transmission-function measurements. From left to right, the target pixels for measurements with an applied 3.8 G(d)-setting, 9.0 G(d)-setting, 3.8 G(s)-setting. The upper hit-maps shows the count rate during transmission-function measurements and the corresponding magnetic field-line simulations below. Radial scans are split in measurement cycles; four, three and one cycles (from left to right). A measurement cycle consist of consecutive measurements. Here the rates of the pile-up peak are shown as an indicator for the e-gun work-function (see text). Rates in the main electron peak are about a factor 1000 higher. In the lower line it is shown that the target pixel distribution can be reproduced by simulations with overcompensation EMCS currents. See also table B.3.

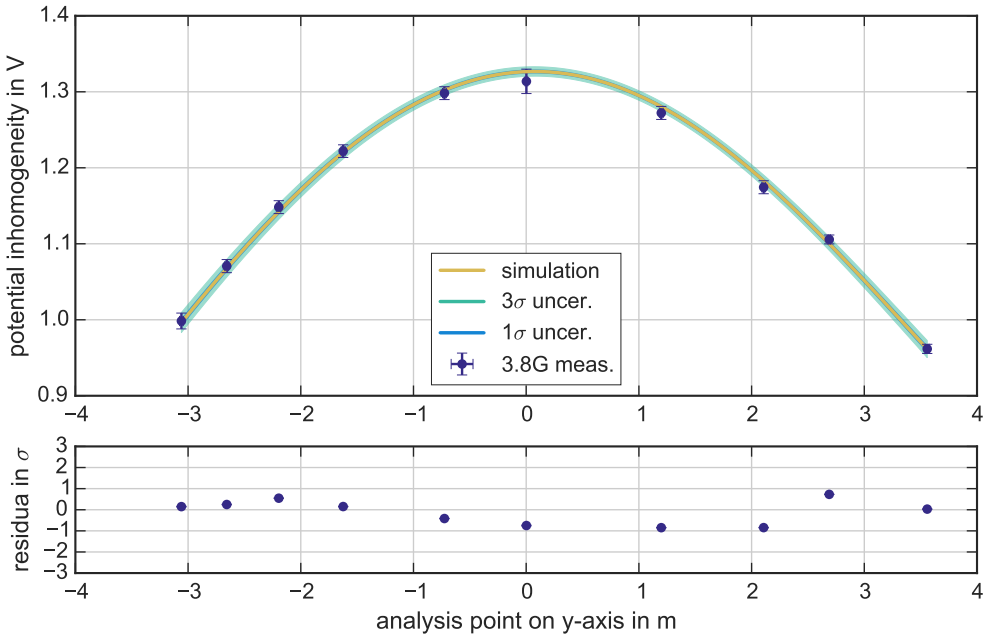

Figure 6.15: Potential mapping of the analyzing plane, here shown for a vertical scan with an applied 3.8 G-setting and an overcompensated EMCS. Simulation of the potential is based on a three dimensional model and the error belts correspond to the systematic uncertainties of the simulation. Fit results of the transmission-function measurements are shown with an work-function correction (see text). Uncertainties of the fit results are dominated by statistical uncertainty. An excellent agreement between simulation and measurement is indicated by residuals within 1σ and no noticeable structure.

The simulation of the radial potential-inhomogeneity is performed with the most advanced magnetic-field model, including the over compensation of the magnetic background field and a realistic three-dimensional potential model as well. The transmission-function measurements are fitted eq. (6.6) with the energy-distribution listed in table 6.1 and the angular distribution determined infig. 6.10. This fit function proves to be a reliable model and feasible for all transmission-function measurements, with a reduced $\chi^2 = 1.2 \pm 0.4$ on average. Individual fit results can be found in table 6.3.

Figure 6.15 shows the results for the vertical potential-mapping with a 3.8 G(d) setting. The uncertainty of a measurement are based on the fit result and the uncertainty belt of the simulation incorporate the systematical uncertainties (section 6.5.2). The shape of the potential simulation features an asymmetry that originates from the vessel deformations and the axial-position variations of the analyzing points. Those effects are well suited to reproduced the observed radial potential-inhomogeneity ΔU_r in the transmission-function measurements. The residual are within an 1σ range for all measurements and feature no obvious structure. A global potential correction of $\Delta\phi = 0.858\,\mathrm{V}$ is applied to account for the work-function differences between the e-gun gold-layer and the inner-electrode system. This values is reasonable in comparison with the work-function literature values of gold

Table 6.3: Potential mapping along the vertical axis with a 3.8 G setting. A global offset $\Delta\phi = 0.858\,\mathrm{V}$ is added to the experimental data of to account for the work-function difference between the e-gun and the main spectrometer. A work-function correction term $\phi_{\mathrm{EGun,corr}}$ is added to runs of different measurement cycles. Simulation uncertainties incorporate the systematic uncertainties and measurements feature the fit uncertainties.

pixel	$\Delta U_{\mathrm{r,sim}}$ in mV	$\Delta U_{\mathrm{r,exp}}$ in mV	$\Delta\phi_{\mathrm{EGun,corr}}$ in V	red. χ^2
103	1820 ± 4	1821 ± 6	0.042	1.344
55	1958 ± 3	1964 ± 6	0.042	1.035
31	2041 ± 3	2038 ± 9	–	1.077
7	2139 ± 2	2135 ± 9	–	0.798
2	2185 ± 2	2170 ± 14	–	1.022
13	2161 ± 2	2164 ± 8	–	1.858
37	2079 ± 3	2088 ± 8	–	1.986
61	2001 ± 3	2012 ± 9	–	1.034
85	1926 ± 4	1935 ± 10	–	1.107
109	1855 ± 4	1858 ± 10	–	0.801

$\phi_{\mathrm{gold}} = 5.1\,\mathrm{eV}$ (ref. [Ber05]) and stainless-steel (SAE 316LN) $\phi_{\mathrm{steel}} = (4.4 \pm 2.0)\,\mathrm{eV}$ (ref. [Pic92]). Profound work function measurements before and after the maintenance break deploying different coatings of the e-gun fiber confirm these results (ref. [Beh14], [Beh16]).

To study the influence of the magnetic-field asymmetry on the accuracy of the potential determination, the analysis was repeated with a falsely assumed azimuth symmetry of the magnetic field (table 6.4). The results are shown in fig. 6.16, represented as a difference of the measured and the simulated potential. Without the implementation of the magnetic asymmetry, a clear trend in the potential deviation becomes evident. This shape is expected from table 6.2. The resulting standard deviation of the radial potential-inhomogeneity is thereby increased by a factor 3.4 to $\Delta U_{\mathrm{r}} = 21.2\,\mathrm{mV}$. The allowed potential uncertainty per pixel is approximated to $\pm 30\,\mathrm{mV}$ and added in the graph as an upper and lower limit. In both cases is the observed potential deviation within the given limits, although the error threshold is nearly reached (see also appendix B.3).

Table 6.4: Potential variation and offset for various magnetic-field settings. The maximal observed potential difference of a potential mapping is given in the second column and the corresponding standard deviation in the third column. The last column is the fitted global offset between the fitted and simulated radial potential-inhomogeneity ΔU_{r}. Such an offset is identified with the unaccounted work-function difference of the e-gun and the electrode system.

Mag. setting	ΔU_{max} in mV	ΔU_{r} in mV	$\Delta\phi$ in meV
3.8 G(d)	18.7	6.2	858 ± 2
9.0 G(d)	29.2	9.4	884 ± 3
3.8 G(s)	64.9	24.3	880 ± 9

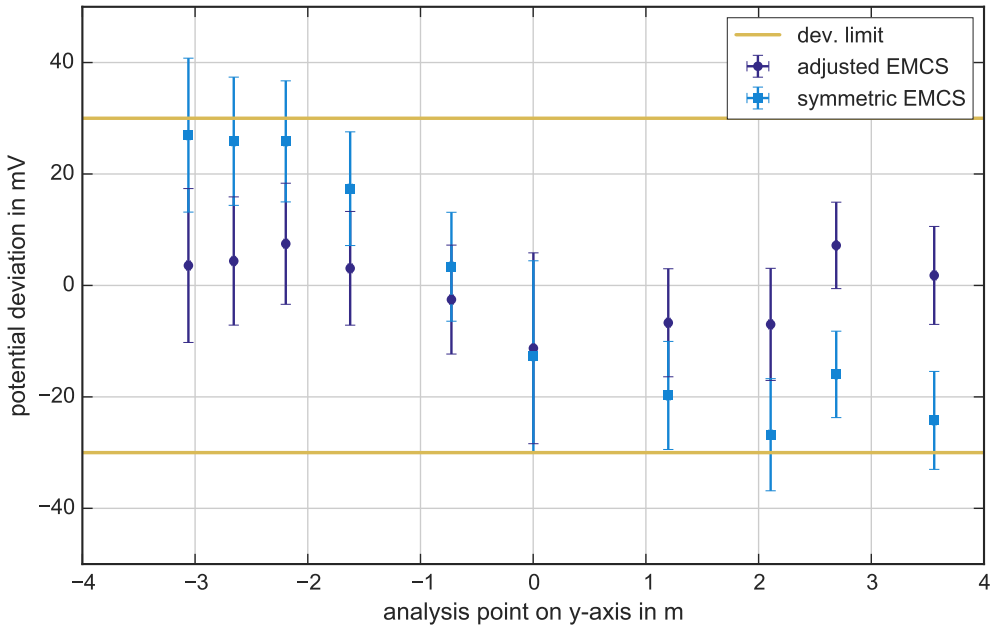

Figure 6.16: Influence of a magnetic-field asymmetry on the obtained potential deviation, here given as the difference of the experimentally and simulated potential $U_{\mathrm{exp}} - U_{\mathrm{sim}}$ with an applied 3.8 G setting. In both cases the full three dimensional electromagnetic model is used. Solely the overcompensation of the magnetic background field is once neglected (symmetric EMCS) and once included (adjusted EMCS) in the analysis.

Finally, the influence of various magnetic settings on the radial potential-mapping is studied. Figure 6.17 show the potential deviations when a 3.8 G(d),9.0 G(d) and 3.8 G(s) magnetic field is applied. Again, a fully realistic magnetic-field model is utilized and the potential is simulated with an three dimensional model. The uncertainties in the plots combine the statistical fit-uncertainty and the systematical uncertainties. In case of the measurements with a 3.8 G(d)-setting, the observed potential deviation is comparable with zero within uncertainty. The shape of the potential deviations are in agreement with the 3.8 G(d) potential mapping, but show a minor tendency compared to a vanishing deviation. A linear dependence on the y-axis position is observed, that is probably caused by an unaccounted magnetic-field on outer radii (compare to fig. 6.16). For 3.8 G(s)-setting the accurate knowledge becomes even more important, as a perfect alignment between the magnetic-field and the potential is an essential pre-request for this setup. Especially on outer radii the analyzing point location variate up to 1 m and thereby the prevailing retarding potential also (fig. B.3). On some of the outer radii thereby the uncertainty threshold is surpassed.

Nevertheless, within a radial position of $y = \pm 2\,\mathrm{m}$ the observed potential deviations are comparable for all magnetic-field settings. Compare to results obtained during SDS 1 (ref. [Gro15]), the variation of the potential difference with a 3.8 G(d) setting feature a reduced standard deviation by a factor 3.

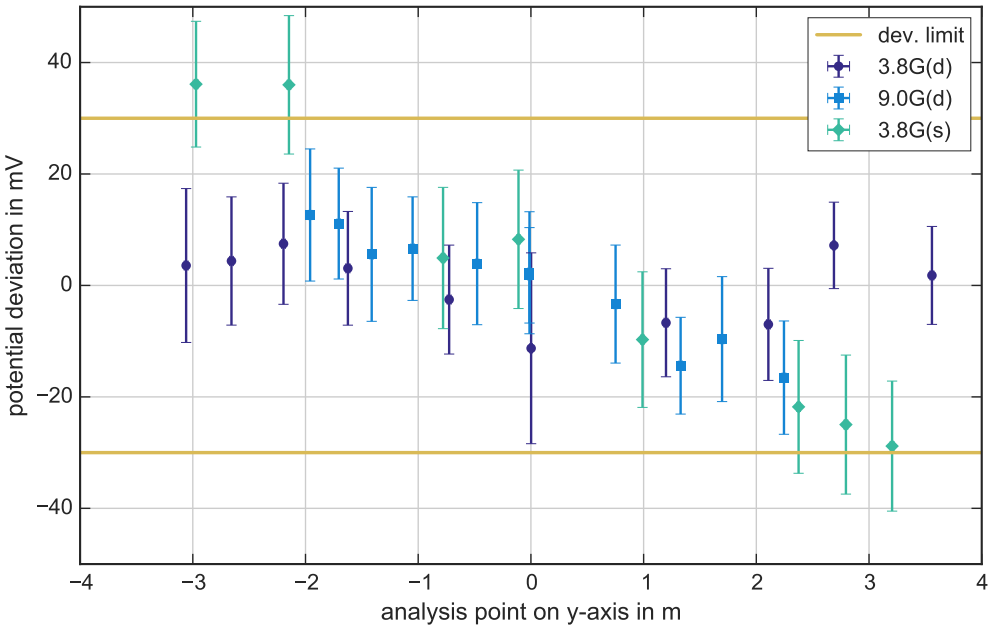

Figure 6.17: Potential deviations for various magnetic-field settings, here given as the difference of the experimentally and simulated potential $U_{\mathrm{exp}} - U_{\mathrm{sim}}$. A global potential offset correction is applied to the individual measurements (table 6.4). The analysis is based on the fully realistic magnetic field with an overcompensation of the magnetic background field and a three dimensional potential calculation. A potential deviation limit is approximated to ±30 mV.

6.6 Radial inhomogeneity of the magnetic field in the analyzing plane

The radial magnetic-field inhomogeneity is the second parameter of the electromagnetic property of the main-spectrometer that is required for a full description of the MAC-E filter. In addition to the transmission-function measurements with a minimal electron polar-angle relative to the magnetic-field, measurements with larger e-gun electron angles were performed B-field mapping. The determination of the radial magnetic-field inhomogeneity is thereby an extension of the potential mapping.

The very electron trajectories that were utilized for potential mapping (fig. 6.14) were also used for the B-field mapping. Transmission-function measurements were performed with at least four different e-gun back-plate angles, usually polar angles of 0°, 3°, 6° and 9° relative to the minimal polar-angle position (fig. 6.8) were selected. The resulting transmission functions share a common value for the radial potential-inhomogeneity ΔU_{r}, but the transmission energy E_{tr} is shifted to larger values for angular distribution with a larger mean value μ_{a} (fig. 6.3). For a given retarding potential and a common field line, the transmission-energy shift $\Delta E_{\mathrm{tr},\Theta}$ is derives from eq. (2.9) for two different angles Θ by

$$\Delta E_{\mathrm{tr},\Theta} = E_{\mathrm{s}} \frac{B_{\mathrm{a}}}{B_{\mathrm{s}}} \left(\sin^2(\Theta_2) - \sin^2(\Theta_1) \right) , \tag{6.23}$$

where E_s is the initial energy of the electrons (fixed to 18.6 keV for the B-mapping) and B_a/B_s the magnetic field ratio between the start- and analyzing-point position. Thus, the observable $\Delta E_{tr,\Theta}$ depends not on the spectrometer properties B_a alone, but the three additional parameter as well. Unfortunately, all these parameter need be be determined with high accuracy as they are all highly correlated.

The influence by the start energy E_s on the B_a determination is neglectable as it is monitored within a few hundred mV which corresponds to a relative uncertainty of a few ppm. In contrast, a thoroughly investigation is necessary on the prevailing start magnetic-field at the e-gun and especially of the polar angles of the electrons in the center of the PS 2 magnet.

6.6.1 Magnetic field at the e-gun chamber position

The start magnetic field for electrons from the e-gun is defined by the relative position of the e-gun chamber to the PS 2 magnet. Alignment measurements in the beginning of SDS 2 enable a modeling of the e-gun geometry with a mm precision (section 3.4.2). Along the radius of the UHV-manipulator rotation the magnetic field is simulated at the position of the electron beam-spot on the e-gun back-plate. For the magnetic-field simulations, the realistic magnetic-field model that includes all alignment information is applied.

In the course of the e-gun commissioning the start magnetic-field was also measured. For this purpose, a hall sensor was mounted at the exact position of the electron emission-spot. The hall sensor measured the magnetic field with a precision of 0.1 mT (ref. [Gro07]). Various UHV-manipulator configurations are selected to cover the full range for possible positions.

In fig. 6.18 the magnetic field along the z-axis is shown for a scan along the vertical axis. With the e-gun alignment, the shape of the measured magnetic-field is rather well reproduced. However, the simulated fields along the z-axis are significantly lower by (-0.15 ± 0.08) mT considering the entire UHV-manipulator range. In terms of the absolute magnetic-field, the deviation is increased to (-0.7 ± 0.4) mT.

Possible effects to introduce such a deviation are

- the current of the PS 2: To generate a 0.15 mT-larger field at the position of the e-gun, an increased current of about 1 A is necessary. However, during the SDS 2 phase no current deviation above 330 mA was observed (fig. 5.7).
- the geometry of the PS 2 coil: The location, the orientation and the radius of the PS 2 coil influences the resulting stray field at the position of the e-gun. In dedicated alignment and magnetic field measurements (section 5.1.4), as well as in a pre-spectrometer standalone measurement campaign (ref. [Frä11]), no hint for a deviation of the geometry to explain the magnetic field difference in the observed regime was found.
- the positioning of the e-gun: This is the most likely explanation of the observed deviation as the e-gun apparatus was dismantled and recommissioned twice after the initial alignment measurement. The observed magnetic field deviation can be translated in an additional alignment uncertainty of the e-gun of about $\vec{x}_{EGun} = (2.7 \pm 1.6)$ cm, a value well within the limits of the determined e-gun misalignment in fig. 3.19. Also is a difference between e-gun back plate and the hall sensor position of a few mm possible.

The additional uncertainty of the e-gun position which arises from the start magnetic field uncertainty is a examined together with the e-gun offset values determined in section 3.4.2 as a possible adjustment parameter in comprehensive simulations in the next section.

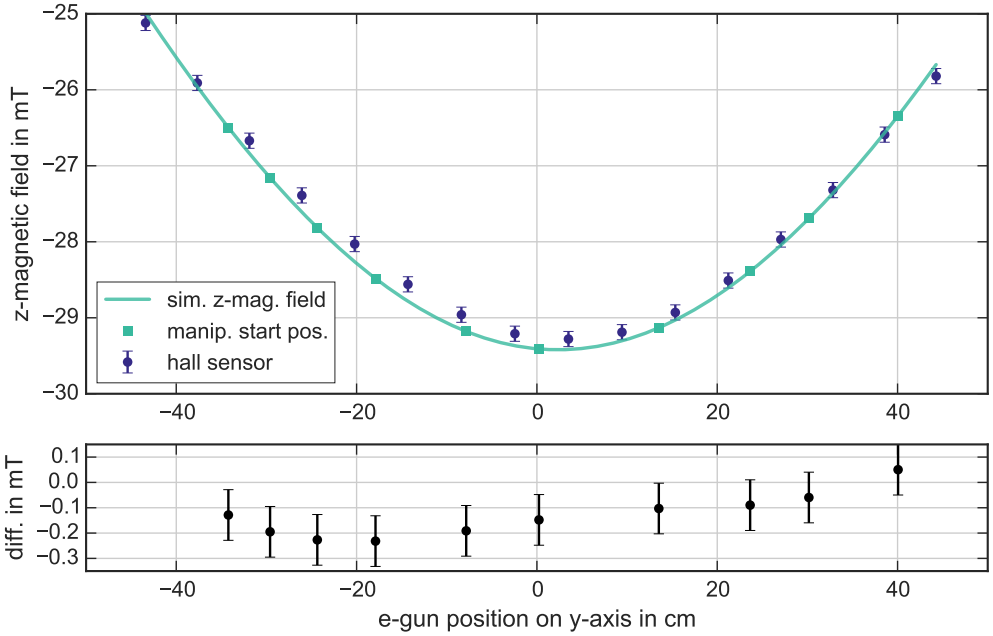

Figure 6.18: Start magnetic-field at the e-gun chamber. The magnetic field is measured and simulated along the vertical UHV-manipulator rotation, here shown for the z-component of the magnetic field. The difference of the magnetic field $\vec{B}_{\mathrm{exp}} - B_{\mathrm{sim}}$ is shown below and features an offset of $(-0.15 \pm 0.08)\,\mathrm{mT}$. Start positions for transmission-function measurements are highlighted.

6.6.2 Simulation of the electron polar-angle in the PS 2 magnet

The angular distribution of the emitted electrons from the e-gun is the most crucial input value to determine the magnetic field in the analyzing plane with eq. (6.23). As there is no biunique process to extract a electron angle from a transmission-function measurement, solely comprehensive electron-tracking simulations make this parameter accessible.

A sophisticated simulation model of the e-gun in the KASSIOPEIA framework was developed in cooperation with [Beh16]. This model is based on the CAD drawings of the e-gun and incorporates the available alignment measurements (fig. 3.19). Due to the complicated geometry and the asymmetric electromagnetic fields, a full three-dimensional model is necessary (fig. 6.19). Thereby is a realistic reproduction of the UHV-manipulator and e-gun chamber configuration options possible, comprising mechanical positions and applied voltages of the dipole electrode, as well as the e-gun back- and front-plate.

A verification of the reliability of e-gun simulations can be found in ref. [Beh16] and [Wie16], where the first addresses the issue of different focus voltages and absolute start energies on the angular distribution, while the later aims on the bias of the angular distribution due to a different dipole voltages. However, both cases study electrons along the symmetry axis exclusively and therefore, no tilt angles of the UHV-manipulator are applied. In this section, the focus is on the simulations with a tilted UHV-manipulator for various radii.

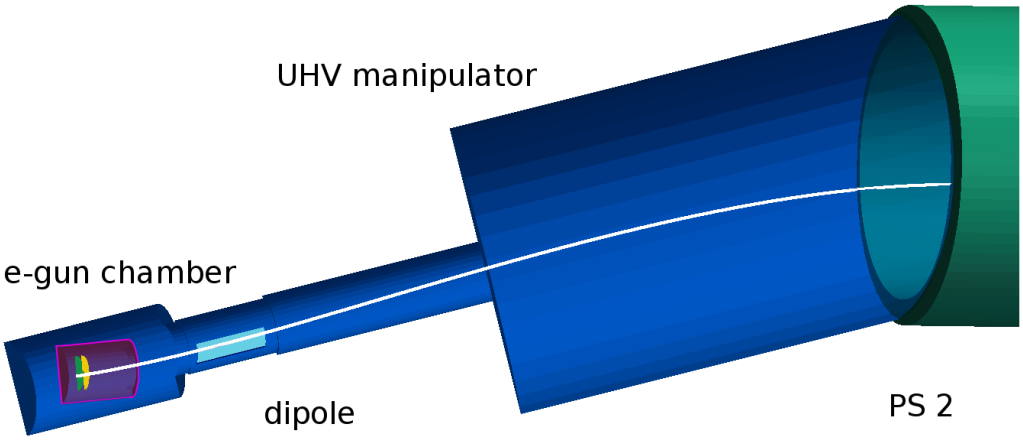

Figure 6.19: Representation of the e-gun in KASPER in the full three dimensional simulation-model with a rotatable UHV-manipulator and the e-gun chamber (compare to fig. 3.8). In the depict example the manipulator features a polar angle of 14.65° and a rotation of the e-gun chamber of 6°, associated with a measurement on px109. An electron track is shown in white, based on a realistic magnetic-field model and the HV setup of the transmission-function measurements where the e-gun back-plate is on $U_{\text{back}} = -18.6\,\text{kV}$ (green), front-plate on $U_{\text{front}} = -13.6\,\text{kV}$ (yellow) and the dipole electrode on $U_{\text{dip}} = 3.0\,\text{kV}$ (light blue). Grounded components are shown in blue, the e-gun chamber is highlighted in violet and the PS 2 magnet in green.

For UHV-manipulator positions and e-gun chamber rotations corresponding to the transmission-function measurements (fig. 6.14), the electron polar angles in the PS 2 unit were simulated in a two level process:

1. First the orientation of the e-gun chamber resulting in a minimal electron polar-angle was determined by a rotation of the e-gun chamber in vertical and horizontal direction. For each configuration, 100 electron tracks from the e-gun to the center of the PS 2 are simulated. This approach is analogous to the measurement process described in fig. 6.8. A time consuming and computation-intensive simulation to determine the minimal transmission energy that includes a full the main spectrometer model can be avoided, when the longitudinal energy of the electrons is analyzed instead. The configuration that results in the maximal longitudinal energy of the electrons in the PS 2 is identified with an e-gun chamber orientation that generates a minimal electron angle.
2. In a second step the e-gun chamber is rotated relative to the minimal angle position to reproduce the measurement configurations. The applied rotations correspond to the azimuth and polar angle of the e-gun back plate during the measurements. 1000 electron tracks are simulated in this setup. The final distribution of the electron polar angle in the PS 2 magnet is used as an input parameter in eq. (6.23).

In both cases, the electron emission at the e-gun back-plate was modeled with the same energy and angular distribution. For the energy distribution a normal distribution of a mean kinetic energy $\overline{E}_{\text{kin}} = 200\,\text{meV}$ and a width of $\sigma_{E_{\text{kin}}} = 200\,\text{meV}$ was used and an isotropic angular distribution was assumed, according to ref. [Pei02].

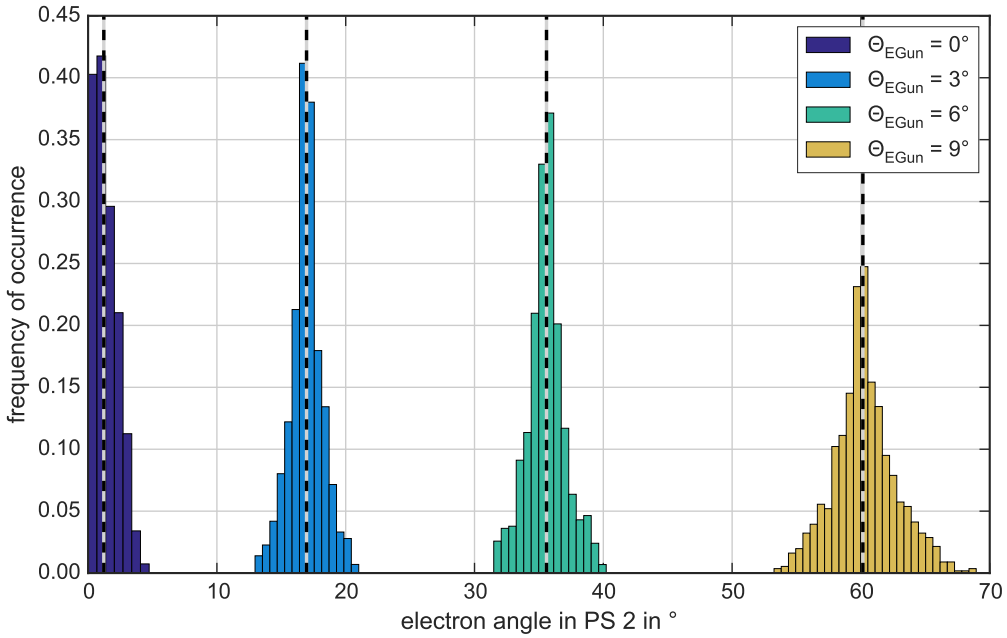

Figure 6.20: Simulation of the electron polar angles at the PS 2 center, here shown for the px109 simulation. Four e-gun configurations were simulated with different e-gun back-plate angles relative to the magnetic field. As expected, the angular distribution shifts to higher mean values and a larger width when the e-gun angle is increased. The dotted line indicate the means of angular distributions as used in further simulations. The angular uncertainty is identified with the width of the distribution.

The simulation results corresponding to an UHV-manipulator position for a measurement on px109 are shown in fig. 6.20. The four simulations are labeled according to the back-plate rotation relative to the minimal angle configuration. A tilt of the e-gun back-plate results in a shift of the angular distribution in the PS 2 center to bigger mean value μ_a as well as an increased width of the angular distribution. In the presented case, a rotation of the e-gun of about 0°, 3°, 6° and 9° results in a mean electron angle in the PS 2 of 1.22°, 16.96°, 35.59° and 60.15°. Here, an azimuth angle of 0° was selected which corresponds to a tilt of the e-gun to the right, perpendicular to the UHV-manipulator rotation. Simulations with rotations in other directions with azimuths of 90°, 180° and 270° give comparable results within uncertainty.

Qualitatively, these observations are in agreement with corresponding simulations in ref. [Zac14] and [Beh16]. However it is noticeable that these simulations were performed for an e-gun on axis where significantly smaller electron angles were observed for the same back-plate rotations. This is indeed the expected trend on outer radii; assuming the initial angular distribution is only defined by the potentials U_{back} and U_{front}, the field ratio $B'_{\text{PS2}}/B'_{\text{S}}$ can be

used to calculate the angular distribution in the PS 2 center

$$\sin^2 \Theta'_{\mathrm{PS2}} = \frac{B'_{\mathrm{PS2}}}{B'_{\mathrm{S}}} \frac{B_{\mathrm{S}}}{B_{\mathrm{PS2}}} \cdot \sin^2 \Theta_{\mathrm{PS2}} \tag{6.24}$$

for various field lines based on a simulation with just one specified UHV-manipulator configuration (see eq. (2.5)). Unfortunately, the calculated angular distribution in eq. (6.24) are smaller by a factor of about 1.32 as the simulations and also feature a minor radial dependence. This means, that the angular distribution is not purely defined by the e-gun back plate orientation relative to the magnetic field and the applied focus voltage U_{foc} between back and front plate. Consequently, comprehensive simulations of the angular distributions have to be performed for every e-gun configuration.

As stated above, there is no biunique method to extract an arbitrary angular distribution from a transmission function measurements, but the overall angular range based on the minimal an maximal angle in PCH magnet can be determined. The later angle is extracted from magnetic reflection measurements and represents the only independent validation test of the simulations. Due to the adiabatic transport between the e-gun chamber and the PCH unit the electron polar angles increase is described by eq. (2.5). Eventually, the electron angel reaches $\Theta_{\mathrm{PCH}} = 90°$ in the PCH magnet for sufficiently large e-gun back-plate angles. Any further increase of the initial electron angle leads to a magnetic reflection in the PCH magnet independent of the surplus energy (see eq. (2.6)). As the electromagnetic configuration of the spectrometer has no influence[1] on this measurement, by this means the generated electron angles can be studied depending on the well known maximal magnetic field in the PCH unit only.

The magnetic reflection was measured for two target pixels, one on the central bulls-eye (px2) and one an outer radius (px109). The measurement strategy was the same in both cases, here the measurement on px109 is presented (fig. 6.21). A surplus energy of about 80 eV was applied to the electrons which is sufficiently large enough to avoid a reflection by the retarding potential and not to high to cause an electron loss due to a non-adiabatic transport (ref. [Bar13a]). For back plate angles above 12° the e-gun electrons are completely reflected. Between back-plate angles of about 10° to 12° a rate drop is observed, which can be described by an error-function with a mean of $(10.860 \pm 0.012)°$ and a width of $(0.61 \pm 0.02)°$. Of main interest is the mean of the error function where half of the electrons are reflected, this value is identified with a mean angular distribution of 90°. The azimuth of the e-gun tilt is in the same direction as in the transmission function measurements to minimize systematic uncertainty, although the results for tilts in opposite directions are comparable within uncertainty.

To identify the magnetic reflection in the simulation data, additional and larger e-gun angles were simulated. To save computation time, the tracks were stopped in the PS 2 center and based on the magnetic field values in the PS 2 magnet of about 5 T, the magnetic reflection is analytically calculated. This approach is reasonable as an adiabatic transport of the electrons in the main spectrometer can be assumed. The angular distribution is formed

1 The independence of the magnetic reflection measurements on the spectrometer potentials refers to the voltage distribution with the additional offsets of the inner electrode system. The absolute potential has an influence on the angular distribution as shown above and in ref. [Beh16].

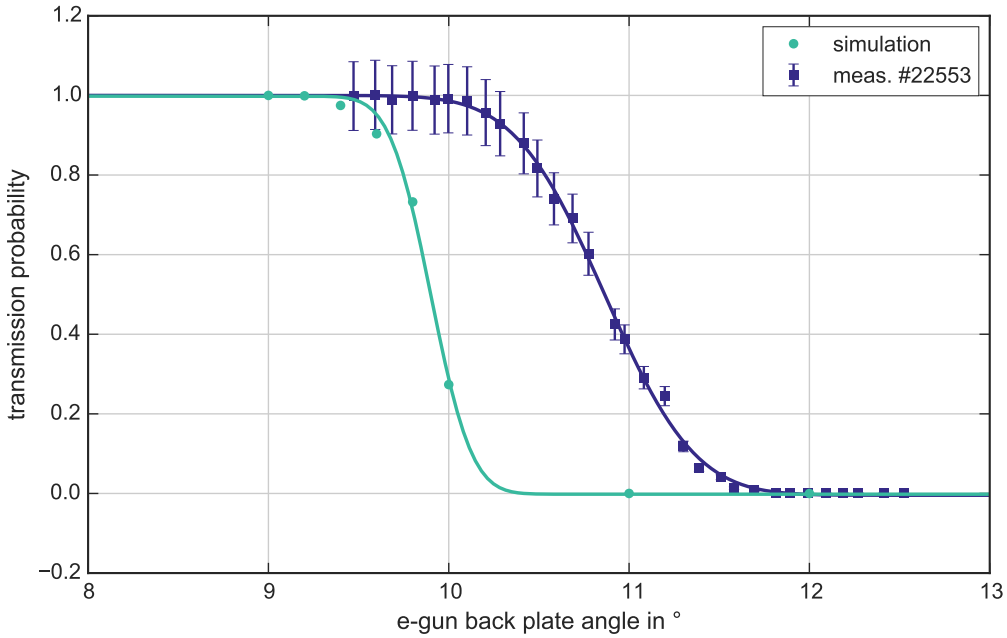

Figure 6.21: Magnetic reflection on target pixel 109. Electrons with a very large polar angle are magnetically reflected in the high magnetic field of the PCH magnet eq. (6.25). The measured and simulated magnetic reflections are fitted to an error function at $\Theta_{\mathrm{EGun}} = 10.9°$ and $\Theta_{\mathrm{EGun}} = 9.9°$ respectively. The ratio between theses two mean values of $\alpha = 0.91$ is used to re-scale the e-gun back-plate angles in the simulations.

by 1000 electrons per simulation and their angles in the PCH magnet

$$\Theta_{\mathrm{PCH}} = \arcsin\sqrt{\frac{B_{\mathrm{PS2}}}{B_{\mathrm{max}}}} \tag{6.25}$$

is calculated to estimated the transmission probability as the ratio $\sum(\Theta_{\mathrm{PCH}} > 90°)/1000$. In fig. 6.21 the transmission probability is shown as a function of the applied e-gun back-plate angle that is fitted to an error function with a mean of $(9.900 \pm 0.009)°$ and a width of $(0.25 \pm 0.02)°$.

The relative differences of the mean of the error functions is a parameter to characterizes the discrepancy between the simulation and experiment. For pixel 109 a correction factor α of 0.912 ± 0.014 is established. When this value is combined with the verified position for minimal electron angles (section 6.4.3), so the e-gun back-plate angle in the simulation can be re-scaled with α to determine realistically angular distributions. The correction factor α amounts to 0.908 ± 0.025 for the central pixel 2 (see [Beh16]). A homogeneous correction factor for all manipulator positions of $\alpha = 0.91$ is therefore a reasonable assumption.

Note that the correction factor can not be directly related with the simulated angular distributions due to the non linear dependence between the applied e-gun back plate angle and the resulting angular distribution of the electrons. Adjusted simulation results for the

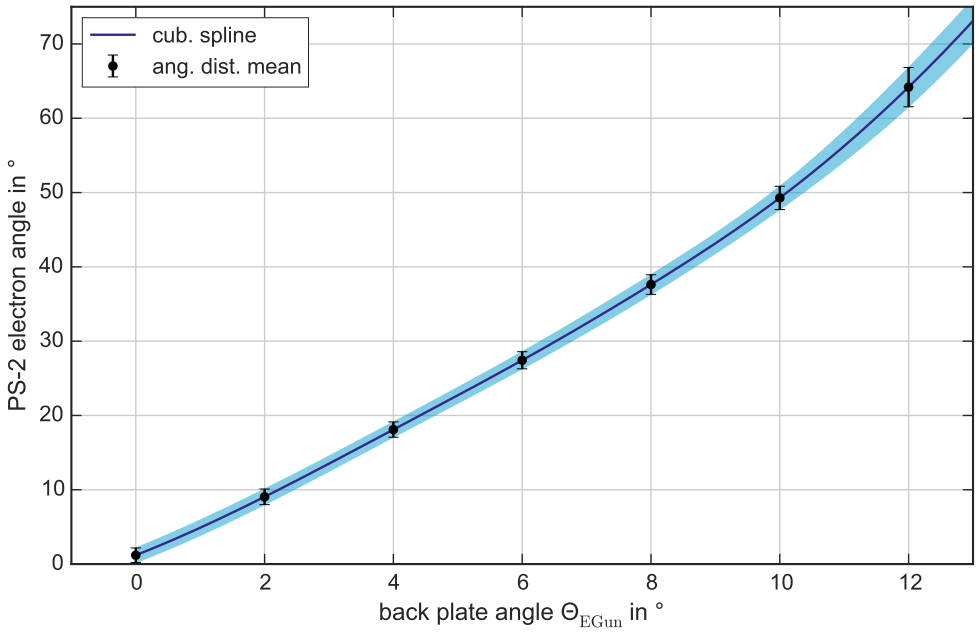

(a)

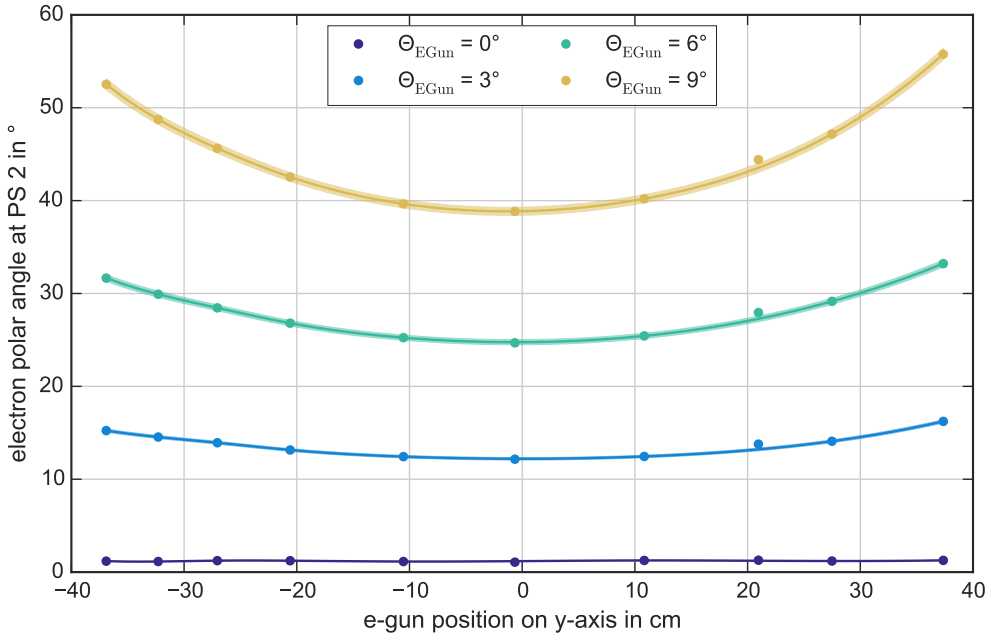

(b)

Figure 6.22: Simulation results of the angle distribution in the PS 2. (a) shows the simulation results of the mean value μ_a of the angular distribution in the PS 2 in dependence of the e-gun back plate angle Θ_{EGun} for px2, described by a arcsin function. The uncertainty correspond to the 1σ-width of the angular distribution. In (b) the polar angle of the electrons at the PS 2 for the usual four e-gun back-plate angles Θ_{EGun} for the vertical B-field mapping are shown. Positions of the UHV-manipulator for transmission function measurements are highlighted. An error-belt is added that correspond to the systematic angular uncertainty of the e-gun on a 1σ-level.

individual UHV-manipulator positions used in the analysis of the transmission function measurements are shown in fig. 6.22.

A significant difference of the angular widths in the simulation and experiment are observed. However, this is of no concern due to the properties of a arcsin distribution close to 90° where a tiny change in the angular distribution is disproportionately magnified. Therefore, the difference of the simulated and actual width in the PS 2 is below 0.1° and the resulting uncertainty of the transmission energy is negligible (fig. 6.2). Whereas the fact that the magnetic reflection can be described by the symmetric error function indicates that no additional bias is introduced to the transmission function due to the angular distribution, for details see [Beh16].

6.6.3 Determination of the magnetic field in the analyzing plane

To determine the radial magnetic-inhomogeneity, transmission-function measurements with various electron angular distributions were performed. In addition to the potential mapping for every UHV-manipulator configuration different transmission energies eq. (6.23) and widths fig. 6.2 are observed. Essentially two approaches are possible to determine the magnetic field in the analyzing plane:

1. Analyze the shape of the transmission function, where a large electron angel introduces an asymmetry. This asymmetry is increased for a larger magnetic field in the analyzing plane (fig. 6.3). The advantage of this method is a simultaneous fit of the inhomogeneity of the retarding potential and magnetic field. But this method requires a very detailed and thereby time consuming transmission-function measurement as well as an highly reliable angular distribution simulation (mean and width) and is therefore discarded.
2. Analyze the shift of the transmission energy, where a large electron angel introduces an shift to high surplus energies. This shift is increased for a larger magnetic field in the analyzing plane (fig. 6.3). This method benefits from the fact that a shift is clearly visible even for small magnetic fields when the electron polar angle is large enough. However, it is only possible to disentangle the correlation between the inhomogeneity of retarding potential and magnetic field when several transmission function measurements are combined (section 6.2.2). Due to the linear dependence of the transmission energy on the retarding potential and on the other hand the arcsin relation between with magnetic field, an unambiguous assignment of the two spectrometer properties is possible.

In this section the measurements with an applied 3.8 G configuration are analyzed. As only a small magnetic field deviation between simulation and measurement is observed by the high precision magnetometers (fig. 5.4) this field setting is perfectly suited to test the accuracy of the analysis tools.

At least four transmission function measurements with different angular distributions were combined to fit the magnetic field in the analyzing plane. The mean values of the angular distributions are fixed (fig. 6.22) and the widths were fixed to 2°, as only minor variations of the angular-distribution widths were observed. Beside the magnetic field, the background and amplitude were fitted for a normalization as well as the radial potential-inhomogeneity ΔU_r. On the one hand it becomes necessary to fit ΔU_r due to the change from empirical angular distributions to simulation results and on the other hand gives this gives the opportunity to check for consistency (see fig. 6.10 and fig. 6.20).

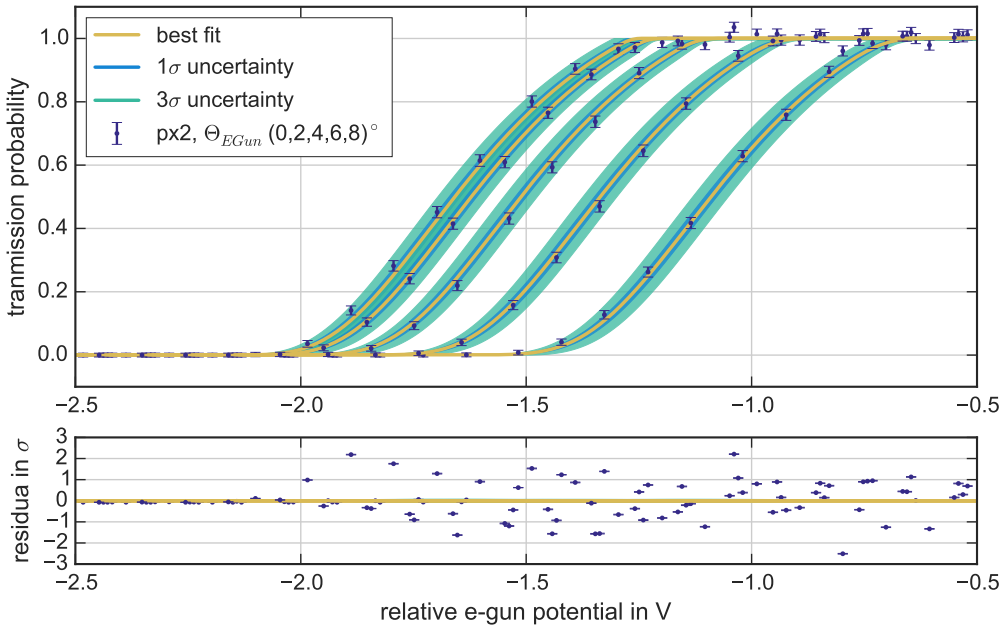

Figure 6.23: Determination of the magnetic field with transmission-function measurements, based on five measurement on px2 with different e-gun back plate angles (0°, 2°, 4°, 6° and 8°). Due to eq. (6.24), the transmission energy is shifted to higher values for bigger polar angles. In this example the fit reveals a magnetic field of $B_\mathrm{a} = (364.8 \pm 1.8)\,\mu\mathrm{T}$ and a magnetic field deviation of $B_\mathrm{a,exp} - B_\mathrm{a,sim} = 3.5\,\mu\mathrm{T}$.

It can be clearly seen, that the radial shape of ΔU_r is in agreement with the previous fit and the simulated values (table 6.5). In comparison to the previous potential fit, the radial potential-inhomogeneity features here more positive value by 32 mV with a standard deviation of 14 mV. Both values can be explained by the increased fit uncertainty due to the correlation with the magnetic field B_A. In the central region reasonable χ^2 values close to 1 are observed, the increase on outer radii are partly attributable with the fixed width of the angular distributions. In conclusion, a reliable fit of the magnetic field can be expected from this fit model, confirmed by the generic fit of the transmission functions on pixel 2 (fig. 6.24). In this case, the simulated and fitted magnetic field B_A agree within 2σ with a fit precision of 1.8 µT. In general, the uncertainty of a magnetic field fit is within a range from 1.2 µT to 2.1 µT and thereby fulfills the requirement of a magnetic field precision inside the spectrometer of 2 µT (ref. [Gro15]).

Before the radial shape of the magnetic field can be discussed, the corresponding systematic uncertainties are introduced. The estimated systematic uncertainties identified in section 6.5.2 apply to the analyses of the magnetic field as well, adjusted and extended for the following:

1. Uncertainty of the electron trajectory. The individual transmission function measurements of the potential mapping are usually followed by three measurements with an e-gun back-plate angle of 3 degree, 6 degree and 9 degree. Consequently, the UHV-manipulator

Table 6.5: Radial magnetic field inhomogeneity along the vertical axis with an applied 3.8 G configuration. The magnetic field simulations $B_{\mathrm{a,sim}}$ were made with an overcompensated earth magnetic-field at the locations of the analyzing points given in table 6.2. The systematic uncertainty of the magnetic field fit is estimated to 4.8 µT. Results of the magnetic field fits are given in column $B_{\mathrm{a,exp}}$. A global offset of $\Delta\phi = 0.858\,\mathrm{V}$ is added to the experimental data to account for the work-function difference (see table 6.3). In column "red. χ^2" the reduced χ^2/ndf is given.

pixel	$B_{\mathrm{a,sim}}$ in µT	$B_{\mathrm{a,exp}}$ in µT	ΔU_{r} in mV	red. χ^2
103	353.8	364.4 ± 1.2	1.759 ± 0.020	3.4
55	356.2	369.7 ± 1.5	1.917 ± 0.018	2.47
31	357.9	362.5 ± 1.7	2.013 ± 0.040	1.47
7	360.2	357.7 ± 2.0	2.112 ± 0.036	1.08
2	361.3	364.8 ± 1.8	2.125 ± 0.015	1.22
13	360.6	334.1 ± 2.1	2.134 ± 0.037	1.28
37	358.5	353.8 ± 1.9	2.063 ± 0.034	0.98
61	356.8	357.8 ± 1.6	1.991 ± 0.034	1.03
85	355.4	377.0 ± 1.5	1.914 ± 0.036	2.27
109	354.3	360.8 ± 1.3	1.837 ± 0.052	2.53

had not been moved in between measurements and the systematic uncertainty of the horizontal and vertical analyzing point position is suppressed[1].

2. Axial position of the analyzing point is shifted as a function of the electron polar angle as shown in fig. 6.12. Thereby, the electrons experience a different retarding potential and magnetic field. However, the potential variation is below the 6 mV-precision of the DVM (see section 3.1.4) and the magnetic field variations are about 10 nT due to the magnetic field optimization (see section 4.1.2). The uncertainty of the analyzing point position can thereby be neglected.
3. Alignment of the entire SDS setup for a accurate calculation of the magnetic field line which connects the electron start position at the e-gun, the analyzing point and the target pixel of the FPD wafer. The alignment of the FPD system and the e-gun feature an intrinsic deviations in their setup relative to the main spectrometer electrode system, as explained in section 3.4.1 and section 3.4.2. It is absolutely necessary to carefully implement all available alignment information as a geometric displacement can not be disentangled from a magnetic field disturbance.
4. The magnetic field disturbance due to magnetic materials in the walls of the spectrometer hall introduce a perturbation of the electron trajectory. In first order, a shift of the entire flux tube is thereby introduced which affects the position of the analyzing-point position and on the FPD wafer. It is expected that the analyzing magnetic field only

1 The measurements on px55 is the only exception for consecutive transmission function measurements on an individual pixel (table B.3)

variates in the sub-µT regime, but the shift of the final position on the wafer is of the same order as the alignment uncertainty (see section 5.5).

5. The magnetic field at the e-gun start position as measured in section 6.6.1. The uncertainty of the magnetic field allows to set the location of the electron emission on different positions on the same magnetic field line. This variation can not be identified by the pattern of the target pixel distribution as presented in fig. 3.19, but may affect the angular distribution of the electrons.

All these uncertainties are or can be expressed as alignment uncertainties. Combined with the overall alignment uncertainty, the effective electron start-position can vary by several cm. Two angular distributions were simulated for a perfectly aligned e-gun and with an offset on the x-axis (y-axis) of 16.25 mm (−7 mm) to estimate the effective systematic uncertainty, expressed as an angular uncertainty in the PS 2 magnet center. The angular distributions vary up to 5° in the PS 2 magnet for a e-gun back plate angel of 9°. Based on this value, the mean magnetic field variation of all trajectories of the transmission function measurements were calculated. Hence, the systematic uncertainty of the magnetic field in the analyzing plane is about 4.8 µT.

In fig. 6.24 the absolute values of the fit results and the corresponding field simulations are shown. The systematic uncertainty is represented by an 1σ and 3σ error belt. With $\bar{B}_{\text{exp}} = (360 \pm 11)\,\mu\text{T}$ and $\bar{B}_{\text{sim}} = (357 \pm 3)\,\mu\text{T}$, the averages of both distributions are in agreement within uncertainty, but the absolute field deviation exceeds the 2 µT limit. However, the bigger drawback is that the radial shape can not be reproduced. As large fluctuations of the individual magnetic field fits are observed, dominated by systematic effects. Influences of magnetic field inhomogeneity can be excluded due to the observed magnetic field variation by the high precision magnetometer (section 5.1.3) and the MobSU (section 5.4.2) within a 2 µT range as well as the time-of-flight analyses by [Bar16a]. Most likely the accuracy of the angular distribution simulation is responsible for the field deviation, caused by unaccounted alignment deviations between the e-gun, the FPD wafer, the spectrometer and the magnet system. E.g., when the 10 %-correction of the angular distribution is neglected, a decreased mean magnetic field value by 53 µT is observed. This means, that the required magnetic field accuracy is already exceeded for an angular inaccuracy of 0.4 %. Consequently, a significance of the fit below the required field limit is not possible with given setup.

To increase the accuracy of the magnetic field with a e-gun in upcoming measurement campaigns, it is strongly recommended that:

- Comprehensive alignment measurements of all sub components should be performed and thoroughly implemented in the analysis framework. FaroArm based measurements of the magnet geometries are favored, as they have the advantage to be fully independent of electromagnetic field configurations. E.g. a magnet in the transport section can introduce an perpendicular shift of the magnetic flux tube which can not be identified by a dedicated e-gun measurement. A target accuracy within 1 mm is proposed.
- magnetic reflection measurements should be performed for all target pixels. The orientation of the e-gun required to generate electrons of a minimal polar angle and the orientation where magnetic reflection occurs can be measured with dedicated e-gun measurements (see fig. 6.9 and fig. 6.21). These two e-gun orientations can be used to

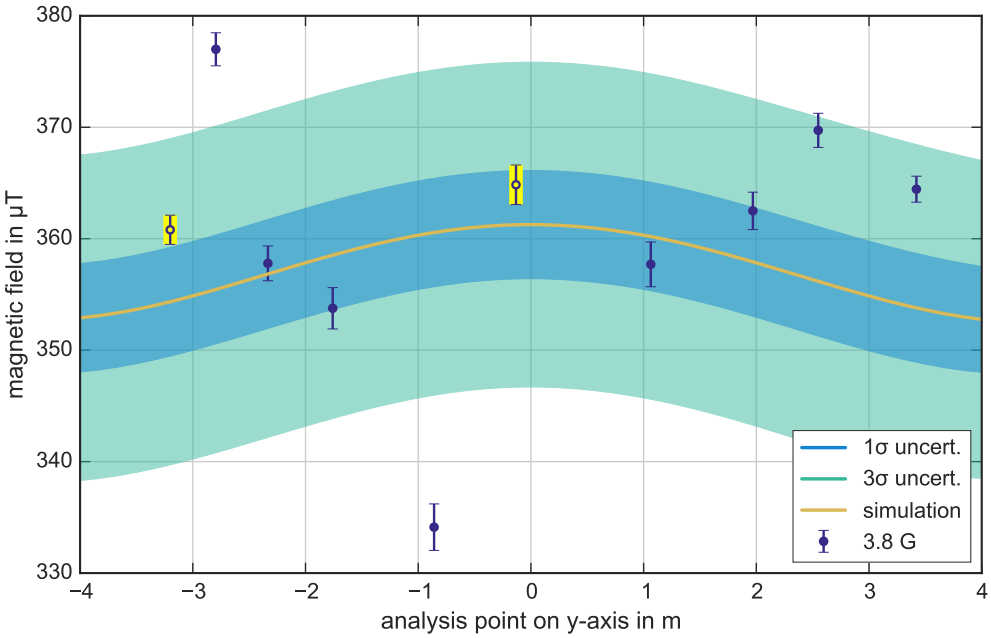

Figure 6.24: Magnetic field mapping of the analyzing plane with an applied 3.8 G setting. The statistical uncertainty is in the order of 1.2 µT to 2.1 µT and corresponds to the precision of the magnetic field fit as demonstrated in fig. 6.17. The accuracy of the magnetic field fit is given by the limited accuracy of the electron angle simulation which causes the large fluctuations. The systematical uncertainty of the simulated magnetic field is dominated by the alignment uncertainty, indicated by the uncertainty belts of 4.8 µT. For the highlighted points, magnetic reflection measurements are available to adjust the simulated electron polar angles. The mean of both angular correction factors of $\alpha = 0.91$ is applied to the remaining measurements.

identify constraints on the generated electron angles (fig. 6.22(a)). Unfortunately, only for two target pixels magnetic reflection measurements could be performed during SDS 2 (see highlighted fit values in fig. 6.24) due to time constrains and e-gun performance issues. These two values feature a reasonable deviation from the magnetic field simulation which is also comparable with the expected radial magnetic field distribution.

- to cancel out systematic e-gun positioning inaccuracies by an adapted B-field mapping routine. The e-gun can be tilted in two opposite directions to account for the uncertainty of the e-gun orientation which generates electrons with some polar angle. Transmission function measurement should be added to the magnetic field measurement sequence where the larger e-gun back-plate angles are emphasized. Proposed is at least one additional measurement. In total e-gun back-plate angles of 0°, 3°, 5°, 7° and 9° should be considered, assuming a magnetic reflection at 11°.

In general, a continuous measurement cycle must be ensured to allow for an analysis with a common energy distribution and the least possible variation of systematic uncertainties.

6.7 Conclusion

In this chapter it is explained how the transmission properties of the MAC-E filter spectrometer can be measured with an angular selective e-gun and the results of these measurements obtained from the SDS 2 campaign were discussed in detail.

In order to characterize the e-gun and spectrometer properties, a profound insight in their specific influence on the electron transport is necessary. As a angular selective e-gun is used instead of an isotropic source, the formulas of the transmission function had to be adjusted (section 6.1.1). The most prominent quantity to describe a transmission function measurement is the transmission energy E_{tr}, where electrons with a start energy of $E_{\mathrm{start}} = q \cdot U_0$, no additional kinetic energy from the photo effect $E_{\mathrm{kin}} = 0\,\mathrm{eV}$ and polar angle of 0° are just transmitted trough the spectrometer $E_{\mathrm{tr}} = E_{\mathrm{start}}$. Any deviation of E_{tr} can be accounted to either a spectrometer or a e-gun property (section 6.1.2). Based on the mean transmission energy, width and shape of the transmission function the complicated interplay between e-gun and spectrometer was depicted and a measurement strategy to disentangle their specific properties was introduced (section 6.2).

To extract the transmission probability from a transmission function measurement it has to be ensured that all e-gun and spectrometer properties are stable during a measurement run and throughout a measurement cycle. One of the most important quantities is the applied potential difference ΔU_{EGun} between the inner electrode system and the e-gun back-plate as it defines the energy of the electrons relative to E_{tr}. Due to an optimized HV layout of the main spectrometer and an ideal implementation of the e-gun in the HV distribution system, a stability of ΔU_{EGun} within 6 mV was achieved (section 6.3.1). Also the magnetic field was operated in optimal settings as defined in chapter 4 and chapter 5.

The e-gun stability during a measurement cycle was verified in dedicated long-term measurements. It was shown that electrons of constant energy and rate can be expected (section 6.3.2. Therefore, the e-gun can be considered as an emitter of poissonian distributed electrons and the spectrometer as an binomial experiment to calculate the transmission probability (section 6.3.3).

Between measurement cycles, unfavorable vacuum conditions in the e-gun chamber may influence the work function of the e-gun and consequently variate the energy distribution of the emitted electrons. It is therefore crucial to have an parametrization that can account for these changes to enable a combined analyses of several measurement cycles. Considerable efforts were made in this thesis to generate a reliable and stable model. Based on a generalized normal distribution, combined with a energy cut parameter that is identified with a minimal kinetic start energy of $E_{\mathrm{kin}} = 0\,\mathrm{eV}$, a generic description of the energy distribution was found (section 6.4.1). A verification of this model was performed by a detailed transmission function measurement with a narrow energy resolution. It could also be shown, that it is crucial to repeat such transmission function measurement whenever measurement interruptions occur. Especially when major hardware modifications are carried out, significant changes of the mean kinetic energy and shape of the energy distribution are observed (section 6.4.2).

In comparison to the previous SDS 1 measurement phase, the angular selectivity of the e-gun could now be verified (section 6.4.3). Based on the introduced energy distribution model, an empirical description of the angular distribution was found that can be applied to the analysis of the radial potential distribution (section 6.4.4).

The radial inhomogeneity of the retarding potential ΔU_r in the analyzing plane is one of the major spectrometer-properties. In was shown, that ΔU_r indeed can be described by the electromagnetic model provided by the Kasper software framework. To do so, it is essential to determine the exact shape of the analyzing plane. In section 5.5 an overcompensation of the constant magnetic-background field was demonstrated, resulting in a biased shape of the analyzing plane (section 6.5.1). Beside the issue of the analyzing plane shape, other systematic effects are fairly well under control (section 6.5.2). Based on this comprehensive electromagnetic model, an excellent agreement between simulation and fit results is achieved. In case of a 3.8 G setting, structures in the residuals are suppressed within a 1σ uncertainty. The observed a standard deviation of $\Delta U_\mathrm{r} = 6.2\,\mathrm{mV}$ is about the measurement precision of the DVM. Also for other magnetic field settings consistent results between simulation and potential values are observed (section 6.5.3).

The second key parameter to describe the electromagnetic characteristic of the spectrometer is the radial inhomogeneity of the magnetic field B_a in the analyzing plane. As B_a is fully correlated with the angular distribution of the electron Θ_EGUN and the start magnetic field B_s, sophisticated simulations of the e-gun are required to disentangle their contribution to E_tr. To minimize systematic uncertainties, the magnetic field at the e-gun chamber position was verified by a dedicated field measurement (section 6.6.1). The remaining position uncertainty was included in the e-gun simulations. The simulation results are tested by independent magnetic reflection measurements, revealing a deviation between measurement and simulation of about 10 % (section 6.6.2. With adjusted angular distributions a difference of only $(3 \pm 11)\,\mu\mathrm{T}$ was observed for the average values of simulated and fitted magnetic field distributions. However, the radial shape could not be reproduced due to the lack of magnetic reflection measurements for most of the investigated FPD target pixels (section 6.6.3).

CHAPTER 7

Influence of the magnetic field on the neutrino mass systematic

The magnetic-field strength and shape in the spectrometer influences several measurable quantities, each with an individual but vague influence on the neutrino-mass systematic of KATRIN. The most prominent parameters of the main spectrometer are outlined in the electromagnetic design requirements (section 2.1.2). All of these requirements were addressed within this thesis[1]. The accuracy and precision of the magnetic field for various settings and electromagnetic-field conditions were evaluated in the previous chapters, but the implications on the neutrino-mass sensitivity are not obvious.

This is due to the fact that the magnetic field in the main spectrometer is not associated with a particular m_ν-systematic (ref. [KAT05]). In fact, the two dominant contributions of the main spectrometer to a m_ν-systematic, the transmission-function and the observed background rate, are influenced by the magnetic field in a complex fashion. In both cases, a non-trivial relation to the absolute field value, shape and uncertainty was verified in ref. [Gro15], [Har15b] and the thesis at hand.

To expose a dependence of the neutrino-mass systematic on the magnetic field, elaborated ensemble tests are required. Monte-Carlo simulations involve the full experimental setup and thereby enable to resolve the influence of a particular experimental quantity; in this case the magnetic field.

In section 7.1 an introduction to the framework for the Monte-Carlo simulation is given, based on the work of ref. [Kle14]. With this tool at hand the influence of the magnetic-field accuracy, precision and shape is evaluated in section 7.2. Based on the measured field deviations and deformations in chapter 5 the simulation results can be linked to the magnetic environment of the KATRIN experiment. This is the crucial step to formulate a generalized description of the field dependencies on a realistic estimation of the magnetic field uncertainty. Thereby a empirical model of the m_ν-systematic in dependence of the absolute field is given and the impact on a neutrino-mass measurement campaign is estimated.

1 Solely the adiabatic transport could not be studied experimentally. Transmission-function measurements dedicated to adiabatic transport of electrons trough the main spectrometer require surplus energies of at least 10 kV. In the utilized setup surplus energies only up to 1 kV were possible. The adiabatic transport should be addressed in an upcoming measurement campaign.

7.1 Framework for Monte-Carlo simulations

To generate a sophisticated model of a realistic β-decay spectrum as measured by the FPD unit, a set of elaborate statistical tools are provided by the Kasper modules Source modeling and β-decay spectrum calculation (SSC) and the KATRIN fit module (KaFit). In section 7.1.1 an analytic model provided by SSC is used to describe the β spectrum shape of molecular tritium. The KaFit module is utilized to identify the influence of specific magnetic field disturbances on the neutrino-mass analysis as a statistical neutrino-mass uncertainty and a systematic neutrino-mass shift.

7.1.1 Tritium spectrum for a Monte-Carlo simulation

The Source modeling and β-decay spectrum calculation (SSC) module facilitates the source- and gas-dynamic specific properties to calculate realistic differential and integrated tritium β-decay spectra (fig. 7.1). In its current state it combines the previous works of ref. [Höt12] with ref. [Käf12] and further improvements are achieved by addressing additional systematic-effects (ref. [Kle14]).

For a realistic description of the WGTS characteristic, the central 10 m long source region is split into individual segments. For each segment the prevailing key parameters are calculated, identified with:

- Gas density and velocity. These parameters result from the full solution of the Boltzmann equation, based on the pressure gradient within the WGTS (ref. [Höt12]). The gas density is identified with the activity in a particular segment and the scattering probabilities for signal electrons with gas molecules. A variation of the gas velocity leads to an energy shift of the spectrum, due to Doppler broadening.
- Temperature profile. An additional Doppler broadening arises from the gas temperature as an influences on the molecular movement, which might vary between individual segments (ref. [Käf12]). By that, scattering probabilities and the angular distribution of the electrons in the source are affected.

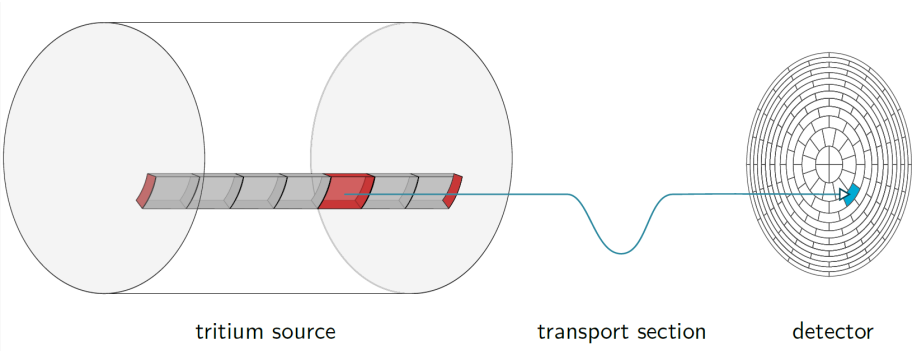

Figure 7.1: Schematic segmentation of the WGTS. In radial and azimuthal direction the segments represent the detector pixels distribution. Additionally, the axial segmentation along the beam direction is used to implement a realistic temperature profile, as well as a gas density and velocity model. The spectrometer section is not depicted in this sketch. Figure adapted from ref. [Kle14].

- Magnetic field distribution. The realistic geometry and the magnetic-field solvers of Kassiopeia are used to simulate the local magnetic-field strength and shape. Thereby the volume of a given source segment, as well as the corresponding maximal acceptance angle Θ_{max} (eq. (2.6)) is calculated. The electron angle defines the electron trajectory and thereby the energy loss due to synchrotron radiation and the probability for elastic and inelastic scattering (ref. [Ase00]). Consequently, the absolute electron rate and the shape of the transmission function is influenced by the start magnetic field in the source (ref. [Gro15]).

Based on the given source model, the calculation of the differential tritium β-decay spectrum is performed utilizing the classical Fermi theory as introduced in section 1.3.3. Several extensions of the basic β-theory become relevant in case of a gaseous, molecular tritium source as used as in KATRIN setip. The major extensions contributions are:

1. The Fermi function $F(Z',E)$ describes the Coulomb interaction between the charge Z' of daughter nucleus and the emitted electron of energy E. In case of a β^--decay, the electron is attracted by the positive charge. Consequently, the tritium spectrum is slightly distorted towards lower energies (ref. [Sim81]).
2. The Radiative corrections for the electron interactions within the Coulomb field of a nucleus via virtual and real photons. These corrections are important close to the tritium endpoint energy (ref. [Rep83]).
3. The exited final states distribution of the molecular decay product $(^3\mathrm{HeT})^+$ and the related isotopologues. These molecules can be in a rotational, vibrational and electronic exited state. All these states with an individual excitation energy E_{F} reduce the maximal spectrum energy. Based on the corresponding probability P_{f} of a specific

Table 7.1: Configuration of the tritium spectrum for Monte-Carlo simulations. Default values are based on ref. [KAT05].

parameter	configuration
column density	$5 \times 10^{17}\,/\mathrm{c^2m}$
magnetic flux	$191\,\mathrm{T\,c^2m}$
cross section of inelastic scattering	$3.456 \times 10^{-18}\,\mathrm{c^2m}$
start magnetic field B_{s}	3.6 T
maximal magnetic field B_{max}	6 T
tritium purity ε_{T}	0.95
background rate R_{bgd}	10 mcps
detector efficiency $\varepsilon_{\mathrm{det}}$	0.9
measurement time distribution	3 years effective, default
tritium endpoint E_0	18.575 keV
detector segmentation	bullseye + 12 rings
total systematic uncertainty budget	$0.017\,\mathrm{eV^2}$

final state, an effective spectrum is calculated. In addition, the small ratio of other tritiated hydrogen isotopologues, namely DT and HT, feature an individual final state contribution. The final state distribution is thereby a weighted sum of the energy shifts of the individual branches (ref.[Sae00]).

4. the nuclear recoil of the molecular decay product $(^3\mathrm{HeT})^+$. Close to the tritium endpoint energy, the recoils leads to a nearly constant energy loss of typically 1.7 meV (ref. [KAT05]).

When the properties of an extended source and the characteristics of a gaseous molecular tritium are combined, a realistic representation of differential β-spectrum of KATRIN is achieved. Source related effect are studied in ref. [Kle15]. In the simulations of the thesis at hand, a homogeneous source is assumed where constant source parameters are applied based on the design values (table 7.1) due to performance reasons and comparability with previous simulations. The combined analysis of all available systematic uncertainties is an ongoing task, first results can be found in ref. [Val16].

As the KATRIN experiment is a MAC-E filter based experiment, only the integrated β-spectrum can be observed, derived from a convolution of the differential spectrum with the transmission function. When the integrated spectrum incorporates the energy loses and modifications listed above, the transmission function is extended to the so-called response function R which describes the realistic experiment setup and is used to calculate the actual observable. For the individual pixels j the integrated rate can be expressed for a given potential U_0 based on

$$R^j_{\mathrm{signal}}(qU_0,E_0 m_\nu^2) = N^j_{\mathrm{tot}}\,\varepsilon^j_{\mathrm{det}}\,\frac{\Omega^j}{4\pi}\int_{qU_0}^{E_0}\frac{\mathrm{d}^2N^j}{\mathrm{d}E\mathrm{d}t}(E_0,m_\nu^2)\cdot R^j(E,qU_0)\mathrm{d}E, \tag{7.1}$$

where N_{tot} is the total number of tritium nuclei, $\varepsilon_{\mathrm{det}}$ the efficiency of the detector and the solid angle of the allowed electron polar angles is described by Ω. In comparison to the pure Fermi theory, the count rate is significantly reduced, the endpoint shifted to an lower energy of about 2.0 eV and the signature of a non-vanishing neutrino mass is smeared out (fig. 7.2 in comparison to fig. 2.3).

To account for a possible distortion of the β-spectrum in the operation of the experiment, the measurement time distribution together with the selected retarding potentials are adapted and the systematic uncertainties are included in the analysis chain. The measurement time distribution is carefully studied in ref. [Kle14] as it also needs to allow for an appropriate blinding scheme (ref. [Mer14]). The impact of individual systematic uncertainties is estimated in ensemble test and likelihood shape studies with the KaFit module of Kasper. In this thesis, ensemble tests are based on the β-decay model presented in this section.

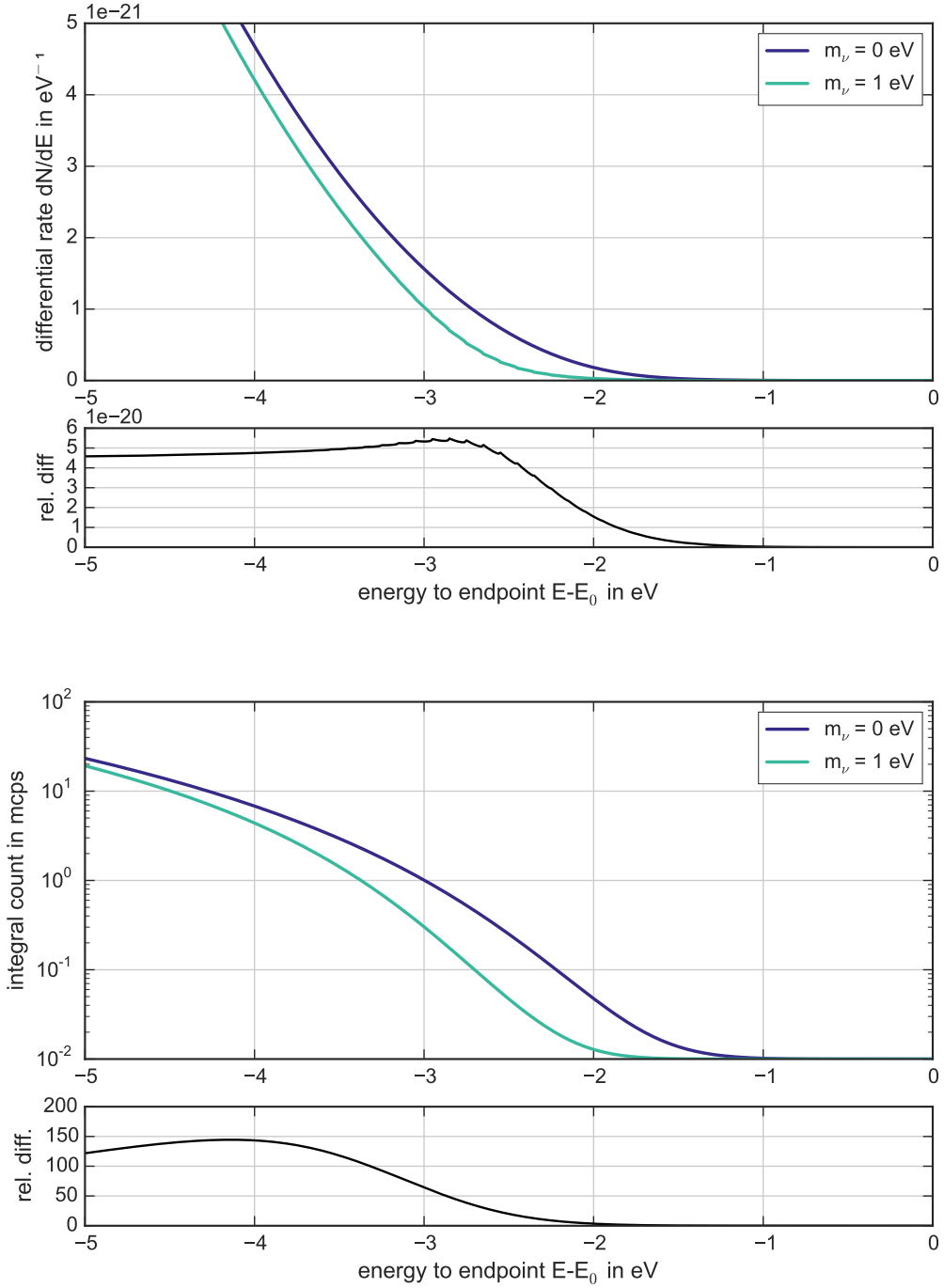

Figure 7.2: Influence of energy corrections on the tritium beta-decay spectrum in differential (upper plot) and integrated form (lower plot). A spectrum with a vanishing neutrino mass is shown in purple and a spectrum with a neutrino mass $m_\nu = 1\,\mathrm{eV}$ in green. For both plots the difference of both spectra is shown. The spectra are calculated with the KATRIN software Kasper (section 3.2.3), including a simplified versions of the most common energy-losses that are encountered at the KATRIN experiment, such as final state distribution, elastic and inelastic scattering in the source (see text). Note the shift of the tritum spectrum to lower energies and a smeared out peak of the neutrino mass influence in comparison to fig. 2.3. Details in ref. [Kle14].

7.1.2 Identify neutrino mass uncertainties and systematics

The KaFit module is developed to combine all relevant statistical tools, mathematical techniques and a probability model to estimate the neutrino mass from an observed spectrum. This module facilitates also sensitivity studies of systematic effects and measurement strategies by generating possible neutrino-mass measurement progressions. By a variation of a certain parameter in the simulation configuration of a neutrino-mass measurement while it remains constant in the associated analysis, the impact on the neutrino mass systematic of the respective parameter can be deduced.

Two different methods can be exploited to setup and analyze the simulations. Either the Profile Likelihood method is utilized to examine a Likelihood function or a chi-square function of KATRIN in its minimal four parameter fit eq. (2.15) (ref. [Kle14]). While being fast to calculate, the influence of a systematic offset of a operation parameter on the statistical uncertainty can not be assessed. The other possibility is to perform a full ensemble test that includes Poissonian statistics of the observed signal. Although the later option is time consuming, this approach is used in this thesis to gain a complete estimation of the impact of the observed magnetic field uncertainties and a possible result of an effective 3-year-long neutrino mass measurement with the KATRIN experiment.

Based on eq. (7.1), the integrated signal rate $R(qU_0)$ with a statistical fluctuation is calculated for each applied retarding potential qU_0. In addition, a Poissonian background component is added. To calculate the number of observed signal electrons

$$N_{\mathrm{S}}(qU_0) = R(qU_0) \cdot t_{qU_0}, \tag{7.2}$$

the individual rates per retarding potential are multiplied with the corresponding measurement time, according to the measurement-time distribution. The measurement-time distribution has a key role in balancing statistical and systematic uncertainties during a measurement phase (ref. [Kle14]).

Based on a chi-square statistic, the difference between a simulated measurement and the theoretical probability model is minimized. Beside the squared neutrino mass ${m_\nu}^2$, the tritium endpoint E_0, the signal amplitude A_{S} and mean background rate R_{bgd} are free parameters in a fit. For each simulated outcome of a KATRIN measurement, a best-fit value of m_ν^2 is estimated. From the resulting m_ν^2 distribution two major information can be extracted:

- The mean difference to the true neutrino mass. A vanishing neutrino mass is selected for the sensitivity studies in this section. A shift can be interpreted as a systematic uncertainty Δm_ν^2 as a result of a difference of parameters in the simulated data and the fit model.
- The variance of the m_ν^2 distribution. From the variance the standard deviation can be calculated, which indicates the statistical sensitivity of m_ν^2. In general the observed variances are normal distributed, thus the standard deviation is $\sigma_{\mathrm{stat}} = \sqrt{Var(x)}$.

Visualized is the determination of the two systematic quantities Δm_ν^2 and σ_{stat} in fig. 7.3.

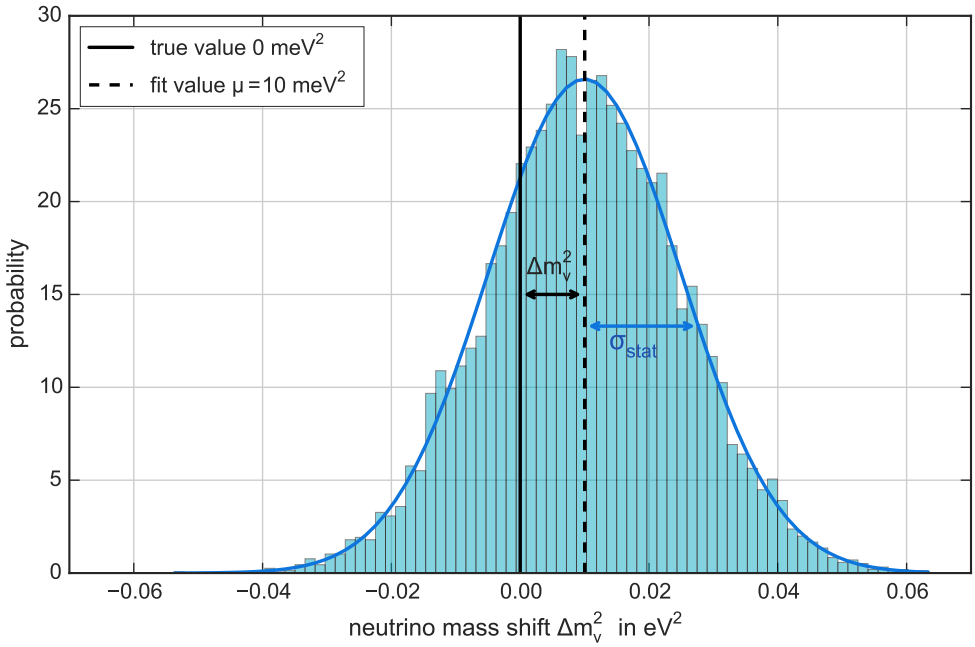

Figure 7.3: Example histogram of an ensemble test. A total of 10 000 fits and a vanishing neutrino mass m_ν^2 of 0 eV are used as input in the histogram, which can be described by a normal distribution. An intentional deviation in the simulation and analysis parameter introduces an artificial neutrino mass shift Δm_ν^2. The standard deviation is a measure of the statistical uncertainty.

7.2 Variations of the magnetic field in the analyzing plane

The systematic budget of the KATRIN experiment is split in nine major contributors where the transmission function is one of them (ref. [KAT05]). However, the systematic shift of the neutrino mass due to the transmission function uncertainty relates to the retarding potential of the MAC-E filter only, contributions by a magnetic field uncertainty are fully neglected in this context. A shift of the neutrino mass due to a magnetic field uncertainty is therefore an extension of the systematic uncertainty parameters. An additional contribution of a field uncertainty on the total systematic on the squared neutrino mass should be limited to 1 % in order to avoid a too heavy load on the uncertainty budget. Based on eq. (2.17), the maximal impact on systematic uncertainty is then restricted to a value below $|\Delta m_\nu^2| = 2.4 \times 10^{-3}\,\mathrm{eV}^2$, in case of quadratic summation.

In this chapter, the results of chapter 4 to chapter 6 are combined for a realistic estimation of the additional uncertainty as a function of the applied magnetic field, although the field uncertainty causes a neutrino mass shift Δm_ν^2. This is due to the fact that the field can be calculated within a few seconds based on the constantly monitored currents of all KATRIN magnets. By this means an analysis of a tritium measurement is possible within a reasonable time span. The comprehensive field studies, especially of chapter 5, allow for an association of an absolute field value with a field uncertainty.

Table 7.2: Basic characteristics of the magnetic fields in the ensemble tests. The field in the center of the spectrometer is given by B_A. The difference of the fields in the center of the analyzing plane and of the outer most radius of the active flux tube is given by ΔB_A where a positive sign indicates an increase of the absolute field towards outer radii and vice versa.

	3.8 G (d)	**3.8 G (s)**	**5.0 G (d)**	**5.0 G (s)**	**9.00 G (d)**
B_A	360 µT	430 µT	490 µT	540 µT	880 µT
ΔB_A	−7.9 µT	−50.9 µT	0.9 µT	−19.0 µT	2.7 µT

Four effects were identified which can cause a perturbation of the magnetic field in the analyzing plane and possibly increase the systematic uncertainty:

1. A magnetic field offset ΔB_z in axial direction. As the field is optimized to be parallel to the spectrometer axis, the absolute field B_z is thereby directly altered by ΔB_z.
2. An azimuthal variation of the magnetic field $\Delta B_\mathrm{z}(\phi)$. The walls of the experimental hall feature magnetic materials which cause a remanent and induced field. In first order this introduces a horizontal asymmetry of the magnetic background field.
3. A magnetic field offset ΔB_y perpendicular to the spectrometer axis. Such a field leads to a shift of the entire flux tube and thereby to a misalignment between the magnetic field and the retarding potential. The actual field variation is rather marginal role as the absolute field value is dominated by B_z, but nevertheless incorporated in the simulation.
4. A fluctuation of the magnetic field $\sigma_{m_\nu^2}$. The power supplies of the LFCS feature a variation of the current output that can cause a fluctuation of the field in the spectrometer.

In section 7.2.1 to section 7.2.4 these four effects are studied in the order given by this list.

A magnetic field in the analyzing plane is characterized by its absolute value and variation within in the active flux tube. Five field settings are selected for ensemble test to study these properties (table 7.2). Based on these settings the absolute value of the magnetic field can be evaluated in relevant range for a KATRIN operation. Also the two types for a magnetic field configuration are utilized, the single and double setting. The single settings feature a much stronger field variation within the analyzing plane in comparison to the double settings, therefore they are distortion-prone to azimuthal and perpendicular field offsets.

According to the FPD wafer pattern (fig. 3.10), the analyzing plane is split in 12 rings and the bulls-eye to modulate these effects. For non-axial-symmetric configurations, the area of the analyzing plane is divided in two halves. This leads to 26 calculations of the integrated rate by a convolution of the individual transmission functions with the β spectrum, where the sum of these spectra is used to estimate the neutrino mass. The average potential and magnetic field of two adjoined rings is used in the simulation to reduce the computation effort. The final effective analyzing plane comprises the bulls-eye and the combined rings 1+2, 3+4, …, 11+12 of the two halves. For a further reduction of the computation time, the axial-symmetric field model is utilized.

In the following sections, ensemble tests of at least 10 000 simulations were performed to achieve a small numerical uncertainty.

7.2.1 Axial magnetic field offset

In the ideal case, the magnetic field in the analyzing plane B_A is axial symmetric and parallel to the spectrometer axis. A magnetic field offset in z-direction ΔB_z is parallel to B_A and progress therefore fully to the absolute field uncertainty. The width of the transmission function (eq. (2.7)) is reduced or increased accordingly, resulting in a bias of the integrated spectrum.

Furthermore, the entire shape of the analyzing plane is modified by an offset ΔB_z. The location of the analyzing points, which form the analyzing plane, are identified with the minimum of $E_{\mathrm{kin},\parallel}$ along a field line (fig. 7.4(a), see also section 6.5.1). In case of a perturbation of the electromagnetic field, such as ΔB_z the location of the analyzing points have to be reevaluated. The analyzing plane is shifted and deformed in axial direction due to an offset ΔB_z, where both effects are increased for larger values of ΔB_z. Although the analyzing plane shift is rather small, minor additional offsets to the analyzing field B_A and the retarding potential need to be accounted for. In case of the magnetic field the modifications of ΔB_z are about 1 % or less (fig. 7.4(b)), whereas the reduction of the retarding potential does not exceed 5 mV in case of the 3.8 G-setting. For field settings of larger absolute values the variation of the analyzing plane shape is not as pronounced.

Based on the original radial shape of the field (the offset ΔB_z and the analyzing plane corrections), a realistic field offset for the ring segments of all fields listed in table 7.2 is calculated. Due to the observed field deviations $B_{\mathrm{dev}} = B_{\mathrm{exp}} - B_{\mathrm{sim}}$ in fig. 5.4, only negative offsets of ΔB_z down to 5 µT are utilized in the ensemble tests. As the magnetic field is oriented anti-parallel to the z-axis, negative offsets ΔB_z increase the absolute field.

A systematic shift of the squared neutrino mass Δm_ν^2 to negative values due to a field offset ΔB_z is observed (fig. 7.5(a)). The dependence between Δm_ν^2 and ΔB_z for an individual field setting is linear, as indicated by the colored lines. The numerical uncertainties of the ensemble tests are shown by error belts. For a larger absolute fields the slope is more distinct, nearly reciprocal to the absolute value. Therefore, the systematic limit of $|\Delta m_\nu^2|$ is already exceeded for an offset ΔB_z of 0.79 µT in case of a 9.0 G setting, while the 3.8 G setting is within the limit up to an offset of 2.51 µT (table 7.3). Dependencies on the magnetic field shape could not be identified.

Certain offset values in the graph are highlighted which correspond to the actual deviations as observed by the high precision magnetometers for the individual field settings. The trend between these highlighted values can be fitted with a polynomial of second degree. Moreover, these values can be converted in a dependence of Δm_ν^2 on the absolute field value, a quantity which is more accessible by simulations and measurements (fig. 7.5(b)). For magnetic field offsets, anti-parallel to the spectrometer axis, a functional correlation between Δm_ν^2 and B_A is found in

$$\Delta m_\nu^2 = \alpha_1 \cdot B_A^2 + \alpha_2 \cdot B_A, \tag{7.3}$$

where α_1 is $(-141.0 \pm 2.0) \times 10^{-10}\,\mathrm{eV^2\,\mu T^{-2}}$ and α_2 is $(42.0 \pm 1.4) \times 10^{-7}\,\mathrm{eV^2\,\mu T^{-1}}$. With these empirical values, a generalized description of a neutrino mass shift Δm_ν^2 in dependence of the absolute field B_A is identified. The maximal allowed absolute value of the magnetic field in the spectrometer center for a Δm_ν^2 within the systematic limit of $2.4 \times 10^{-3}\,\mathrm{eV^2}$ is therefore $B_A = 588\,\mu\mathrm{T}$. Even in case of a change in the magnetic background field, the

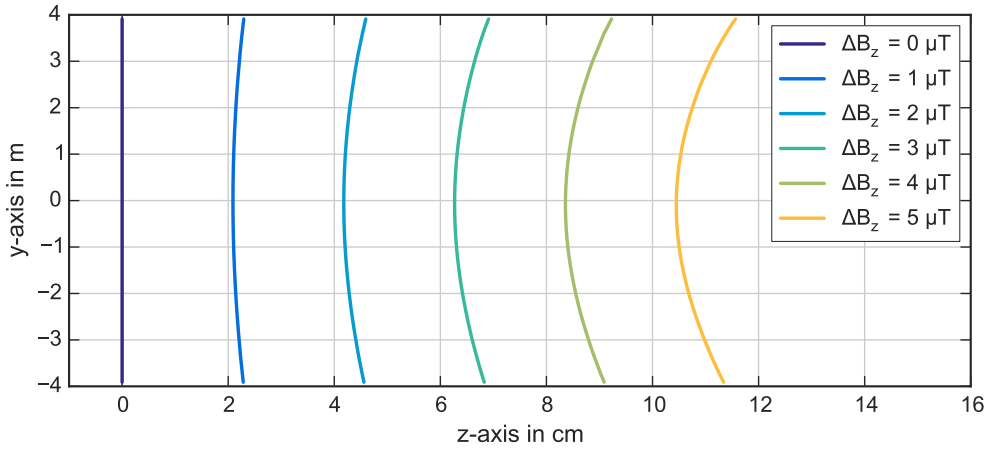

(a) Analyzing plane location and shape due to an axial field offset ΔB_z.

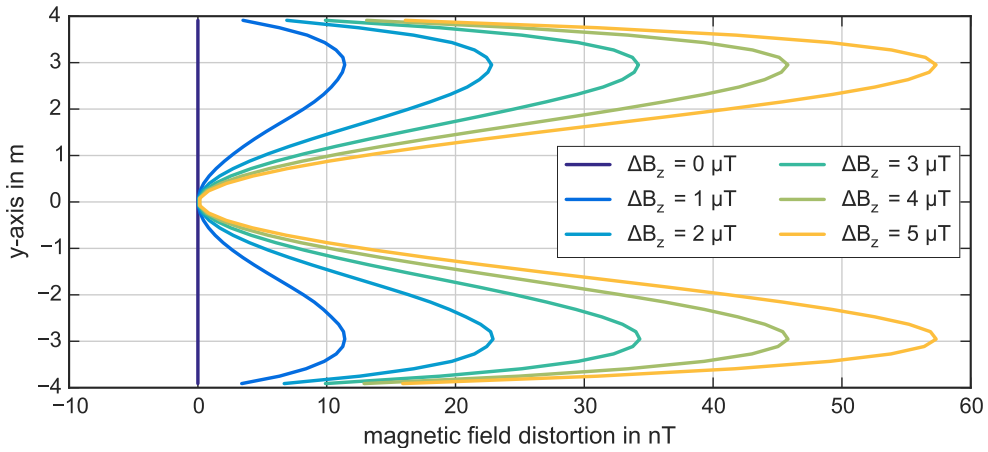

(b) Additional magnetic field variation due to anaylzing plane distortion.

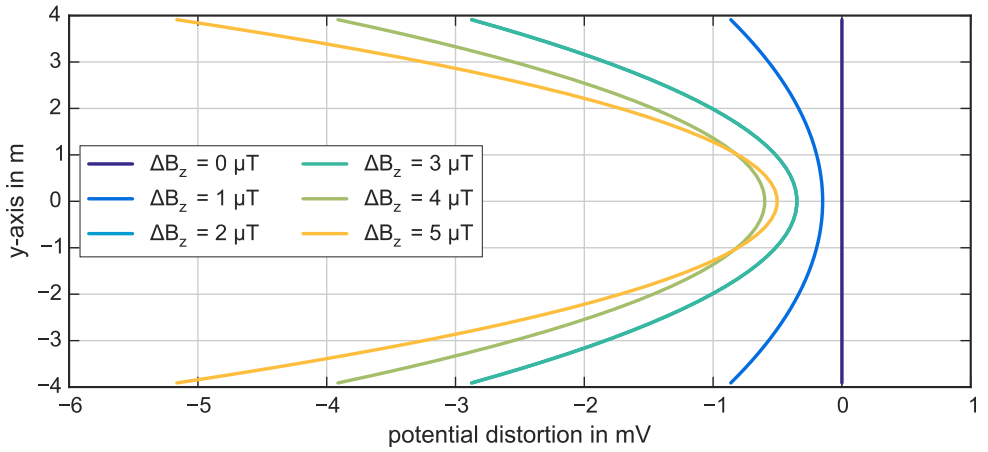

(c) Retarding potential variation due to anaylzing plane distortion.

Figure 7.4: Influence of a magnetic-field offset in axial direction on a 3.8 G setting. Such an offset ΔB_z increases the field in the analyzing plane, as well as a shape distortion of the analyzing plane (fig. 7.4(a)). Consequently, an additional field offset is observed (fig. 7.4(b)) and a decrease of the retarding potential (fig. 7.4(c)). Both quantities are given relative to the unbiased values and represent a minor enhancement of the already introduced magnetic-field offset.

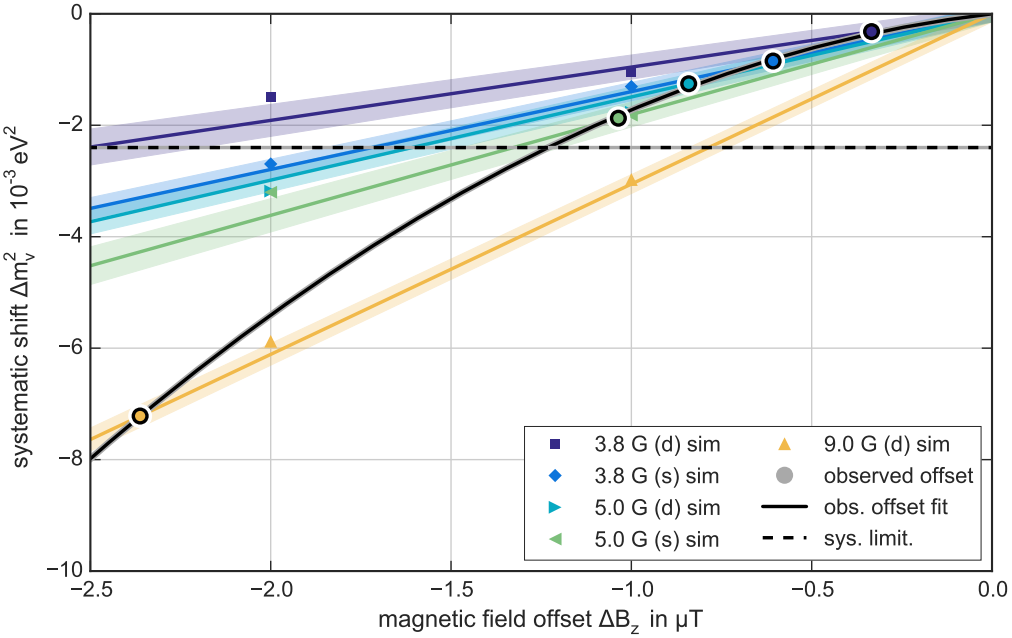

(a) Results of the ensemble tests, realistic axial-field offsets ΔB_z are highlighted.

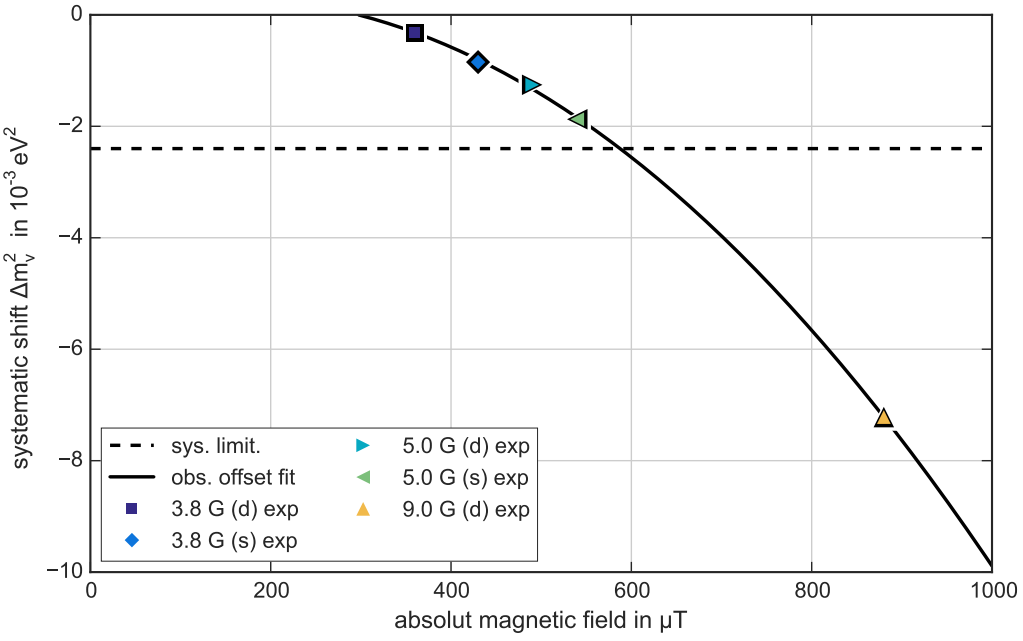

(b) Empirical dependence of Δm_ν^2 on the applied magnetic field due to an axial field offset ΔB_z.

Figure 7.5: Systematic shift Δm_ν^2 due to an axial magnetic field offset ΔB_z. In fig. 7.5(a) the simulation results of the ensemble tests are shown. Offset values of 1 µT, 2 µT, 3 µT, 4 µT and 5 µT were applied to five field settings, each featuring a linear dependence of Δm_ν^2. The error belts are the statistical 1σ fluctuations. The measured field offsets are highlighted (see fig. 5.4). The black line represents the fit result by eq. (7.3). Based on these results the absolute field dependence is identified in fig. 7.5(b). For a field in the spectrometer center of $B_A = 588$ µT the systematic uncertainty is within the limit of 2.4×10^{-3} eV^2 as indicated by the dashed lines.

Table 7.3: Influence of an axial field offset on the neutrino mass. Linear dependence (slope) of the simulated shift of the squared neutrino mass Δm_ν^2. Based on this slope, the upper limit on the field offset $\Delta B_\parallel$ for a Δm_ν^2 below 2.4 meV^2 is calculated. The expected shift of the squared neutrino mass Δm_ν^2 is calculated based on the magnetic field offsets observed in fig. 5.4 together with the resulting total neutrino mass sensitivity $\sigma(m_\nu^2)$. The total sensitivity is calculated with $S_{\mathrm{tot}} = [(\sigma^2_{\mathrm{sys,design}} + \sigma^2_{\mathrm{sys,shift}} + \sigma^2_{\mathrm{stat,sim}})^{1/2} \cdot 1.645]^{1/2}$.

setting	slope (10^{-5} eV^2/μT)	upper limit (μT)	observed offset (μT)	shift Δm_ν^2 (10^{-3} eV^2)	sensitivity (90 %CL) (meV)
3.8 G (d)	95.6 ± 7.1	2.51	−0.33	−0.32	197.6
3.8 G (s)	139.7 ± 1.9	1.72	−0.61	−0.85	198.4
5.0 G (d)	149.2 ± 2.9	1.61	−0.84	−1.26	199.6
5.0 G (s)	180.8 ± 7.7	1.33	−1.04	−1.87	200.7
9.0 G (d)	305.6 ± 2.4	0.79	−2.36	−7.22	216.9

simulation results, given in fig. 7.5(b) and table 7.3, can be used to reevaluate the absolute field dependence and thereby a new value for the maximal allow absolute field.

The consequence of a systematic shift is also that it introduces a mismatch between the actual measurement time distribution and the ideal scanning strategy (table 7.5). This issue is predominantly associated with a larger energy resolution of the MAC-E filter, thereby the observed signal rate is reduced and a larger statistical uncertainty in the neutrino mass analysis is experienced. A new significance of a neutrino mass measurement campaign is estimated by the resulting total sensitivity $S_{\mathrm{tot}} = [(\sigma^2_{\mathrm{sys,design}} + \sigma^2_{\mathrm{sys,shift}} + \sigma^2_{\mathrm{stat,sim}})^{1/2} \cdot 1.645]^{1/2}$ Only for the strongest field setting of 9 G, the KATRIN design sensitivity of 200 meV is clearly surpassed and the neutrino mass detection weakened.

7.2.2 Azimuthal field deformation

Beside a dependence of the field deviation on the axial field B_z, the measurements of the high precision magnetometers feature also a variation within the individual sensor rings. Based on the MobSU measurements, these azimuthal variations $\Delta B_z(\phi)$ were not only be confirmed, but due to the high angular coverage, they could be attributed with the influence of a remanent and induced magnetic field by ferromagnetic materials in the concrete of the spectrometer hall. Consequently, the azimuthal field variation $\Delta B_z(\phi)$ is another magnetic field deviation that needs to be considered.

A simplistic field model based on only three parameters i was developed for an estimation of the remanent and induced field contribution of the experimental hall. The four centers of the side walls (the two top walls are described by one common parameter) are considered as additional magnetic field sources. In section 5.4 the parameters i were fitted to the observed azimuthal field variations of the MobSU measurements on the LFCS ring 6 of radius r_{MobSU} of about 5.8 m (fig. 3.15). Based on these results, the field variations are approximated for rings according to the pixel pattern of the FPD detector projected in the analyzing plane.

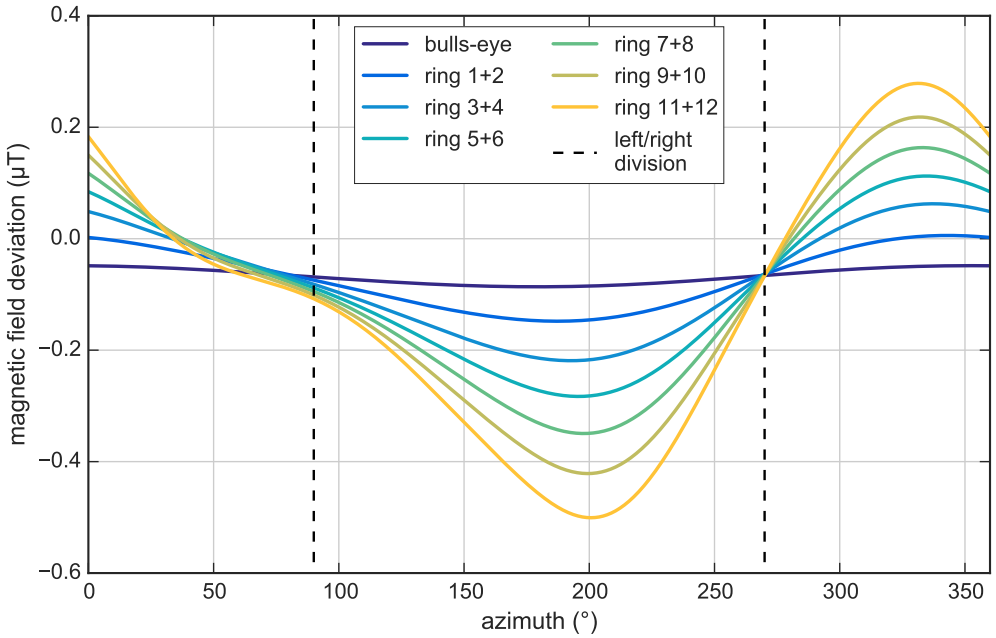

(a) 3.8 G setting

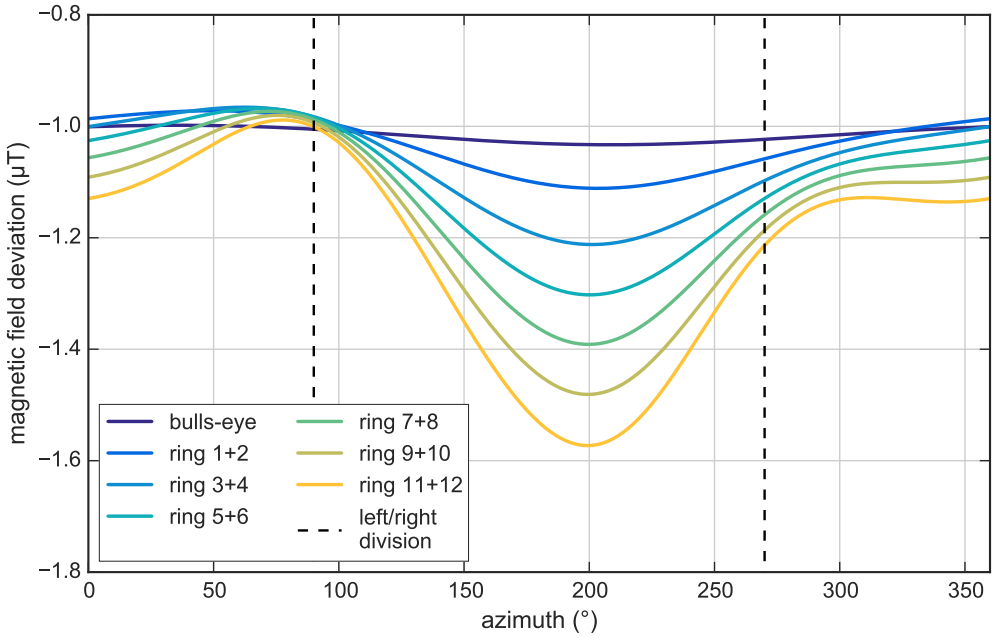

(b) 9.0 G setting

Figure 7.6: Approximation of influence of magnetic materials on the field symmetry. A remanent and induced field by magnetic materials is observed that leads to an azimtuhal variation of the analyzing field $B_z(\phi)$. The field approximations are based on eq. (7.4), with magnetic moments listed in table 5.5 and mean ring radii from field line simulations. The resulting field is split in a left and right spectrometer half (dashed lines) with individual $B_z(\phi)$ values. To introduce solely an azimuth variation, the sum of the individual $B_z(\phi)$ is normalized to zero in the ensemble test.

The azimuthal field is then given by

$$B_{\mathrm{z}}\left(\phi, r_{\mathrm{ap}}\right) = \sum_{i=0}^{3} \frac{-\mu_0 m_{\mathrm{z,i}}}{4\pi} \left(r_i - r_{\mathrm{ap}} \cos\left(\phi - \phi_i\right)\right)^{-3} \tag{7.4}$$

where $m_{\mathrm{z,i}}$ corresponds to the mean magnetic moments of the ring 6 upstream and downstream results in table 5.5 and r_{ap} are based on axial-symmetric field-line simulations (comparable with fig. 6.11). The resulting magnetic field variations in the spectrometer for a 3.8 G and 9.0 G setting are shown in fig. 7.6. As MobSU measurements could only be performed for these two field configurations, the magnetic moments $m_{\mathrm{z,i}}$ for other settings were interpolated relative to the absolute field values.

Compared to a 1.5 µT-variation on a radius of 4.5 m simulated with the previous model of ref. [Rei13], a reduction of 50 % inside the spectrometer is observed. It is important to note, that the model of [Rei13] was based on measurements prior to a large scale demagnetization of the experimental hall while the model developed in this thesis after the demagnetization. Due to the fact that a comparable reduction of the field variation was measured with the high precision magnetometers before and after the demagnetization, both shape and strength of the approximation of the azimuthal field distortion in the simulation seems reasonable.

The simulated field deviations for the two cases of a 3.8 G and 9.0 G setting feature a similar shape and absolute variation within the analyzing plane, although the detected field deviation is larger by about a factor of 2 for the 9.0 G setting. Despite this effect, the applied azimuthal field variations $\Delta B_{\mathrm{z}}(\phi)$ in the ensemble test are nearly invariant of the field setting. This is due to the reduced flux tube volume[1] of a 9.0 G setting compared to the 3.8 G setting where the individual field contributions can cancel each outer out.

However, the ratios between the fields of a 3.8 G and 9.0 G setting feature significant deviations of several µT when the measurement and the simulation results are compared (fig. 5.12). Consequently, much larger azimuthal field deviations are plausible. The magnetic moments in eq. (7.4) are multiplied with an additional factor of 0.5, 1, 2, 3, 5 and 10 to consider different azimuthal variations in the ensemble test. The resulting $B(\phi)$ distribution is split from −90° to 90° in a left (west) and from 90° to 180° in aright (east) division. The mean value in such a ring segment is used as $\Delta B_{\mathrm{z}}(r,\phi)$ in the ensemble tests. To study the shape variation only and suppress an axial field offset as in section 7.2.1, the sum of all azimuthal offsets $\sum \Delta B_{\mathrm{z}}(r,\phi)$ is normalized to zero.

The field differences $\Delta B_{\mathrm{z}}(\phi,r)$ relative to the undisturbed spectrum are calculated for all magnetic moment multiplicity factors. The systematic shift of the neutrino mass Δm_ν^2 is shown in fig. 7.7(a) as a function of $\Delta B_{\mathrm{z}}(\phi)$. For the individual field settings a linear dependence is observed towards a negative shift of the neutrino mass. The linear fit results are shown for the individual settings by colored lines together with an error belt that results from numerical fluctuations. For all field settings the neutrino mass shift is well below the limit of the systematic uncertainty budget for a five-fold increased[2] $\Delta B_{\mathrm{z}}(\phi)$ (table 7.4). In

1 The outer most radius r_{ap} is about 4 m (2.5 m) in case of a 3.8 G (9.0 G) setting.

2 In case of a 9 G setting, simulations with a multiplication factors up to 3 are below the systematic uncertainty budget.

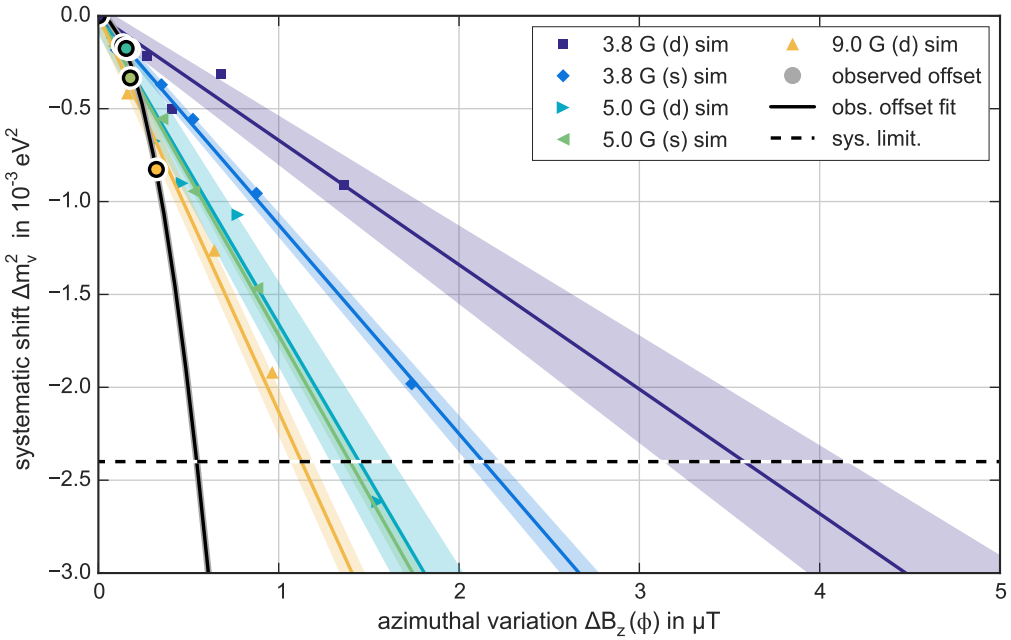

(a) Results of the ensemble tests, realistic azimuthal-field offsets $\Delta B_z(\phi)$ are highlighted.

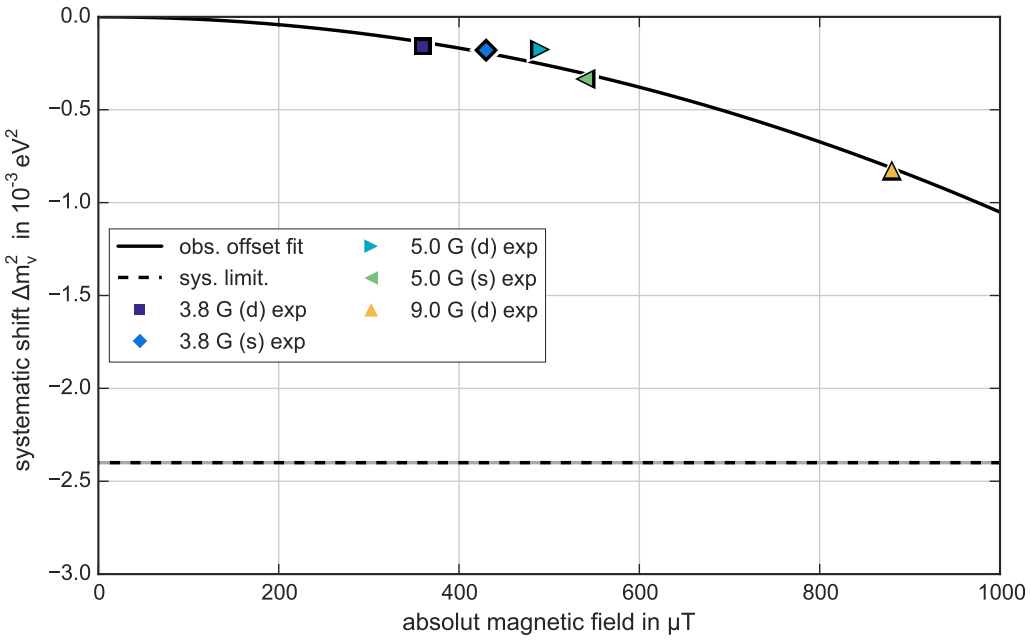

(b) Empirical dependence of Δm_ν^2 on the applied magnetic field due to an azimuthal field offset $\Delta B_z(\phi)$.

Figure 7.7: Systematic shift Δm_ν^2 due to an azimuthal magnetic field offset $\Delta B_z(\phi)$. In fig. 7.7(a) the simulation results of the ensemble tests are shown. The estimated azimuthal variations (fig. 7.6) are enhanced by a factor 0.5, 1, 2, 3, 5 and 10 to generate different $\Delta B_z(r,\phi)$ distributions of reasonable shape. Δm_ν^2 features a linear dependence of $\Delta B_z(r,\phi)$, fit results are shown with an 1σ error belt. Most likely field offset values are highlighted (see fig. 5.4). The black line is the fit result with eq. (7.3) to these values. Based on these results, the absolute field dependence is identified in fig. 7.7(b). For a field in the spectrometer center B_A upto 1422 µT, the systematic uncertainty is within the limit of $2.4 \times 10^{-3}\,\mathrm{eV}^2$ as indicated by the dashed lines.

Table 7.4: Influence of a azimuthal field deformation on the neutrino mass. Linear dependence (slope) of the simulated shift of the squared neutrino mass Δm_ν^2. Based on this slope, the upper limit on the field offset $\Delta B_z(\phi)$ for a Δm_ν^2 below 2.4 meV^2 is calculated. The expected shift of the squared neutrino mass Δm_ν^2 is calculated based on the magnetic field offset observed in fig. 5.11 together with the resulting total neutrino mass sensitivity $\sigma(m_\nu^2)$. The total sensitivity is calculated with $S_{\mathrm{tot}} = [(\sigma^2_{\mathrm{sys,design}} + \sigma^2_{\mathrm{sys,shift}} + \sigma^2_{\mathrm{stat,sim}})^{1/2} \cdot 1.645]^{1/2}$.

setting	slope (10^{-5} eV^2/µT)	upper limit (µT)	observed offset (µT)	shift Δm_ν^2 (10^{-3} eV^2)	sensitivity (90 %CL) (meV)
3.8 G (d)	-67.0 ± 15.7	-3.58	0.14	-0.09	196.9
3.8 G (s)	-112.5 ± 3.3	-2.13	0.17	-0.19	197.5
5.0 G (d)	-165.9 ± 12.8	-1.45	0.15	-0.26	198.8
5.0 G (s)	-172.1 ± 3.1	-1.39	0.18	-0.3	199.9
9.0 G (d)	-213.2 ± 4.8	-1.13	0.32	-0.69	212.8

contrast to the simulation results in section 7.2.1, the slopes feature no obvious dependence on the absolute field. This is expected due to the non-vanishing remanent field and the reduced flux tube volume for larger fields.

The simulation results with a multiplication factor of 1 are interpreted as the most likely azimuthal disturbances for the individual field settings and are therefore highlighted in the plot, labeled as the observed offsets. These values can be used to formulate the empirical dependence between the neutrino mass shift Δm_ν^2 and the absolute field in the spectrometer B_{A} represented by

$$\Delta m_\nu^2 = \beta_1 \cdot B_{\mathrm{A}}^2 + \beta_2 \cdot B_{\mathrm{A}}, \tag{7.5}$$

where β_1 is $(-11.4 \pm 1.8) \times 10^{-10}\,\mathrm{eV}^2\,\mu\mathrm{T}^{-2}$ and β_2 is $(7.0 \pm 1.3) \times 10^{-8}\,\mathrm{eV}^2\,\mu\mathrm{T}^{-1}$ (fig. 7.7(b)). Based on eq. (7.5) it is found that the systematic limit is not exceeded for field settings below 1422 µT. Therefore, no noticeable shift from an azimuthal field perturbation is expected within a reasonable field settings for a standard KATRIN operation. Also the resulting increase of the total sensitivity is negligible.

7.2.3 Perpendicular flux tube alignment

A magnetic field offset perpendicular to the spectrometer axis $\Delta B_\perp$ primarily leads to an overall shift of the entire magnetic flux tube (see fig. 6.11). Thereby, a misalignment between the electric and magnetic field is introduced, and the axial symmetry of the electromagnetic setup revoked. Secondly, the ring structure of the flux tube is impaired as one half is compressed towards the spectrometer center and the other half is straightened out. Such an offset can be introduced by an unknown magnetic field sources or an insufficient EMCS configuration (section 5.5). However, the actual magnetic field in the analyzing plane is only slightly increased when a field offset of few a µT is vectorial added to a field B_{A} of 360 µT or more. So the modification of the analyzing plane shape, as introduced in section 7.2.1, is the dominant contribution to a systematic uncertainty of the neutrino mass. An arbitrary orientation of $\Delta B_\perp$ along the y-axis as ΔB_{y} is chosen without loss of generality.

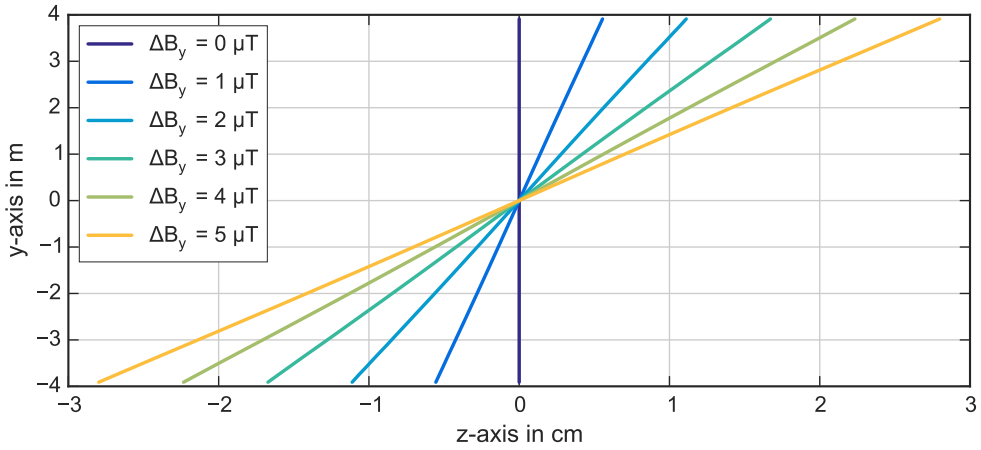

(a) Analyzing plane location and shape due to a perpendicular field offset ΔB_y.

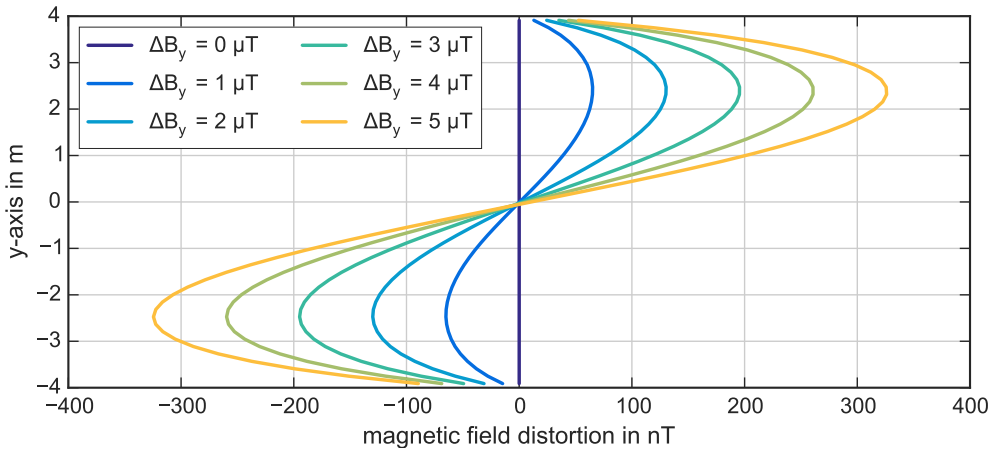

(b) Additional magnetic field variation due to anaylzing plane distortion.

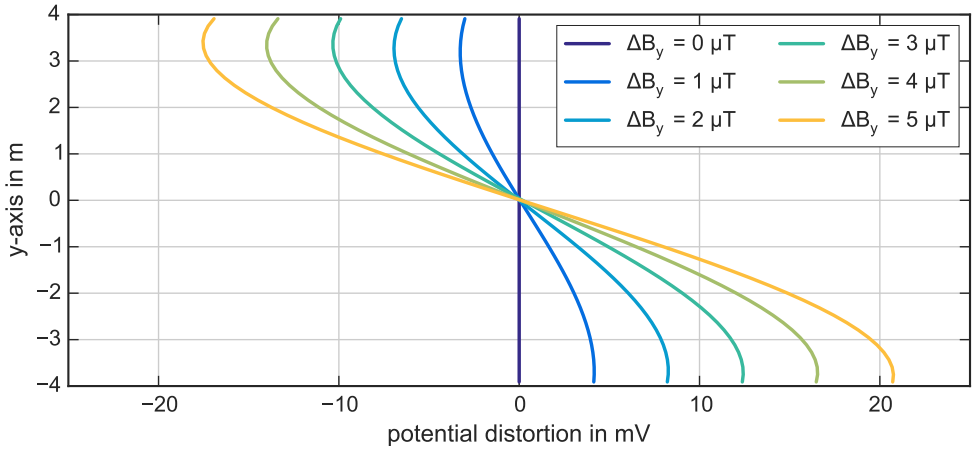

(c) Retarding potential variation due to anaylzing plane distortion.

Figure 7.8: Influence of a perpendicular magnetic field offset along the y-axis. Although the actual field increase is of minor importance, the entire flux tube is shifted in the direction of ΔB_y by several cm and a misalignment between the retarding potential and the magnetic field is introduced. The variation of the magnetic field and the retarding potential are given relative to the unbiased values. In this example the 3.8 G setting was used were the effect is most profound.

From fig. 7.8 it becomes evident that a $\Delta B_\perp$ introduces a shift in direction of the field offset and a tilt of the analyzing plane, point symmetric to the flux tube center. In case of 3.8 G setting and a 5 µT-offset, the flux tube center is shifted by 32.6 cm in y-direction and the outer most radius features an azimuthal variation within ±2.8 cm. As the gradient of the magnetic and electric field points dominantly in radial direction, the resulting variations of the retarding potential and analyzing magnetic field are by one order of magnitude larger then in case of an axial offset ΔB_z. Modifications of a 3.8 G (d) setting feature variations within a range of 0.65 µT with a standard deviation σB_y of 0.26 µT, while the retarding potential features a variation σU_A of 16.7 mV in the range of 38 mV. Other field configurations are less affected by an offset $\Delta B_\perp$. Firstly, bigger absolute fields result in a magnetic stiffness that suppresses a flux tube shift, and secondly the entire flux tube radius is smaller. Therefore, systematic shifts are expected to be reciprocal to the absolute field.

When a perpendicular field offset $\Delta B_\perp$ is large enough, the active flux tube collides with the inner electrode system. This is the maximal plausible offset $\Delta B_{\perp,\max}$ to be considered in simulations, because above $\Delta B_{\perp,\max}$ a sudden rise of background events and a simultaneous lose of signal electrons would be observed which can be easily detected by an operator in a early stage of a measurement. In case of a 3.8 G (d) (3.8 G (s), 5.0 G (d), 5.0 G (s), 9.0 G (d)) setting $\Delta B_{\perp,\max}$ is reached for 8.75 µT (24.5 µT, 18.5 µT, 28 µT, 50 µT). Results of the simulations for a systematic neutrino mass uncertainty Δm_ν^2 are only shown for values up to $\Delta B_{\perp,\max}$. Although offsets above 3.5 µT were not observed within the symmetry studies with the EMCS system (section 5.5), values of $\Delta B_\perp$ up to 12 µT are applied in the simulation to guarantee a significant large systematic shift Δm_ν^2. In fact, the observed effects of the field perturbations are so small that a significant conclusion on a Δm_ν^2 shift can only be made by a likelihood ratio analysis rather than an ensemble test. Nevertheless, the total sensitivity is still evaluated by an ensemble test. In general it is expected that the axial field symmetry is rather a tool to suppress certain background production processes (appendix C, ref. [Wan13b], [Sch14b], [Lei14], [Har15b]) than an impact factor on the systematic uncertainty of the transmission function as a perpendicular field offset.

Table 7.5: Influence of a perpendicular field offset on the neutrino mass. Linear dependence (slope) of the simulated shift of the squared neutrino mass Δm_ν^2. Based on this slope, the upper limit on the field offset $\Delta B_\perp$ for a Δm_ν^2 below 2.4 meV^2 is calculated. The expected shift of the squared neutrino mass Δm_ν^2 is calculated based on the magnetic field offset observed in fig. 5.14 together with the resulting total neutrino mass sensitivity $\sigma(m_\nu^2)$. The total sensitivity is calculated with $S_{\text{tot}} = [(\sigma^2_{\text{sys,design}} + \sigma^2_{\text{sys,shift}} + \sigma^2_{\text{stat,sim}})^{1/2} \cdot 1.645]^{1/2}$. While the total sensitivity is derived from ensemble tests, all other values are results of a likelihood analysis.

setting	slope (10^{-5} eV^2/µT)	upper limit (µT)	observed offset (µT)	shift Δm_ν^2 (10^{-3} eV^2)	sensitivity (90 %CL) (meV)
3.8 G (d)	-4.6 ± 0.8	22.8	3.6	−0.06	197.3
3.8 G (s)	-9.0 ± 1.2	16.37	3.6	−0.11	198.3
5.0 G (d)	-3.1 ± 0.5	27.61	3.6	−0.04	199.4
5.0 G (s)	-7.5 ± 0.7	17.83	3.5	−0.09	200.4
9.0 G (d)	-2.4 ± 0.8	31.43	3.5	−0.03	209.6

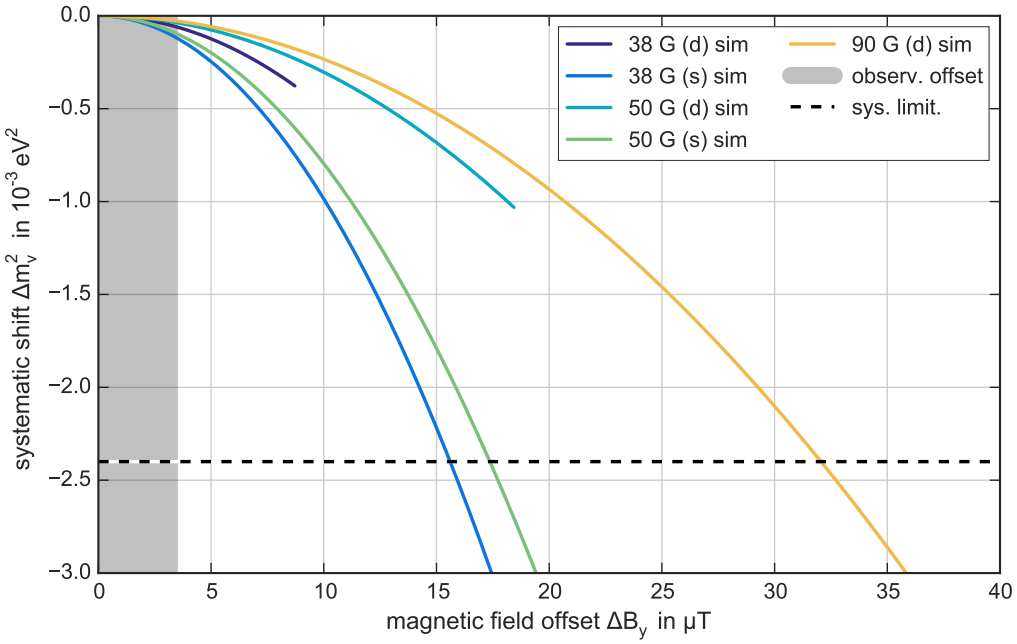

Figure 7.9: Systematic shift Δm_ν^2 due to a perpendicular magnetic field offset ΔB_y that leads to a misalignment of the magnetic field and the retarding potential. Offsets upto 12 µT were simulated, larger values were extrapolated from a fit with eq. (7.6) . The individual fit results are plotted for values upto $\Delta B_{\perp,\mathrm{max}}$ when the inner electrode is touched by the flux tube. Within realistic offset values, only minor systematic shifts were observed.

As only field offsets upto 12 µT are simulated, some of the results of the likelihood analysis are fitted to a parabolic function for an extrapolation to $\Delta B_{\perp,\mathrm{max}}$. In fig. 7.9 are the Δm_ν^2 dependencies shown for the individual field configurations with a 1σ error belt of the fit. It becomes evident that a flux tube deformation introduces a flat trend towards a negative neutrino mass. Below an offset of 16 µT, no significant contribution to the systematic uncertainty of the neutrino mass is observed in any field configuration. Within the observed offset of 3.5 µT, the maximal introduced shift $\Delta B_{\perp,\mathrm{max}}$ is about $0.1 \times 10^{-3}\,\mathrm{eV}^2$.

Therefore, realistic offset values have a subordinate role in the overall systematic uncertainty budget. Only major offsets could have a noticeable effect on the neutrino mass, introduced by events such as a failure of the EMCS. However, the real-time control system for a hardware integrity monitoring and the near-time analysis with the field monitor (section 3.3.3) can register such a malfunction during operation and countermeasures can be applied.

When the Δm_ν^2 as a function of $\Delta B_\perp$ is normalized with the absolute field of the individual magnetic settings, a generalized expression of field dependency is found in

$$\Delta m_\nu^2 = \gamma_1 \cdot \Delta B_\mathrm{y}^2 \cdot B_\mathrm{a}, \tag{7.6}$$

where γ_1 is a factor of 1.8 ± 0.2 that is increased by a factor of 2.4 in case of field settings of a single minimum in comparison to a double minima solution. This value cannot be

linked to the field spread ΔB_A or any other field properties. The origin of the discrepancy should be addressed in further simulations with an updated KaFit version that improves the numerical stability in regions of such small Δm_ν^2. Although, in any field setting the introduced systematic shift is so small that it can be completely neglected in the analysis of the neutrino mass.

The observed values of the total sensitivity on the neutrino mass are increased for larger absolute fields (table 7.5). This increase is predominantly associated with a larger energy resolution of the MAC-E filter that can be adapted for in the measurement time distribution.

7.2.4 Fluctuation of the magnetic field

The field of the LFCS is by far the biggest contributor to the analyzing field B_A, operated with power supplies for which fluctuations of current output of a few mA were verified (section 4.3.2). Therefore, fluctuations of the magnetic field $\sigma B_{z,fluc}$ in the analyzing plane are expected as well for all field configurations (section 4.4). From the analyses of the aircoil current it is known that the individual outputs of all power supplies are normal distributed table A.2. Therefore, fluctuations of the magnetic field can be assumed to be normal distributed also.

The magnitude of the field fluctuations inside the spectrometer is further affected by:

1. The absolute field strength, or more precisely the magnitude of the applied currents. A slight increase of the current fluctuations between 8 mA to 12 mA is observed when the 3.8 G and 9.0 G setting are compared, which is transformed to a field fluctuation $\sigma(B_z)$ rising from 0.14 µT to 0.18 µT. Especially the power supplies in the central region close to the analyzing plane are affecting the magnetic field (table A.2).
2. The correlation between the current outputs of the power supplies can increase $\sigma(B_z)$. A full correlation of the power supplies on a common DAC card (section 4.2.3) leads to a bigger fluctuation by a factor of 2 in comparison to an uncorrelated system. Correlation factors in a range of ± 0.32 were confirmed.
3. Eddy currents and residual magnetizations on and in the vessel hull are counteracting a fluctuating magnetic field. Eddy currents were verified with magnetic pulse measurements (section 4.3.1). Additionally, in parts of the insulation holding structure that surrounds the vessel hull, ferromagnetic materials can be found which enhance the induction.

To estimate the impact by the latter two effects on $\sigma(B_z)$ quantitatively is rather challenging. But as both introduce contrary effects and are sub-dominant, only the uncorrelated, absolute field depended current fluctuations are considered in the following simulations.

A classical ensemble test is not suitable to simulate the impact of a fluctuation of the magnetic field. On the one hand it would increase computation time dramatically, since not only the signal rates need to be randomly generated, but the magnetic field as well. A decent numerical precision would therefore require the square of the original simulation count of $10\,000^2$. On the other hand it can be expected that a fluctuating field relative to its intended mean value introduces a smeared-out systematic uncertainty $\sigma_{m_\nu^2}$ rather than a systematic shift of Δm_ν^2. Therefore an ideal tritium spectrum is assumed in the simulation of the fluctuations while a global magnetic field offset $B_{z,fluc}$ is randomly generated with a

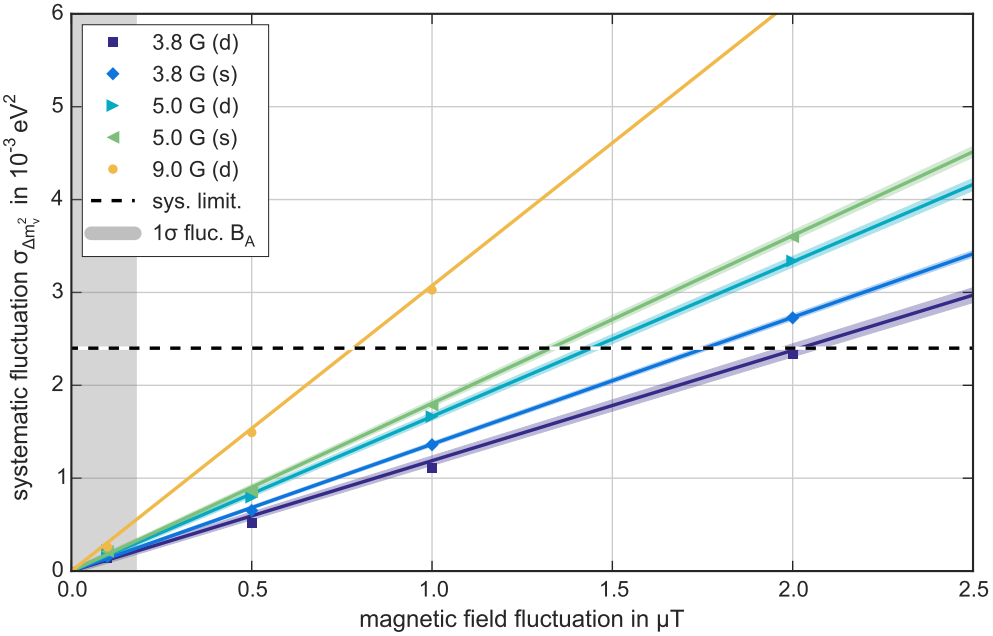

Figure 7.10: Influence of magnetic field fluctuations $\sigma(B_{\mathrm{z,fluc}})$ on the systematic uncertainty $\sigma_{m_\nu^2}$. Fluctuations of 0.1 µT, 0.5 µT, 1 µT, 2 µT and 3 µT are simulated and reveal a linear increase as a function of the absolute field B_{a} (eq. (7.7)). For the observed 1σ fluctuations in fig. 4.11 an additional systematic uncertainty is introduced, for all settings well below the systematic limit.

mean of 0 µT and a standard deviation $\sigma(B_{\mathrm{z,fluc}})$ of 0.1 µT, 0.5 µT, 1 µT, 2 µT and 3 µT for each simulation.

Figure 7.10 shows the broadening of the fitted neutrino mass distribution as a function of the applied fluctuation $\sigma(B_{\mathrm{z,fluc}})$. Fitted to a linear function, the observed trends are plotted together with a 1σ error belt. The systematic neutrino mass shift is clearly below the systematic limit for all field settings. When a 3σ field fluctuation is applied, the additional systematic is about half of the systematic limit, even in case of the 9.0 G setting.

By normalizing the observed slopes for the corresponding absolute magnetic field B_{a} in the center of the spectrometer, a generalized expression is found for the linear dependence of $\sigma_{m_\nu^2}$. When B_{a} and $\sigma(B_{\mathrm{z,fluc}})$ are given in units of µT, the additional systematic uncertainty on the neutrino mass is calculated by

$$\sigma_{\Delta m_\nu^2} = \delta_1 \cdot B_{\mathrm{a}} \cdot \sigma B_{\mathrm{a,fluc}}, \tag{7.7}$$

where δ_1 is $(3.310 \pm 0.018) \times 10^{-6}\,\mathrm{eV^2\,\mu T^{-2}}$.

In comparison to other systematic uncertainties, an improvement of the neutrino mass sensitivity can not be achieved by an adjustment of the measurement time distribution. The calculation of the total sensitivity in table 7.6 is based on the quadratic summation of $\sigma(B_{\mathrm{z,fluc}})$ with the expected statistical and systematic uncertainty of $\sigma_{\mathrm{stat}} = \sigma_{\mathrm{sys}} = 0.017\,\mathrm{eV^2}$. The design value of 200 meV is surpassed by field fluctuation for a setting of 840 µT or more.

Table 7.6: Influence of a fluctuating magnetic field $\sigma(B_{z,\mathrm{fluc}})$ on the systematic uncertainty. Linear dependence (slope) of the systematic uncertainty of the squared neutrino mass $\sigma_{m_\nu^2}$ on a fluctuating magnetic field in the analyzing plane based on fig. 7.10. Based on this slope, the upper fluctuation limit for a value of $\sigma_{m_\nu^2}$ below $2.4 \times 10^{-3}\,\mathrm{eV}^2$ is calculated. The impact of the expected uncertainty of $\sigma_{m_\nu^2}$ is calculated for the maximal observed fluctuation of 0.36 µT (fig. 4.11) $2.4 \times 10^{-3}\,\mathrm{eV}^2$. The total sensitivity is calculated with $S_{\mathrm{tot}} = [(\sigma^2_{\mathrm{sys,design}} + \sigma^2_{\mathrm{sys,fluc}} + \sigma^2_{\mathrm{stat,design}})^{1/2} \cdot 1.645]^{1/2}$ in column 'sens.'.

setting	slope ($10^{-5}\,\mathrm{eV}^2/\mu\mathrm{T}$)	upper limit (µT)	obs. offset (µT)	sys. uncer. $\sigma_{m_\nu^2}$ ($10^{-3}\,\mathrm{eV}^2$)	sens. (90 %CL) (meV)
3.8 G (d)	1.1884	2.019	0.14	0.17	177.1
3.8 G (s)	1.3665	1.756	0.14	0.24	177.0
5.0 G (d)	1.6649	1.442	0.15	0.31	180.5
5.0 G (s)	1.8058	1.329	0.15	0.32	182.7
9.0 G (d)	3.0742	0.781	0.18	0.51	203.0

7.3 Combined magnetic field disturbances and conclusion

In this chapter, all discoveries about the magnetic field properties in the main spectrometer are used to test their influences on the neutrino mass analysis. By means of ensemble tests, shifts and broadening of an expected neutrino mass distribution due to systematic effects can be identified. This method requires a modeling of the tritium spectrum and the entire experimental setup. Due to performance reasons and comparability with previous simulations, a homogeneous tritium source is assumed. Operational parameters are all set to design values (section 7.1.1). The final integrated tritium spectrum after a effective 3-year operation results from the randomly generated tritium signal together with the associated response function, scanned with the default measurement time distribution (section 7.1.2).

In section 7.2 four effects were identified which compromise the magnetic field in the analyzing plane, but were not considered in the uncertainty budget yet. For a realistic simulation of these perturbations, the observed magnetic field deviations identified in chapter 4 and chapter 5 were incorporated. From the previous chapters it also became evident that the currently unparameterized remanent and induced fields by magnetic materials in the spectrometer hall are the prevailing contributors to the observed deviations in the magnetic field model. In this context the result of sensitivity studies need to be interpreted.

An axial ΔB_z and azimuthal $\Delta B_z(\phi)$ offset are direct consequences of the remanent and induced fields (section 7.2.1 and 7.2.2). Since no means to compensate these disturbances are available, one has to incorporate the additional systematic shifts Δm_ν^2 in the neutrino mass analysis. The combined impact of both effects is estimated by quadratic summation. The fact that ΔB_z outweighs the $\Delta B_z(\phi)$ clearly diminishes the rough approximation of the azimuthal distortion and a fairly accurate description of the total systematics can be assumed.

The other two effects must not be accounted to the influence of magnetic materials in the concrete of the spectrometer hall. A perpendicular offset of the magnetic flux $\Delta B_\perp$ may originate from magnet alignment, external disturbances or an imperfect EMCS setting. Not only can the perpendicular field rather well be minimized (description in section 5.5,

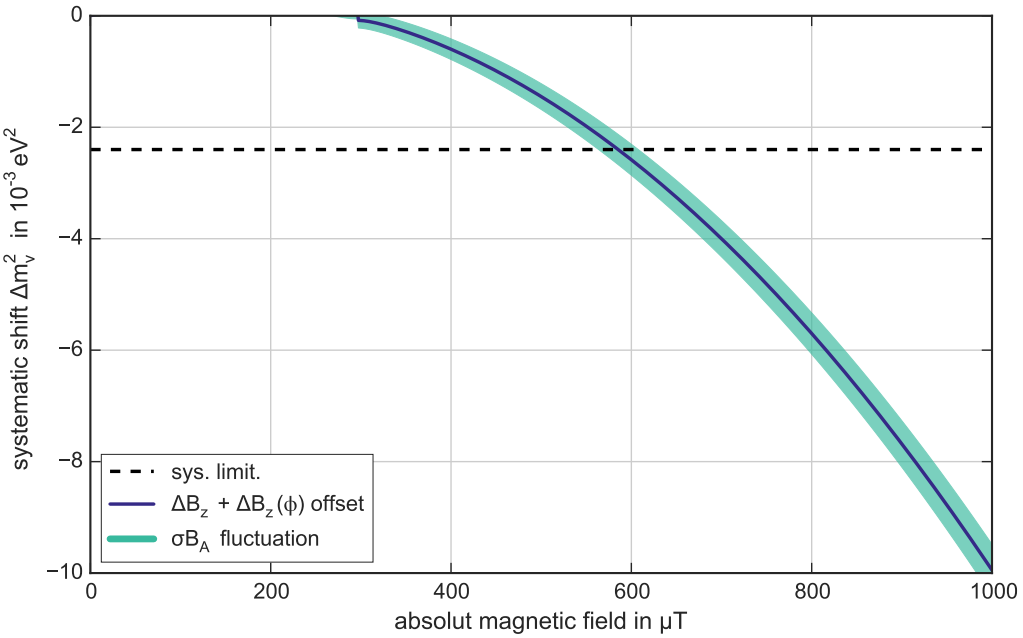

Figure 7.11: Combined influence of magnetic field on the systematic shift Δm_ν^2. The quadratic summation of the offsets ΔB_z and $\Delta B_\mathrm{z}(\phi)$ is shown in blue. A fluctuation of the magnetic field introduces an additional systematic uncertainty as indicated by the green error belt. For a field in the spectrometer center of $B_\mathrm{A} = 585\,\mu\mathrm{T}$ the systematic uncertainty is within the limit of $2.4 \times 10^{-3}\,\mathrm{eV}^2$ as indicated by the dashed lines.

verification in fig. 6.16), but it was also shown that $\Delta B_\perp$ has a marginal impact on the neutrino mass analysis. Merely for field settings with one field minimum, a slightly enhanced effect has been found on outer radii. The last field disturbance is a fluctuation of the magnetic field. The instability of the current output of the air-coil power supplies causes a variation of the analyzing magnetic field. Although these fluctuations are rather small in the low $10^{-7}\,\mu\mathrm{T}$-regime, a non-vanishing systematic uncertainty $\sigma_{m_\nu^2}$ was observed. This additional broadening can be interpreted as a systematic effect that is statistical distributed.

For a final estimation of the impact of the magnetic field on the neutrino mass analysis, the combined effects of ΔB_z and $\Delta B_\mathrm{z}(\phi)$ are considered with $\sigma_{m_\nu^2}$ as an error belt. The resulting systematic shift Δm_ν^2 of the neutrino mass as a function of the absolute magnetic field is shown in fig. 7.11. In order to control Δm_ν^2 within the systematic limit of $2.4 \times 10^{-3}\,\mathrm{eV}^2$ only, the absolute magnetic field must not exceed an absolute value of $585\,\mu\mathrm{T}$. This value features only a minor reduction of $3\,\mu\mathrm{T}$ in comparison to a pure ΔB_z dependent analysis.

In conclusion, the previously unknown impact of the magnetic field in the analyzing plane was parametrized in this chapter and for individual effects generalized expressions were found. Operated with the design parameters, the magnetic field impact on the neutrino mass is sub-dominant. Solely for fields above $585\,\mu\mathrm{T}$ the analyzing field B_A starts to become a major contributor to the uncertainty budget of the KATRIN experiment.

CHAPTER 8

Summary and Outlook

Since the postulation of neutrinos by W. Pauli these neutral fermions have become a key constituent of the Standard Model of modern physics, and driven a vigorous field of research. The discovery of neutrino flavor oscillations has catapulted them to the forefront of interest in the science community as a gateway towards new physics. Here, the determination of the fundamental mass scale of neutrinos is a key parameter to understand the evolution of large-scale structures in our universe.

The Karlsruhe Tritium Neutrino experiment (KATRIN) is the next-generation direct neutrino-mass experiment, targeted to identify the effective mass of the electron anti-neutrino $m_{\bar{\nu_e}}$ with a model-independent sensitivity of $200\,\mathrm{meV/c^2}$ at 90 % C.L. ($350\,\mathrm{meV/c^2}$ with 5σ) after five calendar years of operation. This corresponds to an improvement of the current neutrino mass sensitivity by one order of magnitude compared to predecessor experiments. Electrons from β-decay of molecular tritium are observed close to the β-decay endpoint via the MAC-E filter principle which combines a magnetic adiabatic collimation with electrostatic filtering. Evidently, electromagnetic fields define the key properties of a MAC-E filter based spectrometer and a profound knowledge of their shape, and stability as well as the accuracy of their absolute values is indispensable for a successful neutrino mass measurement. In the recentSDS 2 measurement campaigns the MAC-E filter characteristics were carefully examined, in this thesis with special emphasis on the magnetic component.

The key results of this thesis can briefly summarized as follows:

- Incorporation of all field-generating superconducting and normal conducting coils as well as of background fields has allowed to obtain a profound understanding of the magnetic field shape inside the main spectrometer during the SDS 2 campaign. In doing so, comprehensive tests, especially of the LFCS field, have given the necessary information to detect even small divergences between the measurement results and the simulation model.
- Advanced measurement strategies, mathematical models and analysis methods were developed to analyze the large body of transmission function measurements. In particular, an increased precision in the description of the e-gun characteristics as well as the incorporation of the magnetic field analysis has allowed to determine radial potential inhomogeneities of the spectrometer and resulting in an improved accuracy by a factor of 3. The magnetic field in the analyzing plane was measured for the first time by

means of transmission function curves with an e-gun where an overall agreement to 3 µT was achieved.

- Based on the knowledge obtained on the magnetic field shape in the spectrometer a total of four field perturbations was identified. These previously unconsidered effects were studied via Monte-Carlo based ensemble tests to quantify their impact on the neutrino mass analysis.

In the following these findings are detailed.

Measuring and modeling of the magnetic field

The guiding magnetic field evidently influences electron transport characteristics through the entire experimental setup and the observed rates of FPD detector. Therefore, the field parameters play an essential role in the KATRIN experiment, especially the low field region in the central parts of the main spectrometer volume. There, the field plays a key role to minimize background and optimize transmission properties of signal electrons through the MAC-E-filter. In the ideal case, the magnetic field is axisymmetric relative to the main spectrometer. With dedicated field optimization tools a variety of configurations was calculated within this thesis to derive the standard field settings in use during the extended SDS 2 measurement campaign.

All magnetic field calculations are based on an in-depth field model that comprises all active field-generating sources as well as background fields like the earth magnetic field. To obtain an accurate description of the magnetic field conditions, comprehensive information on the dimensions and alignment of all magnets are indispensable. Accordingly, all deviations relative to the design values were carefully implemented in the field model, in particular the geometry of the air-coil system as well as of the solenoids of pre-spectrometer and FPD system were refined substantially. To investigate the accuracy of the magnetic field model, the full magnetic field range was studied with specific emphasis on stability and reliability.

In order to obtain the required data for in-depth magnetic field analyses, a field monitoring system was installed and commissioned. These works include high-precision magnetometers and initial tests with MobSU system, as well as a thorough calibration of the previously installed sensor system. Together, these three systems allow to study the magnetic field model in the nT regime. This precision exceeds the electromagnetic design requirements of KATRIN, establishing the long-term stability of the magnet system could to $(0.6 \pm 0.8)\,\mathrm{nT/day}$. Most importantly, the magnetic background field could be characterized as well.

A large scale-demagnetization of the experimental hall was instrumental reduce the remanent magnetization of the ferromagnetic steel bars in the reinforcement of the concrete walls significantly. The reduction relates both to the absolute field and the azimuthal variation of the remanent field. A re-magnetization after the turn on of the solenoids of several T has been verified as global field offset, but, and mor importantly, the azimuthal variation remains constant within a 2 µT range. Moreover, the azimuthal variations deduced from the MobSU measurements could be reproduced to first order by an approximate model of the fields from the walls. In addition, the previously unknown induced magnetic field by the magnetic materials was substantiated for large absolute fields. Although the approximated model of the magnetic structures describes the induced field on a more qualitative level at

present, it can be used for important estimates of the magnetic field deformations inside the active flux tube.

In conclusion, it has been demonstrated that a stable and reliable magnetic field can be generated within the stringent KATRIN electromagnetic design requirements. The remaining deviations in the magnetic background field has been successfully traced to remanent and induced fields of ferromagnetic materials in the experimental hall.

Determination of the transmission characteristics of the main spectrometer

The most important electromagnetic design requirement is to strictly fulfill the transmission conditions of the MAC-E filter. Only when this is satisfied, the analyzing points in the central region of the spectrometer will coincide with the ideal perpendicular plane, the so-called analyzing plane. Only then the analytic equations can be applied to calculate the transmission function. In the description of the transmission characteristics of the main spectrometer, the transmission function is of central importance. Although the transmission function can be solely described in terms of the applied electric and magnetic fields, the interplay between these two fields is rather complex with respect to their influence on the longitudinal energy of electrons. An accurate knowledge of the shape of the fields in the main spectrometer volume is therefore indispensable.

The transmission characteristics of the main spectrometer can be determined by means of transmission function measurements with an electron gun. This unit e-gun emits quasi-mono-energetic electrons along a given field line and most importantly, features angular selectivity with a narrow solid angle. A reliable analysis requires a precise alignment of the e-gun and a profound knowledge of the magnetic field distribution in the experimental setup. Due to a thorough alignment and adjustment of geometrical input data in the simulation tools, the start conditions of the electron at the e-gun could be verified in much greater detail than in the previous efforts. In combination with the comprehensive magnetic field model which includes the magnetic materials, the analyzing point of a specific field line could be calculated precisely. As a result, the effective analyzing plane features a bias that results from the magnetic field perturbations.

A detailed measurement and analysis strategy was implemented to enable a determination of the important e-gun properties, namely its energy and angular distribution. A full automatization of the measurement process, in particular of the e-gun control and slow control readout, was utilized to obtain a decisive knowledge of the e-gun properties for individual runs. To enable full comparability between various measurement cycles, a semi-empirical energy distribution model was developed in the course of this thesis. Within this model the properties of the modifying process of electron generation via the photo effect were combined with a generalized normal distribution.

This model is a crucial extension in the description of e-gun measurements. When applied to transmission function measurements targeted to validate the electrostatic potential and its radial shape, an improvement by a factor 3 was achieved compared to previous efforts. For the important "3.8 G setting" an excellent agreement of data with simulations is achieved. Within their 1σ range, the residuals show no deviation from zero or large non-Gaussian perturbations. For the maximally possible field of 9 G, a small tilt in the residuals is observed that is attributed to an insufficient level of modeling of the magnetic structures in the field model. This is consistent with the small divergence of the residuals for the 3.8 G(s) measurement,

that is sensitive to minor field perturbations, especially on outer radii.

In a next step the absolute radial magnetic-field shape was determined. For this purpose several transmission function measurements with different angular distributions on a common field line are used in a joint analysis. The introduced shift of the transmission energy is a well defined function of the angular distribution and the applied magnetic field. To establish the angular distributions independently of the magnetic field, in-depth 3D simulations were utilized. Consequently, the magnetic field of a "3.8 G setting" was determined with an accuracy of $(3 \pm 11)\,\mu\mathrm{T}$. This was only possible when magnetic reflection measurements were incorporated in the analysis. The lack of magnetic reflection measurements for most of the target FPD pixels however has undermined the magnetic field analysis so that a noisy field distribution is observed.

Impact of the magnetic field on the neutrino mass systematic

The magnetic field is the primary parameter to describe the shape of the transmission function, in particular its width. The transmission function has previously been established as a major contribution to the overall systematic uncertainty budget of KATRIN, however its dependence on the magnetic field and the associated field uncertainties were neglected so far. The magnetic field uncertainties identified within the thesis have been studied here for the first time with respect to their impact on the neutrino mass systematic. Accordingly, large-scale ensemble tests were performed to test the individual field perturbations for various field settings.

The field settings were chosen to cover most of the available field range of the air coil power supplies, from the important 3.8 G to the maximal 9.0 G setting. A single ensemble test consists of 10 000 simulations. Magnetic field perturbations were extracted from the observed magnetic field deviations and quantized thoroughly. A total of four field perturbations were tested:

- A global field offset along the spectrometer parallel to the original magnetic field.
- An azimuthal field deformation of the original magnetic field due to magnetic material in the reinforcement of the concrete walls of the spectrometer hall.
- A field offset perpendicular to the original magnetic field that introduces an flux tube misalignment.
- A fluctuation of the magnetic field caused by a fluctuation of the current output of the magnet power supplies.

This list is ordered with respect to the relative impact of a perturbation on the neutrino mass systematic, with the global parallel field offset being the decisive parameter. A major achievement of these studies is the establishment of a generalized functional dependence of the neutrino mass shift on the absolute field for all introduced field perturbations. In order to restrict the additional systematic shift to a level of 1 % of the overall uncertainty budget, the combined analysis of these equations yields an upper limit of the absolute magnetic field of 585 µT.

Outlook

The remanent and induced fields of the magnetic materials in the spectrometer hall can lead to significant deviations of the field inside the main spectrometer, especially on outer flux tube radii. To address this issue two countermeasures are conceivable.

On the one hand, an active compensation of the effective field deformations is possible when additional air coils are installed. These would be distributed along the walls of the spectrometer hall. In this case however, a large number of additional coils would be required. With the installed EMCS system the constant part of these deviations be compensated already. However, it turned out that this approach already reduces the observed azimuthal field deformations by 50 %, as verified by detailed e-gun measurements. As an easy and fast solution, consisting of adjustments of the EMCS currents is therefore recommended for the upcoming measurement campaigns.

On the other hand, the observed remanent and induced fields can be incorporated in the field model. In doing so, the distorted fields can be accounted for in the analysis software. However, the current precision of the approximations introduced is not sufficient to describe the field deformations inside the spectrometer volume. Therefore, a large sensor grid covering most of the lateral side area of the spectrometer is currently being developed, with design specifications based on the results of this thesis. Moreover, this system will also be an important tool to investigate the expected bias in the magnetic background field when the magnets of the source and transport section are commissioned.

By determining the radial inhomogeneity of the retarding potential and the analyzing magnetic field with unprecedented accuracy and precision, an important benchmark has been established for the upcoming commissioning and neutrino mass measurements. In particular such measurements will comprise work-function studies of the spectrometers, detailed investigations of energy losses due to synchrotron radiation and more. As future measurements will rely on electron sources on the upstream end of the KATRIN beam line, the verified alignment of the spectrometer and detector section is a most valuable intermediate stage towards achieving a global alignment. Furthermore, the developed software tools are indispensable to future analyses of transmission function measurements, in particular the rear section e-gun will significantly benefit from these tools.

Based on comprehensive ensemble tests of various effects that cause a magnetic field perturbation, the impact of the magnetic field on a systematic neutrino mass shifts has been verified in detail. A generalized formulation of the resulting shifts as function of empirical offsets was established, so that the resulting neutrino mass shift can easily be reevaluated. This would be necessary in case that the magnetic background field has changed, as is expected for the commissioning of the source and transport section. In combination with the detailed background model of this thesis (and its further refinement over the commissioning phase) a high precision and highly reliable field model will be at hand for the long-term neutrino mass measurements. The newly established systematic effect related to the accuracy of the absolute value and map of the magnetic field in the analyzing plane is an important mile stone in achieving a complete description of the systematic uncertainty budget of KATRIN.

APPENDIX A

Additional data of the air-coil and monitoring system

In this chapter, all relevant tables regarding the air-coil system configurations during SDS 2 are given and figures of the individual air coil performances are presented in addition to section 4.2.1, section 4.3.1 and section 4.3.2.

Also, the analysis of the field relaxation after a magnetic pulse when a 5 G setting is applied is here presented.

Finally, tests as presented in chapter 5 for the high-precision magnetometers, are here shown for the IPE magnetometer system, comprising the temperature calibration table and the long-term monitoring results.

A.1 Performances of individual air coils

The most important magnetic field settings during the SDS 2 measurement phase are summarized in table A.1. All measurements and analysis presented in this thesis are based on these configurations. Please note, that all currents represent ideal set-values, where the individual currents are the result of the optimization procedure section 4.1.2, in case of the symmetric settings. This means also, that the air-coil calibration of section 4.2 is not included and the resulting flux-tube shape may differ from an symmetric shape.

In chapter 4 it was asserted that all power supplies of the air-coil system show similar behavior, which is based on the performance data of the three most frequently used settings (table A.2). Based on these actual currents, the magnetic-field analyses are performed (chapter 5) and the fields inside the spectrometer vessel are performed (chapter 7).

In Chapter 4, only the current read-out of the power supplies of LFCS 7 and 8 or an averaged current of the total air-coil system were used to describe and analysis of the air-coil system. Here the individual behaviors of all air-coil power supplies of the basic analysis as in fig. 4.9 and fig. 4.10 are presented in fig. A.1 and fig. A.2. All observed slops are in agreement with a vanishing drift within a 1σ uncertainty, except for LFCS 10 were this statement is true only within 3σ. For the other field settings no significant drift could be observed.

The initial air coil calibration that triggered the study of correlation between air coil currents is given in fig. A.3. The air-coil power supplies are ordered in pairs and positioned along the spectrometer vessel. Inside the air coil current distribution chamber they are organized by two ADC cards, each with eight power supplies. Power supplies on a common card and especially paired power supplies feature a large current correlation. Example shown in this chapter represent the measurements where the effect was most pronounced.

Table A.1: Currents of the low field correction system used in this thesis. A setting is called symmetric when the spectrometer is operated as a MAC-E filter. In an asymmetric setting no currents are applied to the PS magnets, therefore the magnetic field that is displayed on the FPD penetrates the spectrometer vessel. For symmetric settings the absolute magnetic-field strength in the center of the main spectrometer is given in column B-field. The unit Gauss is only used as an approximation in a name. A setting classification as double (d) (single (s)) has two local magnetic field minima (has one global magnetic field minimum). Column #1-#14 correspond to a LFCS-coil number as shown in fig. 3.1. All values are given in Ampere and the sign indicates the direction of the magnetic field in KATRIN coordinates.

setting	B-field	# 1	# 2	# 3	# 4	# 5	# 6	# 7	# 8	# 9	# 10	# 11	# 12	# 13	# 14
sym. Double															
2.0 G (d)	229 µT	−5.435	−10.70	−7.539	−18.68	−24.26	−20.11	−8.133	−19.58	−6.132	−30.18	−27.58	−8.503	−39.82	63.08
3.8 G (d)	363 µT	−21.14	−25.66	−20.30	−28.36	−38.82	−27.52	−34.37	−50.68	−10.37	−44.44	−37.19	−20.96	−43.32	50.35
5.0 G (d)	490 µT	−52.94	−15.17	−33.73	−34.47	−61.83	−75.65	−27.05	−49.49	−64.38	−46.64	−52.53	−29.78	−52.21	47.82
7.0 G (d)	697 µT	−44.14	−68.53	−71.61	−69.28	−63.50	−76.42	−75.18	−65.80	−89.08	−49.07	−65.95	−60.51	−95.73	46.11
9.0 G (d)	886 µT	−84.63	−99.97	−55.99	−99.54	−99.68	−80.45	−95.40	−98.10	−84.01	−89.12	−68.80	−99.15	−93.43	28.08
sym. Single															
3.8 G (s)	429 µT	−69.75	−53.98	−80.95	−54.88	−5.787	−8.284	−27.05	−4.018	−2.588	−39.16	−60.21	−39.16	−40.98	1.334
5.0 G (s)	538 µT	−79.29	−64.41	−29.80	−31.35	−81.10	−36.84	−33.08	−32.08	−41.61	−61.60	−34.44	−66.99	−52.42	27.51
sym. Special															
L14-40	376 µT	−28.01	−22.76	−22.34	−37.10	−29.43	−13.42	−63.99	−51.63	−10.73	−50.58	−24.53	−20.51	−32.30	40.0
L14-30	385 µT	−30.30	−36.30	−21.84	−33.31	−29.93	−5.645	−68.11	−51.41	−4.451	−52.39	−26.88	−18.10	−31.38	30.0
L14-20	392 µT	−30.86	−45.19	−23.03	−34.89	−28.80	−4.009	−68.04	−40.67	−6.937	−57.36	−27.65	−15.69	−27.56	20.0
L14-10	399 µT	−40.99	−44.27	−31.07	−33.64	−31.05	−4.311	−62.57	−29.35	−10.06	−61.52	−30.79	−13.10	−23.66	10.0
asym.															
B-Asym		0.0	0.0	0.0	0.0	−50.00	−100.0	−100.0	−100.0	−100.0	−100.0	−100.0	−100.0	−100.0	0.0

Table A.2: Air-coil stability for the most common SDS 2 magnetic-field setting. Based on the stable run conditions (see text in section 4.2.1), a mean value with a standard deviation (fig. 4.10) and a slope of a drift per month were extracted (figure 4.9) for the individual settings and air-coils power supplies.

air coil	3.8 G setting		5.0 G setting		9.0 G setting	
	mean (A)	drift (mA/month)	mean (A)	drift (mA/month)	mean (A)	drift (mA/month)
EMCS X	-8.716 ± 0.011	1.4 ± 1.4	-8.714 ± 0.018	-1.6 ± 2.0	-8.717 ± 0.040	-1.6 ± 2.3
EMCS Y	-50.003 ± 0.011	-0.3 ± 0.8	-50.003 ± 0.012	-1.1 ± 3.0	-49.986 ± 0.023	0.2 ± 1.5
LFCS 1	-20.914 ± 0.012	-0.5 ± 0.9	-52.807 ± 0.014	0.0 ± 2.8	-84.553 ± 0.017	0.9 ± 4.1
LFCS 2	-25.486 ± 0.010	-1.2 ± 0.7	-14.966 ± 0.010	-0.5 ± 2.3	-100.013 ± 0.007	-1.5 ± 1.6
LFCS 3	-20.008 ± 0.013	0.1 ± 1.8	-33.507 ± 0.012	1.6 ± 3.4	-55.895 ± 0.014	2.1 ± 4.7
LFCS 4	-28.238 ± 0.012	-0.8 ± 0.6	-34.309 ± 0.012	1.2 ± 6.1	-99.577 ± 0.048	3.8 ± 6.8
LFCS 5	-38.530 ± 0.023	0.7 ± 1.0	-61.666 ± 0.026	0.9 ± 9.5	-99.684 ± 0.017	5.0 ± 8.8
LFCS 6	-27.253 ± 0.013	0.9 ± 2.1	-75.574 ± 0.012	1.1 ± 4.9	-80.424 ± 0.017	1.6 ± 6.8
LFCS 7	-34.162 ± 0.014	0.4 ± 2.3	-26.810 ± 0.017	3.6 ± 10.1	-95.398 ± 0.018	0.8 ± 5.6
LFCS 8	-50.587 ± 0.020	3.0 ± 7.5	-49.343 ± 0.026	2.3 ± 7.2	-98.183 ± 0.019	-0.3 ± 8.2
LFCS 9	-10.047 ± 0.016	2.6 ± 4.7	-64.261 ± 0.019	3.4 ± 7.9	-83.943 ± 0.016	4.9 ± 5.2
LFCS 10	-44.355 ± 0.024	-14.1 ± 6.3	-46.572 ± 0.015	-7.1 ± 6.8	-89.338 ± 0.026	-17.4 ± 8.3
LFCS 11	-37.001 ± 0.013	-2.8 ± 3.4	-52.395 ± 0.012	1.3 ± 4.5	-68.731 ± 0.021	2.9 ± 4.5
LFCS 12	-20.818 ± 0.010	0.1 ± 1.0	-29.651 ± 0.009	0.6 ± 1.7	-99.244 ± 0.010	0.8 ± 3.4
LFCS 13	-43.144 ± 0.014	-0.3 ± 2.6	-52.085 ± 0.015	4.1 ± 4.4	-93.390 ± 0.042	1.2 ± 1.5
LFCS 14	-50.336 ± 0.010	0.2 ± 0.5	-47.804 ± 0.010	0.1 ± 2.9	-28.029 ± 0.018	-0.1 ± 1.4

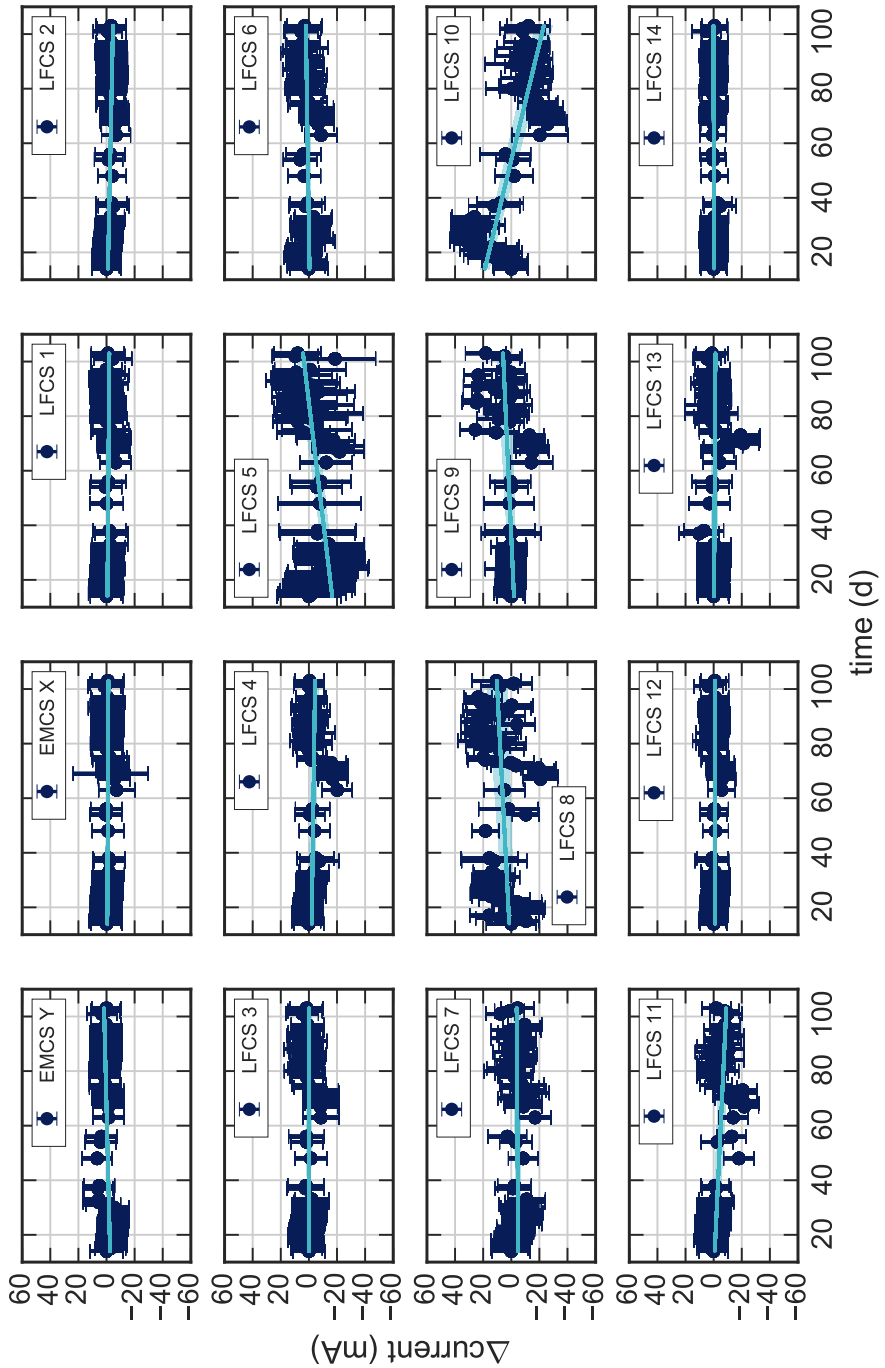

Figure A.1: Long-term trend of the air-coil system for the 3.8 G setting. All values are plotted relative to the first value in the time line and fitted with a 3σ error belt. For the LFCS 13 and the EMCS horizontal, only values after power supply exchange were used for fitting. Largest observed drift is 6 mA of the LFCS 8.

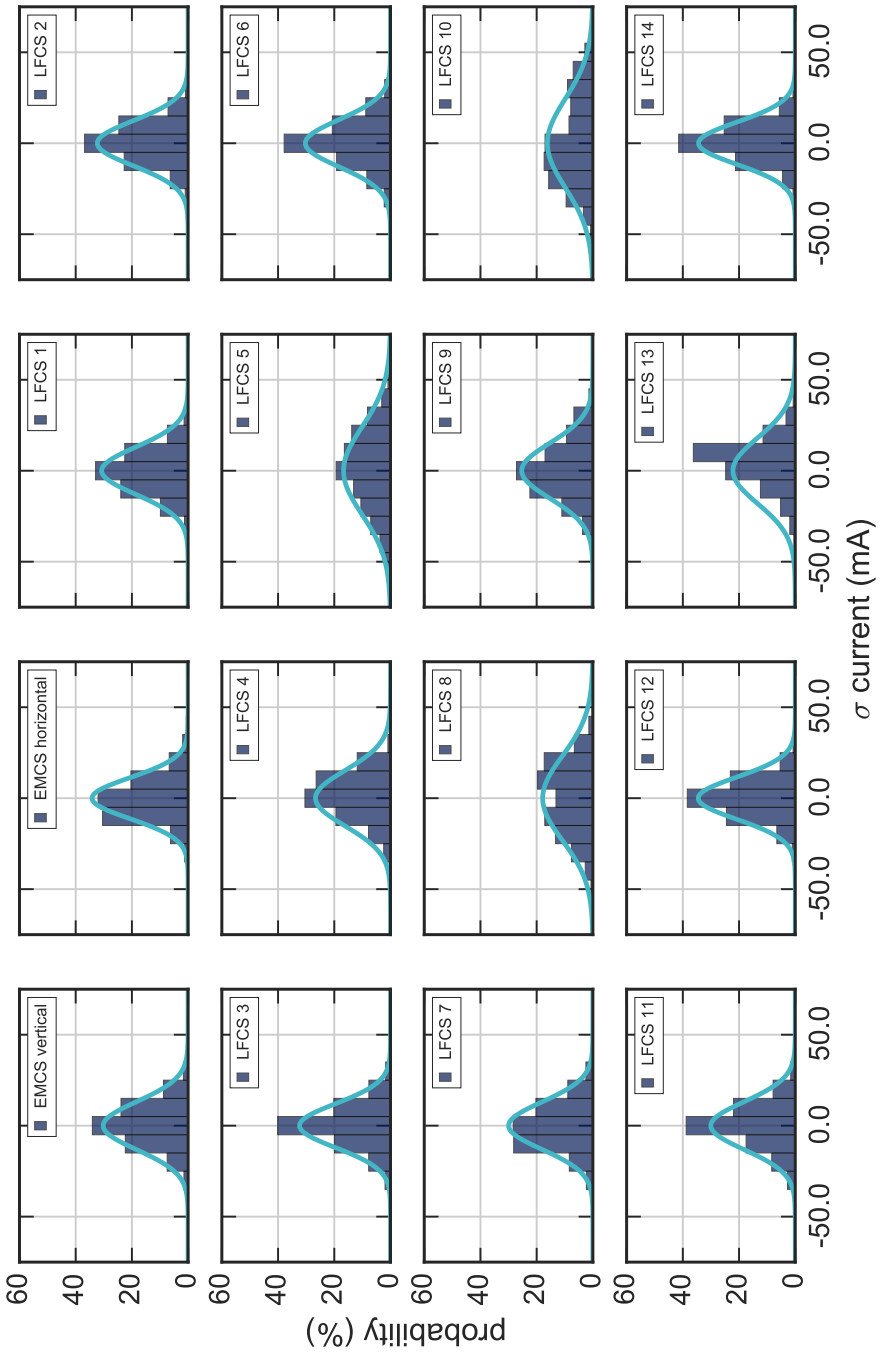

Figure A.2: Fluctuations of the air-coil current for the 3.8 G setting. Based on the conditions for a stable magnetic field (see text in section 4.2.1). The histograms show the normalized current fluctuations of all 3.8 G-runs during SDS 2. All fluctuations can be described by a Gaussian distribution and operate within their specifications, the corresponding results are given in table A.2.

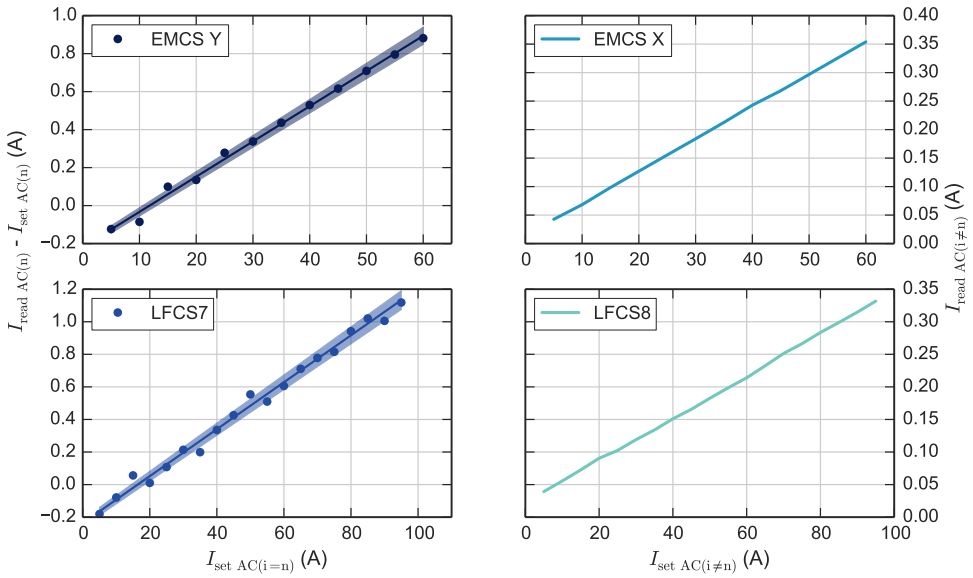

Figure A.3: Initial linearity test of the air-coil system and cross talk between power supplies. On the left, the calibration measurement of the power supplies of EMCS Y (LFCS 7) as a deviation of the readout- and set-value current. On the right the current read-out of the adjoined power-supply EMCS X (LFCS 8) while the other power supply was ramped. A stable, non vanishing current dependency of the order of percent is a indication for a cross talk between the adjoining power supplies.

A.2 Magnetic field relaxation after magnetic pulse at 5.0 G

To study the relaxation of the magnetic in the range of seconds, the development of the magnetic field after a magnetic pulse is studied. Thereby is the measurement comparable to section 4.3.1 as the same magnetic pulse mode is applied. In particular the analogy comprises, the number of pulsed air coils, the duration of a pulse, the duration of the pulse cycle, the total number of pulses. The only difference is the initial field configuration happens to be a 5.0 G setting.

The overall observed structure of the magnetic field relaxation in fig. A.4 is comparable to the fig. 4.8. A similar time offset between the ORCA time and the start of the pulse is observed. When the currents in the air coils are switched, again a linear slope is registered. However, the phase when the voltage is the limiting factor of the current flip is long, which is the reasonable since the absolute currents are larger and consequently takes it longer until the 95 %-current level is reached. The actual time constant in the exponential segment of the relaxation curve coincide with previous result. This observation is in agreement with the assumption that the exponential term is introduced by eddy currents in the spectrometer vessel.

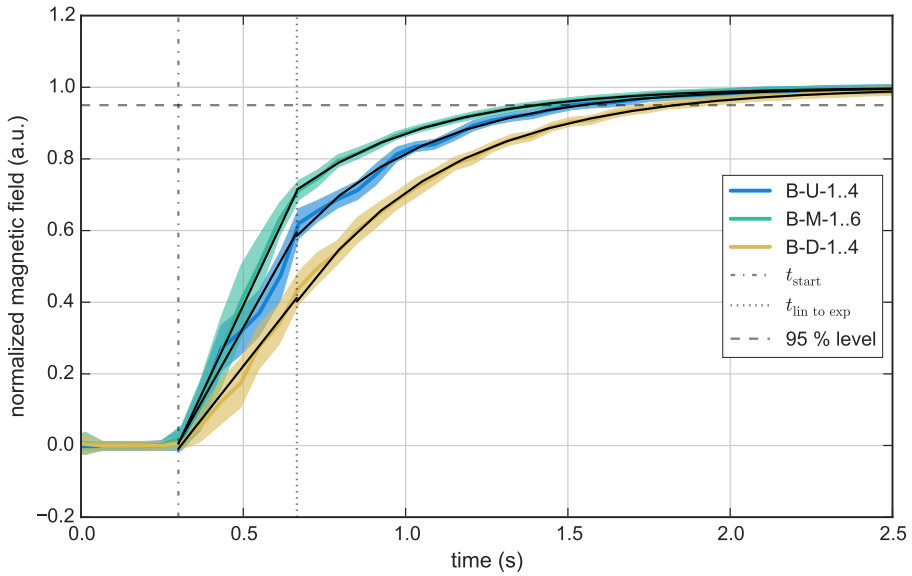

Figure A.4: Relaxation after magnetic pulse of LFCS 1-13 at a 5.0 G setting, measured with the precise magnetometers. Magnetometers values at the same axial position are combined, the resulting mean values are shown with a $1\,\sigma$ uncertainty. The magnetic field is normalized where 0.0 corresponds to reversed and 1.0 the nominal field value. Fit of the relaxation developments are shown with red dotted lines, divided in two intervals. Between t_{start} and $t_{\text{lin to exp}} = 0.6\,\text{s}$ a linear, after that an exponential function is used. A horizontal line marks the 95.0 % level.

A.3 Analysis of the IPE magnetometers

In table A.3 the results of the calibrations, including the magnetic-field and the temperature, of the IPE sensors are given.

For the temperature calibration of the sensors time period of one month was selected were no currents were applied to any of the KATRIN magnets. Therefore, the magnetic field measured by the sensors consists only of the earth magnetic field and the remanent magnetic field of the magnetic materials in the experimental hall. Under such conditions both magnetic field components can be assumed to be constant. Hence, a variation of the magnetic field is ascribed to the temperature dependency of the magnetometer only. Additionally this time period includes the bake-out of the main spectrometer. Therefore the utilizable temperature range is increased, especially for the sensors mounted on top of the spectrometer.

For the calibration of the magnetic field, only extreme and none standard settings were chosen to maximize the measured field range. Thereby the influence of magnetic field disturbance by the remanent field of magnetic materials in the experimental hall and the uncertainty on the linearity of a sensor unit is minimized. To secure a reliable field calibration, another condition is the stability of the temperature of the sensor units. By the manufacture, a temperature-dependency coefficient of 3.5 % is given that is stable in the allowed temperature range and external magnetic-field values. With an average temperature spread of 0.145 °C, the expected uncertainty on the calibration is about 0.5 % and does not exceed 2.5 %.

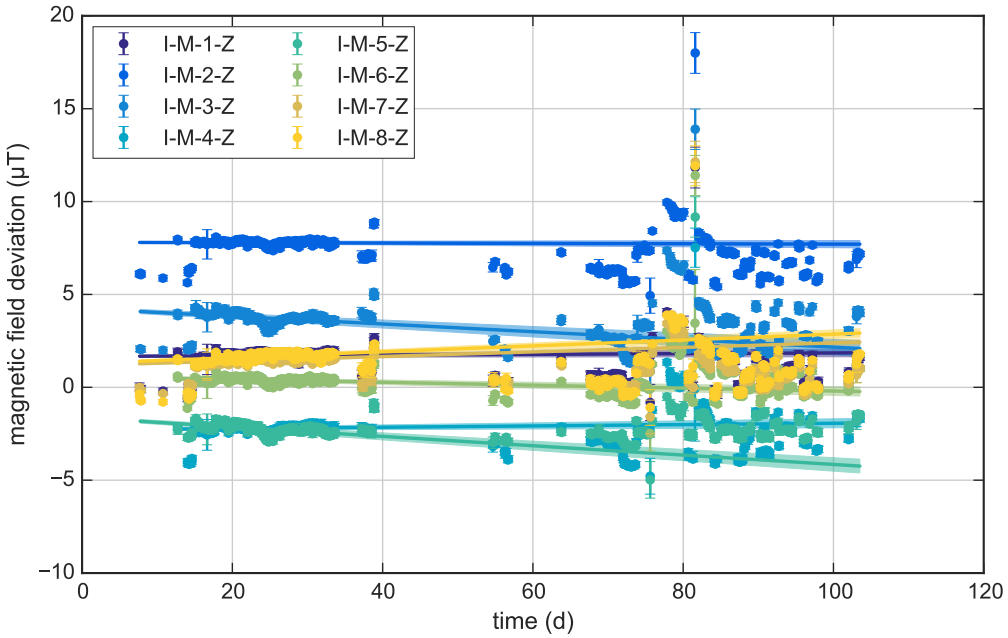

Figure A.5: Long-term analysis of the 3.8 G-setting with IPE magnetometer and status of magnetic sub-systems. In the upper plot the z-component of the magnetic field of a sensor is shown as a deviation to the corresponding simulation.

Table A.3: In the first column a sensor identifier is given that is composed of an axial position, a consecutive number for the individual sensor units and the coordinate of a sensor unit axis. The sensors are mounted at three different axial positions along the spectrometer vessel where D is the downstream position at $\approx -4.5\,\mathrm{m}$, M is the middle position at $\approx -0.2\,\mathrm{m}$ and U is the upstream position at $\approx 4.3\,\mathrm{m}$. Fit results of a linear function of the magnetic field calibration are given in the columns slope and offset. The temperature and the corresponding fluctuation of all measurements used for the magnetic-field calibration are given in column temperature. For the temperature calibration is based on the measurement during the bake-out of the main spectrometer. The resulting temperature variation is given in column range and the fit results in the last two columns.

Sensor	slope (a.u.)	offset (µT)	temperature (°C)	range (°C)	$\mathrm{slope_T}$ (nT/K)	$\mathrm{offset_T}$ (nT)
D 1 X	1.002 ± 0.092	10 ± 10	26.57 ± 0.14	5.33	-358.0 ± 0.4	$52\,410 \pm 10$
D 1 Y	0.958 ± 0.036	9 ± 1	26.57 ± 0.14	5.33	-387.0 ± 0.5	$46\,326 \pm 14$
D 1 Z	0.986 ± 0.007	7 ± 5	26.57 ± 0.14	5.33	360.0 ± 0.4	$11\,905 \pm 11$
D 2 X	0.977 ± 0.007	-4 ± 1	26.73 ± 0.10	4.27	167.0 ± 0.4	-8633 ± 10

continued on next page . . .

Sensor	slope	offset	temperature	range	slope_T	offset_T
D 2 Y	0.959 ± 0.022	4 ± 1	26.73 ± 0.10	4.27	-165.0 ± 0.8	$46\,220 \pm 22$
D 2 Z	1.002 ± 0.002	12 ± 1	26.73 ± 0.10	4.27	-1.0 ± 0.3	$28\,295 \pm 9$
D 3 X	0.966 ± 0.013	22 ± 1	26.53 ± 0.15	7.39	-517.0 ± 0.1	$-20\,535 \pm 3$
D 3 Y	0.855 ± 0.292	-13 ± 11	26.53 ± 0.15	7.39	-49.0 ± 0.1	$33\,847 \pm 4$
D 3 Z	1.003 ± 0.003	-18 ± 2	26.53 ± 0.15	7.39	-50.0 ± 0.1	$24\,378 \pm 4$
D 4 X	-0.951 ± 0.005	6 ± 1	26.10 ± 0.12	8.89	78.0 ± 0.1	$40\,745 \pm 2$
D 4 Y	-0.936 ± 0.046	-2 ± 1	26.10 ± 0.12	8.89	-20.0 ± 0.2	6451 ± 5
D 4 Z	0.990 ± 0.005	8 ± 4	26.10 ± 0.12	8.89	97.0 ± 0.1	$22\,464 \pm 3$
D 5 X	0.968 ± 0.027	-36 ± 4	25.60 ± 0.07	6.89	-488.0 ± 0.1	$-10\,603 \pm 3$
D 5 Y	1.078 ± 0.160	22 ± 7	25.60 ± 0.07	6.89	167.0 ± 0.3	$-46\,802 \pm 7$
D 5 Z	0.977 ± 0.005	35 ± 4	25.60 ± 0.07	6.89	-230.0 ± 0.1	$32\,703 \pm 4$
D 6 X	1.057 ± 0.117	10 ± 13	26.11 ± 0.10	5.57	-42.0 ± 0.3	$20\,908 \pm 8$
D 6 Y	1.016 ± 0.102	-4 ± 4	26.11 ± 0.10	5.57	215.0 ± 0.4	$-54\,714 \pm 12$
D 6 Z	0.985 ± 0.011	9 ± 8	26.11 ± 0.10	5.57	772.0 ± 0.4	3748 ± 10
D 7 X	0.964 ± 0.012	3 ± 1	26.24 ± 0.16	4.49	46.0 ± 0.5	$34\,781 \pm 14$
D 7 Y	0.958 ± 0.046	-1 ± 1	26.24 ± 0.16	4.49	-437.0 ± 0.6	$-13\,753 \pm 16$
D 7 Z	0.993 ± 0.006	7 ± 4	26.24 ± 0.16	4.49	270.0 ± 0.5	$15\,572 \pm 13$
D 8 X	0.897 ± 0.061	-6 ± 8	27.22 ± 0.29	3.51	410.0 ± 0.4	$23\,317 \pm 11$
D 8 Y	0.857 ± 0.181	4 ± 2	27.22 ± 0.29	3.51	86.0 ± 0.8	902 ± 21
D 8 Z	1.002 ± 0.003	10 ± 2	27.22 ± 0.29	3.51	275.0 ± 0.8	$19\,098 \pm 22$
M 1 X	0.709 ± 0.164	-15 ± 19	27.61 ± 0.16	4.27	-76.0 ± 0.5	8831 ± 15
M 1 Y	0.018 ± 0.139	14 ± 20	27.61 ± 0.16	4.27	2.0 ± 0.1	$14\,626 \pm 1$
M 1 Z	0.964 ± 0.003	13 ± 3	27.61 ± 0.16	4.27	-137.0 ± 0.7	$33\,039 \pm 20$
M 2 X	0.691 ± 0.164	-21 ± 19	28.97 ± 0.12	3.28	-117.0 ± 0.5	$-15\,397 \pm 15$
M 2 Y	0.918 ± 0.038	0 ± 2	28.97 ± 0.12	3.28	-60.0 ± 1.3	$40\,331 \pm 38$
M 2 Z	0.982 ± 0.004	18 ± 3	28.97 ± 0.12	3.28	117.0 ± 0.8	$31\,877 \pm 23$
M 3 X	0.908 ± 0.083	-18 ± 7	28.89 ± 0.77	4.58	-124.0 ± 0.3	$-40\,275 \pm 8$
M 3 Y	0.896 ± 0.076	-3 ± 2	28.89 ± 0.77	4.58	-33.0 ± 0.5	$24\,691 \pm 14$
M 3 Z	0.965 ± 0.002	20 ± 2	28.89 ± 0.77	4.58	15.0 ± 0.3	$30\,038 \pm 10$
M 4 X	-0.783 ± 0.153	12 ± 18	28.41 ± 0.08	7.16	-274.0 ± 0.1	$54\,230 \pm 4$
M 4 Y	-0.677 ± 0.235	0 ± 2	28.41 ± 0.08	7.16	162.0 ± 0.2	-2660 ± 6
M 4 Z	0.948 ± 0.004	6 ± 3	28.41 ± 0.08	7.16	114.0 ± 0.3	$17\,109 \pm 9$

continued on next page . . .

Sensor	slope	offset	temperature	range	slope_T	offset_T
M 5 X	-0.655 ± 0.143	15 ± 15	27.27 ± 0.13	4.83	-141.0 ± 0.2	$39\,103 \pm 5$
M 5 Y	0.340 ± 1.183	39 ± 37	27.27 ± 0.13	4.83	24.0 ± 0.2	$26\,772 \pm 5$
M 5 Z	0.969 ± 0.001	3 ± 1	27.27 ± 0.13	4.83	-92.0 ± 0.3	$23\,844 \pm 9$
M 6 X	0.912 ± 0.053	-7 ± 5	26.69 ± 0.12	2.72	-192.0 ± 1.0	5264 ± 28
M 6 Y	0.951 ± 0.003	0 ± 1	26.69 ± 0.12	2.72	50.0 ± 2.2	$-45\,120 \pm 59$
M 6 Z	0.964 ± 0.003	10 ± 2	26.69 ± 0.12	2.72	-21.0 ± 0.9	$27\,221 \pm 25$
M 7 X	0.532 ± 0.093	-5 ± 8	26.71 ± 0.13	6.09	46.0 ± 0.1	$11\,067 \pm 3$
M 7 Y	0.994 ± 0.996	-35 ± 24	26.71 ± 0.13	6.09	29.0 ± 0.4	$-67\,394 \pm 11$
M 7 Z	0.950 ± 0.002	10 ± 1	26.71 ± 0.13	6.09	99.0 ± 0.2	$23\,215 \pm 6$
M 8 X	0.983 ± 0.008	7 ± 1	27.96 ± 0.31	5.73	-9.0 ± 0.2	$43\,481 \pm 5$
M 8 Y	0.851 ± 0.082	6 ± 1	27.96 ± 0.31	5.73	-179.0 ± 0.4	$11\,084 \pm 11$
M 8 Z	1.239 ± 0.002	9 ± 1	27.96 ± 0.31	5.73	-76.0 ± 0.4	$32\,083 \pm 11$
U 1 X	1.002 ± 0.020	-2 ± 1	26.63 ± 0.12	4.25	-550.0 ± 0.9	$41\,985 \pm 24$
U 1 Y	0.939 ± 0.205	21 ± 6	26.63 ± 0.12	4.25	246.0 ± 0.9	$36\,983 \pm 24$
U 1 Z	0.996 ± 0.006	-1 ± 5	26.63 ± 0.12	4.25	520.0 ± 0.7	-2399 ± 18
U 2 X	0.685 ± 0.090	-7 ± 7	27.46 ± 0.09	6.12	-156.0 ± 0.1	$21\,575 \pm 3$
U 2 Y	0.993 ± 0.095	34 ± 4	27.46 ± 0.09	6.12	-41.0 ± 0.4	$48\,604 \pm 11$
U 2 Z	0.987 ± 0.002	41 ± 2	27.46 ± 0.09	6.12	76.0 ± 0.2	$25\,034 \pm 4$
U 3 X	1.015 ± 0.009	25 ± 1	26.73 ± 0.06	7.19	230.0 ± 0.1	$-43\,315 \pm 4$
U 3 Y	0.948 ± 0.026	-15 ± 1	26.73 ± 0.06	7.19	584.0 ± 0.2	$11\,198 \pm 7$
U 3 Z	1.011 ± 0.003	-16 ± 3	26.73 ± 0.06	7.19	74.0 ± 0.2	$19\,814 \pm 4$
U 4 X	-0.955 ± 0.010	35 ± 1	26.73 ± 0.10	8.46	235.0 ± 0.1	$35\,610 \pm 2$
U 4 Y	-0.992 ± 0.066	-29 ± 2	26.73 ± 0.10	8.46	-247.0 ± 0.2	$12\,413 \pm 5$
U 4 Z	0.983 ± 0.002	40 ± 2	26.73 ± 0.10	8.46	268.0 ± 0.1	$16\,421 \pm 3$
U 5 X	1.013 ± 0.014	-10 ± 1	25.80 ± 0.05	7.56	-284.0 ± 0.2	$-25\,731 \pm 5$
U 5 Y	0.768 ± 0.215	-1 ± 6	25.80 ± 0.05	7.56	-378.0 ± 0.2	$-16\,056 \pm 5$
U 5 Z	0.996 ± 0.003	9 ± 3	25.80 ± 0.05	7.56	274.0 ± 0.2	$19\,162 \pm 5$
U 6 X	1.102 ± 0.064	-15 ± 4	25.18 ± 0.09	4.07	250.0 ± 0.6	$-13\,684 \pm 14$
U 6 Y	0.972 ± 0.040	-5 ± 1	25.18 ± 0.09	4.07	375.0 ± 0.8	$-57\,370 \pm 21$
U 6 Z	0.994 ± 0.004	6 ± 3	25.18 ± 0.09	4.07	-444.0 ± 0.5	$36\,780 \pm 13$
U 7 X	1.109 ± 0.069	-47 ± 5	26.30 ± 0.15	5.67	-208.0 ± 0.2	$30\,631 \pm 7$
U 7 Y	0.982 ± 0.080	22 ± 4	26.30 ± 0.15	5.67	-63.0 ± 0.4	$-30\,262 \pm 10$

continued on next page . . .

Sensor	slope	offset	temperature	range	slope_T	offset_T
U 7 Z	0.985 ± 0.004	40 ± 4	26.30 ± 0.15	5.67	47.0 ± 0.3	$22\,388 \pm 7$
U 8 X	1.082 ± 0.060	-10 ± 3	26.99 ± 0.32	4.95	-15.0 ± 0.4	$38\,442 \pm 10$
U 8 Y	0.668 ± 0.093	5 ± 2	26.99 ± 0.32	4.95	-141.0 ± 0.6	8288 ± 15
U 8 Z	0.991 ± 0.002	12 ± 2	26.99 ± 0.32	4.95	-219.0 ± 0.4	$31\,534 \pm 11$

Based on the calibrationed IPE sensors system, including the temperature calibration in fig. 3.14 with table A.3, a long term analysis of the magnetic field was performed (fig. A.5). The analysis is comparable to fig. 5.7 regarding the analyzed phases, the field setting of 3.8 G and the conditions for a stable field configuration.

The long time span of a constant field operation from 17 day to 33 day a mean magnetic field drift of $(-3.0 \pm 15.0)\,\text{nT/day}$ was observed. Therefore the precision and long-term stability of this sensor system is sufficient to monitor the magnetic field. However, the observed magnetic field spread of $(3.01 \pm 0.70)\,\mu\text{T}$ is larger by a factor of 2 compared to the high precision magnetometers. This results from the calibration procedure that unfortunately incorporates the induced fields from the magnetic materials in the walls of the spectrometer build. This assumption is confirmed by the fact that the sideways positioned magnetometers feature the largest deviations, in particular I-M-2. Consequently is the accuracy of the sensor system spoiled. Therefore, the system of the IPE sensors is sufficient in a stable environment as a monitoring system only, a detailed field analysis is not possible.

That the sensors are very sensitive to the absolute magnetic field can be observed in the strong fluctuations between day 70 and day 100. As shown in PS current analysis in fig. 5.7, the currents are adjusted several time during this period and thereby introduce already a strong fluctuation of the observed fields.

APPENDIX B

Additional analyses and result tables of e-gun measurements

In section 6.2.1 and section 6.4.1 it was argued, that the utilized energy distribution, a generalized normal distribution with a skewness and an additional cut of parameter, can be interpreted as a semi-empirical model. However, there are actually two different forms of the generalized normal distribution. Although the second version is difficult to motivate physically, it reduces the required fit parameter even further and minimizes the fit uncertainties. In appendix B.1, a small introduction to the second version is given.

In section 4.1, two approaches to optimize the magnetic-field setting for a MAC-E filter operation are introduced. There it is explained, that a so-called single-minimum setting has the benefit to reduce the observed background rate, while being inferior in terms of the energy resolution. The latter effect can be explained by a larger radial inhomogeneity of the magnetic field and a larger uncertainty on the actual analyzing plane shape, which is discussed in appendix B.2.

The radial potential inhomogeneity is analyzed in section 6.5, based on the measurements when a 3.8 G setting was applied. In appendix B.3 the results of the transmission function measurements with other field settings are listed. In addition to section 6.6, a detailed table of the transmission function measurements with 3.8 G setting, including all angles and the separation in individual measurement cycles is given.

B.1 Alternative description of the energy distribution

The description of the energy distribution in chapter 6 combines the a generalized normal distribution with the photo effect as boundary conditions. In fact, the used shaping is the second version of the generalized normal distribution, here is also the first version tested.

The cumulative distribution function of a first version generalized normal distribution is given by

$$f(x) = \frac{1}{2} + \operatorname{sgn}(x-\mu)\,\frac{\gamma\left[1/\alpha, \left(\frac{|x-\mu|}{\sigma}\right)^{\alpha},\right]}{2\Gamma(1/\alpha)}, \tag{B.1}$$

where sgn is the sign function, γ denotes the lower incomplete gamma function

$$\gamma(s,x) = \int_0^x t^{s-1}e^{-t}dt \tag{B.2}$$

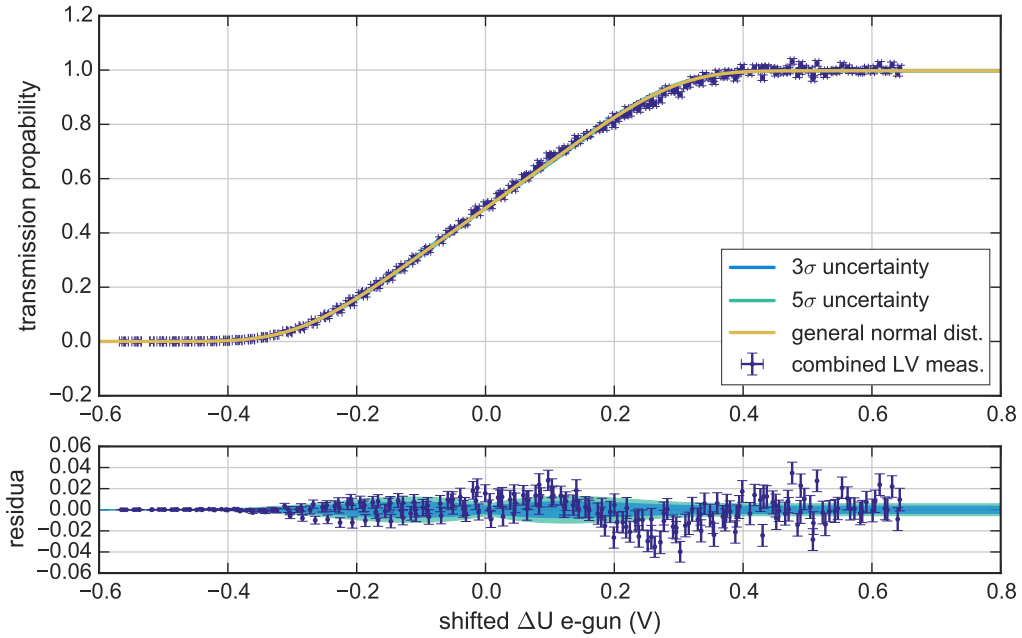

Figure B.1: Transmission probability fitted with alternative energy distribution model. For energy distribution measurements were a 3.8 G magnetic-field setting and a low voltage configuration was applied. The plot shows all measurements before the maintenance break, shifted for their individual radial potential-inhomogeneity.

and Γ is the gamma function

$$\Gamma(t) = \int_0^\infty x^{t-1} e^{-x} dx \quad . \tag{B.3}$$

In fig. B.1 the combined low voltage measurements as in fig. 6.6 are fitted with eq. (B.1). In comparison to the second version of the generalized normal distribution is a cut parameter, and thereby also the re-normalization paramter, not required. The reduction of the fit parameters and the fully analytic calculation of the fit function allows to minimize the computation times and improved uncertainty values with a reduced χ^2 of 1.13 and a precision of transmission energy determination in the sub-meV regime. However, close to full transmission the fit function clearly deviates from the measured transmission probability. This becomes evident not only in the residua, but moreover in the differential form.

The probability density function of the first version of the generalized normal distribution with eq. (B.3) is given by

$$f(x) = \frac{\alpha}{2\sigma\Gamma(1/\alpha)} e^{-(|x-\mu|/\sigma)^\alpha}, \tag{B.4}$$

that becomes a regular normal distribution for $\alpha = 2$. In fig. B.2 it becomes obvious, that the symmetric function is an insufficient description of the energy distribution. Moreover, no

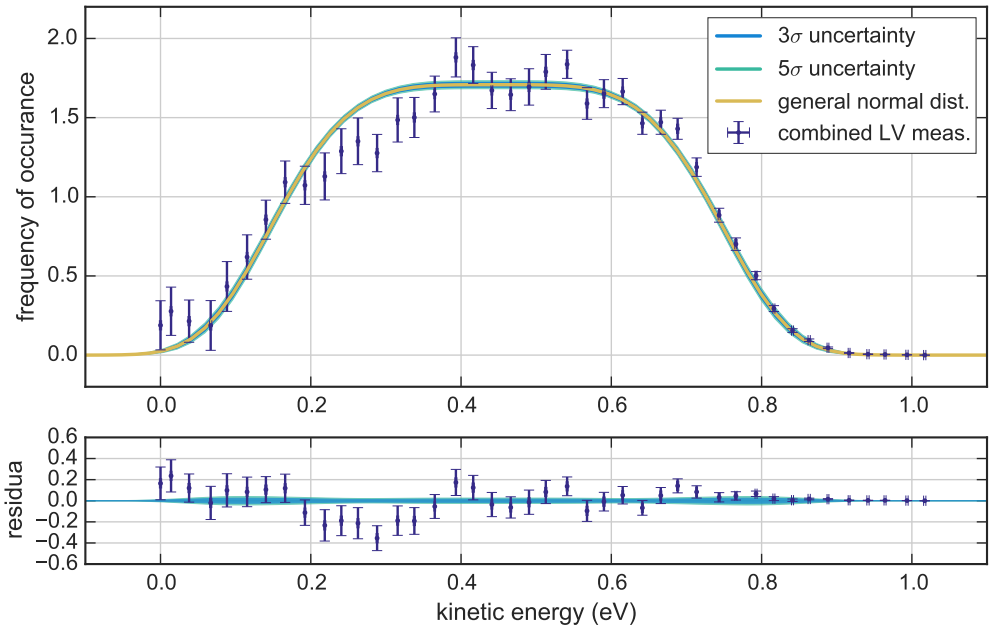

Figure B.2: Energy distribution fit with alternative energy distribution model. Differential energy distribution of combined measurements. The resampled and numerically differentiated low voltage measurements are shown in dark blue. "Combined" fit results (table 6.1) are applied to eq. (B.1) in yellow, along with a 1σ (3σ) fit uncertainty in blue (green). Fit function is the first version generalized normal distribution.

reasonable physical effect was identified that could cause such an broadening of the energy distribution at the e-gun.

However, the radial inhomogeneity of the potential can introduce an plateau in the transmission probability as observed in ref. [Wac15]. In this simulation, the full flux tube was utilized, but a single retarding potential assumed in the analysis. Therefore, the first version generalized normal distribution can be used to account for the potential gradient that is observed by an individual pixel, although it is expected that the variation within a pixel is much smaller then observed in ref. [Wac15].

B.2 Analyzing plane shape in a 3.8 G (s) setting

In section 4.1, the magnetic field settings, that features only one field minimum, were introduced as an option to eventually reduce the observed background rate (ref. [Tro15]). A possible pitfall of such field settings is the required precise alignment of the electric and magnetic field. Any deviation will lead to a shift of the analysis point and introduce an systematic uncertainty of the effective transmission energy. Moreover, the alignment issue is even more distinctive on outer radii where a smeared-out the transmission function is nearly inevitable, as field perturbations are more pronounced in this region (fig. 7.6). Since the measurements with an applied 3.8 G(s) setting where performed without the optimized EMCS setting, significant bias in the analyzing plane shape is expected.

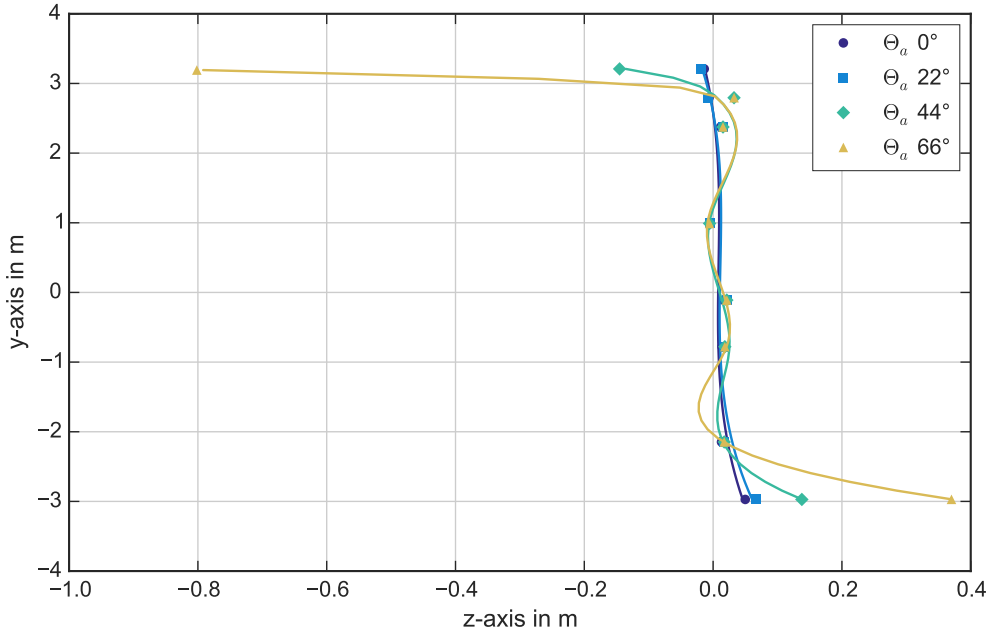

Figure B.3: Analyzing points in the y-z plane in a 3.8 G-setting with a single minimum. The position where the longitudinal kinetic-energy is minimal is shown for four different electron angles, a cubic spline indicates the shape of the analyzing plane. For this setting a perfect alignment of potential to the magnetic field is required. Especially on outer radii this is not fully guaranteed.

The simulation of the analyzing plane shape is performed as described in section 6.5.1. As expected, the shift of the anaylzing points is more profound on outer radii, where a shift up 0.8 m is observed (fig. B.3), in comparison to the 3.8 G(d) setting, where variations only within ±15 cm are observed (fig. 6.12). Alarming is also the fact, that for a given field line, the analyzing point for different electron polar angles are not at the same position, but vary significantly. For stronger field settings or bigger field perturbations, the impact on the transmission function can be even more considerable.

B.3 run numbers of transmission function measurements

In this section the table of the transmission function analysis with a 9.0 G setting (table B.1) and 3.8 G (s) setting (table B.2) are given. Larger χ^2 values of the 9.0 G fits are the result of a not adapted width of the transmission function. The position of the transmission energy however is only affected in the sub-eV regime.

Also the complete table of the measurements with an applied 3.8 G(d) setting listed, used in analysis of the radial potential and the magnetic field is (table B.3), where beside the run number, also a indicator for the different measurement cycles is given.

Table B.1: Potential mapping along the vertical axis with a 9.0 G setting. A global offset $\Delta\phi = 0.884\,\mathrm{V}$ is added to the experimental data of to account for the work-function difference between the e-gun and the main spectrometer. A work-function correction term $\phi_{\mathrm{EGun,corr}}$ is added to runs of different measurement cycles.

pixel	$\Delta U_{\mathrm{r,sim}}$ in V	$\Delta U_{\mathrm{r,exp}}$ in V	$\Delta\phi_{\mathrm{EGun,corr}}$ in V	red. χ^2
103	1.164 ± 0.003	1.122 ± 0.010	–	9.06
55	1.233 ± 0.002	1.197 ± 0.011	–	5.75
31	1.279 ± 0.002	1.260 ± 0.009	–	2.44
7	1.310 ± 0.002	1.280 ± 0.011	–	7.96
2	1.326 ± 0.002	1.303 ± 0.011	–	1.17
13	1.315 ± 0.002	1.293 ± 0.011	–	4.69
37	1.210 ± 0.003	1.195 ± 0.010	–	2.10
61	1.244 ± 0.003	1.224 ± 0.012	–	3.57
85	1.326 ± 0.002	1.302 ± 0.009	–	2.51
109	1.177 ± 0.003	1.163 ± 0.012	–	3.90

Table B.2: Potential mapping along the vertical axis with a 3.8 G (s) setting. A global offset $\Delta\phi = 0.904\,\mathrm{V}$ is added to the experimental data of to account for the work-function difference between the e-gun and the main spectrometer. A work-function correction term $\phi_{\mathrm{EGun,corr}}$ is added to runs of different measurement cycles.

pixel	$\Delta U_{\mathrm{r,sim}}$ in V	$\Delta U_{\mathrm{r,exp}}$ in V	$\Delta\phi_{\mathrm{EGun,corr}}$ in V	red. χ^2
103	1.878 ± 0.001	0.969 ± 0.006	–	3.99
79	1.942 ± 0.002	1.037 ± 0.006	–	2.43
55	2.004 ± 0.003	1.103 ± 0.006	–	2.16
7	2.154 ± 0.002	1.265 ± 0.006	–	3.89
2	2.184 ± 0.002	1.312 ± 0.006	–	1.59
13	2.157 ± 0.001	1.282 ± 0.006	–	1.19
61	2.008 ± 0.003	1.164 ± 0.006	–	1.40
109	1.871 ± 0.001	1.028 ± 0.006	–	1.83

Table B.3: Transmission function measurement with a 3.8 G setting. The first column corresponds to the target pixel on the FPD in ordered along the vertical axis. The labels of the following columns indicate the applied e-gun back plate angle relative to the determined minimal angle position. The sign of the polar angle indicates the direction of the e-gun chamber tilting where positive is a rotation to the right (west) and negative to the left (east). The letter behind the run number indicate the measurement cycle of uninterrupted transmission function measurements in chronological order.

pixel	-3 polar	0 polar	2 polar	3 polar	4 polar	6 polar	8 polar	9 polar
103	23 054 D	23 055 D				23 056 D		23 057 D
55	22 651 C	23 058 D				22 650 C		22 649 C
31	22 644 C	22 646 C				22 647 C		22 648 C
7	22 640 C	22 641 C				22 642 C		22 643 C
2		22 475 A	22 481 A		22 480 A	22 479 A	22 478 A	
13	22 624 C	22 623 C		22 625 C		22 626 C		22 627 C
37	22 631 C	22 630 C				22 629 C		22 628 C
61	22 632 C	22 633 C				22 634 C		22 635 C
85	22 639 C	22 638 C				22 637 C		22 636 C
109	22 559 B	22 560 B		22 561 B		22 562 B		22 563 B

APPENDIX C

Background dependencies on the magnetic field

The background model of the KATRIN experiment describes the energy spectrum, particle type, momentum and spatial distribution of non β-signal electrons in the main spectrometer. It comprises various background generating processes, each with a specific dependence on a multitude of operational parameters of the main spectrometer, such as the vacuum conditions, retarding potential and much more. An estimation of the contribution of individual processes to the overall background rate for different settings and the coresponding parametrization in the simulation framework, is a key task of the KATRIN collaboration. Although great effort to study the background model in terms of simulations (ref. [Mer12],[Wan13b], [Lei14] and [Rei13]) and measurements (ref. [Sch14b], [Har15b]) has been made, a full description and a verification of the background model by simulations is still pending.

It is most likely, that the remaining background is dominated by highly excited hydrogen Rydberg atoms. These Rydberg atoms originate from a long chain of sub-processes that include the already verified background sources, such as ^{220}Rn and ^{210}Pl. Background electrons are emitted when a Rydberg atom is ionized via black-body radiation, or decays due to an electric field gradient or even spontaneous. Either way, the emitted electron has only a little energetic of a few eV. When a Rydberg decay occurs in the central region of the main spectrometer, the low energetic electrons are accelerated by the retarding potential and are detected with the FPD system in the ROI of β-signal electrons (ref. [Har15b]).

Due to the huge phase space of the excitation states of a Rydberg atom, a broad variation of its cross section for ionization and thereby its life time is observed. Consequently, the simulation of the Rydberg atom decay is rather challenging due to the large phase space. However it can be assumed, that the distribution of the resulting background is rather homogeneous distributed in the main spectrometer volume with a slight rate increase towards outer radii (ref. [Tro17]).

It is beyond the scope of this thesis to verify the background introduced by Rydberg atoms. Instead, an introduction to background minimization methods is given, focused on the magnetic field. Thereby, a purely empirical approach to the background model is provided. In appendix C.1 the influence of the absolute magnetic-field strength and the resulting volume variation of the active flux tube is discussed. Depending on the dominant effect that creates background events, the shape of the magnetic field might has an influence on the background rate, which is discussed in the comparison of the so-called single and double field

configurations in appendix C.2. Finally, the flux-tube alignment on the background rate is discussed in appendix C.3 by comparing measurements with the standard EMCS settings and the empirical optimized settings introduced in section 5.5.

C.1 Absolute field and volume dependence

The two major operation parameters of the spectrometer that influence the background rate are the retarding potential and the magnetic field. Especially the configuration of the retarding potential, comprising the absolute value and the potential difference between the vessel and the inner electrode system, has a significant impact on the observed rate and structure of the background events. To study the impact of the magnetic field on the observed background rate, a constant retarding potential setting is applied. The analyses presented in this section is based on measurements of the data set embedded in ref. [Har15b]. When the influence of the absolute field is discussed, one has to distinguish between two different cases; either the strength of the field in the entire KATRIN setup or the field in the analyzing plane.

In the first case, the fields of all magnets of the KATRIN beam-line are scaled in a way that the shape of the active flux-tube eq. (2.12) remains unaltered. Although only limited tests with different solenoid setting could performed during the SDS 2 campaign, merely a minor field dependence is indicated (ref. [Har15b], [Har15a]). Advanced studies of the background with different magnetic field settings are planned for the upcoming measurement phase and will be addressed in ref [Tro17].

In the second case, only the setting of the air-coil system, the major contribution to the analyzing plane field, is change (table 5.1). Higher fields enhance the repulsion of charged particles from the active flux-tube volume and simultaneously, the storage conditions for electrons are improved by the magnetic field. Both effects feature also a complex dependence on the field shape and the applied voltages. Their implications are only accessible via elaborated simulations (ref. [Wan13b]). However, as an increased field leads to an reduced active flux tube volume (and vice versa), the evaluation of the field-volume dependence is straight forward based on the field line calculations in fig. 4.2 and an assumed axial symmetry. Since the field optimization is also tuned to generate an upstream-downstream symmetry in the central region, the volume dependence can be represented by the radius of the analyzing plane alone. Tested under similar conditions, the radial representation of the volume normalized rate features the same rate distribution for all field settings (fig. C.1). The reduction of the absolute background rate can therefore be attributed to a changed flux-tube volume alone (table C.1).

Table C.1: Background dependence on the absolute field in the analyzing plane and the flux tube volume. The applied voltage is 18.6 kV while the vessel and inner electrode system are on a common potential. Each measurement configuration was applied for a duration of 12.5 h. Further details in [Har15b].

magnetic setting	volume (m^3)	rate (mcps)	rate/volume (mcps/m^3)
3.8 G	707	923.3 ± 5.1	1.305 ± 0.007
5.0 G	551	666.6 ± 4.3	1.210 ± 0.008
9.0 G	331	359.0 ± 3.2	1.083 ± 0.010

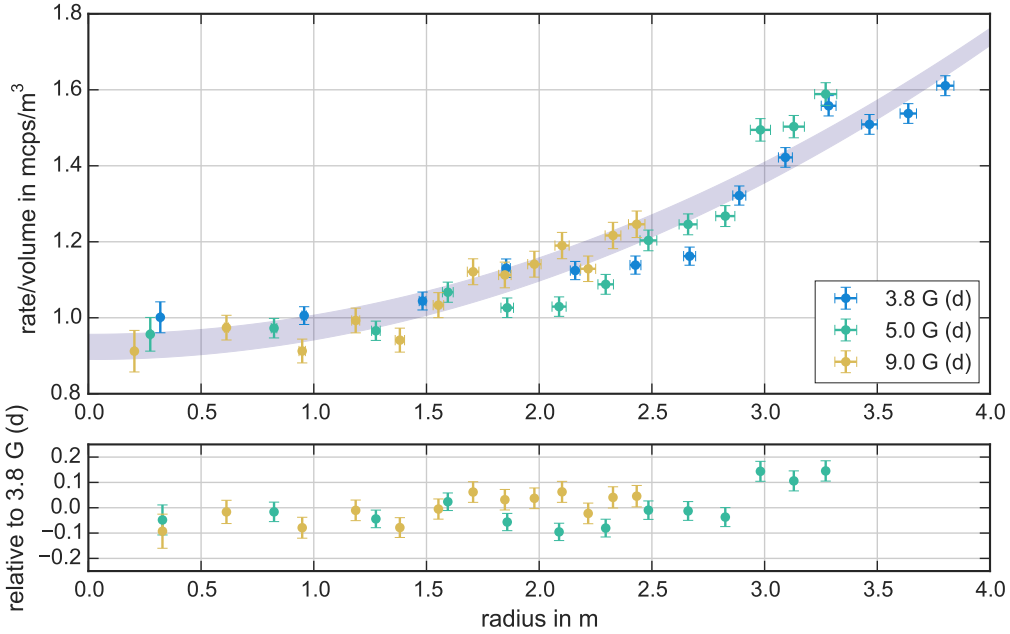

Figure C.1: Background dependence on the absolute field. The ring-wise segmentation of the FPD is used to visualize the radial background distribution in the ROI as a function of the radius at $z = 0\,\mathrm{m}$. Normalized to the magnetic flux-tube volume, a similar count rate is observed for all field settings as indicated by a cubic spline (grey belt) and the direct comparison between the field settings in the lower plot. Measurement settings and count rates can be found in table C.1.

C.2 Dependence of the magnetic field shape – single vs. double minimum

In section 4.1, magnetic field settings with a single minimum were proposed as a possibility to reduce the observed background rate, because simulations revealed that at field minima background electrons can leak into the active flux tube. Based on ref. [Erh15c], it is studied, if the single minimum solution has an effect on the background level.

When background measurement with the 3.8 G(d) and 3.8 G(s) setting are directly compared, is indeed a significant rate reduction observed. However, in the previous section a pure volume dependence was observed and from fig. 4.2 it can be derived, that the volume variate significantly between a single and double minimum solution with a comparable field strength. In fact, even for a background rate normalized for the flux tube volume a significant reduction of 7 % is found (table C.2). The additional rate reduction is not yet fully understood, it might be related to a reduced mean distance of the outer flux tube to internal structures along the spectrometer axis.

To investigate whether the field shape (single or double) or the increased clearance to the flat cone structures is responsible for the observed rate reduction transient field settings are tested. These settings are based on the 3.8 G(d), but the current of air coil 14 was fixed to a value between 10 A to 40 A. Based on this value, the field optimization was repeated (section 4.1.1). While the conditions for the current optimization where set for a double

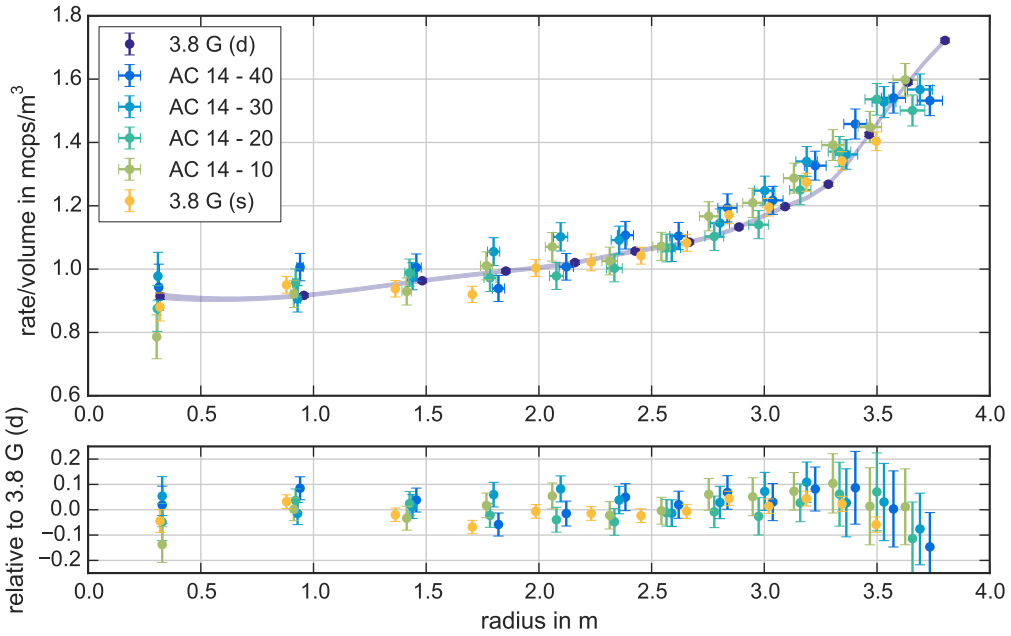

Figure C.2: Dependence of the background rate on the magnetic flux-tube shape. The absolute field of all measurements are comparable (table A.1) as well as the observed rates. The distribution of the other measurements is within an 1σ-deviation. A cubic spline is plotted along the 3.8 G-(d)-measurement.

minimum field configuration, a reduced air coil 14 current pushes the field shape towards a single minimum solution, consequently the flux tube is tightened in the flat cone regions. Unfortunately, the observed rates are indecisive. Although minor rate reduction is observed for reduced AC 14 currents, the rate differences are within a 2σ range and no significant structure is observed in the radial analysis (fig. C.2). This issue should be addressed in upcoming measurement phases.

Table C.2: Influence of magnetic field shape on the background rate. Magnetic field configuration in table A.1. Vessel potential is 18.5 kV, IE common is operated with a −5 V offset and the steep cones with additional 2 V (ref. [Erh15c]).

LFCS setting	rate (mcps)	rate/volume (mcps/m^3)
3.8 G (double)	854.9 ± 1.3	1.209 ± 0.002
AC 14 - 40	834.2 ± 8.8	1.211 ± 0.013
AC 14 - 30	800.1 ± 8.6	1.207 ± 0.013
AC 14 - 20	747.9 ± 8.3	1.161 ± 0.013
AC 14 - 10	739.5 ± 8.3	1.181 ± 0.013
3.8 G (single)	626.8 ± 4.4	1.122 ± 0.008

C.3 Influence of the EMCS

The magnetic field can be utilized to shield against charged particles from the inner surface of the spectrometer. Axial symmetric of the magnetic field is thereby mandatory (section 2.1.2), as it reduces the minimal distance of the active flux-tube volume to the vessel hull and by inhibiting a $\vec{E} \times \vec{B}$ drift of charged particles in the active flux-tube.

In section 5.5 it was shown that the EMCS can be used to account for the magnetic background field, thereby the flux tube is adjusted and the axial symmetry of the magnetic field is improved by about 50 % (section 5.5). This effectiveness of this field correction method has been verified in ref. fig. 6.16 in terms of the transmission probability. Here, the effect of an adjusted EMCS on the observed background rate is studied (ref. [Erh14a]). An optimized symmetry of the flux tube can reduced the observed background by suppress drift processes (ref. [Wan13b]). Also, if the distance between the flux tube and electrode structure indeed affects the count rate, the restored symmetry should reduce the azimuthal dependence of the background rate even further.

The flux tube position has been verified with an asymmetric field setting (fig. 5.15) Based on the online analysis of ref. [Nte14]), the optimized EMCS currents were determined to EMCS-X = 7.5 A and EMCS-Y = 47.0 A for the background measurements. The LFCS was operated with a 3.8 G(s)-setting for the background measurements. In addition, two potential settings were selected to investigate the background rate at outer radii.

For measurements with an IE potential of −100 eV, a minor background reduction is observed, even for the volume normalized rate (table C.3), but not for the other potential setting. The small netto measurement time of 2 h per setting inhibits a significant analysis of the radial and azimuthal structure (fig. C.3) of the background rate (fig. C.4). In can concluded, that an optimized flux tube alignment can only marginally reduce the observed background rate. For decisive results, a clearly increased measurement time is required.

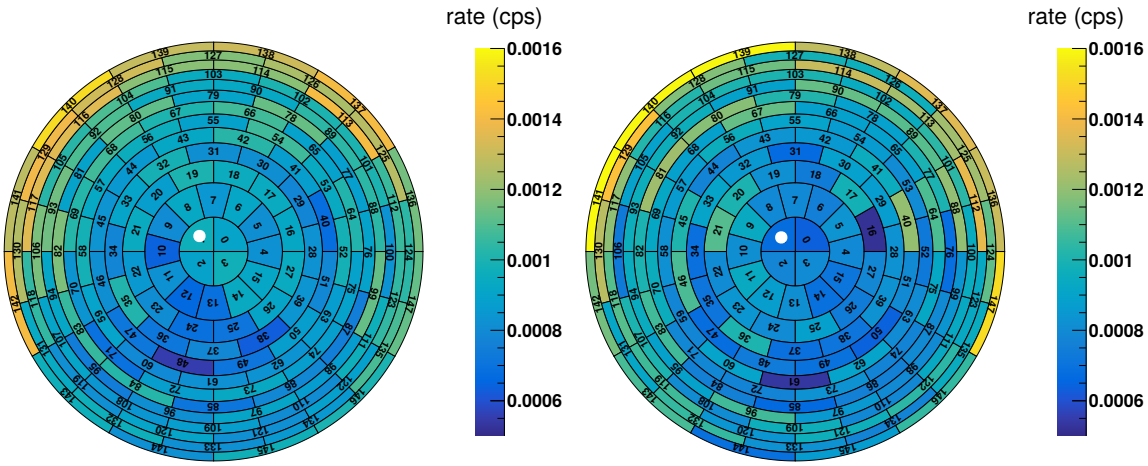

(a) nominal **(b)** optimized

Figure C.3: Background pattern comparison for different EMCS settings. Center of background distribution for the nominal (optimized) EMCS setting is at $x = -1.5765$ mm and $y = 1.625\,41$ mm ($x = -1.559\,73$ mm and $y = 1.419\,03$ mm).

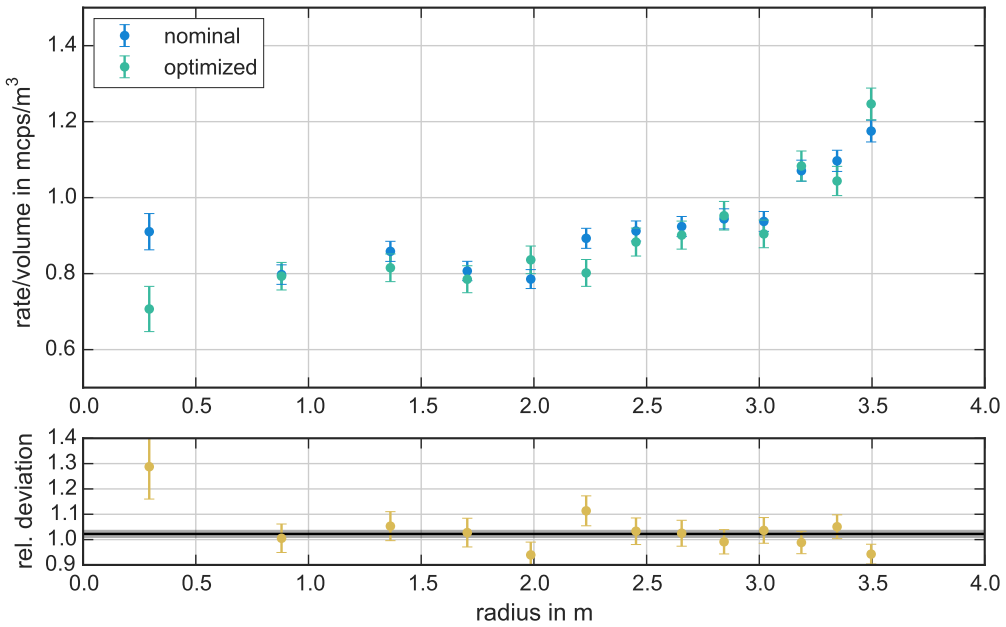

Figure C.4: Radial background distribution for different EMCS settings in a ring-wise representation (table 5.6). In the upper plot the measurements with −100 V offset on the inner electrode are shown. In the lower plot the relative deviation nominal/optimized EMCS setting is shown. With a factor of 1.022 ± 0.014 a minimal reduction is observed.

Table C.3: Background studies for EMCS settings. Column EMCS indicates the setting were "std" ("opt") corresponds to the nominal (optimized) setting. Column IE common is the potential difference of the inner electrode to a vessel potential. The count rate is given for the whole FPD waver in the ROI of about 18.6 keV. For a constant ROI the vessel potential was set to −18.5 kV or −18.595 kV depending on the IE common setting. The steep cones have an additional positive offset of 3 V relative to IE common.

EMCS	volume (m^3)	IE common (V)	rate (mcps)	rate/volume (mcps/m^3)
std	562.5	−100	528 ± 4	0.939 ± 0.008
std	562.5	−5	627 ± 4	1.114 ± 0.008
opt	562.2	−100	518 ± 6	0.922 ± 0.011
opt	562.2	−5	626 ± 6	1.114 ± 0.011

Bibliography

[Aad12] G. Aad et al.: 'Observation of a new particle in the search for the Standard Model Higgs boson with the {ATLAS} detector at the {LHC}'. In*Physics Letters B* (2012), vol. 716(1): pp. 1–29. doi: 10.1016/j.physletb.2012.08.020 (cit. on p. 2).

[Aar15] M. G. Aartsen et al.: 'Determining neutrino oscillation parameters from atmospheric muon neutrino disappearance with three years of IceCube DeepCore data'. In*Phys. Rev. D* (7 Apr. 2015), vol. 91: p. 072004. doi: 10.1103/PhysRevD.91.072004 (cit. on p. 6).

[Abd02] J. N. Abdurashitov et al.: 'Solar neutrino flux measurements by the Soviet-American gallium experiment (SAGE) for half the 22-year solar cycle'. In*Journal of Experimental and Theoretical Physics* (2002), vol. 95(2): pp. 181–193. doi: 10.1134/1.1506424 (cit. on p. 3).

[Abe13] K. Abe et al.: 'Evidence for the Appearance of Atmospheric Tau Neutrinos in Super-Kamiokande'. In*Phys. Rev. Lett.* (18 May 2013), vol. 110: p. 181802. doi: 10.1103/PhysRevLett.110.181802 (cit. on p. 6).

[Abe15] K. Abe et al.: 'Measurements of neutrino oscillation in appearance and disappearance channels by the T2K experiment with 6.6×10^{20} protons on target'. In*Phys. Rev. D* (7 Apr. 2015), vol. 91: p. 072010. doi: 10.1103/PhysRevD.91.072010 (cit. on pp. 6, 7).

[Abe12] Y. Abe et al.: 'Reactor $\overline{\nu}_e$ disappearance in the Double Chooz experiment'. In*Phys. Rev. D* (5 Sept. 2012), vol. 86: p. 052008. doi: 10.1103/PhysRevD.86.052008 (cit. on p. 7).

[Ada14] Birgit Adams: *Demagnetization of steel.* 27. Collaboration Meeting: Parallel Session A1. KATRIN collaboration internal. https://fuzzy.fzk.de/bscw/bscw.cgi/935697, Oct. 2014 (cit. on p. 90).

[Ada15] Birgit Adams: 'Untersuchung magnetischer Materialien und Inbetriebnahme der Magnetfeldüberwachung am KATRIN-Hauptspektrometer'. https://fuzzy.fzk.de/bscw/bscw.cgi/d975195/mth-adams_birgit.pdf. MA thesis. KIT / IEKP, 2015 (cit. on pp. 51, 59, 60, 90, 93, 107).

[Ada16a] P. Adamson et al.: 'First Measurement of Electron Neutrino Appearance in NOvA'. In*Phys. Rev. Lett.* (15 Apr. 2016), vol. 116: p. 151806. doi: 10.1103/PhysRevLett.116.151806 (cit. on p. 7).

[Ada16b] P. Adamson et al.: 'First measurement of muon-neutrino disappearance in NOvA'. In*Phys. Rev. D* (5 Mar. 2016), vol. 93: p. 051104. doi: 10.1103/PhysRevD.93.051104 (cit. on p. 7).

[Ada13] P. Adamson et al.: 'Measurement of Neutrino and Antineutrino Oscillations Using Beam and Atmospheric Data in MINOS'. In*Phys. Rev. Lett.* (25 June 2013), vol. 110: p. 251801. doi: 10.1103/PhysRevLett.110.251801 (cit. on p. 6).

[Aga15] N. Agafonova et al.: 'Discovery of τ Neutrino Appearance in the CNGS Neutrino Beam with the OPERA Experiment'. In*Phys. Rev. Lett.* (12 Sept. 2015), vol. 115: p. 121802. doi: 10.1103/PhysRevLett.115.121802 (cit. on p. 6).

[Ago13] M. Agostini et al.: 'Results on Neutrinoless Double-β Decay of ^{76}Ge from Phase I of the GERDA Experiment'. In*Phys. Rev. Lett.* (12 Sept. 2013), vol. 111: p. 122503. doi: 10.1103/PhysRevLett.111.122503 (cit. on p. 11).

[Aha13] B. Aharmim et al.: 'Combined analysis of all three phases of solar neutrino data from the Sudbury Neutrino Observatory'. In*Phys. Rev. C* (2 Aug. 2013), vol. 88: p. 025501. doi: 10.1103/PhysRevC.88.025501 (cit. on p. 6).

[Aha05] B. Aharmim et al.: 'Electron energy spectra, fluxes, and day-night asymmetries of ^{8}B solar neutrinos from measurements with NaCl dissolved in the heavy-water detector at the Sudbury Neutrino Observatory'. In*Phys. Rev. C* (5 Nov. 2005), vol. 72: p. 055502. doi: 10.1103/PhysRevC.72.055502 (cit. on p. 4).

[Ahn12] J. K. Ahn et al.: 'Observation of Reactor Electron Antineutrinos Disappearance in the RENO Experiment'. In*Phys. Rev. Lett.* (19 May 2012), vol. 108: p. 191802. doi: 10.1103/PhysRevLett.108.191802 (cit. on p. 7).

[Ahn06] M. H. Ahn et al.: 'Measurement of neutrino oscillation by the K2K experiment'. In*Phys. Rev. D* (7 Oct. 2006), vol. 74: p. 072003. doi: 10.1103/PhysRevD.74.072003 (cit. on p. 6).

[All97] W.W.M. Allison et al.: 'Measurement of the atmospheric neutrino flavour composition in Soudan 2'. In*Physics Letters B* (1997), vol. 391(3–4): pp. 491–500. doi: 10.1016/S0370-2693(96)01609-7 (cit. on p. 6).

[Alt03] Guido Altarelli and Klaus Winter: *Neutrino Mass*. Springer Tracts in Modern Physics. Heidelberg: Springer, 2003 (cit. on pp. 1, 12).

[Alt05] M. Altmann et al.: 'Complete results for five years of {GNO} solar neutrino observations'. In*Physics Letters B* (2005), vol. 616(3–4): pp. 174–190. doi: 10.1016/j.physletb.2005.04.068 (cit. on p. 3).

[Ams15] J.F. Amsbaugh et al.: 'Focal-plane detector system for the KATRIN experiment'. In*Nuclear Instruments and Methods in Physics Research Section A: Accelerators, Spectrometers, Detectors and Associated Equipment* (2015), vol. 778: pp. 40–60. doi: 10.1016/j.nima.2014.12.116 (cit. on pp. 31, 40, 48).

[Ams07] C. Amsler: 'Kern- und Teilchenphysik'. In*vdf Hochschulverlag AG an der ETH Zürich* (2007), vol. (paperback) (cit. on p. 5).

[An12] F. P. An et al.: 'Observation of Electron-Antineutrino Disappearance at Daya Bay'. In*Phys. Rev. Lett.* (17 Apr. 2012), vol. 108: p. 171803. DOI: 10.1103/PhysRevLett.108.171803 (cit. on p. 7).

[Ana04] Analog Devices Inc.: *AD22100 Voltage Output Temperature Sensor with Signal Conditioning*. http://www.analog.com/media/en/technical-documentation/data-sheets/AD22100.pdf. 2004 (cit. on p. 51).

[And07] E. Andreotti et al.: 'MARE, Microcalorimeter Arrays for a Rhenium Experiment: A detector overview'. In*Nuclear Instruments and Methods in Physics Research A* (Mar. 2007), vol. 572: pp. 208–210. DOI: 10.1016/j.nima.2006.10.198 (cit. on p. 13).

[Ant13] Marco Antoni: 'Entwicklung eines Sensornetzes zur kontinuierlichen Magnetfeldüberwachung am KATRIN Hauptspektrometer'. https://fuzzy.fzk.de/bscw/bscw.cgi/d875150/dth-antoni_marco.pdf. Diploma thesis. KIT/IEKP, 2013 (cit. on pp. 54, 55).

[Are16] M. Arenz et al.: 'Commissioning of the vacuum system of the KATRIN Main Spectrometer'. In*Journal of Instrumentation* (2016), vol. 11(04): P04011. DOI: 10.1088/1748-0221/11/04/P04011 (cit. on pp. 30, 35, 38).

[Ase00] V.N. Aseev et al.: 'Energy loss of 18 keV electrons in gaseous T and quench condensed D films'. In*The European Physical Journal D - Atomic, Molecular, Optical and Plasma Physics* (2000), vol. 10(1): pp. 39–52. DOI: 10.1007/s100530050525 (cit. on p. 169).

[Aug12] M. Auger et al.: 'Search for Neutrinoless Double-Beta Decay in ^{136}Xe with EXO-200'. In*Phys. Rev. Lett.* (3 July 2012), vol. 109: p. 032505. DOI: 10.1103/PhysRevLett.109.032505 (cit. on p. 11).

[Bab14] Martin Babutzka: 'Design and development for the Rearsection of the KATRIN experiment'. http://d-nb.info/1067496831/34. PhD thesis. KIT/IEKP, 2014 (cit. on pp. 24, 28).

[Bab10] Martin Babutzka: 'Untersuchung eines verfahrbaren Monitordetektors zur Überwachung der Aktivität des Beta-Zerfalls in der kryogenen Pumpstrecke des KATRIN-Experiments'. https://www.katrin.kit.edu/publikationen/dth-babutzka.pdf. Diploma thesis. KIT/IEKP, 2010 (cit. on p. 29).

[Bab12] M. Babutzka et al.: 'Monitoring of the operating parameters of the KATRIN Windowless Gaseous Tritium Source'. In*New Journal of Physics* (2012), vol. 14(10): p. 103046. DOI: 10.1088/1367-2630/14/10/103046 (cit. on p. 27).

[Bah64a] John N. Bahcall: 'Solar Neutrino Cross Sections and Nuclear Beta Decay'. In*Phys. Rev.* (1B July 1964), vol. 135: B137–B146. DOI: 10.1103/PhysRev.135.B137 (cit. on p. 2).

[Bah64b] John N. Bahcall: 'Solar Neutrinos. I. Theoretical'. In*Phys. Rev. Lett.* (11 Mar. 1964), vol. 12: pp. 300–302. DOI: 10.1103/PhysRevLett.12.300 (cit. on p. 2).

[Bah95] John N. Bahcall, M. H. Pinsonneault, and G. J. Wasserburg: 'Solar models with helium and heavy-element diffusion'. In *Rev. Mod. Phys.* (4 Oct. 1995), vol. 67: pp. 781–808. DOI: 10.1103/RevModPhys.67.781 (cit. on p. 3).

[Bah05] John N. Bahcall, Aldo M. Serenelli, and Sarbani Basu: 'New Solar Opacities, Abundances, Helioseismology, and Neutrino Fluxes'. In *The Astrophysical Journal Letters* (2005), vol. 621(1): p. L85. DOI: 10.1086/428929 (cit. on pp. 3, 4).

[Bar13a] J. Barrett, F. Harms, M. Kraus, and J. Schwarz: *Transmission at high-surplus energies*. ELOG: SDS-Measurements Phase 1, ID: 252. KATRIN collaboration internal. https://neutrino.ikp.kit.edu:8080/SDS-Measurements/252, 2013 (cit. on p. 157).

[Bar16a] John Barrett: 'A Spatially Resolved Study of the KATRIN Main Spectrometer Using a Novel Fast Multipole Method'. to be published. PhD thesis. Massachusetts Institute of Technology, 2016 (cit. on p. 163).

[Bar16b] John Barrett: *Particle simulations in three dimensional models with Kassiopeia*. 30. Collaboration Meeting: Parallel Session 2B. KATRIN collaboration internal. https://fuzzy.fzk.de/bscw/bscw.cgi/1008467?op=preview&back_url=20894, Mar. 2016 (cit. on p. 141).

[Bar14] J. Barrett et al.: *Results of the first KATRIN SDS measurement phase*. internal KATRIN document. https://fuzzy.fzk.de/bscw/bscw.cgi/d875500/SDSPhase1Report.pdf, 2014 (cit. on pp. 89, 90).

[Bar13b] Bartington Instruments: *Mag-03: Three-Axis Magnetic Field Sensors*. http://www.bartington.com/Literaturepdf/Datasheets/Mag-03%20DS0013.pdf, 2013 (cit. on pp. 51, 54).

[Bau13a] Stephan Bauer: 'Energy calibration and stability monitoring of the KATRIN experiment'. http://repositorium.uni-muenster.de/document/miami/da3d6759-9202-4b68-bb80-711f52b208d8/diss_bauer_stephan.pdf. PhD thesis. University Münster, 2013 (cit. on pp. 29, 38).

[Bau13b] S. Bauer et al.: 'Next generation KATRIN high precision voltage divider for voltages up to 65kV'. In *Journal of Instrumentation* (2013), vol. 8(10): P10026. DOI: 10.1088/1748-0221/8/10/P10026 (cit. on p. 30).

[Bay09] Bayrische Kabelwerke AG: *Cable Data Sheet Bayka: Datenblatt Nr. 47 903 00*. KATRIN collaboration internal. https://fuzzy.fzk.de/bscw/bscw.cgi/d898539/Cable%20Data%20Sheet%20Bayka.pdf, 2009 (cit. on pp. 41, 72).

[Bea80] G Beamson, H Q Porter, and D W Turner: 'The collimating and magnifying properties of a superconducting field photoelectron spectrometer'. In *Journal of Physics E: Scientific Instruments* (1980), vol. 13(1). http://stacks.iop.org/0022-3735/13/i=1/a=018: p. 64 (cit. on pp. 14, 15).

[Bec92] R. Becker-Szendy et al.: 'Electron- and muon-neutrino content of the atmospheric flux'. In *Phys. Rev. D* (9 Nov. 1992), vol. 46: pp. 3720–3724. DOI: 10.1103/PhysRevD.46.3720 (cit. on p. 6).

[Bec01] Henri Becquerel: 'The Radio Activity of Matter'. In*Nature* (1901), vol. 63: pp. 396–398. doi: 10.1038/063396d0 (cit. on p. 1).

[Beg14] Armen Beglarian: *Slow Control System (news, upgrades)*. 27. Collaboration Meeting: Parallel Session C1. KATRIN collaboration internal. https://fuzzy.fzk.de/bscw/bscw.cgi/936057, Oct. 2014 (cit. on p. 49).

[Beh14] J. Behrens: *Report on the e-gun test measurements at the monitor spectrometer*. https://nuserv.uni-muenster.de/svn/katrin/SDS_commissioning/CommissioningDocument/SDSphase2/MeasurementReports/Egun_MonSpec/. KATRIN collaboration internal. 2014 (cit. on pp. 31, 44, 45, 133, 136, 150).

[Beh15a] J. Behrens, M. Erhard, M. Kraus, P. Ranitzsch, and D. Winzen: *e-gun commissioning*. ELOG: SDS-Measurements Phase 2, ID: 88. KATRIN collaboration internal. https://neutrino.ikp.kit.edu:8080/SDS-Measurements+Phase+2/88, 2015 (cit. on p. 139).

[Beh16] Jan Behrens: 'Background Reduction with a magnetic pulse and development of an electron gun for the KATRIN Experiment'. in preparation. PhD thesis. University Münster, 2016 (cit. on pp. 44, 77, 79, 119, 128, 130, 136, 139, 150, 154, 156–158, 160).

[Beh15b] Jan Behrens: *Magnetic Pulse - first measurement results*. 28. Collaboration Meeting: Parallel Session B1. KATRIN collaboration internal. https://fuzzy.fzk.de/bscw/bscw.cgi/d950152/95-TRP-5809-B1.1-JBehrens.pdf, Mar. 2015 (cit. on p. 77).

[Bel14a] G. Bellini et al.: 'Final results of Borexino Phase-I on low-energy solar neutrino spectroscopy'. In*Phys. Rev. D* (11 June 2014), vol. 89: p. 112007. doi: 10.1103/PhysRevD.89.112007 (cit. on p. 6).

[Bel14b] G. Bellini et al.: 'Neutrinos from the primary proton-proton fusion process in the Sun'. In*Nature* (2014), vol. 512: pp. 383–386. doi: 10.1038/nature13702 (cit. on p. 6).

[Ber05] Ludwig Bergmann and Clemens Schaefer: *Lehrbuch der Experimentalphysik*. Ed. by Rainer [Hrsg.] Kassing and Stefan Blügel. 2., überarb. Aufl. Vol. 6: Festkörper. Gb. : EUR 78.00, sfr 125.00. Berlin: de Gruyter, 2005 (cit. on p. 150).

[Ber12] T. Bergmann et al.: 'FPGA-based multi-channel DAQ systems with external PCI express link to GPU compute servers'. In*Real Time Conference (RT), 2012 18th IEEE-NPSS*. June 2012: pp. 1–5. doi: 10.1109/RTC.2012.6418197 (cit. on p. 48).

[Bes11] Bastian Beskers: 'Messung und Optimierung der Eigenschaften des Monitordetektors für keV-Elektronen in der kryogenen Pumpstrecke bei KATRIN neutrino experiment'. internal: https://fuzzy.fzk.de/bscw/bscw.cgi/733800?op=preview&back_url=859717. Diploma thesis. KIT/IEKP, 2011 (cit. on p. 29).

[Bet34] H. Bethe and R. Peierls: 'The Neutrino'. In*Nature* (1934), vol. 133: p. 532. doi: 10.1038/133532a0 (cit. on p. 2).

[Bet14] Betoule, M. et al.: 'Improved cosmological constraints from a joint analysis of the SDSS-II and SNLS supernova samples'. In*A&A* (2014), vol. 568: A22. doi: 10.1051/0004-6361/201423413 (cit. on p. 10).

[Beu11] Florian Beutler et al.: 'The 6dF Galaxy Survey: baryon acoustic oscillations and the local Hubble constant'. In*Monthly Notices of the Royal Astronomical Society* (2011), vol. 416(4): pp. 3017–3032. doi: 10.1111/j.1365-2966.2011.19250.x (cit. on p. 10).

[BIL12] S. M. BILENKY and C. GIUNTI: 'NEUTRINOLESS DOUBLE-BETA DECAY: A BRIEF REVIEW'. In*Modern Physics Letters A* (2012), vol. 27(13): p. 1230015. doi: 10.1142/S0217732312300157 (cit. on p. 7).

[Bod11] Tobias Bode: 'Optimierung des 2-Phasen-Kühlkonzepts für den WGTS Demonstrator von KATRIN'. Diploma thesis. KIT/IEKP, 2011 (cit. on p. 27).

[Boe94] W De Boer: 'Grand unified theories and supersymmetry in particle physics and cosmology'. In*Progress in Particle and Nuclear Physics* (1994), vol. 33: pp. 201–301. doi: 10.1016/0146-6410(94)90045-0 (cit. on p. 9).

[Bog00] J Boger et al.: 'The Sudbury Neutrino Observatory'. In*Nuclear Instruments and Methods in Physics Research Section A: Accelerators, Spectrometers, Detectors and Associated Equipment* (2000), vol. 449(1–2): pp. 172–207. doi: 10.1016/S0168-9002(99)01469-2 (cit. on p. 4).

[Bot12] Richard Bottesch: 'Set-up of the motion control and characterization of the ablation laser for the condensed 83mKr conversion electron source of the KATRIN experiment'. http://www.uni-muenster.de/Physik.KP/AGWeinheimer/Files/theses/Diplom_Richard_Bottesch.pdf. Diploma thesis. University Münster, 2012 (cit. on p. 29).

[Bru97] Rene Brun and Fons Rademakers: '{ROOT} — An object oriented data analysis framework'. In*Nuclear Instruments and Methods in Physics Research Section A: Accelerators, Spectrometers, Detectors and Associated Equipment* (1997), vol. 389(1–2). New Computing Techniques in Physics Research V: pp. 81–86. doi: 10.1016/S0168-9002(97)00048-X (cit. on pp. 48, 49).

[Cab63] Nicola Cabibbo: 'Unitary Symmetry and Leptonic Decays'. In*Phys. Rev. Lett.* (12 June 1963), vol. 10: pp. 531–533. doi: 10.1103/PhysRevLett.10.531 (cit. on p. 5).

[Cha14] J. Chadwick: 'Intensitätsverteilung im magnetischen Spektrum der β-Strahlen von Radium B + C / The Intensity Distribution in Magnetic Spectrum of β-Rays of Radium B + C'. In*Verhandl. Dtsch. phys. Ges.* (1914), vol. 16: p. 383 (cit. on p. 1).

[Cha12] S. Chatrchyan et al.: 'Observation of a new boson at a mass of 125 GeV with the {CMS} experiment at the {LHC}'. In*Physics Letters B* (2012), vol. 716(1): pp. 30–61. doi: 10.1016/j.physletb.2012.08.021 (cit. on p. 2).

[Com15] Rodolphe Combe: 'Design optimization of the KATRIN transport section and investigation of related background contribution'. https://fuzzy.fzk.de/bscw/bscw.cgi/d964402/mth_combe.pdf. MA thesis. KIT / UJF Grenoble, 2015 (cit. on pp. 24, 89).

[Cor14] Thomas J. Corona: 'Methodology and Application of High Performance Electrostatic Field Simulation in the KATRIN Experiment'. http://search.proquest.com/docview/1648168745. PhD thesis. University of North Carolina, Chapel Hill, 2014 (cit. on p. 37).

[Cos93] E. Cosulich, F. Gatti, and S. Vitale: 'Further results on μ-calorimeters with superconducting absorber'. In*Journal of Low Temperature Physics* (1993), vol. 93(3): pp. 263–268. doi: 10.1007/BF00693430 (cit. on p. 13).

[Cow56] C. L. Cowan, F. Reines, F. B. Harrison, H. W. Kruse, and A. D. McGuire: 'Detection of the Free Neutrino: a Confirmation'. In*Science* (1956), vol. 124(3212): pp. 103–104. doi: 10.1126/science.124.3212.103 (cit. on p. 2).

[Cry03] Cryogenic Ltd.: *4.5 Tesla Cryogen-Free Magnet System. Job number: 2054*. KATRIN collaboration internal. https://fuzzy.fzk.de/bscw/bscw.cgi/d966341/BAL_Cryonenics_PS-Magnets.pdf, 2003 (cit. on p. 40).

[Cry11] Cryomagnetics Inc. and Laura I. Bodine: *User's Manual, 6T Detector and Pinch Superconducting Magnet Pair for University of Washington (KATRIN)*. KATRIN collaboration internal. https://fuzzy.fzk.de/bscw/bscw.cgi/d653154/Magnet%20User%27s%20Manual.pdf, 2011 (cit. on p. 40).

[Dan62] G. Danby, J-M. Gaillard, K. Goulianos, L. M. Lederman, N. Mistry, M. Schwartz, and J. Steinberger: 'Observation of High-Energy Neutrino Reactions and the Existence of Two Kinds of Neutrinos'. In*Phys. Rev. Lett.* (1 July 1962), vol. 9: pp. 36–44. doi: 10.1103/PhysRevLett.9.36 (cit. on p. 2).

[Dav64] Raymond Davis: 'Solar Neutrinos. II. Experimental'. In*Phys. Rev. Lett.* (11 Mar. 1964), vol. 12: pp. 303–305. doi: 10.1103/PhysRevLett.12.303 (cit. on p. 3).

[Del13] Delta Elektronika: *ISO AMP - External module -four channel analog isolation amplifier*. http://www.delta-elektronika.nl/upload/dts_iso-amp-module.pdf, 2013 (cit. on p. 75).

[Del12] Delta Elektronika: *SM 3000 - Series 3000 W DC POWER SUPPLIES*. http://www.delta-elektronika.nl/upload/dts_sm3000.pdf, Sept. 2012 (cit. on pp. 43, 44).

[Día11] Marta Ubieto Díaz: 'Off-line commissioning of a non-destructive FT-ICR detection system for monitoring the ion concentration in the KATRIN beamline'. http://d-nb.info/1070584215/34. PhD thesis. Ruperto-Carola university of Heidelberg, 2011 (cit. on p. 29).

[DiS70] T. H. DiStefano and D. T. Pierce: 'Energy Resolution of the Photoemission Analyzer'. In*Review of Scientific Instruments* (1970), vol. 41(2): pp. 180–188. doi: 10.1063/1.1684464 (cit. on pp. 130, 133).

[Dre13] G. Drexlin, V. Hannen, S. Mertens, and C. Weinheimer: 'Current Direct Neutrino Mass Experiments'. In*Advances in High Energy Physics* (2013), vol. 2013(293986): p. 39. doi: 10.1155/2013/293986 (cit. on p. 12).

[DSc03] E. Rutherford M.A. D.Sc.: 'XV. The magnetic and electric deviation of the easily absorbed rays from radium'. In*Philosophical Magazine Series 6* (1903), vol. 5(26): pp. 177–187. doi: 10.1080/14786440309462912 (cit. on p. 1).

[Dvo11] R. Dvornický, K. Muto, F. Šimkovic, and A. Faessler: 'Absolute mass of neutrinos and the first unique forbidden β decay of ^{187}Re'. In*Phys. Rev. C* (4 Apr. 2011), vol. 83: p. 045502. doi: 10.1103/PhysRevC.83.045502 (cit. on p. 13).

[Dwy15] D. A. Dwyer: 'Antineutrinos from nuclear reactors: recent oscillation measurements'. In*New Journal of Physics* (2015), vol. 17(2): p. 025003. doi: 10.1088/1367-2630/17/2/025003 (cit. on p. 7).

[Dyb14] Stephan Dyba, V. Hannen, H.-W. Ortjohann, and C. Weinheimer: *Inspection and repair of short-circuits in the inner electrode*. 27. Collaboration Meeting: Parallel Session A1. KATRIN collaboration internal. https://fuzzy.fzk.de/bscw/bscw.cgi/d936186/95-TRP-5736-S3-SDyba.pdf, Oct. 2014 (cit. on p. 39).

[Eic08] F. Eichelhardt, B. Bornschein, L. Bornschein, O. Kazachenko, N. Kernert, and M. Sturm: 'First Tritium Results of the KATRIN Test Experiment Trap'. In*Fusion Science and Technology* (2008), vol. 54(2). http://www.new.ans.org/pubs/journals/fst/a_1890: pp. 615–618 (cit. on p. 29).

[Ein05] A. Einstein: 'Über einen die Erzeugung und Verwandlung des Lichtes betreffenden heuristischen Gesichtspunkt'. In*Annalen der Physik* (1905), vol. 322(6): pp. 132–148. doi: 10.1002/andp.19053220607 (cit. on p. 130).

[Eli15] S. Eliseev et al.: 'Direct Measurement of the Mass Difference of ^{163}Ho and ^{163}Dy Solves the Q-Value Puzzle for the Neutrino Mass Determination'. In*Phys. Rev. Lett.* (6 Aug. 2015), vol. 115: p. 062501. doi: 10.1103/PhysRevLett.115.062501 (cit. on p. 13).

[Ell02] Steven R. Elliott and Petr Vogel: 'DOUBLE BETA DECAY'. In*Annual Review of Nuclear and Particle Science* (2002), vol. 52(1): pp. 115–151. doi: 10.1146/annurev.nucl.52.050102.090641 (cit. on p. 11).

[Erh15a] M. Erhard, J. Behrens, and H.-W. Ortjohann: *eGun Alignment*. ELOG: main-spectrometer, ID: 1564. KATRIN collaboration internal. https://neutrino.ikp.kit.edu:8080/main-spectrometer/1564, 2015 (cit. on pp. 46, 59).

[Erh14a] Moritz Erhard: *EMCS optimization*. ELOG: SDS-Measurements Phase 2, ID: 56. KATRIN collaboration internal. https://neutrino.ikp.kit.edu:8080/SDS-Measurements+Phase+2/56, 2014 (cit. on p. 219).

[Erh14b] Moritz Erhard: *magnetic field and potential optimization for SDS-II*. 27. Collaboration Meeting: Plenary Session 5. KATRIN collaboration internal. https://fuzzy.fzk.de/bscw/bscw.cgi/d935943/95-TRP-5724-B1-MErhard.pdf, Oct. 2014 (cit. on p. 68).

[Erh14c] Moritz Erhard: *magnetic field measurements*. 26. Collaboration Meeting: Parallel Session A1. KATRIN collaboration internal. https://fuzzy.fzk.de/bscw/bscw.cgi/876388, Mar. 2014 (cit. on p. 90).

[Erh15b] Moritz Erhard: *Optimized MAC-E-filter and magnetic field monitoring*. 28. Collaboration Meeting: Parallel Session B1. KATRIN collaboration internal. https://fuzzy.fzk.de/bscw/bscw.cgi/d950181/95-TRP-5812-B1.4-MErhard.pdf, Mar. 2015 (cit. on p. 56).

[Erh15c] Moritz Erhard: *Single Minimum Measurement*. ELOG: SDS-Measurements Phase 2, ID: 81. KATRIN collaboration internal. https://neutrino.ikp.kit.edu:8080/SDS-Measurements+Phase+2/81, 2015 (cit. on pp. 217, 218).

[Erh12] Moritz Erhard: 'Untersuchung der Langzeitstabilität des nuklearen Standards für die Energieskala des KATRIN-Experiments'. http://www.katrin.kit.edu/publikationen/dth-erhard.pdf. Diploma thesis. KIT/IEKP, 2012 (cit. on p. 32).

[Erh15d] Moritz Erhard, Philipp Ranitzsch, Oliver Rest, Jan Behrens, Daniel Hilk, Martin Slezak, and John Barrett: *TF Scan radial*. ELOG: SDS-Measurements Phase 2, ID: 95. KATRIN collaboration internal. https://neutrino.ikp.kit.edu:8080/SDS-Measurements+Phase+2/95, 2015 (cit. on pp. 137, 147).

[Erh15e] Moritz Erhard, Enomoto Sanshiro, Jan Behrens, Philipp Ranitzsch, and Johannes Schwarz: *Detector response and backscattering*. ELOG: SDS-Measurements Phase 2, ID: 94. KATRIN collaboration internal. https://neutrino.ikp.kit.edu:8080/SDS-Measurements+Phase+2/94, 2015 (cit. on p. 31).

[Erh14d] Moritz Erhard et al.: 'High-voltage monitoring with a solenoid retarding spectrometer at the KATRIN experiment'. In*Journal of Instrumentation* (2014), vol. 9(6): P06022. doi: 10.1088/1748-0221/9/06/P06022 (cit. on pp. 31, 32).

[Erh16] Moritz Erhard et al.: 'Technical Design and Commissioning of the KATRIN Large Volume Air Coil System'. In*JINST* (2016), vol. in preparation (cit. on pp. 39, 44, 49, 65).

[FAR14] FARO Technologies Inc.: *FaroArm*. http://www.faro.com/en-us/products/metrology/measuring-arm-faroarm/overview, 2014 (cit. on p. 58).

[Fer34] E. Fermi: 'Versuch einer Theorie der β-Strahlen. I'. In*Zeitschrift für Physik* (1934), vol. 88(3): pp. 161–177. doi: 10.1007/BF01351864 (cit. on pp. 1, 11).

[Fis14] Sebastian Fischer: 'Commissioning of the KATRIN Raman system and durability studies of optical coatings in glove box and tritium atmospheres'. http://d-nb.info/1061069125/34. PhD thesis. KIT/IEKP, 2014 (cit. on p. 27).

[Fix09] D. J. Fixsen: 'The Temperature of the Cosmic Microwave Background'. In*The Astrophysical Journal* (2009), vol. 707(2): p. 916. doi: 10.1088/0004-637X/707/2/916 (cit. on p. 9).

[Flu06] Fluke Corporation: *Fluke 8845A/8846A Digital Multimeters - Precision and versatility for bench or systems applications*. https://d3fdwrtpsinh7j.cloudfront.net/Docs/datasheet/flu_884xa.pdf, 2006 (cit. on p. 46).

[Fra15] F. Fraenkle and P. Doe: *calibration run after Pinch magnet swap*. ELOG: SDS-Measurements Phase 2, ID: 143. KATRIN collaboration internal. https://neutrino.ikp.kit.edu:8080/SDS-Measurements+Phase+2/143, 2015 (cit. on p. 105).

[Frä10] Florian Fränkle: 'Background Investigations of the KATRIN Prespectrometer'. http://digbib.ubka.uni-karlsruhe.de/volltexte/1000019392. PhD thesis. KIT/IEKP, 2010 (cit. on pp. 24, 30, 45).

[Frä14] F.M. Fränkle et al.: 'Penning discharge in the KATRIN pre-spectrometer'. In*Journal of Instrumentation* (2014), vol. 9(7): P07028. doi: 10.1088/1748-0221/9/07/P07028 (cit. on p. 26).

[Frä11] F.M. Fränkle et al.: 'Radon induced background processes in the KATRIN pre-spectrometer'. In*Astroparticle Physics* (2011), vol. 35(3): pp. 128–134. doi: 10.1016/j.astropartphys.2011.06.009 (cit. on pp. 30, 153).

[FUG15] FUG Elektronik GmbH: *Power supplies for superconducting coils Series NTS to 65 V / to 10000 A*. http://www.fug-elektronik.de/en/products/superconductor/nts.html, 2015 (cit. on p. 40).

[FuG15a] FuG Elektronik GmbH: *Examples for customer specific power supplies*. http://www.fug-elektronik.de/en/files/8800/Customized_power_supplies.pdf, 2015 (cit. on p. 45).

[FuG15b] FuG Elektronik GmbH: *Medium voltage power supplies Series MCP from 125 V to 2000 V / 14 W to 15000 W*. http://www.fug-elektronik.de/en/files/132000/MCP_data_sheet.pdf, 2015 (cit. on p. 46).

[Fuk02] S. Fukuda et al.: 'Determination of solar neutrino oscillation parameters using 1496 days of Super-Kamiokande-I data'. In*Physics Letters B* (2002), vol. 539(3–4): pp. 179–187. doi: 10.1016/S0370-2693(02)02090-7 (cit. on pp. 4, 6).

[Fuk98] Y. Fukuda et al.: 'Evidence for Oscillation of Atmospheric Neutrinos'. In*Phys. Rev. Lett.* (8 Aug. 1998), vol. 81: pp. 1562–1567. doi: 10.1103/PhysRevLett.81.1562 (cit. on p. 6).

[Fuk96] Y. Fukuda et al.: 'Solar Neutrino Data Covering Solar Cycle 22'. In*Phys. Rev. Lett.* (9 Aug. 1996), vol. 77: pp. 1683–1686. doi: 10.1103/PhysRevLett.77.1683 (cit. on p. 3).

[Fur15] Daniel Lawrence Furse: 'Techniques for direct neutrino mass measurement utilizing tritium [beta]-decay'. https://dspace.mit.edu/handle/1721.1/99313. PhD thesis. MIT/Department of Physics, 2015 (cit. on p. 49).

[Gas14] L. Gastaldo et al.: 'The Electron Capture ^{163}Ho Experiment ECHo'. In*Journal of Low Temperature Physics* (2014), vol. 176(5): pp. 876–884. doi: 10.1007/s10909-014-1187-4 (cit. on p. 13).

[GFZ15] GFZ Helmholz centre Potsdam: *IGRF Declination Calculator*. IGRF Generation 12, 1900 - 2020. International Geomagnetic Reference Field. http://www.gfz-potsdam.de/en/section/earths-magnetic-field/services/igrf-declinaion-calculator/, June 2015 (cit. on p. 43).

[Gil10] W. Gil, J. Bonn, B. Bornschein, R. Gehring, O. Kazachenko, J. Kleinfeller, and S. Putselyk: 'The Cryogenic Pumping Section of the KATRIN Experiment'. In*IEEE Transactions on Applied Superconductivity* (2010), vol. 20(3): pp. 316–319. doi: 10.1109/TASC.2009.2038581 (cit. on p. 29).

[Glü13] F. Glück, G. Drexlin, B. Leiber, S. Mertens, A. Osipowicz, J. Reich, and N. Wandkowsky: 'Electromagnetic design of the large-volume air coil system of the KATRIN experiment'. In*New Journal of Physics* (2013), vol. 15(8): p. 083025. doi: 10.1088/1367-2630/15/8/083025 (cit. on pp. 24, 70).

[Glü14] Ferenc Glück: *Electromagnetic design of the magnetic material compensation system (MMCS)*. 26. Collaboration Meeting: Parallel Session A1. KATRIN collaboration internal. https://fuzzy.fzk.de/bscw/bscw.cgi/876388, Mar. 2014 (cit. on pp. 62, 104).

[Glü05] Ferenc Glück: *Steel in the KATRIN buildings and the magnetic field in the main spectrometer*. KATRIN collaboration internal. KIT/IEKP. http://fuzzy.fzk.de/bscw/bscw.cgi/d176563/steel_buildings_Glueck.pdf, 2005 (cit. on p. 104).

[Glü09] Ferenc Glück, Susanne Mertens, Alexander Osipowicz, Peter Plischke, Jan Reich, and Nancy Wandkowsky: *Design Document - Air Coil System & Magnetic Field Sensor System*. internal KATRIN document. KATRIN collaboration internal. http://fuzzy.fzk.de/bscw/bscw.cgi/d530439/Air%20Coil%20System%20and%20Magnetic%20Field%20Sensor%20System.pdf, Mar. 2009 (cit. on pp. 24, 50, 66, 67).

[Goe35] M. Goeppert-Mayer: 'Double Beta-Disintegration'. In*Phys. Rev.* (6 Sept. 1935), vol. 48: pp. 512–516. doi: 10.1103/PhysRev.48.512 (cit. on p. 10).

[Gör14] Stefan Görhardt: 'Background Reduction Methods and Vacuum Technology at the KATRIN Spectrometers'. http://nbn-resolving.org/urn:nbn:de:swb:90-380506. PhD thesis. KIT/IEKP, 2014 (cit. on pp. 30, 40).

[Gör10] Stefan Görhardt: 'Reduktion der durch Radon induzierten Untergrundprozesse in den KATRIN Spektrometern'. https://www.katrin.kit.edu/publikationen/dth-goerhardt.pdf. Diploma thesis. KIT/IEKP, 2010 (cit. on p. 30).

[Gou10] Johannes Goullon: 'Installation and commissioning of the monitor spectrometer'. http://www.katrin.kit.edu/publikationen/dth-goullon.pdf. Diploma thesis. KIT/IEKP, 2010 (cit. on p. 32).

[Gro15] Stefan Groh: 'Modeling of the response function and measurement of transmission properties of the KATRIN experiment'. http://digbib.ubka.uni-karlsruhe.de/volltexte/1000046546. PhD thesis. KIT/IEKP, 2015 (cit. on pp. 16, 18, 23, 24, 28, 35, 49, 68, 77, 119, 122, 127, 134, 141, 151, 161, 167, 169).

[Gro10] Stefan Groh: 'Untersuchung von UV-Laser induziertem Untergrund am KATRIN Vorspektrometer'. http://www.katrin.kit.edu/publikationen/dth-groh.pdf. Diploma thesis. KIT/IEKP, 2010 (cit. on pp. 24, 30).

[Gro] Stefan Groh et al.: 'Kassiopeia: A Modern, Extensible C++ Particle Tracking Package'. in preperation (cit. on p. 49).

[Gro13] S. Grohmann, T. Bode, M. Hötzel, H. Schön, M. Süsser, and T. Wahl: 'The thermal behaviour of the tritium source in KATRIN'. In *Cryogenics* (2013), vol. 55-56: pp. 5–11. doi: 10.1016/j.cryogenics.2013.01.001 (cit. on p. 27).

[Gro11] S. Grohmann, T. Bode, H. Schön, and M. Süsser: 'Precise temperature measurement at 30 K in the KATRIN source cryostat'. In *Cryogenics* (2011), vol. 51(8): pp. 438–445. doi: 10.1016/j.cryogenics.2011.05.001 (cit. on p. 27).

[Gro07] Group3 Technology Ltd.: *DTM-151 DIGITAL TESLAMETER with serial communications*. http://www.group3technology.com/vdb/document/51, 2007 (cit. on p. 153).

[Gum13] R. Gumbsheimer and J. Lichter: *KATRIN – Prüfung Luftspuleninnenradius*. KATRIN collaboration internal. https://fuzzy.fzk.de/bscw/bscw.cgi/d898608/Kontrollvermessung_Luftspule.pdf, 2013 (cit. on pp. 41, 94).

[Haa34] W.J. de Haas, J. de Boer, and G.J. van dën Berg: 'The electrical resistance of gold, copper and lead at low temperatures'. In *Physica* (1934), vol. 1(7): pp. 1115–1124. doi: 10.1016/S0031-8914(34)80310-2 (cit. on p. 80).

[Hab09] Florian Habermehl: 'Electromagnetic Measurements with the KATRIN Pre-Spectrometer'. http://d-nb.info/1014223032/34. PhD thesis. KIT/IEKP, 2009 (cit. on p. 30).

[Hac15] Moritz Hackenjos: 'Die differentielle Pumpstrecke des KATRIN-Experiments-Inbetriebnahme und Charakterisierung des supraleitenden Magnetsystems'. http://www.katrin.kit.edu/publikationen/MaT_Hackenjos.pdf. MA thesis. KIT / IEKP, 2015 (cit. on pp. 28, 29).

[Ham99] W. Hampel et al.: 'GALLEX solar neutrino observations: results for GALLEX IV'. In *Physics Letters B* (1999), vol. 447(1–2): pp. 127–133. doi: 10.1016/S0370-2693(98)01579-2 (cit. on p. 3).

[Han13a] V. Hannen, H.-W. Ortjohann, M. Zacher, and Ch. Weinheimer: *Electrical short circuits in the main spectrometer wire electrode*. KATRIN collaboration internal. https://fuzzy.fzk.de/bscw/bscw.cgi/d875473/430-doc-3-9001-shortcircuit_report.pdf, 2013 (cit. on p. 39).

[Han13b] V. Hannen et al.: *Main Spectrometer Electron-Gun Specification*. internal report. KATRIN collaboration internal. 2013 (cit. on p. 44).

[Har15a] F. Harms and F. Fraenkle: *measurement of intrinsic FPD background at nominal magnetic field*. ELOG: SDS-Measurements Phase 2, ID: 174. KATRIN collaboration internal. https://neutrino.ikp.kit.edu:8080/SDS-Measurements+Phase+2/174, 2015 (cit. on p. 216).

[Har12] Fabian Harms: 'Assembly and First Results of the KATRIN Focal-Plane Detector System at KIT'. http://www.katrin.kit.edu/publikationen/dth_Fabian_Harms.pdf. Diploma thesis. KIT/IEKP, 2012 (cit. on p. 31).

[Har15b] Fabian Thomas Harms: 'Characterization and minimization of background processes in the KATRIN main spectrometer'. PhD thesis. KIT/IEKP, 2015. doi: 10.5445/IR/1000050027 (cit. on pp. 30, 31, 38, 50, 59, 167, 184, 215, 216).

[Har09a] Julius Hartmann: *Calibration of the KATRIN monitoring magnetometers*. KATRIN collaboration internal. KIT/IPE. https://fuzzy.fzk.de/bscw/bscw.cgi/d578795/KATRIN_Calibration_Magnetometer_Documentation.pdf, 2009 (cit. on p. 51).

[Har09b] Julius Hartmann: *Status of the Multi-Point Low-Field Monitoring Magnetometer System*. 17. Collaboration Meeting: Parallel Session B1. KATRIN collaboration internal. https://fuzzy.fzk.de/bscw/bscw.cgi/578678, Oct. 2009 (cit. on p. 51).

[Hau13] Norman Haussmann: 'Development of Analysis Tools and Automatisation of Run Control for KATRIN'. http://www.katrin.kit.edu/publikationen/dth-Haussmann.pdf. Diploma thesis. KIT/IEKP, 2013 (cit. on p. 48).

[Hax13] W.C. Haxton, R.G. Hamish Robertson, and Aldo M. Serenelli: 'Solar Neutrinos: Status and Prospects'. In*Annual Review of Astronomy and Astrophysics* (2013), vol. 51(1): pp. 21–61. doi: 10.1146/annurev-astro-081811-125539 (cit. on p. 6).

[Hay14] William M. [Hrsg.] Haynes, ed.: *2014 - 2015*. CRC handbook of chemistry and physics ; 95. Boca Raton, Fla. [u.a.]: CRC Press, 2014 (cit. on p. 72).

[Hec12] Gerald Hechenblaikner et al.: 'Energy distribution and quantum yield for photoemission from air-contaminated gold surfaces under ultraviolet illumination close to the threshold'. In*Journal of Applied Physics* (2012), vol. 111(12), 124914. doi: 10.1063/1.4730638 (cit. on pp. 130, 133).

[Hel02] R.L. Helmer: 'First results from the Sudbury Neutrino Observatory'. In*Nuclear Physics B - Proceedings Supplements* (2002), vol. 111(1–3): pp. 122–127. doi: 10.1016/S0920-5632(02)01693-6 (cit. on p. 4).

[Her10] Jan Hergenhan: 'Das KATRIN-Luftspulensystem: Messungen des Feldverlaufs und Überwachung mit einem Sensorsystem'. https://fuzzy.fzk.de/bscw/bscw.cgi/d675956/dth-hergenhan.pdf. Diploma thesis. KIT/IEKP, 2010 (cit. on pp. 43, 44, 90).

[Hil16] Daniel Hilk: *New numerical integration routines in KEMField for high-accuracy field simulations*. 30. Collaboration Meeting: Plenary Extra 2. KATRIN collaboration internal. https://fuzzy.fzk.de/bscw/bscw.cgi/1007641?op=preview&back_url=1007512, Mar. 2016 (cit. on p. 146).

[Hil11] Björn Hillen: 'Untersuchung von Methoden zur Unterdrückung des Spektrometeruntergrunds beim KATRIN Experiment'. http://repositorium.uni-muenster.de/document/miami/1c6278eb-3176-4658-b37c-8133a3b12e3b/diss_hillen.pdf. PhD thesis. University Münster, 2011 (cit. on p. 59).

[Him15] Alexander Himmel: 'New Limits on Sterile Neutrino Mixing with Atmospheric Neutrinos'. In*Physics Procedia* (2015), vol. 61. 13th International Conference on Topics in Astroparticle and Underground Physics, {TAUP} 2013: pp. 612–618. doi: 10.1016/j.phpro.2014.12.060 (cit. on p. 8).

[Höt12] Markus Hötzel: 'Simulation and analysis of source-related effects for KATRIN'. http://d-nb.info/1029141932/34. PhD thesis. KIT/IEKP, 2012 (cit. on pp. 27, 168).

[How04] M.A. Howe, G.A. Cox, P.J. Harvey, F. McGirt, K. Rielage, J.F. Wilkerson, and J.M. Wouters: 'Sudbury neutrino observatory neutral current detector acquisition software overview'. In*Nuclear Science, IEEE Transactions* (2004), vol. 51(3): pp. 878–883. doi: 10.1109/TNS.2004.829527 (cit. on p. 48).

[How14] Mark Howe et al.: *ORCA webpage*. http://orca.physics.unc.edu/. 2014 (cit. on p. 48).

[Hsu76] T. Hsu and J. L. Hirshfield: 'Electrostatic energy analyzer using a nonuniform axial magnetic field'. In*Review of Scientific Instruments* (1976), vol. 47(2): pp. 236–238. doi: 10.1063/1.1134594 (cit. on p. 15).

[Hug08] Karen Hugenberg: 'Design of the electrode system of the KATRIN main spectrometer'. http://www.uni-muenster.de/Physik.KP/AGWeinheimer/theses/Diplom_Karen_Hugenberg.pdf. Diploma thesis. University Münster, 2008 (cit. on pp. 24, 30, 38).

[Jan15] Alexander Jansen: 'The Cryogenic Pumping Section of the KATRIN Experiment - Design Studies and Experiments for the Commissioning'. http://nbn-resolving.org/urn:nbn:de:swb:90-471467. PhD thesis. KIT/IEKP, 2015 (cit. on pp. 29, 81).

[Jr79] R. Davis Jr., J. C. Evans, and B. T. Cleveland: 'The solar neutrino problem'. In*AIP Conference Proceedings* (1979), vol. 52(1): pp. 17–27. doi: 10.1063/1.31802 (cit. on p. 3).

[Käf12] Wolfgang Käfer: 'Sensitivity studies of the KATRIN experiment'. http://nbn-resolving.org/urn:nbn:de:swb:90-260214. PhD thesis. KIT/IEKP, 2012 (cit. on p. 168).

[KAT05] KATRIN collaboration: 'KATRIN Design Report'. In*FZKA scientific report* (2005), vol. 7090. http://bibliothek.fzk.de/zb/berichte/FZKA7090.pdf (cit. on pp. 15, 16, 24, 33, 81, 167, 169, 170, 173).

[Kir69] T. Kirsten and H.W. Müller: 'Observation of 82Se double-beta decay in selenium ores'. In*Earth and Planetary Science Letters* (1969), vol. 6(4): pp. 271–274. doi: 10.1016/0012-821X(69)90167-8 (cit. on p. 10).

[Kle14] Marco Kleesiek: 'A Data Analysis and Sensitivity-Optimization Framework for the KATRIN Experiment'. http://digbib.ubka.uni-karlsruhe.de/volltexte/1000043301. PhD thesis. KIT/IEKP, 2014 (cit. on pp. 47–49, 167, 168, 170–172).

[Kle15] Marco Kleesiek: *Neutrino Mass Sensitivity - early data and high-statistics data.* 29. Collaboration Meeting: Plenary 4. KATRIN collaboration internal. https://fuzzy.fzk.de/bscw/bscw.cgi/d973712/95-TRP-5939-P4-MKleesiek.pdf, Oct. 2015 (cit. on pp. 57, 170).

[Kna73] A.G. Knapp: 'Surface potentials and their measurement by the diode method'. In*Surface Science* (1973), vol. 34(2): pp. 289–316. doi: 10.1016/0039-6028(73)90120-9 (cit. on pp. 130, 133).

[KOB73] Makoto KOBAYASHI and Toshihide MASKAWA: 'CP-Violation in the Renormalizable Theory of Weak Interaction'. In*Prog. Theor. Phys.* (2 Feb. 1973), vol. 49: pp. 652–657. doi: 10.1143/PTP.49.652 (cit. on p. 5).

[Kod01] K. Kodama et al.: 'Observation of tau neutrino interactions'. In*Physics Letters B* (2001), vol. 504(3): pp. 218–224. doi: 10.1016/S0370-2693(01)00307-0 (cit. on p. 2).

[Kop14] Andreas Kopmann: *Status DAQ + Slow Control.* 26. Collaboration Meeting: Plenary Session 4. KATRIN collaboration internal. https://fuzzy.fzk.de/bscw/bscw.cgi/d876809/95-TRP-5622-S4-AKopmann.pdf, Mar. 2014 (cit. on p. 49).

[Kop08] Andreas Kopmann and et al.: 'FPGA-based DAQ system for multi-channel detectors'. In*Nuclear Science Symposium Conference Record, 2008. NSS 08. IEEE* (2008), vol.: pp. 3186–3190. doi: 10.1109/NSSMIC.2008.4775027 (cit. on p. 48).

[Kop15] Andreas Kopmann et al.: *ADEI (Advanced Data Extraction Infrastracture).* https://www.ipe.kit.edu/293.php. KIT/IPE, 2015 (cit. on p. 49).

[Kra16] Marcel Kraus: 'Energy-scale systematics at the KATRIN main spectrometer'. PhD thesis. KIT/IEKP, 2016. doi: 10.5445/IR/1000054447 (cit. on pp. 30, 38, 39, 119, 121, 128, 130).

[Kra12] Marcel Kraus: 'Kalibration und Entwicklung von Komponenten für das KATRIN Präzisions-Hochspannungssystem'. http://www.katrin.kit.edu/publikationen/dth-kraus-M.pdf. Diploma thesis. KIT/IEKP, 2012 (cit. on p. 30).

[Kru83] P Kruit and F H Read: 'Magnetic field paralleliser for 2π electron-spectrometer and electron-image magnifier'. In*Journal of Physics E: Scientific Instruments* (1983), vol. 16(4): p. 313. doi: 10.1088/0022-3735/16/4/016 (cit. on pp. 14, 15).

[Lak15] Lake Shore Cryotronics Inc.: *Specifications Three-Axis Probes.* http://www.lakeshore.com/products/hall-probes/multi-axis-probes/pages/Specifications.aspx, 2015 (cit. on p. 58).

[Lam09] Melanie Lammers: 'Untersuchung der Untergrundrate des KATRIN Vorspektrometers im Bereich hoher Feldstärken'. https://fuzzy.fzk.de/bscw/bscw.cgi/d578755/dth-lammers.pdf. Diploma thesis. KIT/IEKP, 2009 (cit. on p. 24).

[Lei14] Benjamin Leiber: 'Investigations of background due to secondary electron emission in the KATRIN-experiment'. http://digbib.ubka.uni-karlsruhe.de/volltexte/1000042415. PhD thesis. KIT/IEKP, 2014 (cit. on pp. 24, 26, 35, 89, 184, 215).

[LEM14] LEM: *Current Transducer IT 200-S ULTRASTAB*. http://www.lem.com/docs/products/it_200-s_ultrastab.pdf. June 2014 (cit. on pp. 43, 44, 49).

[Let15] J. Letnev, P. Marte, A. Osipowicz, and W. Seller: *MobSU - NEWS '15*. 28. Collaboration Meeting: Plenary Session 5. KATRIN collaboration internal. https://fuzzy.fzk.de/bscw/bscw.cgi/d951194/95-TRP-5862-S5-JLetnev.pdf, Mar. 2015 (cit. on p. 55).

[Let] Johann Letnev: 'Commissioning of the mobile sensor-unit system at the KATRIN experiment'. in preparation. PhD thesis. Hochschule Fulda (cit. on p. 113).

[Let11] Johann Letnev: 'Systemintegration des Magnetfeldsensornetzes'. https://fuzzy.fzk.de/bscw/bscw.cgi/775179. Master thesis. Hochschule Fulda, 2011 (cit. on pp. 55, 109).

[Lob85] V.M. Lobashev and P.E. Spivak: 'A method for measuring the electron antineutrino rest mass'. In*Nuclear Instruments and Methods in Physics Research Section A: Accelerators, Spectrometers, Detectors and Associated Equipment* (1985), vol. 240(2): pp. 305–310. doi: 10.1016/0168-9002(85)90640-0 (cit. on pp. 14, 15).

[Luc00] L. L. Lucas and M. P. Unterweger: 'Comprehensive Review and Critical Evaluation of the Half-Life of Tritium'. In*J.Res.Natl.Inst.Stand.Technol* (2000), vol. 105(4): pp. 541–549. doi: 10.6028/jres.105.043 (cit. on p. 14).

[Luk12] S. Lukić, B. Bornschein, L. Bornschein, G. Drexlin, A. Kosmider, K. Schlösser, and A. Windberger: 'Measurement of the gas-flow reduction factor of the KATRIN DPS2-F differential pumping section'. In*Vacuum* (2012), vol. 86(8): pp. 1126–1133. doi: 10.1016/j.vacuum.2011.10.017 (cit. on p. 29).

[Luo08] X. Luo and C. Day: 'Test particle Monte Carlo study of the cryogenic pumping system of the Karlsruhe tritium neutrino experiment'. In*Journal of Vacuum Science & Technology A* (2008), vol. 26(5): pp. 1319–1325. doi: 10.1116/1.2956628 (cit. on p. 29).

[Luo06] X. Luo, Chr. Day, V. Hauer, O.B. Malyshev, R.J. Reid, and F. Sharipov: 'Monte Carlo simulation of gas flow through the KATRIN DPS2-F differential pumping system'. In*Vacuum* (2006), vol. 80(8): pp. 864–869. doi: 10.1016/j.vacuum.2005.11.044 (cit. on p. 28).

[Maj37] Ettore Majorana: 'Teoria simmetrica dell'elettrone e del positrone'. In*Nuovo Cim.* (1937), vol. 14. In Italian: pp. 171–184. doi: 10.1007/BF02961314 (cit. on pp. 8, 10).

[Maj15] B. Majorovits: 'Phase {II} Upgrade of the {GERDA} Experiment for the Search of Neutrinoless Double Beta Decay'. In*Physics Procedia* (2015), vol. 61. 13th International Conference on Topics in Astroparticle and Underground Physics, {TAUP} 2013: pp. 254–259. doi: 10.1016/j.phpro.2014.12.041 (cit. on p. 11).

[Mak62] Ziro Maki, Masami Nakagawa, and Shoichi Sakata: 'Remarks on the Unified Model of Elementary Particles'. In*Progress of Theoretical Physics* (1962), vol. 28(5): pp. 870–880. doi: 10.1143/PTP.28.870 (cit. on p. 3).

[Mea08] Measurement Specialties, Inc.: *KMY/KMZ Linear Magnetic Field Sensors*. http://www.datasheetlib.com/datasheet/191909/kmz20m_msi-measurement-specialties-inc.html, 2008 (cit. on p. 51).

[Mer12] Susanne Mertens: 'Study of Background Processes in the Electrostatic Spectrometers of the KATRIN Experiment'. http://nbn-resolving.org/urn:nbn:de:swb:90-270589. PhD thesis. KIT/IEKP, 2012 (cit. on pp. 28, 215).

[Mer14] Susanne Mertens, Alan Poon, and Joachim Wolf: *KATRIN Blind Analysis*. 26. Collaboration Meeting: Plenary Session 5. KATRIN collaboration internal. https://fuzzy.fzk.de/bscw/bscw.cgi/877195?op=preview&back_url=21079, Mar. 2014 (cit. on p. 170).

[Mon15] Ben Monreal and Florian Priester: *Rear Section status update*. 28. Collaboration Meeting: Plenary 1. KATRIN collaboration internal. http://fuzzy.fzk.de/bscw/bscw.cgi/d950718/95-TRP-5841-S1-BMonreal.pdf, Mar. 2015 (cit. on p. 28).

[Mon09] Benjamin Monreal and Joseph A. Formaggio: 'Relativistic cyclotron radiation detection of tritium decay electrons as a new technique for measuring the neutrino mass'. In*Phys. Rev. D* (5 Sept. 2009), vol. 80: p. 051301. doi: 10.1103/PhysRevD.80.051301 (cit. on p. 14).

[Mue14] Axel Mueller: 'Field Alignment Studies at the KATRIN Pinch Magnet'. https://fuzzy.fzk.de/bscw/bscw.cgi/977642?op=preview&back_url=831858. BA thesis. KIT/IEKP, 2014 (cit. on p. 58).

[Mül02] Beatrix Müller: 'Umbau des Mainzer Neutrinomassenexperiments und Untergrunduntersuchungen im Hinblick auf KATRIN'. https://www.katrin.kit.edu/publikationen/dth-mueller.pdf. Diploma thesis. University of Mainz, 2002 (cit. on p. 24).

[Mur12] Murata Electronics Oy: *DATA SHEET - THE SCA121T DUAL AXIS INCLINOMETER MODULES*. http://www.mouser.com/pdfdocs/sca121t_inclinometer_datasheet_82127400a2.PDF. 2012 (cit. on p. 55).

[N A14] F. T. Avignone III et al. N. Abgrall E. Aguayo: 'The MAJORANA DEMONSTRATOR Neutrinoless Double-Beta Decay Experiment'. In*Advances in High Energy Physics* (2014), vol. 2014: p. 18. doi: 10.1155/2014/365432 (cit. on p. 11).

[Nad05] Saralees Nadarajah: 'A generalized normal distribution'. In*Journal of Applied Statistics* (2005), vol. 32(7): pp. 685–694. doi: 10.1080/02664760500079464 (cit. on p. 131).

[Noe06] M. Noe, R. Gehring, S. Grohmann, H. Neumann, O. Kazachenko, B. Bornschein, and J. Bonn: 'The development of the KATRIN magnet system'. In*Journal of Physics: Conference Series* (2006), vol. 43(1): p. 710. doi: 10.1088/1742-6596/43/1/174 (cit. on p. 24).

[Nte14] Athina Ntefidou, Fabian Harms, Johannes Schwarz, and Thomas Thümmler: *BG08.02 FPD-Mainspec Alignment*. ELOG: SDS-Measurements Phase 2, ID: 7. KATRIN collaboration internal. https://neutrino.ikp.kit.edu:8080/SDS-Measurements+Phase+2/7, 2014 (cit. on pp. 59, 219).

[Obl13] N. S. Oblath: 'Project 8: Using Radio-Frequency Techniques to Measure Neutrino Mass'. In*Meeting of the APS Division of Particles and Fields (DPF 2013) Santa Cruz, California, USA*. https://arxiv.org/abs/1310.0397. 2013 (cit. on p. 14).

[Oli14] K.A. Olive and Particle Data Group: 'Review of Particle Physics'. In*Chinese Physics C* (2014), vol. 38(9): p. 090001. doi: 10.1088/1674-1137/38/9/090001 (cit. on pp. 4, 5, 7, 14).

[Osi14] A. Osipowicz, F. Feige, J. Letnev, P. Marte, and W. Seller: *Installation and Performance of 2 Mobile Sensor Units (MobSU) - Field homogeneity in spectrometer hall*. 27. Collaboration Meeting: Plenary Session 5. KATRIN collaboration internal. http://fuzzy.fzk.de/bscw/bscw.cgi/d936551/95-TRP-5759-S5-AOsipowicz.pdf, Oct. 2014 (cit. on p. 56).

[Osi12a] A. Osipowicz, U. Rausch, A. Unru, and B. Zipfel: 'A scheme for the determination of the magnetic field in the KATRIN main spectrometer'. In*arXiv* (2012), vol. Instrumentation and Detectors. http://arxiv.org/abs/1209.5184 (cit. on p. 88).

[Osi12b] A. Osipowicz, W. Seller, J. Letnev, P. Marte, A. Müller, A. Spengler, and A. Unru: 'A mobile magnetic sensor unit for the KATRIN main spectrometer'. In*Journal of Instrumentation* (2012), vol. 7(06): T06002. doi: 10.1088/1748-0221/7/06/T06002 (cit. on pp. 55, 87, 109).

[Ott94] E. W. Otten: 'The Mainz neutrino mass experiment'. In*Progress in Particle and Nuclear Physics* (1994), vol. 32: pp. 153–171. doi: 10.1016/0146-6410(94)90016-7 (cit. on p. 14).

[Ott10] Ernst Otten: 'Searching the absolute neutrino mass in tritium β-decay—interplay between nuclear, atomic and molecular physics'. In*Hyperfine Interactions* (2010), vol. 196(1): pp. 3–23. doi: 10.1007/s10751-009-0150-2 (cit. on p. 12).

[Par08] Stephen J. Parke: 'CP Violation in the Neutrino Sector'. In*arXiv* (May 2008), vol. hep-ph(Flavor Physics and CP Violation, Taipei, Taiwan.). https://arxiv.org/abs/0807.3311 (cit. on p. 8).

[Pau30] W. Pauli: *Offener Brief an die Gruppe der Radioaktiven bei der Gauvereins-Tagung zu Tübingen*. http://www.symmetrymagazine.org/sites/default/files/legacy/pdfs/200703/logbook_letter.pdf. 1930 (cit. on p. 1).

[Pei02] Zeting Pei and C. Neil Berglund: 'Angular Distribution of Photoemission from Gold Thin Films'. In*Japanese Journal of Applied Physics* (2002), vol. 41(1A): p. L52. doi: 1347-4065/41/i=1A/a=L52 (cit. on pp. 139, 155).

[Per04] Donald H. Perkins: *Particle Astrophysics*. Oxford master series in physics: 2. ed., reprint. Oxford Univ. Press, 2004 (cit. on p. 1).

[Phi98] Philips Semiconductors: *KMZ10B - Magnetic field sensor*. http://pdf.datasheetcatalog.com/datasheet/philips/KMZ10B_3.pdf, 1998 (cit. on p. 51).

[Phi10] D. G. Phillips and et al.: 'Characterization of an FPGA-based DAQ system in the KATRIN experiment'. In*Nuclear Science Symposium Conference Record (NSS/MIC), 2010 IEEE* (2010), vol.: pp. 1399–1403. DOI: 10.1109/NSSMIC.2010.5874002 (cit. on p. 48).

[Pic92] A. Picard et al.: 'A solenoid retarding spectrometer with high resolution and transmission for keV electrons'. In*Nuclear Instruments and Methods in Physics Research Section B: Beam Interactions with Materials and Atoms* (1992), vol. 63(3): pp. 345–358. DOI: 10.1016/0168-583X(92)95119-C (cit. on pp. 15, 150).

[Pla14] Planck Collaboration et al.: 'Planck 2013 results. XVI. Cosmological parameters'. In*A&A* (2014), vol. 571: A16. DOI: 10.1051/0004-6361/201321591 (cit. on p. 10).

[Pla16] Planck Collaboration et al.: 'Planck 2015 results'. In*A&A* (2016), vol. 594: A1. DOI: 10.1051/0004-6361/201527101 (cit. on p. 9).

[Pli10] P. Plischke, A. Felden, and J. Grimm: *Resistance tests for air coil cable*. KATRIN collaboration internal. https://fuzzy.fzk.de/bscw/bscw.cgi/709559, 2010 (cit. on p. 78).

[Pon68] Bruno Pontecorvo: 'Neutrino experiments and the problem of conservation of leptonic charge'. In*Sov. Phys. JETP* (1968), vol. 26(984). http://www.jetp.ac.ru/cgi-bin/dn/e_026_05_0984.pdf: p. 25 (cit. on p. 3).

[Pra11] Matthias Prall: 'Background Reduction of the KATRIN Spectrometers: Transmission Function of the Pre-Spectrometer and Systematic Tests of the Main-Spectrometer Wire Electrode'. https://fuzzy.fzk.de/bscw/bscw.cgi/d895377/phd-prall.pdf. PhD thesis. University Münster, 2011 (cit. on pp. 29, 30, 38).

[Pra12] M. Prall et al.: 'The KATRIN pre-spectrometer at reduced filter energy'. In*New Journal of Physics* (2012), vol. 14(7): p. 073054. DOI: 10.1088/1367-2630/14/7/073054 (cit. on p. 29).

[Pri15] Florian Priester, Michael Sturm, and Beate Bornschein: 'Commissioning and detailed results of {KATRIN} inner loop tritium processing system at Tritium Laboratory Karlsruhe'. In*Vacuum* (2015), vol. 116: pp. 42–47. DOI: 10.1016/j.vacuum.2015.02.030 (cit. on p. 27).

[Qia15] X. Qian and P. Vogel: 'Neutrino mass hierarchy'. In*Progress in Particle and Nuclear Physics* (2015), vol. 83: pp. 1–30. DOI: 10.1016/j.ppnp.2015.05.002 (cit. on p. 7).

[Rei13] Jan Reich: 'Magnetic Field Inhomogeneities and Their Influence on Transmission and Background at the KATRIN Main Spectrometer'. http://digbib.ubka.uni-karlsruhe.de/volltexte/1000033076. PhD thesis. KIT/IEKP, 2013 (cit. on pp. 44, 65, 87, 89, 90, 94, 97, 104, 180, 215).

[Rei09] Stefan Reimer: 'Ein elektrostatisches Dipolsystem zur Eliminierung von Ionen in der DPS2-F des KATRIN Experimentes'. http://www.katrin.kit.edu/publikationen/dth-reimer.pdf. PhD thesis. KIT/IEKP, 2009 (cit. on p. 29).

[Rei05] F. Reinert and S. Hüfner: 'Photoemission spectroscopy - from early days to recent applications'. In*New Journal of Physics* (Apr. 2005), vol. 7: p. 97. doi: 10.1088/1367-2630/7/1/097 (cit. on pp. 130, 133).

[Rei60] F. Reines, C. L. Cowan, F. B. Harrison, A. D. McGuire, and H. W. Kruse: 'Detection of the Free Antineutrino'. In*Phys. Rev.* (1 Jan. 1960), vol. 117: pp. 159–173. doi: 10.1103/PhysRev.117.159 (cit. on p. 2).

[Rem16] Marcel C. Remillieux, Robert A. Guyer, Cédric Payan, and T. J. Ulrich: 'Decoupling Nonclassical Nonlinear Behavior of Elastic Wave Types'. In*Phys. Rev. Lett.* (11 Mar. 2016), vol. 116: p. 115501. doi: 10.1103/PhysRevLett.116.115501 (cit. on p. 13).

[Ren14] Christoph Renner: 'Charakterisierung und Kalibration der Spannungsquellen zur Versorgung der Drahtelektrode des KATRIN-Experiments'. https://fuzzy.fzk.de/bscw/bscw.cgi/1007176?op=preview&back_url=831858. BA thesis. KIT / IEKP, 2014 (cit. on p. 127).

[Ren11] Pascal Renschler: 'KESS - A new Monte Carlo simulation code for low-energy electron interactions in silicon detectors'. http://digbib.ubka.uni-karlsruhe.de/volltexte/1000024959. PhD thesis. KIT/IEKP, 2011 (cit. on p. 31).

[Rep83] Wayne W. Repko and Chong-en Wu: 'Radiative corrections to the end point of the tritium β decay spectrum'. In*Phys. Rev. C* (6 Dec. 1983), vol. 28: pp. 2433–2436. doi: 10.1103/PhysRevC.28.2433 (cit. on p. 169).

[Res14] Oliver Rest: 'Inbetriebnahme der Präzisionshochspannung am Hauptspektrometer des KATRIN-Experiments'. http://www.uni-muenster.de/Physik.KP/AGWeinheimer/Files/theses/master_oliver_rest.pdf. MA thesis. University Münster, 2014 (cit. on p. 30).

[Res15] Oliver Rest and Sascha Wüstling: *KATRIN high voltage status for SDS-II and general outlook*. 28. Collaboration Meeting: Plenary Session 2. KATRIN collaboration internal. https://fuzzy.fzk.de/bscw/bscw.cgi/d950863/95-TRP-5849-S2-ORest.pdf, Mar. 2015 (cit. on p. 46).

[Rob88] R G H Robertson and D A Knapp: 'Direct Measurements of Neutrino Mass'. In*Annual Review of Nuclear and Particle Science* (1988), vol. 38(1): pp. 185–215. doi: 10.1146/annurev.ns.38.120188.001153 (cit. on p. 14).

[Röl13] M. Röllig et al.: 'Activity monitoring of a gaseous tritium source by beta induced X-ray spectrometry'. In*Fusion Engineering and Design* (2013), vol. 88(6–8). Proceedings of the 27th Symposium On Fusion Technology (SOFT-27); Liège, Belgium, September 24-28, 2012: pp. 1263–1266. doi: 10.1016/j.fusengdes.2012.11.001 (cit. on p. 27).

[Rov13] Philipp Rovedo: 'Muon induced secondary electrons at the KATRIN experiment - Detector installation and setup and data analysis'. https://fuzzy.fzk.de/bscw/bscw.cgi/d862453/dth_rovedo.pdf. Diploma thesis. KIT/IEKP, 2013 (cit. on p. 90).

[Sac15] Rodolf Sack: 'Aufbau einer Ionenquelle und Simulation der Transporteigenschaften der DPS am KATRIN Experiment'. in preperation. MA thesis. KIT / IEKP, 2015 (cit. on pp. 29, 89).

[Sae00] Alejandro Saenz, Svante Jonsell, and Piotr Froelich: 'Improved Molecular Final-State Distribution of HeT^+ for the *fi*-Decay Process of T_2'. In*Phys. Rev. Lett.* (2 Jan. 2000), vol. 84: pp. 242–245. doi: 10.1103/PhysRevLett.84.242 (cit. on p. 170).

[Sch14a] Boris Schäling: *the Boost C++ Libraries*. XML Press, 2014 (cit. on p. 49).

[Sch13] Magnus Schlösser: 'Accurate Calibration of Raman Systems - At the Karlsruhe Tritium Neutrino Experiment'. In*Springer, Berlin* (2013), vol. doi: 10.1007/978-3-319-06221-1 (cit. on pp. 10, 12, 27).

[Sch97] Norbert Schmitz: *Neutrinophysik : mit 23 Tabellen*. Teubner-Studienbücher : Physik. Stuttgart: Teubner, 1997 (cit. on pp. 1, 8).

[Sch88] *Proceedings of the 13th International Conference on Neutrino Physics and Astrophysics : Boston (Medford)*. ISBN: 9971-5-0778-1. International Conference on Neutrino Physics and Astrophysics. Singapore [u.a.] : World Scientific, 1988 (cit. on p. 1).

[Sch16] Kerstin Schönung: 'Development of a Rear Wall for the KATRIN Rear Section and investigation of tritium compatibility of Rear Section components'. PhD thesis. KIT/IEKP, 2016. doi: 10.5445/IR/1000056077 (cit. on p. 27).

[Sch11] Michael Schupp: 'Inbetriebnahme des Monitorspektrometers und erste Messungen'. http://www.katrin.kit.edu/downloads/dth-schupp.pdf. Diploma thesis. KIT/IEKP, 2011 (cit. on p. 32).

[Sch04] Hans Rudolf Schwarz and Norbert Köckler: *Numerische Mathematik*. 5., überarb. Aufl. Lehrbuch Mathematik. Stuttgart: Teubner, 2004 (cit. on p. 134).

[Sch14b] Johannes Schwarz: 'The Detector System of the KATRIN Experiment - Implementation and First Measurements with the Spectrometer'. http://digbib.ubka.uni-karlsruhe.de/volltexte/1000042772. PhD thesis. KIT/IEKP, 2014 (cit. on pp. 10, 12, 17, 24, 26, 31, 35, 40, 41, 48, 59, 184, 215).

[Sco35] F. A. Scott: 'Energy Spectrum of the Beta-Rays of Radium E'. In*Phys. Rev.* (5 Sept. 1935), vol. 48: pp. 391–395. doi: 10.1103/PhysRev.48.391 (cit. on p. 1).

[Sel13] Waldemar Seller: 'Elektromechanische Realisierung eines Magnetfeldmesssystems für den KATRIN Hauptspektrometertank'. https://fuzzy.fzk.de/bscw/bscw.cgi/775179. Master thesis. Hochschule Fulda, 2013 (cit. on p. 55).

[Sim81] J. J. Simpson: 'Measurement of the β-energy spectrum of ^3H to determine the antineutrino mass'. In*Phys. Rev. D* (3 Feb. 1981), vol. 23: pp. 649–662. doi: 10.1103/PhysRevD.23.649 (cit. on p. 169).

[Sis04] M. Sisti et al.: 'New limits from the Milano neutrino mass experiment with thermal microcalorimeters'. In*Nuclear Instruments and Methods in Physics Research A* (Mar. 2004), vol. 520: pp. 125–131. DOI: 10.1016/j.nima.2003.11.273 (cit. on p. 13).

[Sle16] Martin Slezák: 'Monitoring of the energy scale in the KATRIN neutrino experiment'. https://www.katrin.kit.edu/publikationen/phd-Martin_Slezak.pdf. PhD thesis. Charles University, Prague, 2016 (cit. on p. 32).

[Sle13] M. Slezák et al.: 'Electron line shape of the KATRIN monitor spectrometer'. In*Journal of Instrumentation* (2013), vol. 8(12): T12002. DOI: 10.1088/1748-0221/8/12/T12002 (cit. on p. 32).

[Sta13] Nils Stallkamp: 'Optimierung und erste Messung der Transmissionseigenschaften des KATRIN-Hauptspektrometers'. https://fuzzy.fzk.de/bscw/bscw.cgi/d847501/dth-stallkamp.pdf. diploma thesis. KIT/IEKP, 2013 (cit. on pp. 59, 68, 78).

[Stu10] Michael Sturm: 'Aufbau und Test des Inner-Loop-Systems der Tritiumquelle von KATRIN'. http://d-nb.info/1005447187/34. PhD thesis. KIT/IEKP, 2010 (cit. on p. 27).

[Stu12] Michael Sturm: *DPS: New concept for the differential pumping section*. 23. Collaboration Meeting: Plenary Session 2. KATRIN collaboration internal. https://fuzzy.fzk.de/bscw/bscw.cgi/750514, Oct. 2012 (cit. on p. 24).

[Sud15] David Sudermann: 'Optimization of the demagnetizing parameters of construction steel in the KATRIN experimental hall'. https://fuzzy.fzk.de/bscw/bscw.cgi/831858. BA thesis. KIT / IEKP, 2015 (cit. on p. 107).

[Thu] Thomas Thuemmler et al.: 'System setup for the first commissioning measurements with the KATRIN main spectrometer'. in preperation (cit. on p. 35).

[Tro15] Nikolaus Trost: *Background Simulations*. 28. Collaboration Meeting: Plenary Session 5. KATRIN collaboration internal. https://fuzzy.fzk.de/bscw/bscw.cgi/d950468/95-TRP-5831-D1.1-NTrost.pdf, Mar. 2015 (cit. on pp. 66, 211).

[Tro17] Nikolaus Trost: 'Validation of the KATRIN Background Model'. in preparation. PhD thesis. KIT/IEKP, 2017 (cit. on pp. 215, 216).

[Ubi09] M. Ubieto-Díaz, D. Rodríguez, S. Lukic, S. Nagy, S. Stahl, and K. Blaum: 'A broad-band FT-ICR Penning trap system for KATRIN'. In*International Journal of Mass Spectrometry* (2009), vol. 288(1â€“3): pp. 1–5. DOI: 10.1016/j.ijms.2009.07.003 (cit. on p. 29).

[Val10] K. Valerius: 'The wire electrode system for the KATRIN main spectrometer'. In*Progress in Particle and Nuclear Physics* (2010), vol. 64(2). Neutrinos in Cosmology, in Astro, Particle and Nuclear PhysicsInternational Workshop on Nuclear Physics, 31st course: pp. 291–293. DOI: 10.1016/j.ppnp.2009.12.032 (cit. on pp. 30, 38).

[Val16] Kathrin Valerius: *Direct mass searches: KATRIN and Project 8 and searches with Holmium*. Proceedings of the XXVII international conference on neutrino physics and astrophysics, in preperation. http://neutrino2016.iopconfs.org/IOP/media/uploaded/EVIOP/event_948/kvalerius_directnumass_v4_web.pdf. 2016 (cit. on p. 170).

[Val09] Kathrin Valerius: 'Spectrometer-related background processes and their suppression in the KATRIN experiment'. http://repositorium.uni-muenster.de/document/miami/93137705-73f4-404a-a438-09d487cbff63/diss_valerius.pdf. PhD thesis. University Münster, 2009 (cit. on pp. 17, 30, 38).

[Wac15] Oliver Wack: 'Automation of the high precision calibrations for the KATRIN high voltage setup'. https://fuzzy.fzk.de/bscw/bscw.cgi/d977499/mth_wack_oliver.pdf. MA thesis. KIT / IEKP, 2015 (cit. on pp. 30, 121, 145, 211).

[Wal13] Brandon Lee Wall: 'Karlsruhe Tritium Experiment: Detector System Commissioning and In-Situ PIN-Diode Array Dead-Layer Measurement'. internal: https://fuzzy.fzk.de/bscw/bscw.cgi/776423?op=preview&back_url=859868. PhD thesis. University of Washington, 2013 (cit. on p. 31).

[Wan13a] N. Wandkowsky, G. Drexlin, F.M. Fränkle, F. Glück, S. Groh, and S. Mertens: 'Validation of a model for radon-induced background processes in electrostatic spectrometers'. In*Journal of Physics G: Nuclear and Particle Physics* (2013), vol. 40(8): p. 085102. doi: 10.1088/0954-3899/40/8/085102 (cit. on p. 24).

[Wan13b] Nancy Wandkowsky: 'Study of background and transmission properties of the KATRIN spectrometers'. http://digbib.ubka.uni-karlsruhe.de/volltexte/1000036631. PhD thesis. KIT/IEKP, 2013 (cit. on pp. 25, 28, 30, 45, 184, 215, 216, 219).

[Wei35] C. F. v. Weizsäcker: 'Zur Theorie der Kernmassen'. In*Zeitschrift für Physik* (1935), vol. 96(7): pp. 431–458. doi: 10.1007/BF01337700 (cit. on p. 10).

[Wie16] Kevin Wierman: 'Simulations of the penning trap between the KATRIN pre- and main-spectrometer'. in preparation. PhD thesis. Universtiy of North Carolina, 2016 (cit. on pp. 141, 154).

[Wie09] J. S. E. Wieslander et al.: 'Smallest Known Q Value of Any Nuclear Decay: The Rare β^- Decay of $^{115}\mathrm{In}(9/2^+) \rightarrow ^{115}\mathrm{Sn}(3/2^+)$'. In*Phys. Rev. Lett.* (12 Sept. 2009), vol. 103: p. 122501. doi: 10.1103/PhysRevLett.103.122501 (cit. on p. 13).

[Win11] Alexander Windberger: 'Berechnungen und Simulationen zum Verhalten von Ionen in der differenziellen Pumpstrecke des KATRIN-Experiments'. http://www.katrin.kit.edu/publikationen/dth-windberger.pdf. Diploma thesis. KIT/IEKP, 2011 (cit. on p. 29).

[Wol14] Joachim Wolf: *De-Magnetization of the Spectrometer Building*. 27. Collaboration Meeting: Plenary Session 5. KATRIN collaboration internal. https://fuzzy.fzk.de/bscw/bscw.cgi/d936561/95-TRP-5760-S5-JWolf.pdf, Oct. 2014 (cit. on pp. 90, 104).

[Won15] Björn Wonsak: 'Status and Perspectives of the {COBRA} Experiment'. In*Phy. Procedia* (2015), vol. 61. 13th International Conference on Topics in Astroparticle and Underground Physics, {TAUP} 2013: pp. 295–299. doi: 10.1016/j.phpro.2014.12.048 (cit. on p. 11).

[Wüs07] Sascha Wüstling: *Magnetometer for the KATRIN main spectrometer*. 12. Collaboration Meeting: Parallel Session C1. KATRIN collaboration internal. https://fuzzy.fzk.de/bscw/bscw.cgi/d358586/95-TRP-4250-C1-SWuestling.pdf, Mar. 2007 (cit. on p. 51).

[Yan80] Tsutomu Yanagida: 'Horizontal Symmetry and Masses of Neutrinos'. In*Progress of Theoretical Physics* (1980), vol. 64(3): pp. 1103–1105. doi: 10.1143/PTP.64.1103 (cit. on p. 9).

[Zac09] Michael Zacher: 'Electromagnetic design and field emission studies for the inner electrode system of the KATRIN main spectrometer'. http://www.uni-muenster.de/Physik.KP/AGWeinheimer/Files/theses/Diplom_Michael_Zacher.pdf. Diploma thesis. University Münster, 2009 (cit. on pp. 30, 38).

[Zac14] Michael Zacher: 'High-field electrodes design and an angular-selective photoelectron source for the KATRIN spectrometers'. https://fuzzy.fzk.de/bscw/bscw.cgi/d968937/PhD_Michael_Zacher_only_internal.pdf. PhD thesis. University Münster, 2014 (cit. on pp. 16, 22, 44, 119, 130, 136, 139, 156).

[Zbo11] Miroslav Zbořil: 'Solid electron sources for the energy scale monitoring in the KATRIN experiment'. http://repositorium.uni-muenster.de/document/miami/79b74253-2dcd-493b-a08d-4eeb5a10b8c1/diss_zboril.pdf. PhD thesis. University Münster, 2011 (cit. on p. 32).

[Zub12] Kai Zuber: *Neutrino physics*. 2. ed. Series in high energy physics, cosmology, and gravitation. Boca Raton, Fla. [u.a.]: CRC Press, 2012 (cit. on pp. 1, 5–7, 9).

List of Figures

List of Tables

Glossary

Acronyms

ADC	analog digital converters
BIXS	β-induced X-ray spectroscopy
CDM	cold dark matter
cFP	compact Field Point
CKM-Matrix	Cabibbo-Kobayashi-Maskawa-Matrix
COBRA	Cadmium Zinc Telluride 0-Neutrino Double-Beta Research Apparatus
CPS	Cryogenic Pumping Section
DAC	digital analog converters
DAQ	data-acquisition
DET	detector magnet
DPS	differential pumping section
DVM	digital voltmeter
e-gun	electron gun
ECHo	Electron Capture ^{163}Ho
EMCS	earth magnetic field compensation system
EXO-200	Enriched Xenon Observatory
FLT	first-level trigger
FPD	focal-plane detector system
GERDA	Germanium Detector Array
GUT	Grand Unified Theory
HOPG	highly ordered pyrolytic graphic
HV	high voltage

IPE	Institute for Data Processing and Electronics
K2K	KEK to Kamioka
KaFit	KATRIN fit module
KATRIN	Karlsruhe tritium neutrino
LFCS	low field correction system
MAC-E filter	magnetic adiabatic collimation with electrostatic filtering
MINOS	Main Injector Neutrino Oscillation Search
MobSU	mobile magnetic sensor unit
MoS	monitor spectrometer
MSW	Mikheyev-Smirnov-Wolfenstein
NEG	non-evaporable getter
NOνA	NuMI Off-Axis ν Appearance
OPERA	Oscillation Project with Emulsion Tracking Apparatus
ORCA	object-oriented real-time control and acquisition
PAE	post-acceleration electrode
PCH	pinch magnet
PMNS	Pontecorvo–Maki–Nakagawa–Sakata
PS 1	pre-spectrometer magnet 1
PS 2	pre-spectrometer magnet 2
PSU	power supply unit
px	pixel
RENO	Reactor Experiment for Neutrino Oscillations
ROI	region of interest
SDS	spectrometer and detector section
SDS 1	first commissioning measurement phase of the spectrometer and detector section
SDS 2	second commissioning measurement phase
SLT	second-level trigger
SM	standard model
SNO	Sudbury neutrino observatory

SSC	Source modeling and β-decay spectrum calculation
SSM	standard solar model
T2K	Tokai to Kamioka
TMP	turbo-molecular pumps
UHV	ultra-high vacuum
WGTS	windowless gaseous tritium source

Danksagung

An dieser Stelle möchte ich mich ganz herzlich bei allen bedanken, die mich die letzten Jahre während meiner Promotion begleitet und zum Gelingen meiner Doktorarbeit beigetragen haben. Insbesondere gilt mein Dank den folgenden Personen:

- Prof. Dr. Guido Drexlin der mir die Promotion ermöglichte in diesem anspruchsvollen und spannenden Umfeld, sowie seine Unterstützung während der Promotion.
- Prof. Dr. Wim de Boer für die Übernahme der Aufgabe des Korreferenten dieser Doktorarbeit.
- Für das Korrekturlesen dieser Arbeit und ihre wertvollen Ratschläge bedanke ich mich bei Klaus Schlösser, Susanne Mertens, Thomas Thümmler, Florian Fränkle, Ferenc Glück, Philipp Ranitzsch, Stefan Groh und Marco Kleesiek.
- Bei Birgit Adams und Armin „Bego“ Beglarian für die tolle Zusammenarbeit beim Aufbau und Inbetriebnahme der Magnetometer.
- Den E-Gaunern, Jan Behrens, Marcel Kraus, Philipp Ranitzsch, John Barrett und Kevin Wierman mit denen die SDS 2 Messungen und Zeit im Kontrollraum zum Erfolg wurden, und das trotz (oder wegen?) Ace of Base und Roxette.
- Den Münsteranern des E-Gun Teams Prof. Dr. Christian Weinheimer, Volker Hannen, Daniel Winzen und Hans Werner Ortjohann die sich hervorragend um die Hardware kümmerten.
- Stefan Groh für dessen großartige Hilfestellung in der Vorbereitung der Transmissionsmessungen und deren Auswertung.
- Beim Monitorspektrometer Team um Klaus Schlösser und Martin „Šiška“ Slezák bei denen ich das Laufen als Experimentalphysiker lernte.
- Fabian Harms und Daniel Hilk für die tolle Zusammenarbeit seit der Diplomarbeit und über die gesamte Promotion hinweg.
- Klaus Mehret dem ich die die tollen Fotos zu verdanken habe.
- Dem MobSU Team Alexander Osipowicz, Johann Letnev und Waldemar Seller für die spontane Hilfe und effiziente Durchführung der Messungen.
- Marco Antoni, Ferenc Glück und Jan Reich für die Entwicklungsarbeit an dem Magnetometersystem.

- Jan Behrens und Nikolaus Trost, das sie mir python näher brachten und ich damit (fast) vollständig auf ROOT verzichten konnte.
- Bei allen Young Scientists in 402 die sich meinem Nerf-Gun Beschuss erwehren mussten.
- Marcel Kraus, für seine Hilfe beim Lösen rein mathematischer Problem und die freundschaftliche Atmosphäre im Büro.

Ein ganz herzliches Dankeschön geht an meine Familie, meine Eltern Ingrid und Wolf-Dietrich die immer für mich da waren und sind, sowie mein Bruder Markus auf den ich immer zählen kann.

Je voudrais tout particulièrement remercier ma magnifique Pauline, qui m'a donné la force pour supporter les nuits blanches et pour travailler les weekends. Grâce à toi je sais qu'il y a une vie outre KATRIN, et un avenir après l'achèvement de cette thèse.